DUST AND GAS IN DIFFERENT GALACTIC ENVIRONMENTS

by

Daniela Pinheiro Gonçalves

A thesis submitted in conformity with the requirements
for the degree of Doctor of Philosophy
Graduate Department of Astronomy & Astrophysics
University of Toronto

Abstract

Dust and gas in different Galactic environments
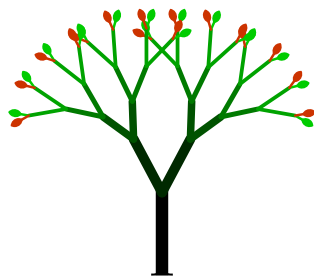
Daniela Pinheiro Gonçalves
Doctor of Philosophy
Graduate Department of Astronomy & Astrophysics
University of Toronto
2013

This thesis encompasses the study of the mid-infrared (IR) dust properties in diffuse high latitude cirrus and in the dense environments of supernova remnants (SNRs) in the plane of our Galaxy. Unlike the well known emission properties of dust grains in the diffuse ISM in the far-IR and submillimeter, the mid-IR spectrum is still relatively unconstrained. We extend the correlation of dust emission with H I column densities to mid-IR wavelengths and look for evidence of variations in the emissivity of dust associated with local and halo gas. This is accomplished by spatially correlating the IR maps from the IRIS/IRAS survey at 12, 25, 60 and 100 μm with H I column density maps inferred from 21-cm line emission observations obtained with the GBT (at a $9'$ resolution). We find that IVCs (halo clouds thought to be part of the Galactic fountain) show color ratios consistent with a dust evolution scenario in which large dust grains are shattered into smaller ones (VSGs). The low 12 μm emission found suggests a reduced abundance of PAHs in IVCs. We also address the IR extragalactic emission seen in our residual maps and quantify its power spectrum behaviour. Continuing with the mid-IR theme, we conducted a comprehensive study of the morphology and energetics of SNRs in the plane of our Galaxy. We make use of the *Spitzer* MIPSGAL (at 24 and 70 μm) and GLIMPSE (at 8 μm) surveys to detected infrared counterparts to SNR candidates in Green's catalog. We find that a third of the sample shows IR emission and calculate the corresponding fluxes. We explore the relation between IR colors to place constraints on the different IR SNRs emission mechanisms. Aided by archival radio data, we find that most candidates detected show IR-to-radio ratios consistent with SNRs with a few exceptions displaying ratios seen in H II regions. Finally, we explore the connection between the IR and the high-energy X-ray emission of SNRs and find a good morphological association between the 24 μm emission and the X-ray features in younger remnants. The IR power is often greater.

TO MY
MOM & DAD

Acknowledgements

Contents

Chapter 1

Introduction

We know accurately only when we know little, with knowledge doubt increases.

— Goethe

In a cosmic context, the phrase *"Death and Taxes, they are certain"* [1] gets roughly translated to *"H I gas and dust, they are certain"*. We can find them almost anywhere we look in the sky. So ubiquitous is their presence, that when cosmic H I was first detected in our Galaxy by Ewen & Purcell (1951), it cemented the importance of radio studies. Unfortunately, dust has gained a reputation for being a nuisance given its ability to block and extinguish radiation from other celestial bodies. H I was first discovered as an independent chemical element by Henry Cavendish in 1766 and it is by far the most abundant atom in the Universe. On the other hand, dust (solid particles made up by heavy chemical elements) has been established as a key factor in the chaotic environment that is the Interstellar Medium (ISM). H I gas and dust are thus the building blocks of the Universe, from simple H I clouds to chemical reservoirs of elements that end up running in our blood.

In this thesis, we will explore the interplay between these two components. In the first part, we will focus on the correlation between gas and dust in the mid-IR range, in diffuse regions found at high Galactic latitudes. In the second part, we will continue to give emphasis to mid-IR observations, but now in the much denser medium of the Galactic plane via the detection of supernova remnants. In the following section, we will discuss the properties of the IR and submillimeter emission properties of dust (mainly in the diffuse ISM) and explore results from previous studies which use gas as a spatial template for obtaining dust emissivities. Finally, we will discuss the importance of dust emission associated with supernova remnants and report on previous studies.

---

[1] Coined by Ward in 1724

1.1 The Interstellar Medium

The ISM is a loose term used to encompass anything in our Galaxy that is not a star, a planet or planetary-system related (such as asteroids and comets) or a black hole. In reality, its main constituents are gas and dust. This definition also includes the carriers of mid-infrared spectral features, often attributed to polycyclic aromatic hydrocarbons (PAHs), besides the usual solid grains. The density and spatial distribution of matter in the ISM can vary greatly throughout the Galaxy depending on the physical conditions that it is subject to, either via velocity gradients or the amount of radiation it is exposed to. Regarding the latter, Mathis *et al.* (1983) showed that the energy density of the InterStellar Radiation Field (ISRF) increases by a factor of 7 when we go to smaller Galactocentric radius ($\sim$ 5 kpc) . Another perspective from this work is that the ISRF is the cumulative contribution of light from stars shining in the ultraviolet (UV) to the near-IR, while the IR to millimeter region is produced by re-emission by dust that has absorbed part of that energetic starlight. In close proximity to the stars, UV photons can easily ionize the gas and heat dust grains to locally higher temperatures. This is the case for most OB clusters where new born stars are strong radiation sources. Such a scenario is commonly observed in our Galactic plane.

1.1.1 Dust

Dust grains have been found to exist in a wide range of Galactic environments, from small planetary disks to large supernova remnant loops (see Figure 1.1 for a brief synopsis of the dust life cycle). The effects of dust are felt via different processes, depending on the dust chemical composition and size and on the strength of the light shining upon it. Dust scatters and absorbs optical and UV radiation from stars and extragalactic sources (see an early review by Savage & Mathis, 1979). Observations of the color excess E(B-V) revealed that gas (in particular, H) is almost always spatially associated with dust extinction (see Figure 1.2). This prompted the creation of the first reddening maps of our Galaxy by Burstein & Heiles (1982) using H I column density and galaxy counts maps. Because of the relation between gas column density and dust extinction, it is not surprising that dust emission can also follow the distribution of gas in the galaxy. This is also seen in many extragalactic observations of spiral galaxies for example. Later on, with the launch of space missions such as IRAS and DIRBE, Schlegel *et al.* (1998) produced higher resolution far-IR-based reddening maps (`http://www.astro.princeton.edu/~schlegel/dust/`) that have been extensively used as a foreground-removal tool for extragalactic studies.
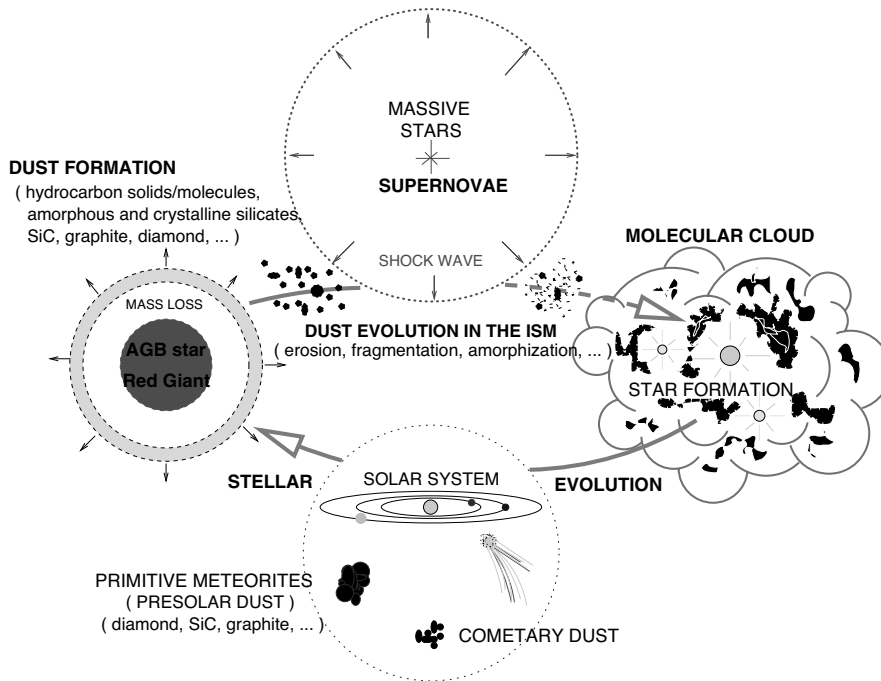
Figure 1.1: This diagrams briefly explains the life cycle of dust in the ISM. From its production in stars at the end of their lives to incorporation in new stars and planetary systems, dust is clearly an integral and active part of the ISM. (Taken from Jones, 2004.)
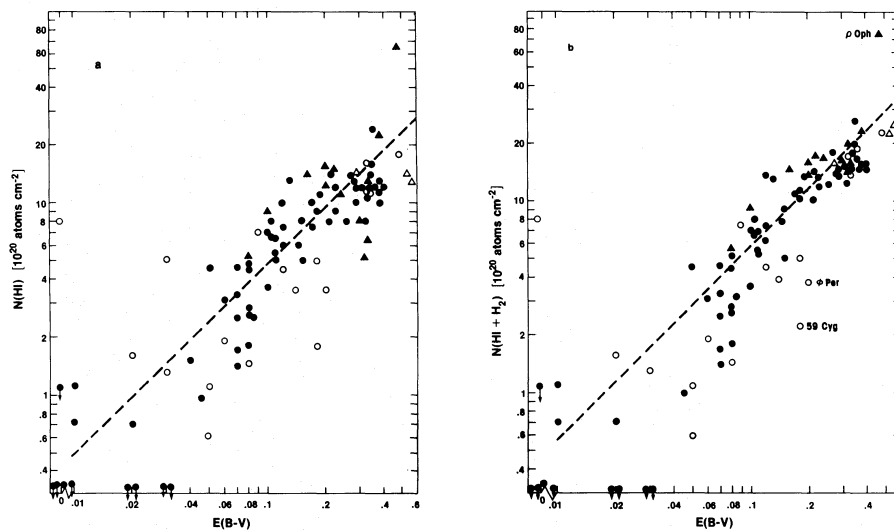
Figure 1.2: Linear correlation between the dust template E(B-V) and atomic H column density (N_{HI}) on the *left* and total H column density on the *right* ($N_H = N_{HI} + 2N_{H_2}$). (Taken from Bohlin *et al.* 1978.)

1.1.2   Dust properties modelled by theory

Theoretical dust models have been built in an incremental fashion, with much of the patch-work guided by observational and laboratory constraints. For example, evidence for the dust composition can come indirectly from the relative depletion of heavy atoms in the gas phase with respect to solar abundances (e.g., Palme & Jones 2005). Another constraint is the wave-length dependence of observed extinction. One of the first models to explain the UV to the near-IR extinction spectrum used particles mainly made up from graphite and silicates with sizes described by a power-law distribution of the form $n(a) \propto a^{-3.5}$, where a is the size of the grain (Mathis *et al.* 1977). More recent models also incorporate and try to understand the dust emission spectrum through variations of the relative abundances of grains of different size and chemical composition and of the ISRF strength.

The dust emission spectrum from the near-IR to the millimeter range in diffuse regions of our Galaxy is argued to be the sum of three different types of grain populations. Observa-tional evidence also indicates that this is the case for other spiral galaxies (e.g., Walterbos & Greenawalt 1996). The spectral shape at the near-IR up to about 15 μm (Figure 1.3) is largely dominated by emission bands characteristic of the stretching and bending modes in PAHs (e.g., Leger & Puget 1984). Most of the mid-IR emission is produced by very small dust grains with radius less than 10 nm. These (carbon) particles are so small that when they absorb single high energy photons, they spike to a high temperature. They cool as they emit non-equilibrium continuum emission profile between about 15 to 80 μm. From the far-IR to the millimeter range, the emission is governed by grains big enough to be in thermal equilibrium with the ISRF; they emit the same amount of energy as absorbed, at constant temperature. This type of dust grain emits empirically as a blackbody modified by a frequency dependent opacity as

$$I_\nu = \sigma_0 \left(\frac{\nu}{\nu_0}\right)^\beta B_\nu(T) N_H, \tag{1.1}$$

where ν is the frequency, $B_\nu(T)$ is the Planck function with a shape and peak set by the dust grain temperature T, σ_0 is the dust opacity (per H) at some fiducial frequency ν_0 and N_H is column density of hydrogen. β is a parameter in the range 1 and 2 depending on the chemical composition and structure (see Hildebrand 1983).

For example, a β of about 2 describes the graphite and silicate grains in Draine & Lee (1984). This model provided an understanding of the thermal emission of bigger dust grains and it was followed by a tentative description of the stochastic emission of smaller dust grains heated to very high temperatures (1000 K) by Draine & Anderson (1985). Later on, Desert *et al.* (1990) introduced a more complete model by including coated silicates as constituents for larger grains, very small grains (VSGs) mostly made of carbon and introducing PAHs to explain the observed UV extinction curve and near-IR emission bands.
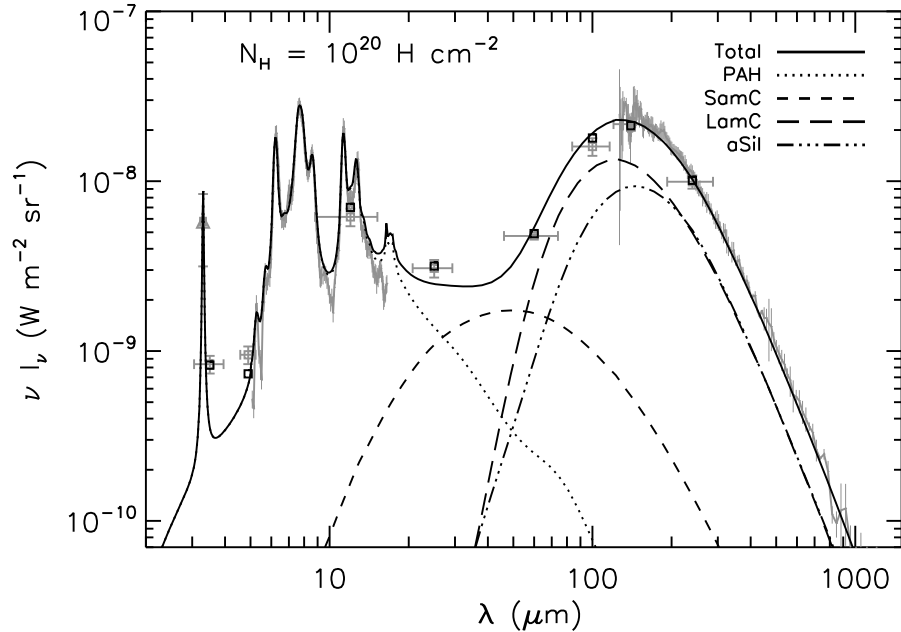
Figure 1.3: DustEM model fit to the dust emission and extinction at diffuse high Galactic latitudes. Contributions to the total SED by the different dust populations are highlighted by the various linestyles. Observational constraints in grey. (Taken from Compiègne *et al.* 2011.)

In a more recent model called DustEM, Compiègne *et al.* (2011) find that a mixture of grains composed of PAHs and amorphous carbon (without graphite) and 'astronomical' silicates is a good template for characterizing the observed emission in diffuse high Galactic latitude regions (see Figure 1.3). They produce a model of the spectral energy distribution of diffuse ISM dust (denoted 'DHGL') that we will use in this thesis as a standard reference for comparison.

1.1.3 Dust evolution

The ISM is by no means a static environment; one can therefore expect grains to be subjected to all sorts of different physical conditions. When McKee & Ostriker (1977) first proposed the 3-phase ISM model, they predicted a hot component (out of equilibrium) resulting from shocks driven by supernova phenomena. Such shocks can impart the gas-grain and grain-grain velocity necessary for grain destruction (e.g., vaporization) which would return part of the locked heavy elements to the gas phase. However, many other processes can affect dust grains without completely destroying them. In such cases, the effect is felt through changes in the size distribution, whether because the grain is broken down into smaller constituents (shattering) or effectively becomes smaller because atoms are removed from its surface (sputtering). Shattering via grain-grain collisions seems to be the easiest way to process dust because it only requires velocities on the order of 1-2 km s^{-1} as proposed by Jones *et al.* (1996). This is thought

to be the main driving mechanism for dust evolution in the warm ISM. These authors showed that shattering can even get rid of most of the bigger dust grains by redistributing their mass into smaller sized grains for shock velocities around 100 km s^{-1}. Such velocity shocks can efficiently destroy PAHs as well as shown by Micelotta *et al.* (2010).

Such evolution of the dust properties can be indirectly inferred from IR observations. For example, in the literature, a high 60/100 ratio is commonly interpreted as a marker for an increased relative abundance of VSGs to big grains. Furthermore, supernova shocks are the key ingredient in the Galactic Fountain scenario in which ionized shocked gas (and dust) gets launched into the halo, where it then recombines and comes down to the Galactic plane due to gravity (e.g., Shapiro & Field, 1976). Bregman (1980) suggested the recombination had to happen at least at a scale height of about 5-10 kpc.

In fact, it would be naïve to assume that all dust in a certain direction in the sky, but in clouds with different velocities, would have the same properties. This sets the stage for the study of intermediate and high-velocity clouds (IVCs and HVCs, respectively) and their dust content (and consequently, their metallicity). Studies in the Large Magellanic cloud (LMC) can also be important for understanding the variations of dust properties in different environments. For example, Bernard *et al.* (2008) conducted a study using *Spitzer* and IRAS data and looked for the spatial correlation of CO, Hα, and the usual H I with the near to far-IR emission. They found a 70 μm excess consistent with an increase in the abundance of large VSGs and suggest its origin lies in the lower metallicity environment found in the LMC.

In the context of dust evolution, there is also evidence for the inverse route, e.g., dust particles getting bigger via aggregation processes in the shadowed regions of molecular clouds (see the recent model proposed by Köhler *et al.* 2012). For example, evidence for grain growth was suggested in the work of Stepnik *et al.* (2003) who observed a low 60/100 ratio and a high opacity relative to the diffuse ISM in a filament of the Taurus molecular cloud. Furthermore, grain coagulation has been proposed by Paradis *et al.* (2009) to explain the increase in opacity in the far-IR to submillimeter found in low Galactic latitude molecular regions with low dust temperatures. Further evidence of dust aggregation has also been advanced in early studies by Kim *et al.* (1994). The authors find different size distributions when fitting distinct extinction curves in two environments, the diffuse medium (R$_V$ = 3.1) and dark molecular clouds (R$_V$ = 5.3); the dense region size distribution showed less of the smaller big grains (20 < a < 100 nm) and a greater number of even larger dust grains. The size of silicate dust grains can also increase via the growth of ice mantles (see Whittet *et al.* 1988) in dense molecular clouds.

1.1.4   H I column density as a template for tracing dust emission

Because the H I gas column density is such a good tracer of Galactic dust emission, many studies have taken place in the last few decades combining large area sky surveys in the infrared,

submillimeter and millimeter range with 21-cm H I surveys. These datasets have been employed to gain insight into the dust spectral energy distribution (SED). Among them, the early analysis by Boulanger & Perault (1988) at high Galactic latitude showed a strong correlation between infrared IRAS (InfraRed Astronomical Satellite; Neugebauer *et al.* 1984) maps (especially at 100 μm) and the H I gas structure. These authors found I_{100}/N_{HI} of 0.85 ± 0.05MJy sr^{-1} (10^{20} H atoms cm^{-2})$^{-1}$. The ratio of I_{ν}/N_{HI} is commonly denoted by ϵ_{ν} (emissivity) and we will use this nomenclature throughout this thesis. In that same work by Boulanger & Perault (1988), Galactic cirrus dust emission at mid-IR wavelengths was detected, establishing that very small grains also contribute to the overall dust spectrum.

Later on, in order to unbiasedly detect the Cosmic Infrared Background (CIB) at IR wavelengths, Arendt *et al.* (1998) estimated the Galactic dust contribution to the observed sky brightness from 1.25 to 240 μm in the DIRBE (Diffuse Infrared Background Experiment) data from the COBE satellite. These authors started by first calculating the correlation between the 100 μm emission and the H I column density (using a linear least-squares fit) at the North Ecliptic pole (*nep*) and the Lockman Hole (both regions have a low H I column density). They found an average intercept of 19.8 nW m^{-2} sr^{-1}, an estimate of the CIB. They determined the relative dust emissivity at 12, 25 and 60 μm (similar filters to the IRAS mission) by correlating higher Galactic latitudes of these IR maps with the 100 μm dust template, and found the following ratios: 0.046, 0.048 and 0.171, respectively.

We briefly note that the signals in the near-and mid-IR filters in both missions are plagued by a strong foreground emission component from our own Solar system (generally called Zodiacal emission or 'zody' for short); its implications for the accurate determination of dust emissivities in the mid-IR range will be addressed later in this thesis. Among the many studies conducted to constrain the SED of the big dust grains, Boulanger *et al.* (1996), using DIRBE and FIRAS (Far Infrared Absolute Spectrophotometer) data, found that diffuse dust had a spectrum (from 100 μm to 1 mm) well fitted by a single modified blackbody with $\beta = 2$ with an average temperature of about 17.5 K and an opacity of $\tau_{250}/N_{HI} = 1 \times 10^{-25}$ cm^2 (at the fiducial wavelength of 250 μm). This temperature estimate has been widely used as the typical dust temperature of big grains in thermal equilibrium in the ISRF.

1.1.5   Deviations from the dust-to-gas correlation

In most dust and atomic gas spatial correlation studies, deviations from the average correlation are seen at high H I column densities. One factor is that the H I line becomes optically thick and the true column density is no longer easily traced. But more importantly, after a certain column density threshold, the self-shielding is enough to maintain a significant molecular H_2 abundance. Therefore, it is common to find denser gas regions with IR or far-IR excess (see Figure 1.4), and this excess has indirectly been interpreted as the result of dust emission associ-

ated with molecular gas instead of atomic gas associated with warmer dust. For example, the work of Reach *et al.* (1994) has revealed the presence of excess IR emission (not attributed to dust associated with atomic gas via spatial correlation analysis) in a sample of clouds of about 1 degree in size which displayed 100 μm emission in the IRAS data. After linearly correlating H I and CO column densities with the far-IR maps, the excess found was assumed to be due to the presence of H_2 (not traced by CO). It is relevant to mention that there are a limited number of CO surveys and H_2 cannot be directly observed; this limits our knowledge regarding the emissivity properties of dust associated with molecular clouds. While the CO molecule forms in the gas phase, H_2 is thought to be created in the surface of dust grains (Spitzer 1978). Nevertheless, this kind of study still sheds light into understanding the density threshold required for self-shielding.

Reach *et al.* (1994) also found that the 60/100 color ratio is smaller in regions with IR excess confirming the existence of cold big dust grains in denser regions. Later on, Reach *et al.* (1998) conducted a similar spatial correlation analysis to that by Boulanger *et al.* (1996) but in this case in the far-IR using DIRBE and the Leiden-Dwingeloo H I data and identified regions with excess far-IR emission (with the ratio of 100 to 240 μm emission). They found that the dust temperature associated with bonafide molecular sites is colder (15.5 K) when compared to the 19.0 K encountered in diffuse atomic regions (which showed a slope of 0.89 MJy sr^{-1} $(10^{20}$cm$^{-2})^{-1}$ at 100 μm).

It is also worth noting that excess emission could also be potentially due to dust associated with ionized gas. Although early searches have failed to find any significant correlation between the two (e.g., Boulanger & Perault, 1988 and Arendt *et al.*, 1998 at high Galactic latitudes), recent studies in our Galaxy by Lagache *et al.* (2000) and in the LMC by Paradis *et al.* (2011) seem to suggest otherwise. The latter authors detect warm dust in the ionized medium of the LMC and note that the low 12 μm emission seen there is suggestive of PAH destruction, possibly due to the strong ISRF in ionized sites.

1.1.6   Recent observational results

More up-to-date studies of dust properties have taken place with the latest generation of space telescopes, in particular, *Spitzer*, *Herschel* and PLANCK, and also encompass a larger sampling of different dust sites than ever before. Using the all-sky PLANCK data, Planck Collaboration *et al.* (2011b) have studied the overall properties of dust in the plane of our Galaxy as a function of Galactocentric distance, while Planck Collaboration *et al.* (2011a) have focused on the dense Taurus cloud. Both studies find that the dust temperature associated with molecular gas is about 5 K lower than what is seen in the diffuse medium; with some causal relationship, the dust opacity is higher too.

On the diffuse ISM side, Planck Collaboration *et al.* (2011c) have for the first time been able
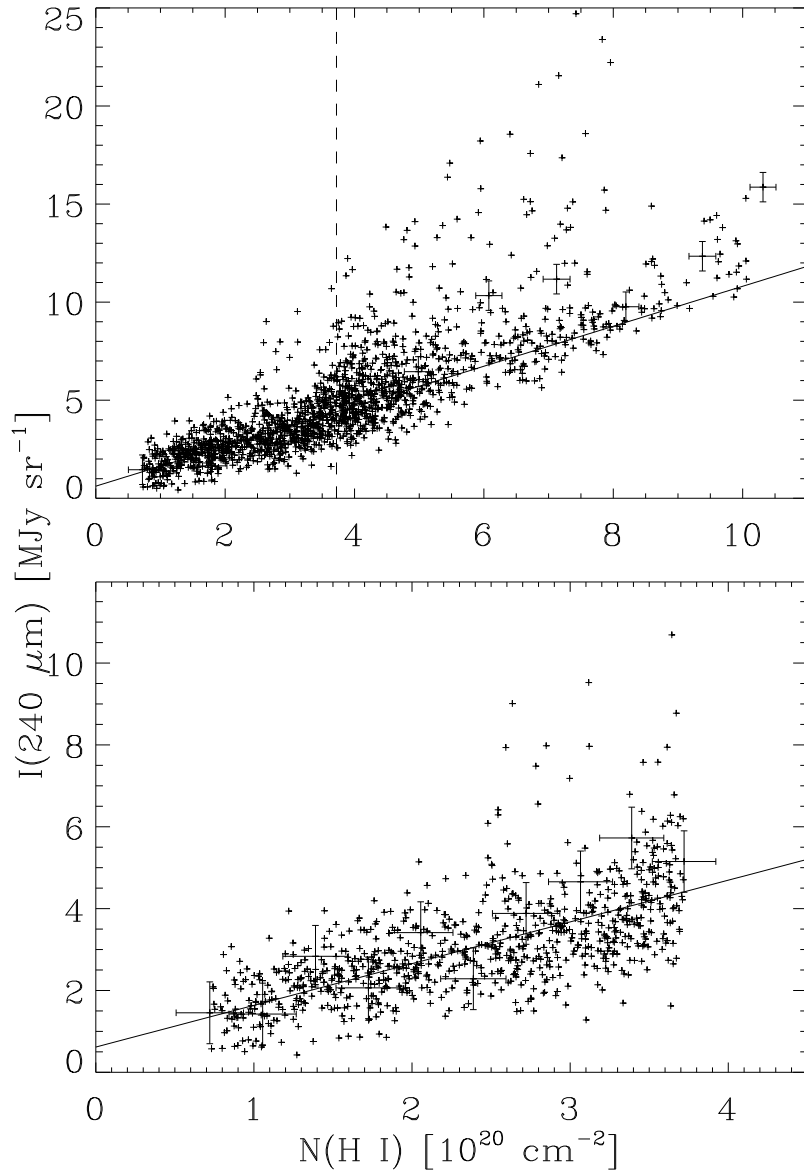
Figure 1.4: The top plot clearly illustrates the type of residual typically found at higher column densities when correlating far-IR emission (in this case, 240 *µm* DIRBE data) with H I column densities. The lower plot shows the new range of data points selected for the linear least-squares fit. The authors impose a column density threshold cut to avoid contaminating their fit with regions that are not atomic. (Taken from Reach *et al.* 1998.)

to produce statistically significant results on the variation of emissivities of dust associated with different velocity gas clouds at high Galactic latitudes. This study has also revealed that dust associated with some IVCs has a lower opacity (τ_{250}/N_{HI}) than local dust. Such a finding seems to reflect the turbulent nature of IVCs, and therefore dust evolution, rather than a different ISRF.

Although our understanding of the dust spectrum has been substantially increased over the past decades, there is still a need to quantify the emission of Galactic cirrus at mid-IR wavelengths. Therefore, part of this work is focused on finding emissivities of dust associated with different velocity gas at 12 and 25 μm with better resolution than previous studies. This work is complementary to that of Planck Collaboration *et al.* (2011c) in the far-IR and submillimeter wavelength range.

1.1.7   Power spectrum and CIBA

Although the goal here is primarily to do Galactic science via spatial correlations of mid-IR dust emission and H I column density at high Galactic latitudes, we can also explore other extragalactic backgrounds in the IR sky brightness maps. Once the Zodiacal and Galactic emission (cirrus and point-sources) have been accounted for, the remaining structure is the cumulative integrated light from distant galaxies in the Universe, also called the Cosmic Infrared Background (CIB). Source counts have proven to be a reliable method to measure the resolved part of the CIB (e.g., Béthermin *et al.* 2010). But because most galaxies are unresolved at the IR and submillimeter wavelengths and also because it is hard to obtain completely calibrated total power measurements, many studies deal only with the fluctuations or anisotropies (CIBA). Multiple studies have taken place to study CIB statistics in order to discern the clustering of bright Galaxies and their relation with dark matter halos (see the review by Hauser & Dwek 2001). The statistical behaviour of these fluctuations can be constrained using the angular power spectrum of IR or submillimeter maps when free of the Galactic contaminants.

Gautier *et al.* (1992) used 100 μm IRAS data to find that the power spectrum of Galactic cirrus emission is well fitted by a power law with a slope of about -3. The same slope was also found by Wright (1998) in the 60 to 240 μm DIRBE data. This estimate is commonly used when removing the cirrus contribution in CIBA studies (e.g., Miville-Deschênes *et al.* 2002). These authors reported CIB fluctuations in the far-IR IRAS data of the order of 0.048 and 0.09 MJy sr^{-1} at 60 and 100 μm. They also derive an upper limit to the mean CIB at 60 μm of 0.27 MJy sr^{-1} using a contrast $\sigma_{CIB}/I_{CIB} = 0.18$ (the CIBA to mean CIB ratio). Later on, Pénin *et al.* (2012) used IRAS and *Spitzer* maps of the *n1* field to extract information on the mean CIB at 100 and 160 μm. This study, however, made use of the H I template to remove the Galactic cirrus emission from the maps, instead of typically removing it in power spectrum space. They reported mean CIB levels of 0.24 and 0.77 MJy sr^{-1} at 100 and 160 μm. With the new PLANCK

data, Planck Collaboration *et al.* (2011d) find the contrast σ_{CIB}/I_{CIB} to be 0.15 at submillimeter wavelengths and advance a model for the CIB consistent with galaxies at different redshifts producing the fluctuations seen at different wavelengths.

1.2 The not so diffuse interstellar medium

In this section, we lay the groundwork for Chapter 5. Keeping with the mid-IR theme, we address the emission of supernova remnants in the dense regions of the Galactic plane within this wavelength range. A version of the introduction that follows has been published in the Astronomical Journal as "The MIPSGAL view of Supernova Remnants in the Galactic Plane", Pinheiro Gonçalves, D., Noriega-Crespo, A., Paladini, R., Martin, P. G., and Carey, S. J., 142:47 (33pp), 2011 August.

1.2.1 Context for SNRs studies

With the help of Galactic surveys (e.g., Arendt 1989, Saken *et al.* 1992), our understanding of the infrared energetics, morphology and evolution of supernova remnants (SNRs) has increased substantially in the past decades. However, even at IRAS resolution, confusion with other IR sources in the Galactic plane is a limiting factor that can prevent a clear picture from emerging. Such confusion, for example, can make the correct assessment of ejecta dust masses for Type II SNRs difficult, a key factor for interpreting high redshift dust in the Universe (Sibthorpe *et al.* 2010, and references therein). Infrared emission from SNRs can also provide insight into the radio-IR correlation of external galaxies (Helou *et al.* 1985). Additionally, the study of dust re-emission is relevant for determining the cooling rate of SNRs, an important quantity that shapes their evolution (Dwek 1987).

1.2.2 Previous SNRs Galactic IR surveys

Using the Galactic Legacy Infrared Mid-Plane Survey Extraordinaire, GLIMPSE (Benjamin *et al.* 2003; Churchwell *et al.* 2009), Reach *et al.* (2006) searched the Galactic Plane for infrared counterparts to known SNRs. Out of 95 objects, 18 were clearly detected, a detection rate of about 20%. Previous searches were conducted using the IRAS all-sky survey. According to Reach *et al.* (2006), within the GLIMPSE surveyed area, Arendt (1989) and Saken *et al.* (1992) obtained a detection rate of 17% and 18%, respectively.

1.2.3 SNR IR emission mechanisms

The IR part of the spectral energy distribution of SNRs can result from multiple sources ranging from dust (either stochastically or thermally heated), atomic/molecular line emission, PAH emission, and even synchrotron emission. In fact, the amount of the latter emission can vary substantially and is dependent on the type of remnant. In plerion remnants such as the Crab Nebula (Strom & Greidanus, 1992), it accounts for about 90% of the mid-infrared flux density (at 25 μm). In contrast, about 2% of the mid-infrared flux density (at around 25 μm) in Cas A is due to synchrotron emission (Sibthorpe *et al.*, 2010).

Dust emission is expected to be a substantial component of the IR emission of SNRs since their spectra are well fitted by one or more thermal dust populations, as revealed by previous infrared surveys (IRAS; Arendt, 1989, Saken *et al.*, 1992), or by stochastic heating of the grains, as proposed by Hines *et al.* (2004) to explain the mid-infrared emission from Cas A. The dust is heated by charged particles in hot plasma generated by shocks (e.g., Dwek & Werner, 1981, Dwek, 1987, Dwek & Arendt, 1992). Direct evidence for the shock-heated plasma is provided by X-ray observations in the continuum, and X-ray lines are a good diagnostic of high energy interactions and abundances (Vink, 2004). While for the majority of SNRs, the observed dust emission is thought to originate from the interaction of the shockwave with the surrounding interstellar medium (ISM; e.g., Douvion *et al.*, 2001, Borkowski *et al.*, 2006, Williams *et al.*, 2006, Blair *et al.*, 2007), evidence of SNRs with ejecta dust is scarce (e.g., Arendt *et al.*, 1999) even with the help of higher resolution IR telescopes such as *ISO* and *Spitzer*. However, observations with the *Spitzer Infrared Spectrograph* (IRS) (Rho *et al.*, 2008) of the young remnant Cas A have pointed to the presence of a large hot dust continuum peaking at 21 μm, from ejecta dust formed through condensation of freshly synthesized heavy elements. This component has temperatures ranging from 60 to 120 K. Furthermore, recent far-infrared and submillimeter work (Sibthorpe *et al.*, 2010) on the same remnant, also suggested the existence of a 'tepid' ($\sim$ 35 K) central dust component in the ejected material (see also Barlow *et al.*, 2010).

Observational evidence for the importance of IR lines has been provided by multiple SNRs spectroscopic studies which identified a plethora of lines from elements such as Fe and O (e.g., Oliva *et al.* 1999b; Reach *et al.* 2002). Much of the infrared line emission seen in SNRs results from the interaction of the blastwave with the surrounding environment where they are born as the shocked gas cools down. For example, IC443 is encountering an atomic region at the northeast side and a molecular cloud at the southern border (e.g., Rho *et al.* 2001). Spectral observations by Oliva *et al.* (1999a) on the north of the remnant revealed that most of the emission at 12 and 25 μm, previously surveyed with IRAS, was in fact due to ionized line emission (e.g., [Fe II]) with only a small contribution from dust. Because optical spectra also showed strong collisionally excited fine structure atomic lines (Fesen & Kirshner 1980), the infrared line emission is not unexpected. Likewise, for the 'optically bright regions' in N49, an old remnant in the Large Magellanic Cloud (LMC), Williams *et al.* (2006) found that IR line

emission can be a substantial fraction of the total IR flux, up to 80% at 24 μm. On the south of IC443, however, the spectrum is dominated by the H_2 pure rotational lines S(2) through S(7) (Cesarsky *et al.*, 1999), once again with a faint dust continuum. Moreover, Troja *et al.* (2006) found a good agreement between the soft X-ray emitting plasma and the radio/optical structure on the northeastern part of the remnant where the plasma density is highest. Such energetic encounters change the morphology of the neighboring ISM and of the remnant itself thereby creating prominent emission lines (e.g., molecular hydrogen) which can be detected in the infrared. OH masers (in particular, the 1720 MHz line) are also good tracers of the remnant encounter with dense molecular regions with 10% of Galactic SNRs showing associated masers (Wardle & Yusef-Zadeh, 2002 and references therein).

The existence of infrared emission associated with PAHs in SNRs was first observed in a LMC remnant by Tappe *et al.* (2006). Plus, evidence for such emission in some Galactic SNRs has also been shown through near-infrared color-color ratios by Reach *et al.* (2006). This is likely excitation of PAHs from the ISM, rather than PAHs from supernova dust.

1.3 Thesis overview

This thesis hopes to shed light into the emission of dust grains in the mid-IR range with emphasis on the diffuse sky at high Galactic latitudes. In order to do so, we have assembled a vast (about 800 sq degrees) 21-cm H I survey using the Green Bank Telescope (Boothroyd *et al.*, 2011; Blagrave *et al.*, 2010 and Martin et al., in preparation). In Chapter 2, we present the H I data and build column density maps associated with gas at different velocities (and estimate its uncertainties). This H I data set has been used in other studies, either as a template for tracing dust emission at far-IR and submillimeter wavelengths in the local neighborhood and Galactic halo (Planck Collaboration *et al.* 2011c) or to study the anisotropies of the CIB (Planck Collaboration *et al.* 2011d and Pénin *et al.* 2012). Here, we use it primarily to determine dust emissivities in the mid-IR range (IRAS/IRIS data, Chapter 3) associated with local, intermediate and high velocity gas (LVC, IVC and HVC) as described in Chapter 4. We build dust emissivity SEDs from the mid-IR to submillimeter and compare them to a theoretical diffuse ISM dust model (DustEM, Compiègne *et al.* 2011). We look for trends between emissivities and calculate color ratios. We also assess the dispersion and power spectra behaviour of the residual maps. In Chapter 5 we report on the detection of Galactic plane SNRs at 24 and 70 μm. We calculate the mid-IR flux for the detected remnants and compare it to other wavelength emission (radio and X-ray) which gives us insight into their morphology, energetics and evolution. Finally, in Chapter 6 we summarize our work and outline future endeavours.

Chapter 2

H I Observations

Here, we describe the 21-cm H I survey completed with the Green Bank Telescope (GBT), which is used primarily in this thesis as a template to estimate dust emissivities in the mid-IR (see Chapter 4). We begin in §2.1 by briefly discussing the physics of the 21-cm H I emission line and introduce some useful definitions/notations relevant to radio observations. Part of this survey data has already been discussed in Boothroyd et al. (2011), where an accurate estimation of the uncertainties associated with measuring 21-cm line emission with the GBT has been addressed. In §2.2-2.3, we summarize some of the observational and reduction aspects of the 21-cm data. A detailed article on the physical and morphological characteristics of all survey fields is currently under preparation and some of its contents are discussed in §2.4. Separation of different velocity gas components and integrated emission maps are presented in §2.5. In §2.6, noise properties and uncertainties associated with column density maps are addressed.

2.1   The H I 21-cm line and radio 'lingo'

21-cm neutral hydrogen emission is an important sampler and tracer of the density distribution of gas structures. Although the 21-cm transition is forbidden (it has a very small Einstein coefficient and thus takes a very long time to occur), it is commonly observed given the vast amounts of atomic hydrogen present throughout the Universe. The emission itself is produced by hydrogen atoms when the electron spin changes from parallel to anti-parallel in relation to the proton spin (see, for example, Draine, 2011 for more details). Using the Boltzmann equation to calculate the population in each hyperfine structure level, we can see that this emission is practically independent of the spin temperature. The fact that the emissivity does not depend on the spin temperature is useful because in the optically thin limit we can obtain the H I column density simply by doing the zero-th statistical moment of the emission spectrum (Kulkarni & Heiles, 1988). Given that our survey targeted regions at high Galactic latitude, away from the plane, we can assume that most gas clouds suffer negligible self-absorption.

In practice, the road to achieve meaningful physical gas quantities such as column density starts with a radio telescope. The quantity directly measured is called antenna temperature T_a, which is affected by atmospheric extinction and instrumental considerations like the telescope beam and efficiency. From this measure, we can derive the desired brightness temperature T_b. In the long wavelength regime, where the 21-cm line is observed, the brightness temperature is derived from the Rayleigh Jeans approximation of the Planck function

$$T_b = \frac{I_\nu(T)c^2}{2\,k\nu^2}\,,\tag{2.1}$$

where $I_\nu(T)$ is the sky intensity or brightness, ν is the frequency, k the Boltzmann constant and c the speed of light. In our case, we measure the 21-cm T_b in a certain region of the sky and integrate that emission profile for the velocity range of interest to obtain the column density maps (see §2.5.2).

2.2 Survey Strategy

2.2.1 Motivation

Given the vast amounts of neutral hydrogen present in our Galaxy, several studies of H I emission properties have already been conducted. For example, the LAB survey (Kalberla *et al.*, 2005) created a map of the entire sky with an equivalent angular resolution of 36′ by combining the northern LDS (Hartmann & Burton, 1997) and southern IAR (Arnal *et al.*, 2000; Bajaja *et al.*, 2005) surveys. With the increasing development of radio interferometric techniques, spatial imaging of the Galactic mid-plane has improved substantially with surveys such as the Canadian and VLA Galactic Plane surveys (CGPS, Taylor *et al.*, 2003 and VGPS, Stil *et al.*, 2006, respectively). Unfortunately, due to instrumental constraints, such interferometric surveys are focused on targeted regions. They also need to be corrected for the missing flux present on large scales, using observations from large single dishes. Currently, however, there are a few single dish surveys in motion that will provide coverage of large areas in the sky with high resolution and sensitivity such as the Parkes Galactic All Sky Survey (GASS, McClure-Griffiths *et al.*, 2009) and the Effelsberg-Bonn HI Survey (EBHIS, Kerp *et al.*, 2011).

In the meantime, using the Green Bank Telescope, our team has constructed an impressive survey of about 800 square degrees, mainly in the North Hemisphere, with a higher sensitivity than on-going surveys will offer. Besides providing an important high resolution (9′.55) neutral hydrogen data set valuable for spatial correlation studies with dust (Planck Collaboration *et al.*, 2011c) and for removing foreground emission for studies of the CIB (Planck Collaboration *et al.*, 2011d), it can also be used to study the statistics of structural properties of H I using the emission profiles.
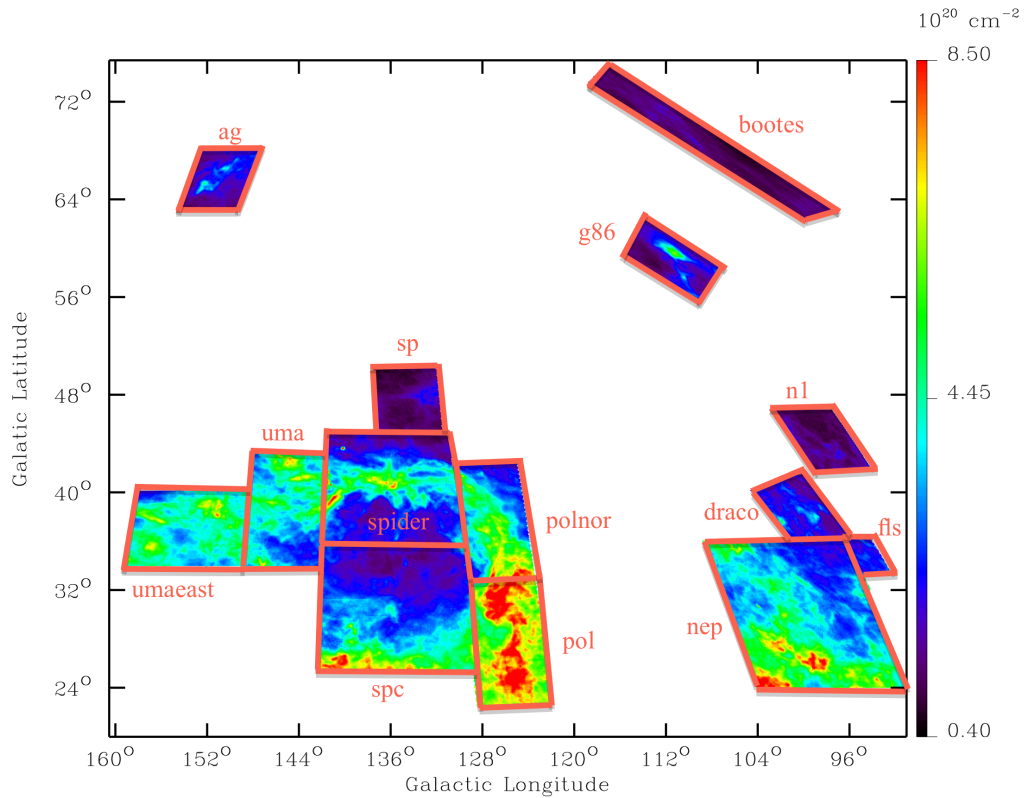
Figure 2.1: Column density map of the fields observed in the northern Galactic Hemisphere, integrated between 200 to -300 km/s. Survey fields are rectangular in the GLS coordinate system used in the observations, but appear distorted in this cartesian projection.

2.2.2   Targeted Areas

A great deal of effort was devoted to mapping the majority of the North Celestial Pole Loop, North Ecliptic Pole and several other diffuse faint fields. Figure 2.1 gives an idea of the size and location of the fields in our survey. Particular attention was given to structures known to have a strong H I signal at either intermediate (e.g., *g86* and *draco*) or high velocities (e.g., *n1* and *ag*). Such fields are relevant for tracking the evolution and processing of dust mixed with atomic H I in different environments.

About half of the fields were observed more than once (when possible) to improve the signal to noise ratio and to enable a direct measure of the errors (reproducibility). Table 2.1 reports the number of different observations for each field as well as their central Galactic coordinates, size and scientific motivation (we will expand on this in §2.4).

Table 2.1. GBT survey fields

Name	Number of IO[a]	Coordinates[b]	Size[c]	Motivation[d]
ag	2	G164.85 + 65.50	5×5	HVC
bootes	2†	G058.11 + 68.57	12.4×4	EGF
draco	3	G092.24 + 38.43	5×5	IVC
g86	3	G087.94 + 59.05	5×5	IVC
mc	2	G056.84 − 81.50	6×5	HVC
n1	2	G085.33 + 44.28	5×5	HVC
nep	3	G096.40 + 30.00	12×12	NEP
pol	1	G125.00 + 27.50	6×10	NCP
polnor	1†	G125.00 + 37.40	6×10	NCP
sp	2	G132.38 + 47.50	5×5	HVC
spc	1	G135.70 + 29.80	12×9.5	NCP
spider	1†	G134.98 + 40.00	10×10	NCP
uma	1	G143.60 + 38.50	9×9	NCP
umaeast	1	G155.80 + 37.00	10.5×6	NCP

[a]IO is short for independent observations. The † indicates fields with an extra *partial* coverage available. For example, *bootes* has 2 full coverages and third partial one.

[b]Central coordinates of the field given in the Galactic coordinate system.

[c]The size of the fields is given in degrees. The first value refers to the horizontal direction which is either at constant Galactic latitude or Declination, while the second value refers to the length of the vertical direction which is either at constant Galactic longitude or Right Ascension.

[d]Principal program motivation to observe each field. IVC and HVC refer to the presence of relatively significant intermediate or high velocity gas clouds. EGF stands for regions commonly used in deep extragalactic studies. NCP identifies fields which are part of the North Celestial Pole Loop structure and NEP is the region located in the direction of the North Ecliptic Pole, where several all-sky infrared and submillimeter surveys from space have deeper coverage due to their scanning strategy.

Table 2.2. Observing characteristics of our survey with the GBT

Central frequency	Bandwidth	Frequency res.	Velocity res.	Angular res.	T_{sys}
1420 MHz	12.5 MHz	760 Hz	0.16 km/s	9.′55	~ 18 K

Note. — Res. is short for resolution. T_{sys} is typically 18 K but depends on weather and the elevation of the observation.

2.2.3 Instrument: Green Bank Telescope

In order to cover large parts of the sky with high sensitivity, we made use of the single-dish 100-m Green Bank Telescope. The GBT can collect radio waves between the millimetre and the metre range depending on the receiver used. For example, at 21-cm we exploit its 9′ spatial resolution and high sensitivity to probe the atomic H I faint gas structures at high Galactic latitudes. The GBT was designed to have an unblocked aperture, which is unusual when compared to traditional radio telescopes, to minimize contributions from stray radiation. Because of the strategic location in West Virginia, where human radio interference has been greatly limited, we are able to obtain high velocity resolution spectra with minimal radio frequency interference (RFI) in our selected waveband. For more information on the GBT, see the proposing and observing guides at the GBT website (`https://science.nrao.edu/facilities/gbt`).

2.2.4 Observing Mode

Here, we briefly discuss the observational setup and configuration adopted in our survey. For more technical details, we refer the reader to §3 of Boothroyd *et al.* (2011). This article discusses the effort our team developed to produce accurate 21-cm H I spectral data with the GBT, which includes a more comprehensive method for data reduction that takes into account the removal of stray radiation.

The survey area was built up over the course of 4 years, using on-the-fly mapping which allows fast and reliable coverage of large areas of the sky. The majority of the observations were done remotely with the help of the telescope operator on site. In particular, I was responsible for designing and executing over 200 hours of observations which included most of the fields surrounding the *spider* region in the North Celestial Pole Loop. We used the L-band receiver which has a frequency range from 1.15 to 1.73 GHz and can detect both linear and circular polarizations (see Table 2.2 of the GBT observing guide `https://science.nrao.edu/facilities/gbt/observing/GBTog.pdf`). The GBT spectrometer observing mode was fixed to a bandwidth of 12.5 MHz which, with about 16000 channels, allows for a velocity resolu-

tion of 0.16 km s^{-1} (see Table 2.2). Observations were carried out using a frequency switching method, useful to get rid of the underlying continuum (composed of free-free and synchrotron radiation), leaving behind a very flat baseline.

At the beginning of each observing session, a script is run to determine pointing and focus solutions to achieve maximum accuracy and sensitivity. During the observing period, the spectral data are read out every 4 seconds corresponding to a 3'.5 section of a given scan, which is the name assigned to an ensemble of readouts. Both latitude and longitude spacings were chosen to be the same. Observations were done along lines of constant Galactic latitude (and varying Galactic longitude) which define the in-scan direction. The telescope is stepped by 3'.5 in the cross-scan direction before the next reserve scan. The raw spectrum of each readout can be inspected almost immediately. Our observations are converted to a local standard of rest (LSR) velocity frame, where V_{LSR} is defined by $c\,(1 - \nu/\nu_0)$ following the 'radio' definition and where ν_0 is the frequency of the line at the LSR. We read linear polarizations from the receiver separately as XX and YY. Furthermore, to avoid saturation and nonlinearity in the detectors, we re-set the power levels for the spectrometer components (also known as 'balancing') every 20 minutes or so. During each run we also observe (when possible) known standards (either S6 or S8; Williams, 1973 and Kalberla *et al.*, 1982, respectively) for our calibration and gain stability checks.

2.3 Reduction Strategy

Spectra obtained in each observing run were reduced using available GBT software (AIPS and GBTIdl). We now briefly discuss some of these procedures. Again, for a more comprehensive account, see Boothroyd *et al.* (2011). Data reduction starts with the main beam correction and is followed by stray radiation removal. As the name suggests, this radiation originates outside the main beam and is picked up by the sidelobes. Although the radiation response received by the sidelobes of the telescope is generally much smaller than what is registered by the main beam (as expected), its contribution is non-negligible. Figure 2.2 shows an example of stray radiation correction for a section of the *n1* field in our survey. The estimated stray radiation is about 10% of the observed peak amplitude, and even more in the wings. Also, we see that it affects primarily the channels close to the rest frame frequency, because the sidelobes register the 21-cm signal from our Galaxy. In fact, the amount of stray radiation is dependent on the time of the observation and can be most serious when the sidelobe peak is near the Galactic plane and we are trying to observe faint cirrus. It should therefore be removed as best as possible. Our team has mapped the sidelobe beam and developed a code for estimating the all-sky telescope response (see Figures 8, 9 and 10 and §6 in Boothroyd *et al.*, 2011) which can be used to accurately predict the profile of stray radiation to be removed from the spectrum in each pointing.
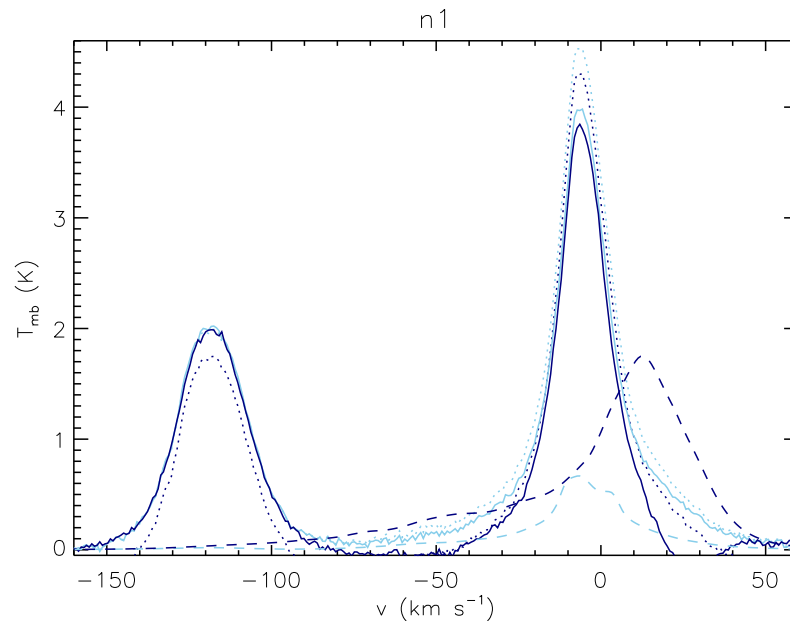
Figure 2.2: Stray radiation removal from the average spectra for a selected part of the *n1* field (adapted from Boothroyd *et al.*, 2011). The two different colors refer to independent observations. Dotted lines represent the observed 21-cm signal, dash lines, the stray radiation and full lines, the final profile.

It is not uncommon to find spectra with artifacts or weird baseline behaviours. In such cases and whenever possible, we re-observed those locations and replaced faulty spectra by acceptable ones. We still keep all scans, regardless of their quality, and maintain a record of bad spectra (flags). Because replacement spectra are generally obtained at a later date and at a different local standard time (LST), the stray radiation is different and if left untreated, can be readily seen as patch work in the final assembly of all the scans into a data cube. We then fit and subtract a 3-order polynomial function from the spectral signal to reduce baseline effects leftover from the frequency switching process (see §3.3 of Boothroyd *et al.*, 2011). The coefficients of the polynomial function are determined using only the end channels which are free of sky signal. The H I data are both taken and projected in a pseudo-cylindrical grid called GLS that preserves areas (for more details see Calabretta & Greisen, 2002). Originally, a pill-box gridding strategy for the 21-cm H I data cubes was employed. This preliminary H I product release was used in our collaboration with the PLANCK team (Planck Collaboration *et al.*, 2011c and Planck Collaboration *et al.*, 2011d). We have, in the meantime, improved the spatial accuracy of the H I maps by using precise pointing information and by adopting a modified Bessel function when gridding. Because of smoothing, this type of gridding lowers the noise level in each pixel and evens out any sudden brightness jumps between neighbouring pixels that might exist. In this approach, however, pixels are no longer independent from each other in that their final amplitude value is now weighted by surrounding spectra as well. This process also slightly degrades the beam full-width half maximum (FWHM) from 9.′2 to 9.′55. The
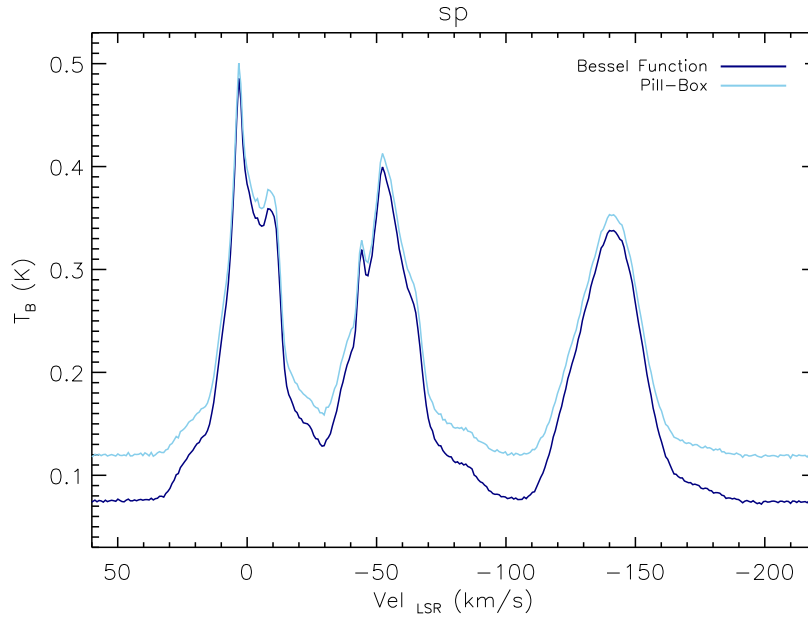
Figure 2.3: Standard deviation of the average spectra for the faint *sp* field. *Light blue*: Pill-box gridding (original data release). *Dark blue*: Modified Bessel function gridding. The noise level decreases when the gridding is improved via a Bessel function smoothing and is more noticeable in the low intensity channels.

beam FWHM is about $9.'55$ in both the direction of the scan and perpendicular to it and the pixel size is chosen to be $3.'5$ (less than the Nyquist sampling of $3.'86$). To illustrate the effect of the different gridding methods, we compare the standard deviation of each channel map in the cube. Figure 2.3 shows the decrease in noise when a modified Bessel function is used to grid the data for one of the fainter fields *sp*.

Although we originally observe with a 0.16 km s^{-1} resolution, our final cubes have a velocity resolution of 0.8 km s^{-1}. This velocity degradation (smoothing) is done to increase the signal to noise ratio and is certainly worthwhile because no real structure in the line is expected at finer resolution (the thermal linewidth at 100 K is about 1 km s^{-1}). The cubes were built with 1057 channels spanning about 800 km s^{-1}, from -450 to 350 km s^{-1} approximately. This range choice guarantees that there are no profile inversions in the spectra from frequency switching.

2.4   H I fields

The H I survey comprises about 800 square degrees in the sky and is the result of several proposals and observing runs. The goal was to assemble a varied and comprehensive ensemble of H I regions with different physical characteristics. We restricted our observations to high
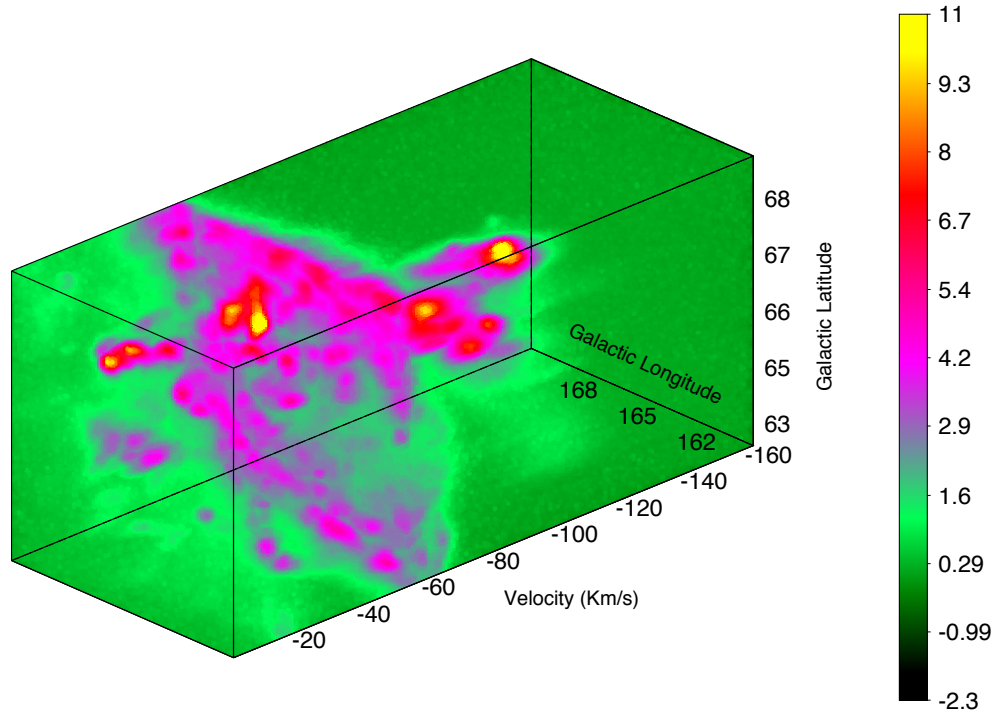
Figure 2.4: Velocity cube for the *ag* field. The colorbar has a linear scale and is in units of Kelvin degrees. There is very little low velocity local gas, but widespread emission of intermediate velocities and clumpy high velocity gas.

Galactic latitude regions in order to avoid the line of sight crowding found in the disk of our Galaxy which is rich and abundant with H I clouds. Furthermore, at these high latitudes, the interstellar medium is fairly diffuse and therefore most lines are optically thin. Nevertheless, we do correct for possible self-absorption (see Equation 2.3) when calculating the column density.

By studying the dust properties associated with neutral hydrogen gas within diverse and distinct environments, we are able to draw important clues regarding dust evolution in the diffuse ISM. For example, *draco* and *g86* were chosen primarily due to their prominent intermediate velocity gas structure. Additionally, it is expected that dust in shocks, should suffer some kind of shattering (Jones *et al.*, 1994). Because of non-equilibrium emission, processed dust will emit at higher frequencies leading to greater 60/100 *μm* color ratios when compared to the local dust (see Heiles *et al.*, 1988). Also, the detection of dust in high velocity clouds has proven quite elusive with the possible exception of the analysis by Miville-Deschênes *et al.* (2005) in the *Spitzer XFLS* field, close to the *draco* cloud. The HVC gas has radial velocities which cannot be associated with the rotation curve of our Galaxy, leaving their origin an open question. A consistent picture of the dust content in HVCs would be an important step forward for understanding their history (see Wakker & van Woerden, 1997 for a review). With this in mind, we targeted regions like *mc* in the direction of the Magellanic Stream (this, by

the way, is our only observation in the Southern Galactic Hemisphere) as well as some regions at the northern high Galactic latitudes called *ag*, *sp*, and *fls*. These particular directions were chosen by searching for high contrast between the HVCs and the local gas column densities in the coarser resolution LAB survey. A 3D view of the *ag* field can be seen in Figure 2.4. Also, *bootes* and *n1* are common deep fields used in extragalactic studies, while the *nep* field, at the north Ecliptic pole, is an area in the sky where, generally, infrared and sub-millimetre surveys such as IRAS, AKARI and PLANCK, have deeper coverage given their scan strategy. Finally, we covered the North Celestial Pole Loop with several observations of its central part (*spider*). This interesting geometrical loop is thought to be the result of an expanding cylindric cavity as proposed by Meyerdierks *et al.* (1991). We added to this adjacent fields located in the Polaris flare (*pol* and *polnor*) and Ursa Major to the east (*uma* and *umaeast*), along with a faint region below which we called *spc*. Regions like *uma* are known to have molecular gas associated with dust as found by de Vries *et al.* (1987). The *ag*, *bootes*, *g86*, *n1*, *mc* and *sp* fields have an average local column density below 2×10^{20} cm^{-2} and were designated as *faint* fields by Planck Collaboration *et al.* (2011c). Likewise, fields with H I densities in the line of sight of above 2×10^{20} cm^{-2} are called *bright* fields (*draco*, *nep*, *pol*, *polnor*, *spc*, *spider*, *uma*, and *umaeast*). Figure 2.5 contains the total column density maps for the faint fields. These are calculated by integrating the spectra from channels with V_{LSR} from -200 to 150 km s^{-1}. Figure 2.6 and 2.7 depict the equivalent maps for the bright fields.
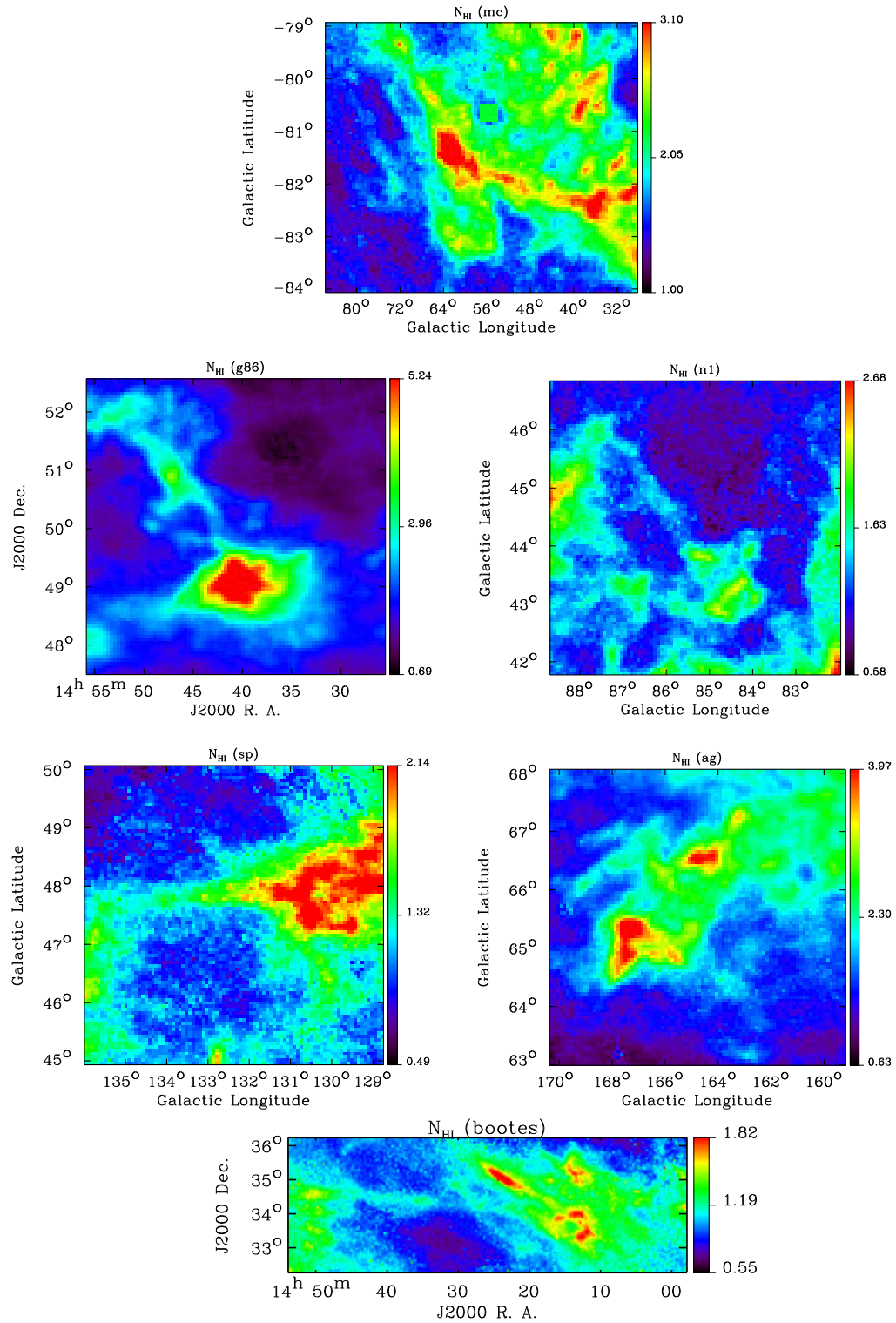
Figure 2.5: Total column density maps for the faint fields. Units in 10^{20} cm^{-2}.
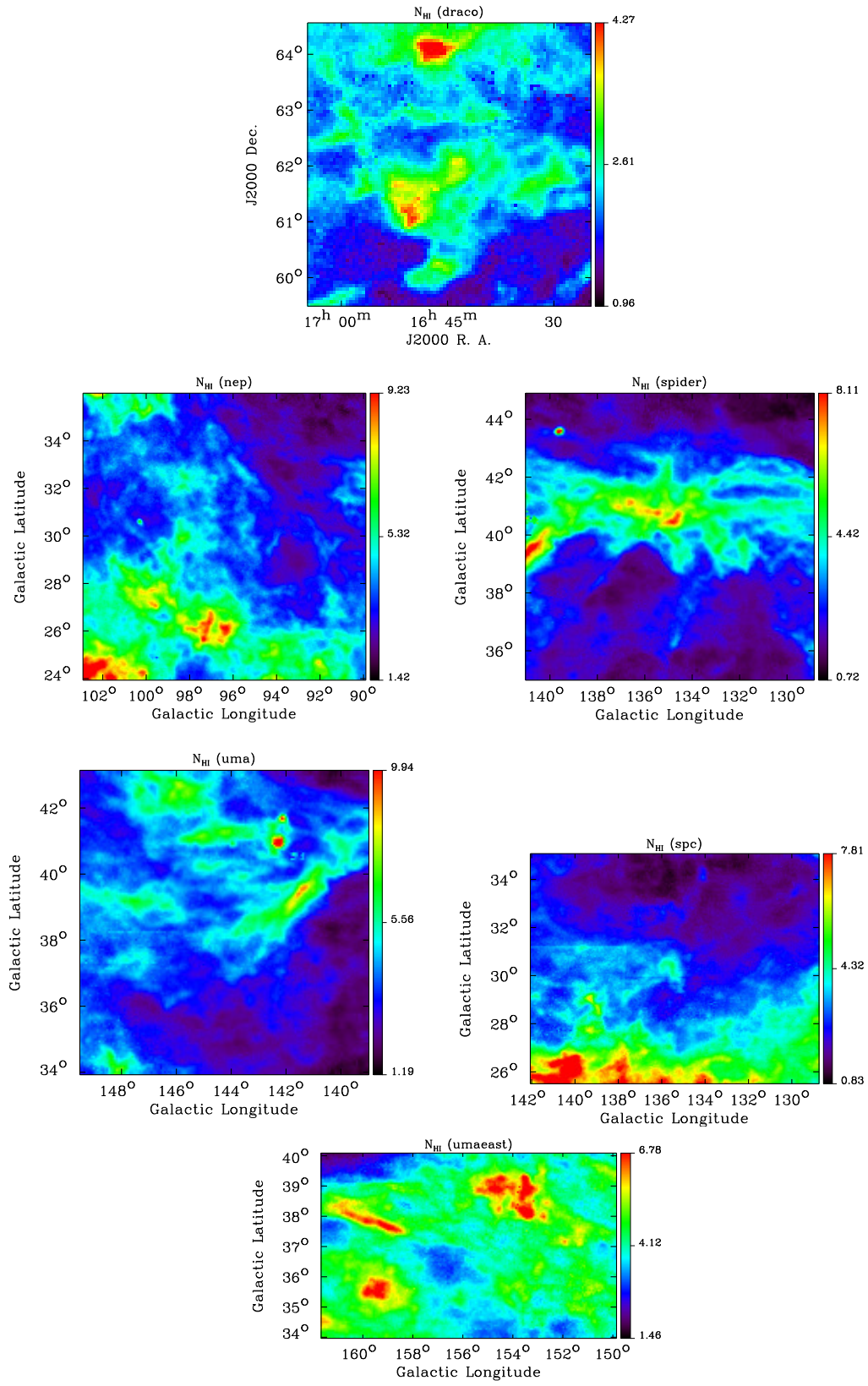
Figure 2.6: Total column density maps for some of the bright fields. Units in 10^{20} cm^{-2}. Note the very different coverages.
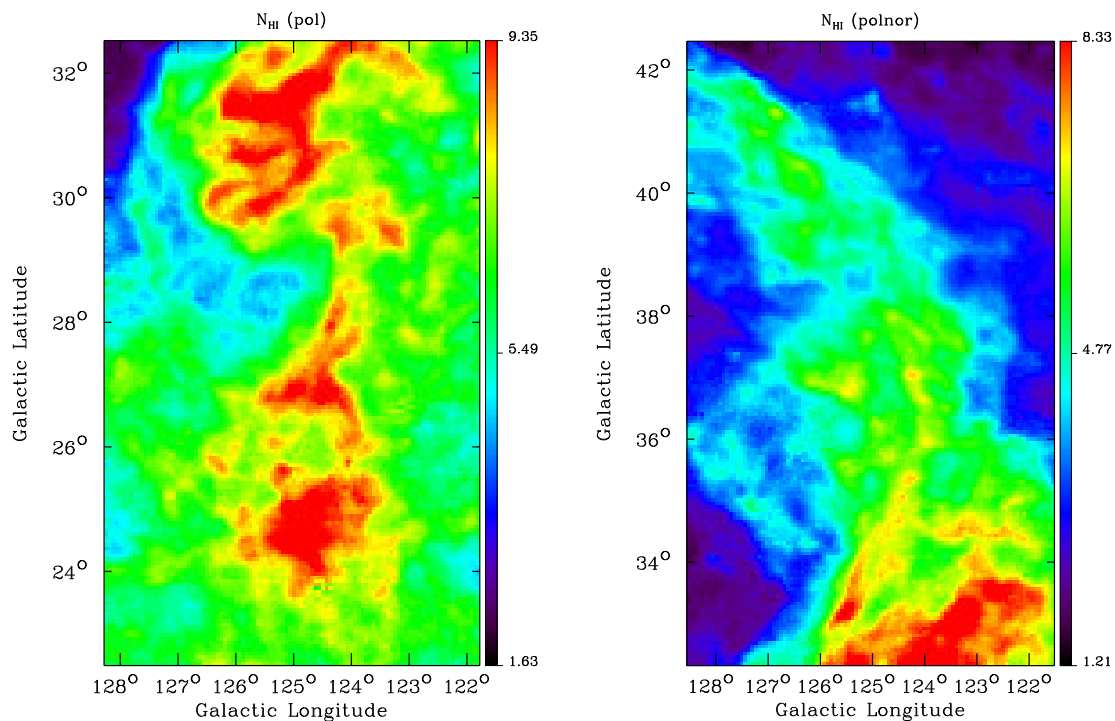
Figure 2.7: Total column density maps for the bright fields in the Polaris region. Units in 10^{20} cm^{-2}.

2.5 Separating gas at different velocities

H I is predominant throughout the Galaxy and thus is observed in every possible direction of the sky. The complexity of the H I spectrum in any direction is influenced by the amount of atomic gas found along the line of sight and the velocity at which these parcels of gas are moving. Upon visual inspection of the H I spectrum, one can see various emission features at different velocities. Those are indicative of different gas clouds along the line of sight. We can use that extra dimension to separate clouds of atomic gas based on their typical radial velocity.

2.5.1 LVC, IVC and HVC

It is customary to catalog gas along the line of sight as belonging to either low, intermediate and high velocity clouds (LVC, IVC and HVC, respectively). Low velocity gas also tends to be local. The exact velocity range of these components can vary greatly (keep in mind that the measured velocity is solely the radial component). For example, one can have an IVC range between $|10|$ and $|80|$ for a certain region in the sky while in another it can be between $|50|$ and $|100|$ km s^{-1}.
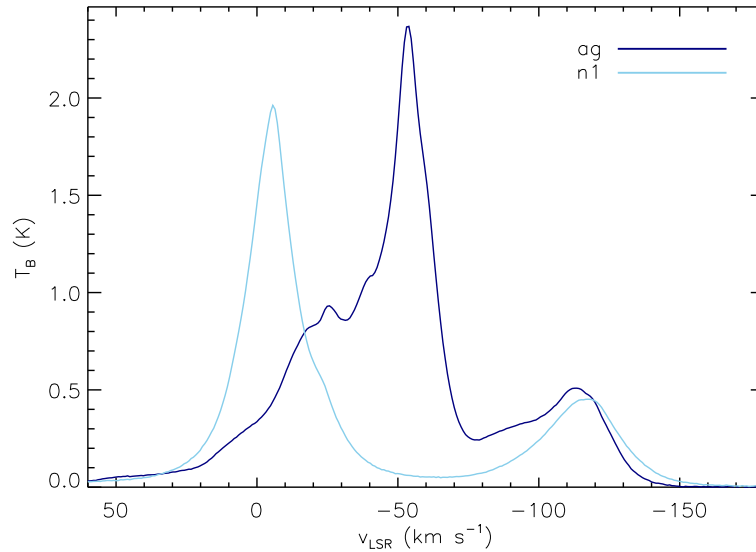
Figure 2.8: Average emission profiles of the *n1* and *ag* fields. The complexity of neutral H I gas clouds along the line of sight is considerably greater in the *ag* field (see also Figure 2.4) which complicates the separation of the different radial velocity gas components.

Several methods have been developed to distinguish these clouds from one another. The simplest approach is a visual one. Regions in the sky showing an average H I spectrum well defined by peaks and valleys are easily separated at spectral minima as shown in Figure 2.8 for the *n1* field. However, we find that for most fields in our survey, the average emission profile is a multitude of blended emission peaks, producing a complex broad peak. Furthermore, differentiating between LVC and IVC is a somewhat subjective procedure given the ubiquity of the so-called *bridge* gas which permeates the velocity space between the two. Figure 2.8 also shows the complicated emission profile of the *ag* field which has weak local emission mixed with stronger emission at intermediate velocities. A naïve, although informative method of separating components, is simply to cut slices out of the cube with a certain velocity partition. This approach works in the fields where the different velocity components are well separated (like in the case of the *n1* field shown above). Cuts are made at either side of the peak emission at channels where little signal is seen. We can use this simple method to construct LVC, IVC and HVC column density maps. However, for fields where the components overlap in velocity space, Planck Collaboration *et al.* (2011c) has found that the standard deviation spectrum is more sensitive to the presence of H I structure and therefore offers a cleaner criterion to separate components. Figure 2.9 shows the mean, median and standard deviation spectrum for the *ag* field. Gaussian decomposition is yet another method that can be used to separate velocity components in the line profile. For the purpose of this thesis, we adopt the same velocity cuts as used in the Planck Collaboration *et al.* (2011c) (see their Table 1).
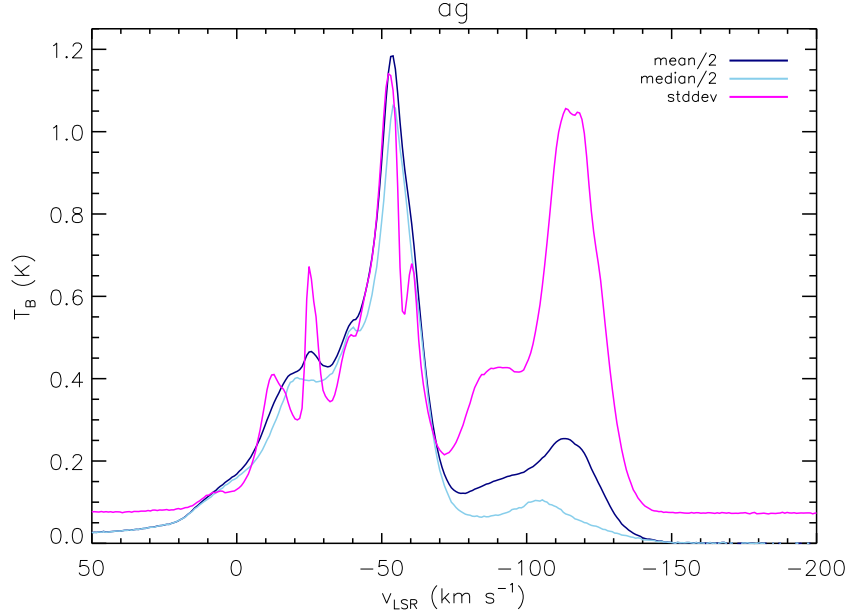
Figure 2.9: Mean, median and standard deviation emission profiles of the *ag* field. Although blended in the mean and median profiles, some local and intermediate velocity components become separate entities in the standard deviation spectrum.

2.5.2 Zero-th Moment Maps

After separating the H I cubes into different velocity components, we can integrate these slices and obtain the zero-th moment maps:

$$W = \int_{v_i}^{v_f} T_b(v) \, dv \tag{2.2}$$

where v_i and v_f are the initial and final velocity channels and W is in units of K km s^{-1}. These maps display the spatial distribution of neutral hydrogen for a given velocity range. Assuming the line of light is not optically thick, we can deduce the H I column density by multiplying the W maps by 1.82×10^{18} to get units of cm^{-2} (see Kulkarni & Heiles, 1988). Although the emissivity of the 21-cm line does not depend on the temperature (in this case T$_{\rm spin}$), the absorption coefficient *does* and the effects of H I self-absorption can be important. In this case, we have adopted a more sophisticated version of the line integral that includes an opacity correction (as used in Planck Collaboration *et al.* (2011c)) to calculate the H I column density,

$$N_{\rm HI} \sim 1.823 \times 10^{18} \, T_{\rm spin} \int_{v_i}^{v_f} -\log(1 - T_b(v)/T_{\rm spin}) \, dv. \tag{2.3}$$

Given the typical T$_b$ (see Table 2.3), the column density maps obtained are not very sensitive to our choice of T$_{\rm spin}$ = 80 K. We calculate column densities maps for each field and for each

velocity component. Equivalent LVC, IVC and HVC maps can be seen in Figures 2 and 3 of Planck Collaboration *et al.* (2011c) which use the first version of our H I survey data.

2.6 Noise in the H I data

The noise associated with the 21-cm H I observations can be estimated in a number of different ways. In addition to the instrumental noise, other contributions include errors in the stray radiation and baseline subtraction (see §2.3). We wish to measure the uncertainties associated with the H I column density maps created using the velocity ranges defined by Planck Collaboration *et al.* (2011c). These estimates will be of importance when calculating the uncertainties related to the mid-IR dust emissivities in Chapter 4. Table 2.3 reports some statistics of the H I line profiles for all velocity components for each survey field. The last column shows that the standard deviation of the end channels (channels free of sky signal) is smaller for fields observed multiple times (0.06 K for *nep*) and higher for fields observed only once (0.11 K for *uma*). In the following sections, we derive errors from the velocity integrated H I maps.

2.6.1 Error estimation in fields observed multiple times

Eight of our fields were observed more than once. This was necessary to improve the data quality since these fields are at high Galactic latitudes and thus faint in H I emission. Besides increasing the signal to noise ratio of the H I brightness temperature when averaged together, it also provides independent measures of the same part of the sky. This can be used to estimate the uncertainty in the H I data. Each data cube, resulting from each independent observing run, is reduced using the procedure described in §2.3. Let $c_1, \ldots, c_n$ designate the cubes for the same field observed independently at different occasions. Given that the sky signal remains constant, when we subtract different c_i's, we obtain a cube whose sole emission should represent the noise level. The noise is appreciably higher where the V_{LSR} is close to zero and where the sky signal is at its maximum. Since we are interested in measuring the column density along certain parts of the line of sight, it is important to note that the uncertainty value depends on the number of channels used when determining the zero-th moment map.

For fields with N full coverage visits, an estimate of the uncertainties associated with the H I column density maps is obtained by

$$\sigma(N_{HI}) = \sqrt{\frac{2}{N} \sum_{n=1}^{M} \frac{\sigma_n}{M}}, \tag{2.4}$$

where $M = N(N-1)/2$ is the number of distinct difference maps $c_i - c_j$ and σ_n is the standard deviation of the n-*th* column density map associated with each difference cube (note that σ_n is in fact a vector with LVC, IVC and HVC components). For some fields, in addition to

Table 2.3.   Characteristics of Temperature Brightness for the H I data

Field Name	T_b (LVC) Mean[a]	Max.[b]	T_b (IVC) Mean	Max.	T_b (HVC) Mean	Max.	σ_{ec}[c]
ag	0.36	9.64	1.27	12.71	0.26	11.59	0.07
bootes	1.20	8.65	0.38	8.30	0.02	0.88	0.06
draco	1.09	20.73	0.98	19.52	0.15	3.26	0.06
g86	1.26	16.31	0.92	28.38	0.03	0.93	0.06
mc	0.76	8.46	1.18	6.11	0.28	3.52	0.08
n1	0.50	6.86	0.31	8.64	0.19	5.30	0.07
nep	2.01	28.91	1.29	27.34	0.11	3.62	0.06
pol	3.87	56.09	0.56	6.94	0.00	0.00	0.11
polnor	2.48	48.06	0.38	9.55	0.00	0.00	0.09
sp	0.58	4.66	0.33	4.60	0.13	2.01	0.07
spc	1.86	32.04	0.35	9.86	0.04	10.55	0.10
spider	2.35	51.58	0.57	11.59	0.02	0.99	0.09
uma	2.34	41.54	0.71	18.09	0.05	8.47	0.11
umaeast	2.64	40.16	0.75	19.41	0.12	11.28	0.11

[a]The mean brightness temperature is obtained by averaging in all dimensions of the subsection of the cube defined by the velocity cuts for each of the LVC, IVC and HVC.

[b]The maximum brightness temperature in the corresponding subsection of the cube.

[c]Standard deviation noise determined in the end channels free of sky signal; channels with V_{LSR} between 150 and 250 km/s.

Note. — All units in K.

Table 2.4. Uncertainties[a] in the H I column density maps for fields observed multiple times

Field Name	IO[b]	σ_{HI}(LVC)	σ_{HI}(IVC)	σ_{HI}(HVC)
ag	2	0.026	0.015	0.023
bootes	2[†]	0.020	0.019	0.014
draco	3	0.010	0.020	0.045
g86	3	0.011	0.016	0.012
mc	2	0.018	0.010	0.039
n1	2	0.021	0.016	0.025
nep	3	0.026	0.024	0.018
polnor	1[†]	0.037	0.019	-
sp	2	0.021	0.022	0.027
spider	2	0.032	0.026	0.016

[a]Uncertainty in column density units (10^{20} cm^{-2}).

[b]Number of independent observations. The uncertainty in the column density decreases with increasing number of observations. The dagger [†] indicates fields with an extra partial visit.

N full coverages, there is an extra partial visitation as is the case for example for *bootes* and *polnor*. If we restrict ourselves to the common areas, we can estimate the H I column density uncertainties using the above method. Since the common area is usually a significant fraction of the entire field, it is reasonable to take these estimates as representatives for the whole field. This is valid as long as the amplitude of the temperature brightness range does not change drastically throughout the field. Table 2.4 shows the typical noise levels found for different velocity components for fields with multiple visits using Equation 2.4. From now on, we will refer to $\sigma(\mathrm{N_{HI}})$ as σ_{HI} for brevity.

2.6.2 Error estimation in fields with a single visit

Error assessment is more complicated for fields with a single visit. Based on our understanding of the phenomena involved, we have developed an educated guess as to the uncertainties associated with measuring 21-cm emission with the GBT. Such estimators are described in detail in Boothroyd *et al.* (2011) (see their Table 3). Here, our goal is to calculate the uncertainties as propagated to the final H I column density maps for our survey fields. These will be used in Chapter 4 in the assessment of the errors on the dust emissivities in the mid-IR.

Following Boothroyd *et al.* (2011), a robust estimation of the uncertainty associated with the H I column densities can be found by adding in quadrature four independent sources of

noise. The first component, termed *line noise* (σ_{ln}), can be characterized as follows

$$\sigma_{\mathrm{ln}}(x,y) = \delta v \sqrt{\sum_{v=v_i}^{v_f} \left[\sigma_{\mathrm{ec}} \left(1 + \frac{T_b(x,y,v)}{T_{\mathrm{sys}}} \right) \right]^2}, \tag{2.5}$$

where δv is the velocity interval between successive channels, σ_{ec} is the standard deviation of the end channels (see end column of Table 2.3), T_{sys} is the system temperature and $T_b(x,y,v)$ is the measured sky temperature brightness. We sum between velocity intervals which correspond to either LVC, IVC or HVC ranges. The second component, named *baseline noise* (σ_{bn}) depends linearly on the number of channels N_{ch} and is defined as $0.03\,\delta v\,N_{\mathrm{ch}}$. The third contribution comes directly from errors in the stray radiation subtraction (σ_{st}). In Boothroyd *et al.* (2011), we assessed the stray radiation for the GBT to be generally about $10 \pm 7\%$ of the real sky signal strength and found it to affect primarily the local gas with $|v_{\mathrm{LSR}}| \leq 20\,\mathrm{km\,s^{-1}}$. Note, however, that the stray radiation does not increase or depend on the signal strength but rather on where the side lobes are pointing. We build stray radiation cubes for each of the fields. If the field has been observed multiple times, we produce an average stray radiation cube from different visits. We integrate the stray radiation cube to produce W_{stray} maps for local, intermediate and high velocity ranges. Table 2.5 contains the average value of the stray radiation per velocity range for each field. The third noise component is then defined to be $0.007\,W_{\mathrm{stray}}$. The final error component (σ_{cal}) is related to a calibration factor needed to match the H I data brightness with other well calibrated 21-cm sources observed with the GBT. Although we include σ_{cal} when summing all sources of uncertainty, this is more of a systematic type error. The total error in the column density maps for fields observed only once is thus estimated to be

$$\sigma(\mathrm{N_{HI}})(x,y) \sim \sqrt{\sigma_{\mathrm{ln}}^2(x,y) + \sigma_{\mathrm{bn}}^2 + \sigma_{\mathrm{st}}^2(x,y) + \sigma_{\mathrm{cal}}^2(x,y)}. \tag{2.6}$$

We note that in opposition to the *scalar* σ_{HI} in Equation 2.4, this one is in fact a matrix. We determine these quantities for the different velocity components for all fields. σ_{HI} is then obtained by averaging those maps and represents the uncertainty associated with each velocity component when calculating dust emissivities (see Chapter 4). Uncertainties for LVC, IVC and HVC are shown in Table 2.6 for fields observed only once.

Figure 2.10 shows the three distinct velocity component maps for the *spider* field and includes the corresponding uncertainty maps obtained via the method explained in this section. These maps reflect the history of the observing strategy for this particular field. They show that a variety of smaller fields were added together to form the final mosaic. This is indeed the case for half of our fields (it is impractical to observe such large sky areas in a single observing session). Also evident is the effect of the residual stray radiation whose strength varies with the observing time, thus producing horizontal stripes in the final mosaic when the cubes are stitched back together. The morphology of the uncertainties, especially in the LVC map, mim-

Table 2.5.   Average stray radiation in the H I velocity integrated maps for all fields .

Field Name	W_{stray}(LVC)	W_{stray}(IVC)	W_{stray}(HVC)
ag	0.132	0.040	0.005
bootes	0.094	0.041	0.005
draco	0.101	0.090	0.012
g86	0.086	0.053	0.006
mc	0.107	0.098	0.022
n1	0.202	0.087	0.022
nep	0.564	0.267	0.050
pol	1.332	0.219	-
polnor	0.323	0.049	-
sp	0.276	0.061	0.007
spc	0.827	0.129	0.007
spider	0.407	0.219	0.014
uma	0.558	0.124	0.012
umaeast	0.449	0.109	0.011

Note. — Average stray radiation in 10^{20} cm^{-2} units.

Table 2.6.   Uncertainties in the H I column density maps for fields observed only once

Field Name	σ_{HI}(LVC)	σ_{HI}(IVC)	σ_{HI}(HVC)
pol	0.055	0.027	-
spc	0.046	0.022	0.042
uma	0.037	0.037	0.055
umaeast	0.038	0.037	0.067

Note. — Uncertainty values in 10^{20} cm^{-2} units. These estimates are the mean values derived from the uncertainty maps built using Equation 2.6.
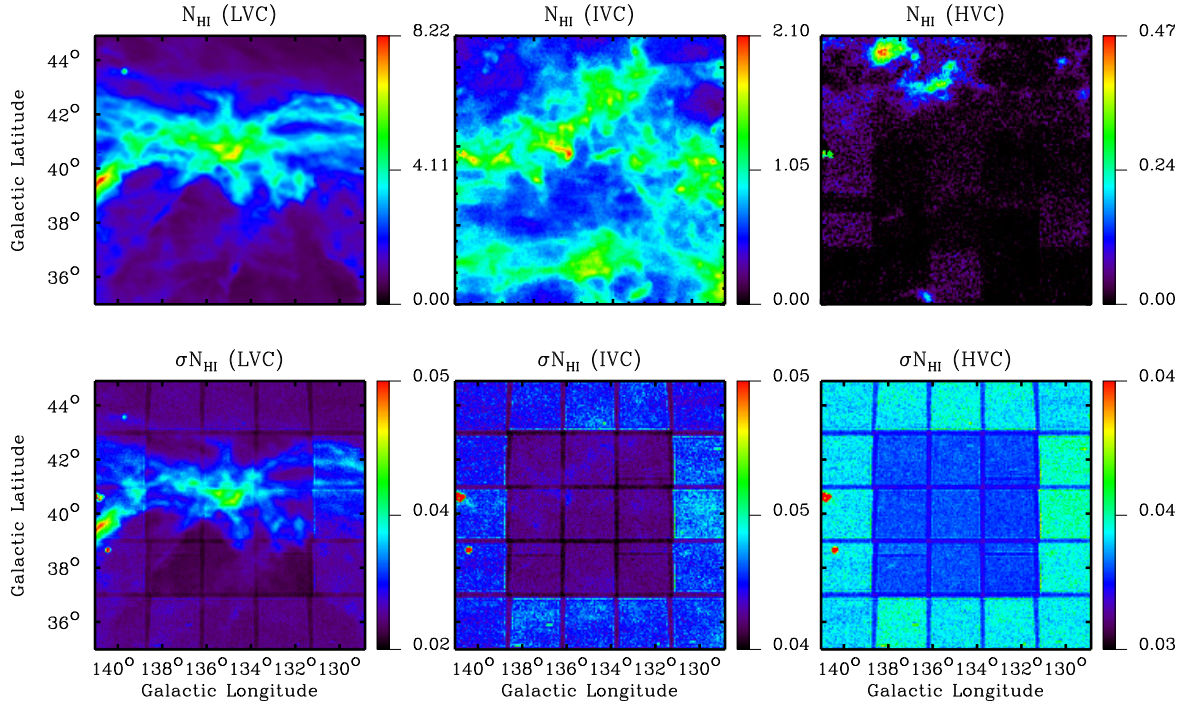
Figure 2.10: *Top*: H I column density maps for the total and the three differ-
ent velocity components for the *spider* field. *Bottom*: Uncertainty difference
maps (see text) associated with above column density maps. The error maps
show a similar sky pattern as the column density maps because of the error
component associated with the line emission. Units are 10^{20} cm^{-2}.

ics the actual H I column density shape, a result of the uncertainty dependence on the real sky
signal (although two orders of magnitude lower).

We also calculate the column density uncertainties using Equation 2.6 for fields observed
multiple times and then compare the two sets of column density error estimates in Figure
2.11. We slightly modify Equation 2.6 by dividing the first two terms in the expression under
the square root by N to accommodate for multiple visits. We find similar uncertainties as
in the multiple visit case if we take into account measurements from multiple independent
observations when using Equation 2.6. This demonstrates the accuracy of our method for
estimating the uncertainties for fields observed only once.

2.6.3   Noise power spectrum

The power spectrum is a commonly used mathematical tool to study the structure present
within H I or cirrus clouds (see, for example, Miville-Deschênes *et al.*, 2003). The power spec-
trum of an image is the amplitude of its Fourier transform collapsed to one dimension by
azimuthal averaging; it is usually denoted by $P(k)$ where k is the inverse of a spatial scale
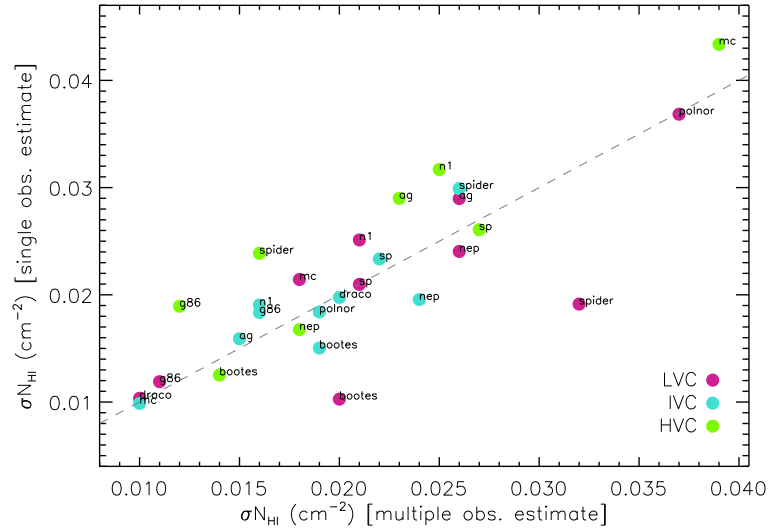
Figure 2.11: Comparison between the H I column density uncertainty estimates for fields observed several times. The uncertainty value estimated using the different coverages is similar to the one based on a theoretical assessment of the error sources (when accounting for multiple visits in Equation 2.6). The dashes represent a unit slope line.

(e.g., in units of arcmin^{-1}). The pixel size constrains the smallest scales being sampled while the low k regime is set by the size of the map. The H I gas structure is well characterized by a somewhat steep power law of about -3 in Fourier space reflecting its turbulent nature (see Stephan et al., in preparation or Miville-Deschênes *et al.*, 2003). In order to fit a power law to as large a range in k as possible, one has to use a model that takes into account the different components that affect the measurement, such as noise and beam convolution. The noise level can be deduced using the end channels of the H I data cubes (σ_{ec} above). These channels are free of H I signal and should give a good estimate of the instrumental uncertainties. We calculate zero-th moment maps of emission free channels by integrating over the same number of channels as the ones used in the real signal integrated maps and compute their power spectra. If the character of the noise is Gaussian, then its power spectrum should be relatively flat for almost all k's. This is clearly seen in Figure 2.12 (dotted line) and is a lower limit to the noise. For survey fields observed multiple times as in §2.6.1, we can make use of the difference cubes to produce difference maps integrated over the actual velocity range used for LVC and IVC. These maps, which contain the uncertainties related to the observations and data reduction, are good estimators of the noise. We compute the power spectra of the difference maps and compare them with the power spectra of the N$_{HI}$ for the three velocity components. Figure 2.12 shows this comparison for the *draco* field (observed twice) and the *nep* mosaic (observed 3 times). The drooping behaviour of all power spectra (signal, noise and end channels) at high k (greater than 0.08 arcmin^{-1}) is a consequence of the gridding used in the creation of the cube. At high k, we can see that both signal and noise power spectra overlap. On the other hand, the

amplitude of the power spectrum, obtained from the emission free end channels, is smaller on all k scales than the one using the difference maps. This indicates that the uncertainty in our measurement increases with the strength of the sky signal and is also affected by errors from baselines and stray radiation. These additional contributions have been taken into account when estimating the total H I uncertainty associated with the column density maps for fields visited only once.

An estimate of the uncertainty in the N_{HI} map can be obtained from the level of the noise power spectrum relative to the level from the end channels, an equivalent alternative to the use of Equation 2.4. For example, for the IVC component in the *draco* field, that ratio is about 8 (Figure 2.12), and so the noise is $\sigma_{ec} \times \sqrt{8\,N_{ch}} \times 1.823 \times 10^{20} \mathrm{cm}^{-2} \sim 0.027 \times 10^{20} \mathrm{cm}^{-2}$, which is in good agreement with the entry $0.020 \times 10^{20} \mathrm{cm}^{-2}$ in Table 2.4. The N_{ch} here corresponds to the number of channels used to do the intermediate velocity integrated map for the *draco* field and is about 80.
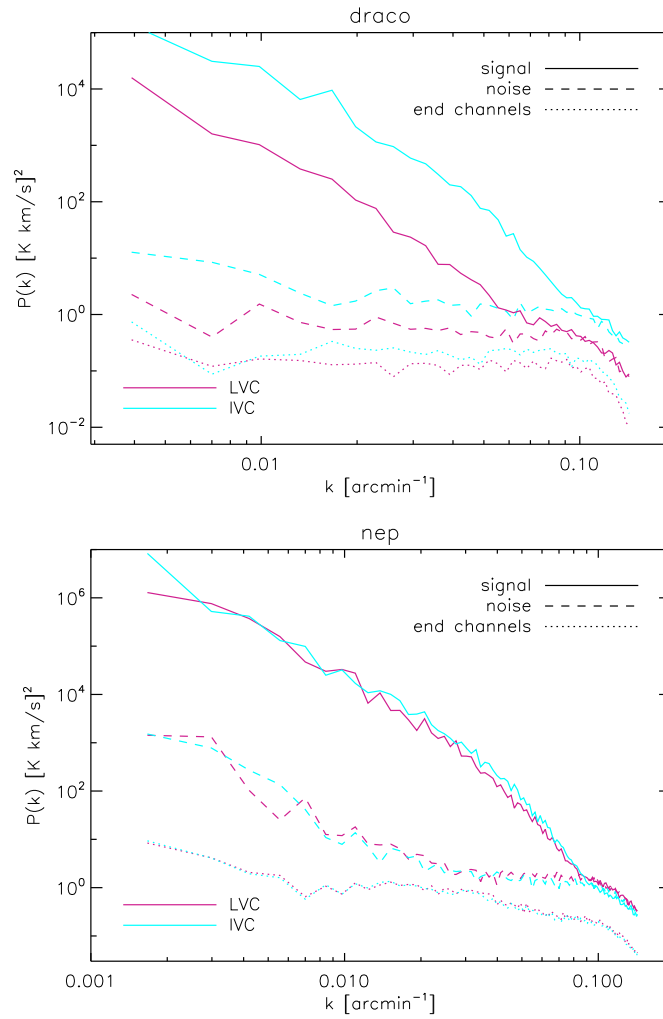
Figure 2.12: Power spectra of N_{HI} maps (solid) and the noise estimator maps (dash) from the difference for independent observations. For the *draco* field (left) and *nep* mosaic (right). Dotted lines display the power spectra of integrated end channels maps using the same number of channels as in the LVC and IVC maps.

Chapter 3

IRIS data: Morphology and noise properties

In this brief chapter, we start by introducing the IRAS/IRIS infrared data in §3.1, which in conjunction with the 21-cm H I observations of the previous chapter, are used to obtain mid-IR dust emissivities in Chapter 4. In §3.2 and §3.3, we discuss some of the IR data characteristics and caveats. The uncertainties associated with each IR map are calculated in §3.4.

3.1   Introduction

The IRAS survey (Neugebauer *et al.*, 1984) was a major step foward in our understanding of the physics of dust structures in both our solar system (Hauser *et al.*, 1984) and our Galaxy (Low *et al.*, 1984). The whole sky in the IR range with nominal filters at 12, 25, 60 and 100 μm was observed. At these wavelengths, the primary source of emission comes from dust grains present in different environments from star-forming regions to diffuse structures such as cirrus clouds. The high frequency bands trace the PAHs and stochastic emission from small dust grains (although overwhelmed by the bright zodiacal light emission background), while at the long IR wavelengths the emission is mostly thermal and originates from the large dust grains in equilibrium with the local ISRF. Despite being an invaluable dataset, the IRAS survey had some deficiencies and about two decades later, IRIS (short for 'Improved Reprocessing of the IRAS Survey') was developed by Miville-Deschênes & Lagache (2005) to correct them. Primarily, these authors have substantially decreased the stripe pattern seen in some IRAS data (also called ISSA plates) and adjusted the IRAS zero-level and calibration using the DIRBE survey. The IRIS product has been successfully used to draw meaningful physical insights on the nature of Galactic dust and the CIB (e.g., Planck Collaboration *et al.*, 2011c) and we make use of it in this thesis to calculate mid-IR dust emissivities at high Galactic latitudes.
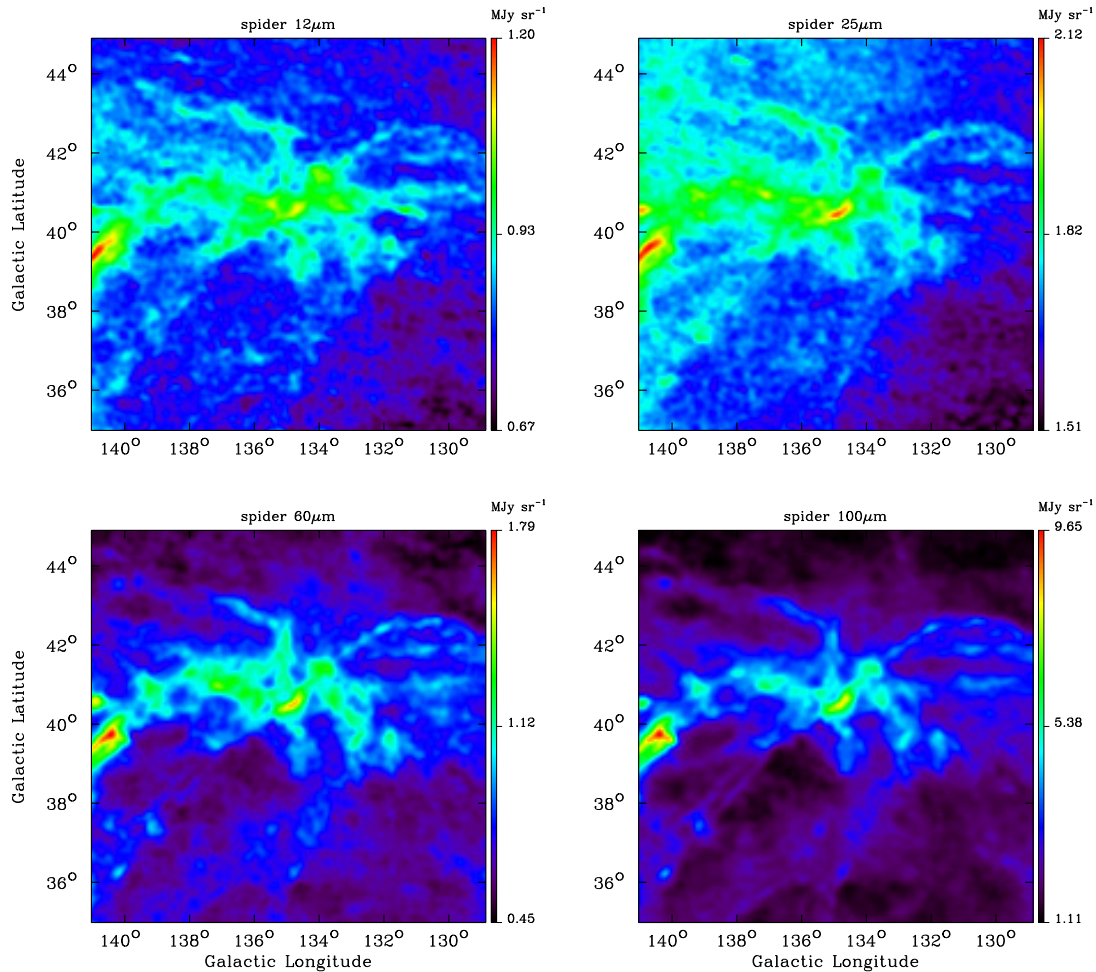
Figure 3.1: IRIS maps for the *spider* field with point sources subtracted. The maps have a 9.́55 resolution and a pixel size of 3.́5. The corresponding total H I column density map of this field is displayed in Figure 2.6 in §2.4.

3.2   Data Set Characteristics & Definitions

We build IRIS maps at 12 and 25 μm of the fields presented in Chapter 2. Often, more than one plate is necessary and a mosaic is constructed using bilinear interpolation. The IRIS plates have a native resolution of 3.́8 at 12 and 25 μm with a grid size of 1.́7 (see Table 1 of Miville-Deschênes & Lagache, 2005). At 60 and 100 μm that resolution is 4′ and 4.́3, respectively. Once we have produced IR maps with the same sky size as the H I column density maps, we convolve them with an appropriate gaussian kernel so as to bring them to the H I resolution of about 9.́55 and change the pixel size to 3.́5 via a bilinear interpolation. As an example, Figure 3.1 shows the mid- and far-IR maps for the *spider* field with point sources subtracted.

In the following discussion, we use the term HCON ('Hours Confirmation') to refer to the different viewing periods of the IR satellite. IRAS covered the entire sky twice and about 2/3
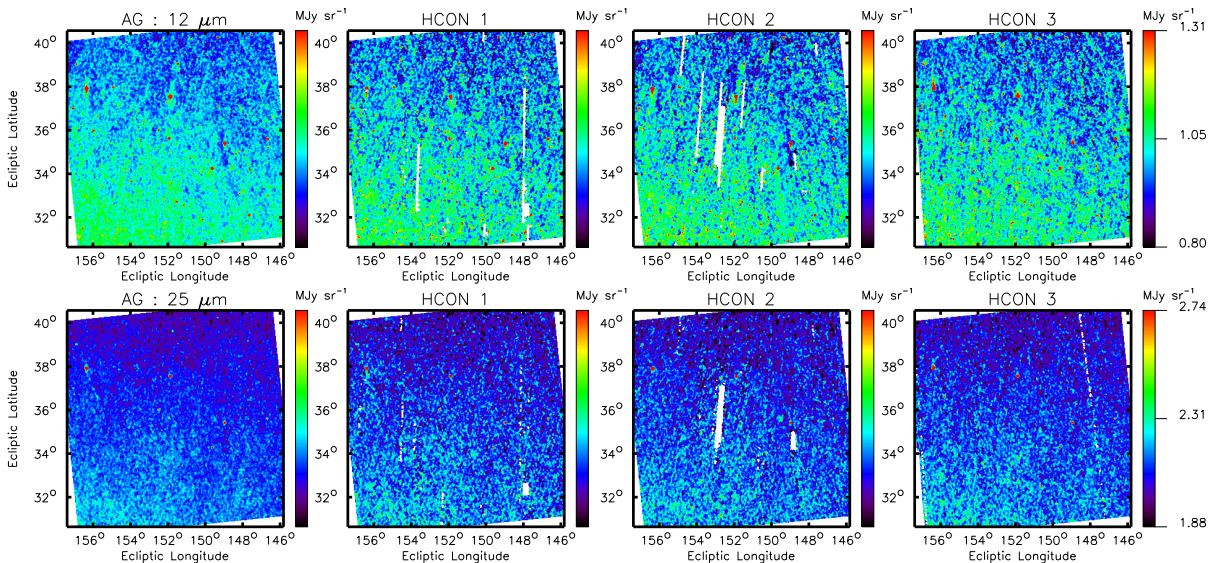
Figure 3.2: HCONs for the *ag* field at 12 *µm* (top) and 25 *µm* (bottom). $HCON_0$ (on the far left) is the final map and is the combination of the 3 different HCONs on the right. At both mid-IR wavelengths, the maps reveal a gradient increasing towards the lower ecliptic latitudes.

a third time (see http://irsa.ipac.caltech.edu/IRASdocs/iras_mission.html). For most fields in our H I survey, IRAS has 3 independent observations. Figure 3.2 shows the 3 HCONs ($HCON_1$, $HCON_2$ and $HCON_3$) as well as the final data product, $HCON_0$ for the *ag* field at mid-IR wavelengths. These are projected on ecliptic coordinates, the natural coordinate system for IRAS, which scanned along lines of constant ecliptic longitude. The vertical blank stripes in the HCONs reflect this scanning strategy. The source of the strong gradient seen increasing towards the ecliptic plane, is discussed in the next section.

3.3   Caveats

3.3.1   Zodiacal Light in the 12 and 25 *µm* data

As in any mid-IR all sky survey, the IRAS data is affected by a striking surface brightness gradient growing in the direction of the ecliptic. This reflects the emission of dust particles which inhabit our solar system. Coined *zodiacal light*, it plagues the mid-IR (and to a lesser extent the far-IR) filters of the IRAS survey. The 25 *µm* maps are the most affected by it since this interplanetary dust is thought to emit like a 250 K blackbody (Kelsall *et al.*, 1998 and references therein). Later work by Reach *et al.* (1996) with ISOcam data also suggested that Zodiacal light (between 5 to 16.5 *µm*) was well fitted by about a 260 K blackbody composed of silicates. According to the *ISSA explanatory supplement* (http://irsa.ipac.caltech.edu/IRASdocs/issa.exp.sup/ch3/C.html#2), the IPD (Interplanetary Dust) model used by the ISSA team
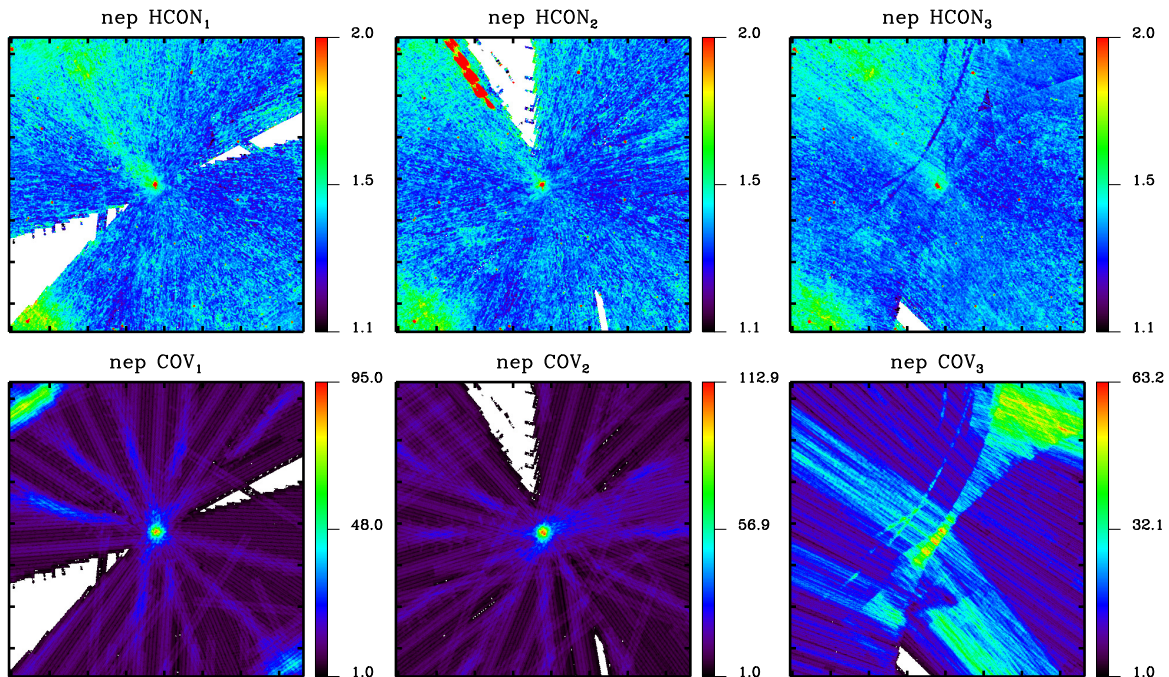
Figure 3.3: *Top:* individual HCONs for the *nep* field at 25 μm in MJy sr^{-1}. *Bottom:* corresponding coverage maps in arbitrary units (the higher the value, the greater the number of times that direction was observed). The artificial ridge of strong surface brightness is easily seen on the top left part of HCON$_2$ (middle image in the top row).

is parameterized by a gradient on large scales and its removal occurs at the timestream level. Further reading of their Appendix G (`http://irsa.ipac.caltech.edu/IRASdocs/issa.exp.sup/Ap/G.html`), shows that the zodiacal light in the IRAS filters is well fitted by a blackbody of about 266 K peaking in the mid-IR. The dust density distribution varies with distance from the sun and height relative to the Ecliptic plane. No dust rings or bands are included in this model.

Miville-Deschênes & Lagache (2005) have improved the existing IRAS HCONs by calibrating them with the DIRBE data. This was made possible given the fact that the filters nominal wavelengths and shapes are very similar. Although the spatial resolution of the DIRBE data is worse when compared to IRAS, they note that the zodiacal light signal should not vary greatly at small scales and thus improved the subtraction of the zodiacal light from the HCONs. Nevertheless, Gorjian *et al.* (2000) argued that even the model used to remove the IPD component from the DIRBE data showed residuals consistent with leftover zodiacal light. Figure 1 of Wright (1998) shows difference maps at 100 μm (between odd and even weeks of observing) which display residual stripes of zodiacal emission seen in the DIRBE IPD corrected data. In particular, Gorjian *et al.* (2000) state that at Galactic coordinates of approximately $l = 121°$
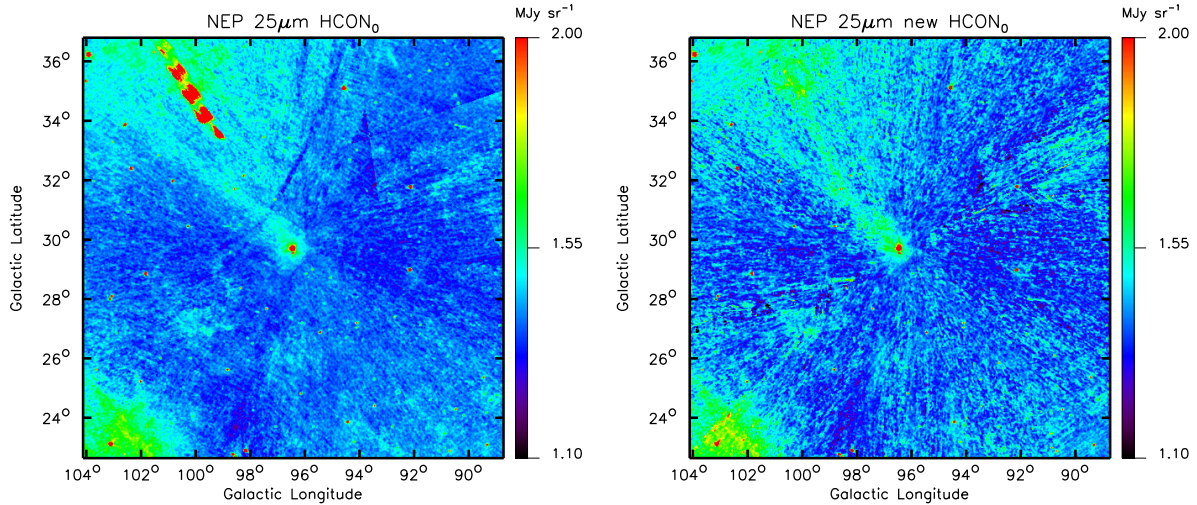
Figure 3.4: Original $HCON_0$ 25 μm *nep* map (*left*) and corrected map (*right*).

and $b = 69°$, the DIRBE IDP corrected 25 μm map, has residual zodiacal light of about 96% compared to the total surface brightness. In order to estimate the CIB contribution to the near-IR sky, these authors have instead used a model (discussed in the appendix of Wright, 1998) which makes a 'zero-level' IPD surface brightness assumption for the Ecliptic Pole regions. In this thesis, we will assume that the residual shape of the zodiacal light still present in the IPD corrected IRIS maps can be parametrized by a tilted plane (see Chapter 4).

3.3.2 Point sources

Far-away galaxies can show up as point sources in the IRAS wavelengths depending on their redshift and stars are increasingly visible towards higher frequencies (i.e., at 12 and 25 μm). For the IRIS product, Miville-Deschênes & Lagache (2005) used a contrast method for point source identification in bright regions, while for fainter plates a simple sigma-clipping method was employed (see their Appendix A). We use a version of the IRIS data from which the point sources are removed via a sigma-clipping procedure so that the IR maps are left only with diffuse extended structures (private communication, Miville-Deschênes).

3.3.3 Other issues

While inspecting the HCONs for our fields, we noticed that in *nep*, $HCON_2$ had a bright ridge at Galactic coordinates of about $l = 100$ and $b = 35$ which did not appear in the other two HCONs (see Figure 3.3). After visually inspecting the HCONs for the other IRAS wavelengths it was clear that such structure was not real and most likely related to a sporadic problem with the telescope detector. Following the usual pipeline, this feature is propagated to the final map

(HCON$_0$) and could seriously compromise the calculation of the dust emissivity at 25 μm for this field. Thus, we built a new HCON$_0$ map using only those parts of each individual HCON that are free of artifacts. Figure 3.4 shows the original and the corrected HCON$_0$.

3.4   Noise properties

The HCONs are averaged to produce a final map, HCON$_0$, which has a nominal signal to noise ratio $\sqrt{n}$ times better than a single observation (or HCON), where n is the number of times the field was observed. A simple way of determining the uncertainties inherent to a map constructed via the mean of multiple maps, is to use the methodology applied to the H I fields observed multiple times from Chapter 2. As in §2.6.1, we produce all possible difference maps (i.e., HCON$_1$-HCON$_2$, etc). We divide these by 2 so that they follow the same statistical properties of the mean. We apply this method to all 14 fields and all 4 IR wavelengths. The original HCONs have a pixel size of 1$'\!.7$ and the same spatial resolution as the final IRIS plates (see Table 1 of Miville-Deschênes & Lagache, 2005). Because we want to determine the uncertainties associated with the mid-IR dust emissivities in Chapter 4, we convolve the difference maps to the 9$'\!.55$ resolution at which the spatial correlation analysis is done. Besides being convolved, the difference maps are also re-sampled using bilinear interpolation onto the GBT grid (3$'\!.5$). We then apply Equation 2.4 to the IR difference maps. We find the standard deviation, σ_{IR}, for these maps (see Table 3.1). The values at 60 and 100 μm are similar to those published by Planck Collaboration *et al.* (2011c).

Table 3.1. IRIS noise estimates (σ_{IR})

Field Name	σ_{12}	σ_{25}	σ_{60}	σ_{100}
ag	0.0174	0.0205	0.0165	0.0297
bootes	0.0162	0.0169	0.0143	0.0224
draco	0.0149	0.0136	0.0135	0.0266
g86	0.0158	0.0138	0.0153	0.0248
mc	0.0166	0.0242	0.0146	0.0249
n1	0.0156	0.0129	0.0128	0.0230
nep	0.0159	0.0137	0.0146	0.0278
pol	0.0156	0.0133	0.0146	0.0350
polnor	0.0158	0.0132	0.0137	0.0267
sp	0.0157	0.0149	0.0153	0.0262
spc	0.0161	0.0150	0.0147	0.0293
spider	0.0163	0.0150	0.0149	0.0296
uma	0.0174	0.0170	0.0163	0.0372
umaeast	0.0175	0.0186	0.0171	0.0369

Note. — Standard deviation of each noise map for all IRAS wavelengths. The noise maps are derived from difference maps between different coverage periods or HCONs. Units in MJy sr^{-1}.

Chapter 4

Correlations of mid-IR dust emission and H I at High Galactic Latitudes

This chapter is devoted to the analysis of spatial correlations between the H I survey maps described in Chapter 2 and the mid-IR IRIS maps presented in Chapter 3 and is in preparation as Pinheiro Gonçalves et al., 2013. In §4.1, we start by introducing some of the earlier work done on H I and dust correlations in the far-IR and submillimeter. In §4.2, we present a multilinear template model used to correlate the two data sets and other relevant procedures such as masking. We derive uncertainties (in §4.3.1) associated with mid-IR dust emissivities and discuss these preliminary results in §4.3.2. We find that the residual maps obtained from the least-squares fit show a surface brightness gradient consistent with poorly subtracted zodiacal emission (in §4.3.3) and propose a simple way to remove it in §4.3.4. A new set of dust emissivities which account for the surface brightness gradient are shown in §4.3.5 with revised uncertainties in §4.3.7. In §4.3.7, we display the probability distribution of the dust emissivities obtained via the Monte-Carlo method and address the significance of the new dust emissivities found in §4.4. We also calculate new dust emissivities at far-IR wavelengths in §4.5 and compare these with the ones published in Planck Collaboration et al. (2011c). We show the complete SEDs for each field from the mid-IR to the sub-millimiter in §4.6 and present color-color diagrams and emissivity ratios in §4.7. Finally, we discuss the derived mid-IR CIBA value in §4.8 and the residual maps power spectra in §4.9.

4.1   Introduction

In this chapter, we analyze the H I and mid-IR data sets previously described in Chapters 2 & 3 and calculate dust emissivities per hydrogen column density (I_ν/N_{HI}). In particular, we look for differences in the emissivities of dust associated with local, intermediate and high velocity gas. These differences, usually reflected in dust emissivity ratios between different infrared wavelengths, are indicative of a change in the grain size distribution or a change in the inter-

stellar radiation field (ISRF). For example, the shattering of grains by shocks can significantly alter the spectral energy distribution (SED) whereas an increase in the ISRF might result in increased emissivities all round. We compare our estimates of the dust emissivities with a theoretical model (DustEM, Compiègne *et al.*, 2011) which evaluates the emission of a consistent distribution of dust grains for a variety of radiation fields. Previous work by Boulanger & Perault (1988) asserted a strong empirical spatial correlation between IR dust clouds and H I gas between -400 to 400 km/s. Using multiple 21-cm observations with a resolution of about half a degree, they correlated velocity integrated H I maps (in units of K km s^{-1}) with infrared all-sky data from the IRAS survey. The average dust emissivity at 100 μm was found to be about 0.85 MJy sr^{-1} (10^{20} H atoms cm^{-2})$^{-1}$ and deviations from this value were attributed to regions heated by different interstellar radiation field strengths (given that star-forming and known molecular regions were removed from their analysis). Additionally, motivated by the need to remove zodiacal light from the IRAS bands, they also extrapolated the dust model obtained at 100 μm to mid-IR wavelengths, which estimated the Galactic surface brightness emission to range between 0.1 to 0.2 MJy sr^{-1} at 12 and 25 μm. A direct measure of the IRAS/IRIS data shows that the average high Galactic latitude surface brightness at mid-IR wavelengths is a decade brighter than their extrapolated predictions.

Here, we conduct a similar analysis at mid-IR wavelengths. Along with the IRAS/IRIS data at 12 and 25 μm, we use the higher resolution H I data presented in Chapter 2. Since the H I data were also used by Planck Collaboration *et al.* (2011c), this allows us to probe the dust spectral energy distribution from the submillimeter to the mid-IR wavelengths at high Galactic latitudes at the higher resolution of the GBT.

4.2   Data Analysis

We use an improved version of the methodology described in Planck Collaboration *et al.* (2011c) to analyze the H I and mid-IR data. We start by assuming a basic multilinear model (template) for the spatial correlations of the form:

$$I_\lambda(x,y) = \sum_{i=1}^{3} \epsilon_\lambda^i \, N_{HI}^i(x,y) + c_\lambda, \tag{4.1}$$

where I_λ represents the surface brightness (in MJy sr^{-1}) in the mid-IR maps, N_{HI}, the column densities of the H I gas and ϵ_λ, the dust emissivities. The index $i = 1, 2, 3$ refers to the local, intermediate and high velocity components, respectively, and c_λ is a constant that represents a uniform background level of the infrared map over the field, for example, from the cosmic infrared background (CIB), at least at longer wavelengths.
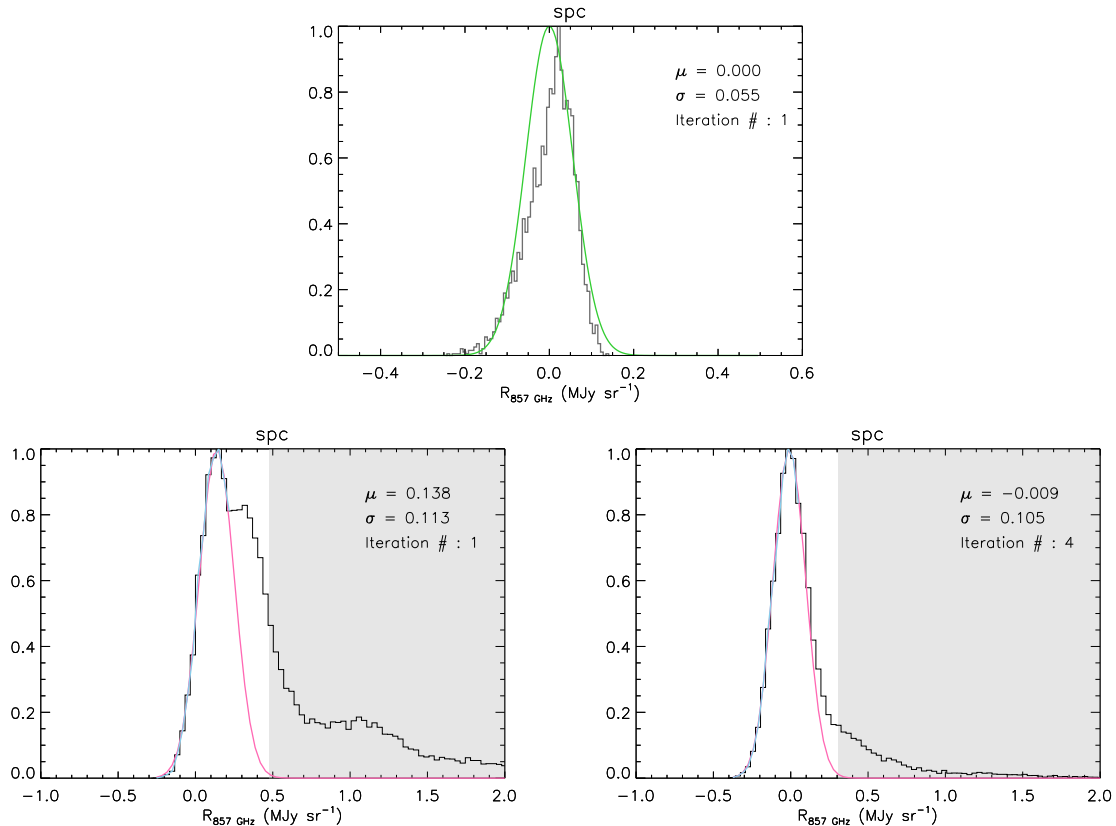
Figure 4.1: Residual distribution histograms for the *spc* field. *Top*: using only the 10% lowest surface brightness pixels. The green line traces the gaussian shape built from the mean and standard deviation of the residuals. *Bottom left*: using *all* pixels for iteration #1. The blue line traces the histogram data used to extract the pink gaussian shape. Pixels in the grey area are rejected. *Bottom right*: iteration #4, where the masking procedure stops.

4.2.1 Masking

Large deviations from the template model are traditionally interpreted as a sign of dust emission associated with gas other than the atomic being traced by N_{HI} (i.e., molecular and ionized gas). Masking is commonly used to avoid such problematic areas usually suspected of having dust mixed with molecular gas. For example, Boulanger *et al.* (1996) use a simple column density cut-off criterion as a basis for masking. However, it turns out that this method is overly aggressive in the sense that it masks many areas well fit by the linear model. More flexible procedures have been developed as in Arendt *et al.* (1998) and Planck Collaboration *et al.* (2011c), which iteratively reject problematic pixels.
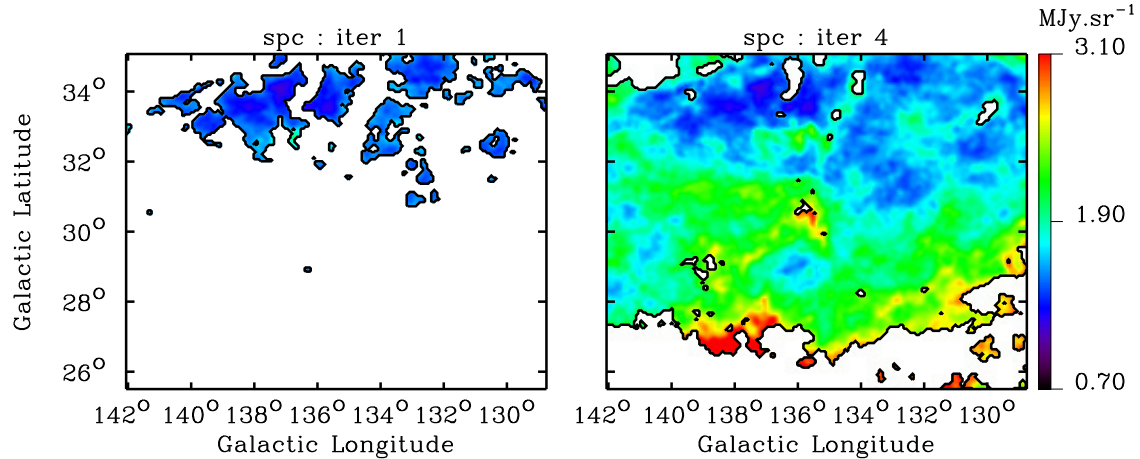
Figure 4.2: IRIS 100 μm maps of the *spc* field with masked areas in white. *Left*: mask used in the least-squares fit at iteration #1. The field is almost completely masked because we only use the 10% faintest pixels in the first iteration. *Right*: same as in left but for iteration #4. The number of pixels has increased substantially and it is determined by the $3\,\sigma$ cut as shown in Figure 4.1.

Masking method

In order to ensure a consistent measure of the physical properties of the dust, and that the dust is correlated with the same parcels of atomic gas used in Planck Collaboration *et al.* (2011c), we develop morphologically similar masks using the PLANCK 857 GHz data (the original masks were not readily available). We start by selecting the 10% lowest surface brightness pixels in the dust emission map, the rationale being that such pixels have a better chance of actually tracing low density gas, which is expected to be mainly atomic. The corresponding pixels in the H I column density maps are used in conjunction with the submillimeter data to obtain preliminary dust emissivities using Equation 4.1 (see §4.3 for details). Based on these ϵ_λ, we obtain the residual emission with respect to the model for the entire field and form a histogram of the residuals. If the template model is indeed a good fit to all of the data, then one would expect white noise statistics for the residuals, a Gaussian distribution with a dispersion predictable from the errors in the data. Departures are indicative of 'deviant' data (see Figure 4.1 for an illustration). In the case of dust associated with molecular regions, we expect to find large positive residuals compared to the mean of the distribution. This is especially evident in brighter fields, i.e., fields with generally higher column densities where the increase in surface brightness is not necessarily matched by a corresponding increase in the H I column density. We therefore extract the Gaussian shape $\mathcal{N}(\mu, \sigma)$ from the residual distribution as best as possible (by determining the peak and using its left wing) and mask (reject) pixels having residuals that fall above the $\mu + 3\,\sigma$ region.

Next, we calculate a new set of emissivities using the masked field and proceed in a similar
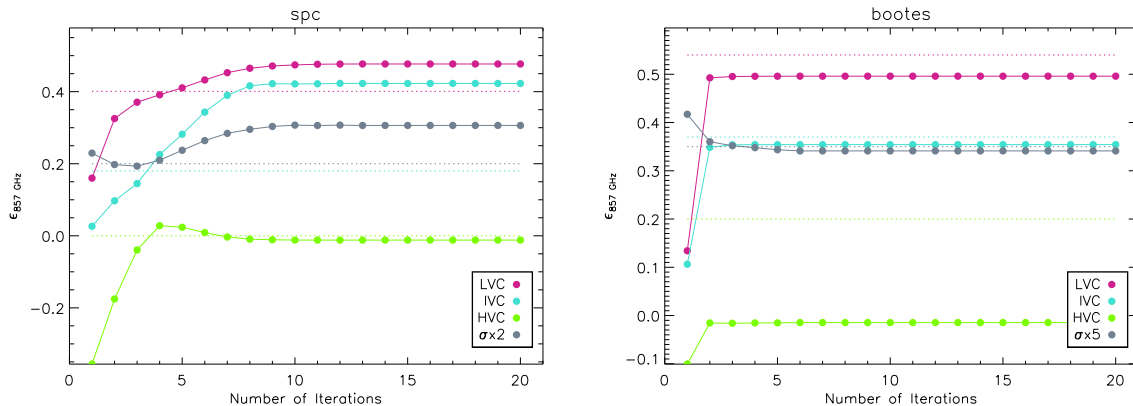
Figure 4.3: Dust emissivity estimates *vs.* iteration number for all velocity components at 857 GHz. The standard deviation of the residual distribution, σ from $\mathcal{N}(\mu, \sigma)$, is shown in grey and has been scaled for easier visualization. Dotted lines represent the dust emissivity estimates quoted in Planck Collaboration *et al.* (2011c).

fashion by extracting the Gaussian shape from the new residual histogram and by rejecting pixels with residuals greater than $\mu + 3\sigma$. We iterate this procedure and find that it typically converges to a stable solution within 20 steps; we keep a record of all the masks and (μ, σ) for each iteration. For a specific example of how the ϵ_λ evolve with different masks, see plot on the left in Figure 4.3 which refers to the *spc* field. Note that the mask is not cumulative and that much of it may change at each iteration step according to the current (μ, σ). Figure 4.2 displays in white the area masked prior to the least-squares fit for iteration #1 and 4.

Mask differences

Although we use the exact same fields, in some cases our masks differ slightly from those in Planck Collaboration *et al.* (2011c). Given that we follow the same workflow, one would expect identical masks; however, certain tasks like histogram binning and gaussian extraction depend on implementation details. As can be seen in Figure 4.3 (for the case of the *spc* field), at the lowest σ our masking procedure yields values close but not equal to those quoted in Planck Collaboration *et al.* (2011c). Because we want to mimic their procedures, we select our masks from iteration steps that best reproduce their emissivities, e.g., iteration #3 and 4 for this particular field. Furthermore, we also rely on visual inspection to ensure morphological similarity and choose between close iterations. These slight changes may be attributable to data reduction refinements which have occurred after Planck Collaboration *et al.* (2011c) was published. We have improved the gridding of the GBT H I data from pill-box to one based on a modified Bessel smoothing and finalized its calibration (see Boothroyd *et al.*, 2011). For some fields such as *bootes*, we are never able to reproduce their emissivities exactly (see plot on the right of Figure 4.3) which might be attributed to slight calibration changes in the different

Planck data releases. Nevertheless, our masks are still well suited for comparison. We do a least-squares fit analysis at 60 and 100 μm based on these masks and retrieve similar estimates (within the 1σ error) for the dust emissivities as those published in Planck Collaboration *et al.* (2011c) as will be shown in §4.5.

4.3   Dust emissivities in the mid-IR

Dust emissivities ϵ_λ are calculated via a least-squares fitting algorithm. In particular, we use MPFIT, a common IDL routine for linear and non-linear problems (for more details, see Mark-wardt, 2009). For comparison purposes, we also use REGRESS (for linear problems), which produces similar results. Our goal is to find the coefficients that best fit the multilinear template model (Equation 4.1). Note that we do not constrain the parameter space. In other words, we do not force, a priori, emissivity estimates to be positive. Tables 4.2 and 4.3 contain the dust emissivities we find for both 12 and 25 μm. Also quoted are the 3σ uncertainties which are obtained through a Monte-Carlo simulation explained in more detail in the following section.

4.3.1   Uncertainties

To estimate the uncertainties associated with dust emissivities, we employ a similar Monte-Carlo technique to the one described in Planck Collaboration *et al.* (2011c). Let $\mathrm{I}_{\lambda,0}(x,y)$ represent the model surface brightness map derived from the least-squares fit. In each step j, we build the following mid-IR emission map model:

$$\mathrm{I}_\lambda^j(x,y) = \mathrm{I}_{\lambda,0}(x,y) + \mathcal{N}^j_{\mathrm{IR}}(\sigma_{\mathrm{IR}}) + \mathcal{N}^j_{\mathrm{CIB}}(\sigma_{\mathrm{CIB}}) + \sum_{i=1}^{3} \mathcal{N}^j_{\mathrm{HI}}(\sigma^i_{\mathrm{HI}}). \tag{4.2}$$

Here, $\mathcal{N}^j_{\mathrm{HI}}$ and $\mathcal{N}^j_{\mathrm{IR}}$ are 2D random realizations of white noise with σ^i_{HI} and σ_{IR} standard deviations and represent the uncertainties in the H I and IRIS data, respectively. $\mathcal{N}^j_{\mathrm{CIB}}$ is also a random realization with a standard deviation σ_{CIB}, but now with a power spectrum $P(k) \propto k^{-1}$ believed to best represent the CIB component (Planck Collaboration *et al.*, 2011d). We now briefly describe how σ_{HI}, σ_{IR} and σ_{CIB} are derived from the knowledge of instrumental and observational uncertainties.

Given the identical choice of velocity ranges for each gas component, we could adopt the N_{HI} uncertainty values cited in Table 1 of Planck Collaboration *et al.* (2011c). However, these were calculated at an early stage of the H I pipeline development, using the difference between *xx* and *yy* polarization H I cubes and provide only a rough estimate of the noise without taking into consideration the effect of stray radiation. Instead, we use the N_{HI} uncertainties estimated in Chapter 2. For fields observed more than once, we rely on the estimates obtained via difference maps between multiple observations and for fields observed only once, we calcu-

late expected uncertainties using Equation 2.6. The IRAS data uncertainties are also calculated based on difference maps determined by subtracting pairs of independent HCONs of the same field (see §3.4 for details). We convolve and re-grid the HCON difference maps to the H I data format (9′55 resolution with a 3′5 pixel). Finally, we apply Equation 2.4 to determine the uncertainties associated with the IRIS maps. This method is similar to the one adopted by Planck Collaboration *et al.* (2011c) to determine the uncertainties in the IRIS 60 and 100 μm data with the only difference being that we do not use the coverage maps information and our final resolution is slightly different (9.55′ *vs* 9.4′). Table 3.1 in Chapter 3 shows the standard deviation $\sigma_{\rm IR}$ derived using the HCON difference maps at 12 and 25 μm for all fields. These values are used to build the IRIS 2D random realization of white noise maps ($\mathcal{N}_{\rm IR}$).

According to Planck Collaboration *et al.* (2011c), the CIB sky should be the greatest error source in the template model. Its dispersion, $\sigma_{\rm CIB}$, can be obtained by approximating the uncertainty of the residual maps, $\sigma_{\rm R}$, by

$$\sigma_{\rm R}^2 = \sigma_{\rm CIB}^2 + \sigma_{\rm IR}^2 + \sum_{i=1}^{3} \left[\epsilon_\lambda^i \, \sigma_{\rm HI}^i \right]^2. \tag{4.3}$$

This equation is valid if the residual distribution does not reflect other sources of emission ill-fitted by the template model, for example dust associated with molecular gas not traced by H I. Therefore, we derive $\sigma_{\rm CIB}$ only for 'faint' fields. These have such a small masking percentage that dust emission associated with molecular gas should be negligible. Consequently, we can confidently assume that their residual distribution reflects primarily the effects of the CIB anisotropies with minimal contributions from $\sigma_{\rm IR}$ and $\epsilon_\lambda^i \, \sigma_{\rm HI}^i$. Table 4.1 shows $\sigma_{\rm R}$ and the corresponding $\sigma_{\rm CIB}$ for the faint fields once $\sigma_{\rm IR}$ and $\sigma_{\rm HI}$ have been removed following Equation 4.3. We find that the average $\sigma_{\rm CIB}$ is about 0.016 and 0.022 MJy sr^{-1} at 12 and 25 μm, respectively.

Monte-Carlo simulations

We use the average $\sigma_{\rm CIB}$ value of the faint fields to create CIB maps with a power spectrum slope of -1 since it is commonly accepted that the CIB displays such behaviour in the IR and submillimeter, as found by Pénin *et al.* (2012) and Planck Collaboration *et al.* (2011d). Furthermore, white noise maps for the mid-IR IRIS data ($\mathcal{N}^j_{\rm IR}$) and H I velocity integrated maps ($\mathcal{N}^j_{\rm HI}$) are created and added to build a new $I_\lambda{}^j$. We generate 1000 realizations of these. For each iteration j, we calculate new dust emissivities ϵ_λ^i associated with the different velocity components (via a least-squares fitting method) while continuing to mask areas previously thought to originate from dust associated with molecular gas. By calculating the dispersion of the resulting probability distributions, we have initial measurements and estimates of 1σ for each of the dust emissivities. The 3σ uncertainty is used in Tables 4.2 and 4.3.

Table 4.1.   Preliminary σ_R and σ_{CIB} at mid-IR wavelengths for the faint fields

Field Name	σ_R (12 μm)	σ_{CIB} (12 μm)	σ_R (25 μm)	σ_{CIB} (25 μm)
ag	0.029	0.023	0.038	0.032
bootes	0.023	0.016	0.029	0.024
g86	0.020	0.013	0.028	0.025
mc	0.036	0.032	0.036	0.027
n1	0.015	-	0.017	0.010
sp	0.021	0.013	0.027	0.022

Note. — Units in MJy sr^{-1}. There is no σ_{CIB} (12 μm) estimate for the *n1* field because the IRIS noise level is greater than the actual dispersion of the residual map.

4.3.2 Preliminary Results

Interpretation of negative dust emissivities is problematic. If dust grains and atomic gas are indeed well mixed within the diffuse ISM, one would naturally expect positive emissivities for Galactic material. Therefore, we reject fields with negative emissivities associated with either local and/or intermediate velocity gas. On the other hand, for high velocity clouds, there is little to no empirical evidence for dust emission (see Planck Collaboration *et al.*, 2011c or Peek *et al.*, 2009); in other words, negative ϵ_{HVC} are not immediately worrisome. For 12 μm, we can report 3σ detections for ϵ_{LVC} and ϵ_{IVC} in *g86*, *spc* and *umaeast*. At 25 μm, such detections extend only to *g86*, *uma* and *umaeast*. These results suggest that there is almost no mid-IR emission associated with the H I column density for the majority of the fields surveyed. Alternatively, we can view so few detections as a sign that the template model is not a good one. Either this happens because the correlations are not linear or, if we are not ready to abandon such an assumption, some 'contamination' must be affecting the data. Analyzing the maps of the residuals provides a reasonable diagnostic to ascertain the validity of the template in question. In general, if a given model is a good fit to the data, we expect the residuals to have no discernible structure, i.e., to mimic white noise. Figure 4.4 shows this is not necessarily the case; the *g86* residual maps, in both mid-IR wavelengths, unexpectedly reveal a surface brightness gradient. This turns out to be a characteristic feature for most fields; and we discuss this further in the following section.

Table 4.2. Preliminary estimates of dust emissivities and $3\,\sigma$ errors at 12 μm

Field Name	ϵ_{LVC}	ϵ_{IVC}	ϵ_{HVC}	c_λ
ag	0.014 ± 0.034	0.010 ± 0.024	-0.000 ± 0.011	0.994 ± 0.022
bootes	-0.047 ± 0.045	0.057 ± 0.031	-0.005 ± 0.108	0.880 ± 0.032
draco	0.003 ± 0.038	0.018 ± 0.011	0.013 ± 0.021	0.628 ± 0.030
g86	0.034 ± 0.016	0.011 ± 0.008	-0.062 ± 0.113	0.725 ± 0.016
mc	0.045 ± 0.043	0.022 ± 0.043	-0.032 ± 0.012	1.144 ± 0.041
n1	0.015 ± 0.029	0.014 ± 0.033	-0.015 ± 0.019	0.650 ± 0.024
nep	-0.011 ± 0.004	0.020 ± 0.004	0.014 ± 0.028	0.638 ± 0.011
pol	0.023 ± 0.003	0.006 ± 0.016	-	0.648 ± 0.020
polnor	0.028 ± 0.002	-0.014 ± 0.019	-	0.672 ± 0.010
sp	-0.021 ± 0.039	-0.055 ± 0.037	0.001 ± 0.036	0.833 ± 0.026
spc	0.007 ± 0.003	0.041 ± 0.019	0.018 ± 0.011	0.724 ± 0.007
spider	0.040 ± 0.003	-0.024 ± 0.011	0.117 ± 0.053	0.763 ± 0.010
uma	0.039 ± 0.004	0.004 ± 0.008	-0.007 ± 0.008	0.750 ± 0.011
umaeast	0.023 ± 0.006	0.042 ± 0.012	-0.008 ± 0.011	0.770 ± 0.020

Note. — Units in MJy sr^{-1} (10^{20}cm^{-2})$^{-1}$.

Table 4.3. Preliminary estimates of dust emissivities and $3\,\sigma$ errors at 25 μm

Field Name	ϵ_{LVC}	ϵ_{IVC}	ϵ_{HVC}	c_λ
ag	0.034 ± 0.050	-0.011 ± 0.031	-0.000 ± 0.015	2.105 ± 0.031
bootes	-0.041 ± 0.059	0.077 ± 0.041	-0.135 ± 0.140	1.832 ± 0.041
draco	-0.077 ± 0.051	0.040 ± 0.014	0.015 ± 0.024	1.427 ± 0.039
g86	0.044 ± 0.020	0.016 ± 0.010	-0.062 ± 0.141	1.593 ± 0.019
mc	-0.029 ± 0.062	-0.006 ± 0.059	-0.023 ± 0.017	2.140 ± 0.058
n1	0.019 ± 0.038	0.038 ± 0.041	-0.036 ± 0.024	1.412 ± 0.030
nep	-0.016 ± 0.006	0.030 ± 0.005	0.077 ± 0.037	1.403 ± 0.014
pol	0.022 ± 0.004	0.005 ± 0.021	-	1.467 ± 0.024
polnor	0.023 ± 0.003	-0.017 ± 0.024	-	1.502 ± 0.014
sp	-0.104 ± 0.050	-0.076 ± 0.047	0.036 ± 0.045	1.835 ± 0.034
spc	0.003 ± 0.004	0.069 ± 0.025	0.012 ± 0.014	1.566 ± 0.009
spider	0.043 ± 0.005	-0.074 ± 0.014	0.399 ± 0.066	1.677 ± 0.013
uma	0.061 ± 0.005	0.028 ± 0.010	-0.009 ± 0.010	1.614 ± 0.014
umaeast	0.058 ± 0.008	0.017 ± 0.016	-0.034 ± 0.014	1.757 ± 0.027

Note. — Units in MJy sr^{-1} (10^{20}cm^{-2})$^{-1}$.
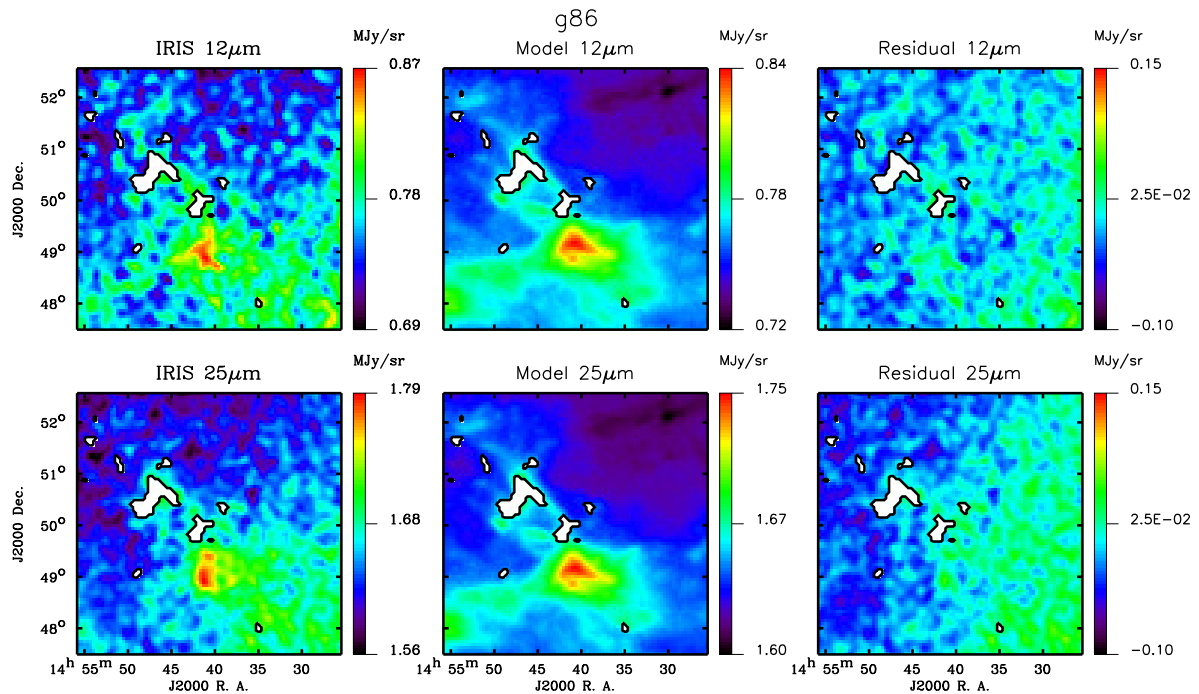
Figure 4.4: Comparison of the IRIS, model and residual maps at 12 and 25 μm for *g86*. White pixels represent masked regions ignored by the fit. Both residuals show a clear underlying surface brightness gradient. Units in MJy sr^{-1}.

4.3.3   Evidence for residual zodiacal light in the mid-IR data

The observed IR sky emission is a cumulative signal made from several components, including dust emission from the ISM, our Solar System (zodiacal light), Galactic sources and the CIB (see Figure 4.5). Decomposing the observed total signal into its constituent parts, however, is a complicated and difficult process that is often model dependent. For example, to remove the unwanted contribution of the zodiacal light in the DIRBE data, Kelsall *et al.* (1998) use a particular interplanetary dust (IPD) model with a geometry that includes a smooth cloud, dust bands and a ring. They estimated the total mid-IR IPD contribution to be about 3000 nW m^{-2} sr^{-1} at the Lockman Hole (with ecliptic coordinates of $\lambda = 137°$ and $\beta = 46°$), which translates roughly to 12 and 25 MJy sr^{-1} at 12 and 25 μm, respectively (see their Figure 9). Model uncertainties were quoted at 0.55 and 1.30 MJy sr^{-1} arising from the degeneracy of different possible model geometries.

As previously mentioned, the mid-IR data we use in this analysis, IRIS, is a derivative product of the IRAS all-sky survey. Although the original ISSA (IRAS Sky Survey Atlas) data were already corrected for zodiacal light, Miville-Deschênes & Lagache (2005) improved it by convolving and calibrating the original plates to the already clean DIRBE maps. This is because DIRBE is assumed to have had a better IPD model subtraction when compared to IRAS.
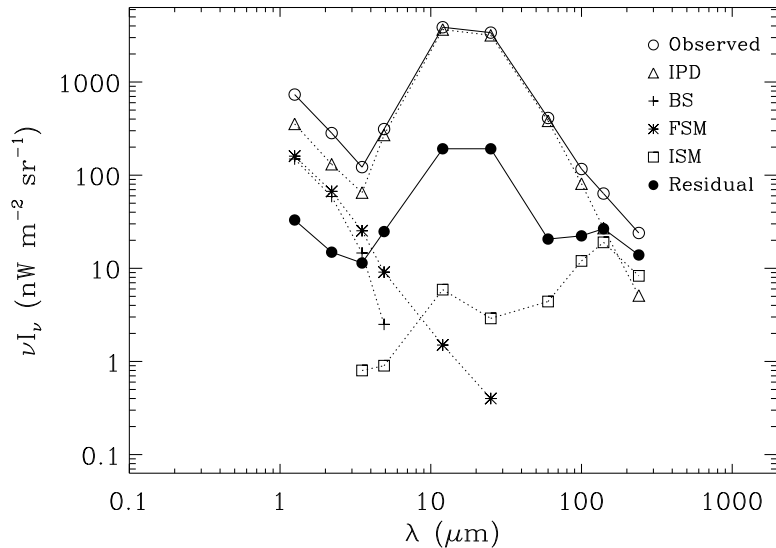
Figure 4.5: Different plotting symbols show the different contributions to the total observed DIRBE sky emission. At 12 and 25 μm, the strength of the modelled zodiacal light (IPD) is almost the same as the total sky mid-IR emission (observed). (Taken from Hauser *et al.* 1998.)

Nevertheless, despite these best efforts, a visual inspection of the 12 and 25 μm IRIS data (especially for the fainter fields) still shows some residual effects. Figure 4.6 displays the *ag* field in ecliptic coordinates in all four IRIS bands (at 12, 25, 60 and 100 μm). We present this field as an example because it is both low in ecliptic latitude and faint in surface brightness. We can see a surface brightness gradient, at 12 and 25 μm, increasing in the direction of the Ecliptic plane. Such contamination is even more prominent and particularly well exposed in the residual maps originating from the least-squares fit. In fact, once the cirrus contribution has been removed (from zodiacal light subtracted data), only the CIB is supposed to be left behind as a smooth and isotropic background (for a review, see Hauser & Dwek, 2001). Therefore, it is relatively easy to diagnose if the residual images show possible contamination from poorly subtracted zodiacal emission. Figure 4.7 shows residual maps at mid-IR wavelengths for two fields (*ag* and *mc*) at relatively low ecliptic latitudes and Figure 4.8, for an intermediate latitude field (*spider*) and close to the North Ecliptic Pole (*draco*). Given that the template model for the dust emission does not have a component representing the aforementioned residual zodiacal light contribution, this appears in these residual maps as a surface brightness gradient increasing towards the Ecliptic plane (also seen in the images on the right in Figure 4.4 for the *g86* field). (It is worth mentioning that an over subtraction of zodiacal light emission would show up as a reverse gradient.)

Other possible explanations

Although a reasonable explanation for the observed gradient in the residuals is a poor zo-
diacal light subtraction, we must consider other plausible scenarios. It is known that dust
emission can also correlate with either ionized hydrogen or its molecular form, H_2. Therefore,
it is conceivable that the residual maps still contain dust emission not correlated with the col-
umn density of atomic H I as defined by our model in Equation 4.1. However, molecular gas
has been shown to be generally present in localized structures (e.g., molecular clouds) and,
therefore, associated dust emission should not lead to a surface brightness gradient on the size
scale of our fields. Furthermore, we are looking at high galactic latitudes where the presence
of molecular gas is thought to be much smaller when compared to the Galactic mid-plane.
Even if molecular gas has a substantial presence, masking should prevent it from appearing
in the residual maps.
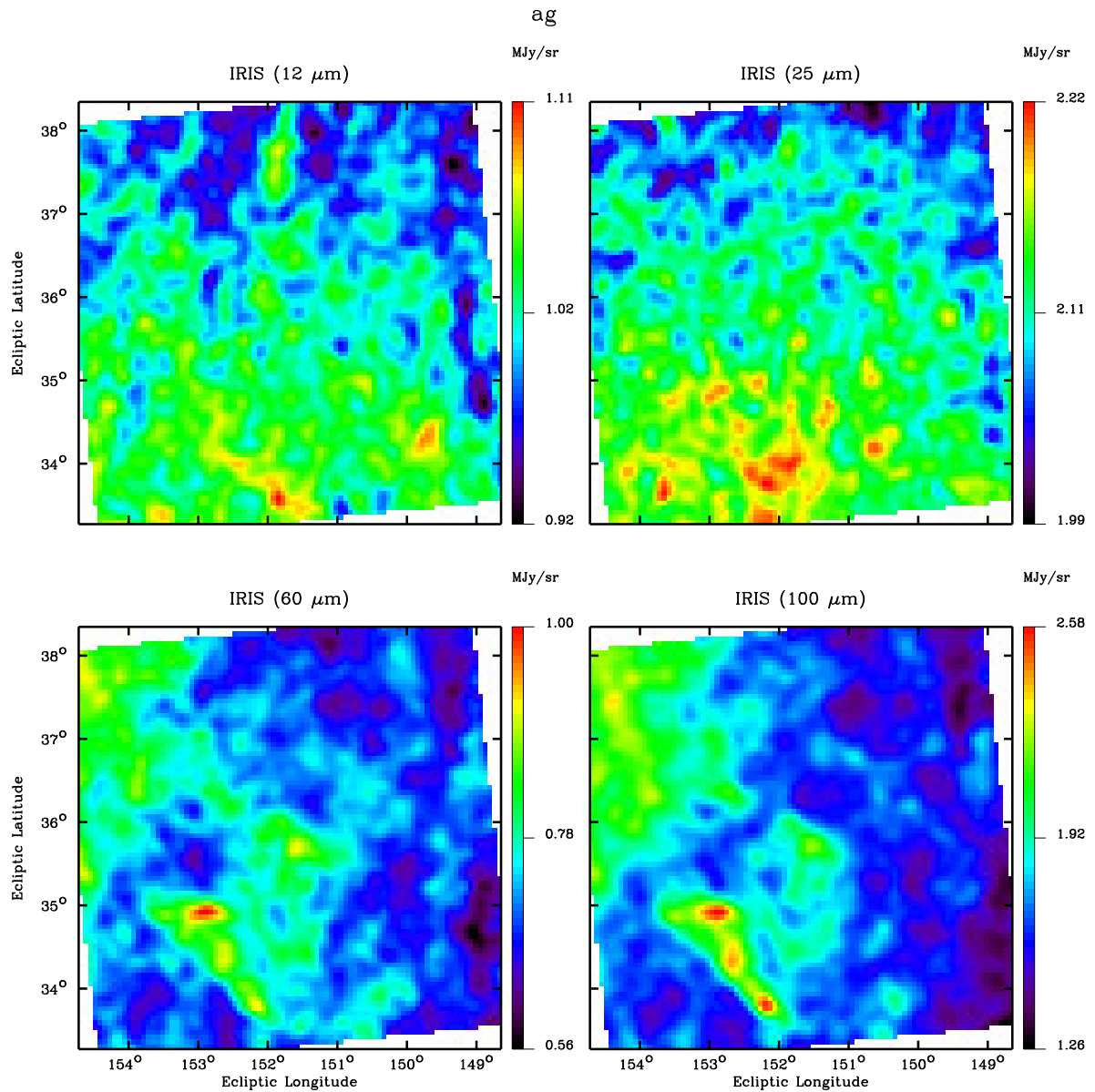
Figure 4.6: *From left to right, top to bottom*: IRIS images for 12, 25, 60 and 100 *μm* for the *ag* field. There is a strong gradient of decreasing surface brightness towards the north ecliptic pole. Note that this effect decreases substantially as the wavelength increases. This is because as the cirrus signal strength goes up, the IPD signal strength goes down.
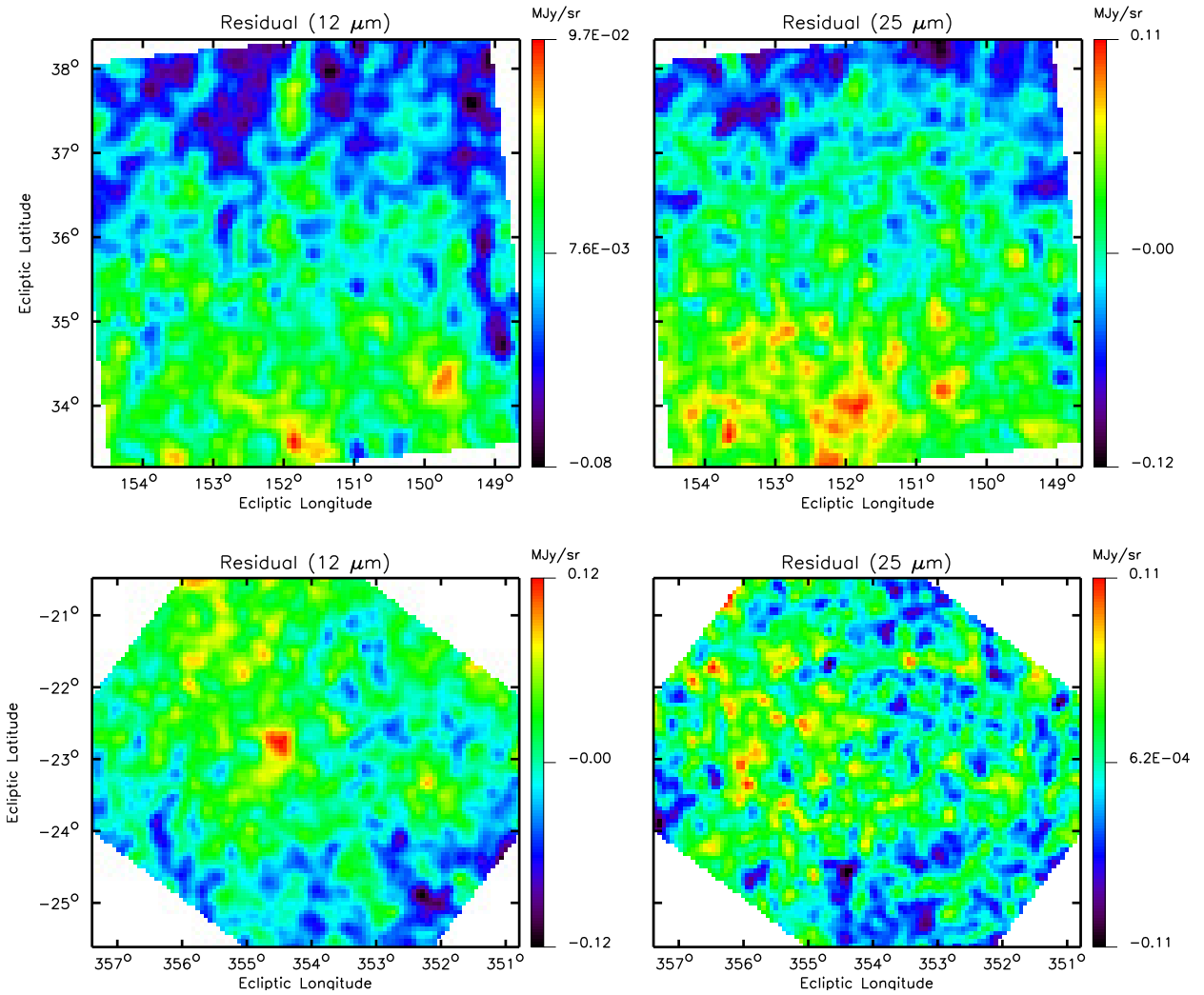
Figure 4.7: Residual maps at 12 and 25 μm for fields closer to the Ecliptic plane for the *ag* (*top*) and *mc* (*bottom*) fields. There is a gradual increase of surface brightness in the direction of lower ecliptic latitudes. Note that the morphology present in the mid-IR residual maps of the *ag* field seems to mimic the original mid-IR maps seen in the top row of Figure 4.6.
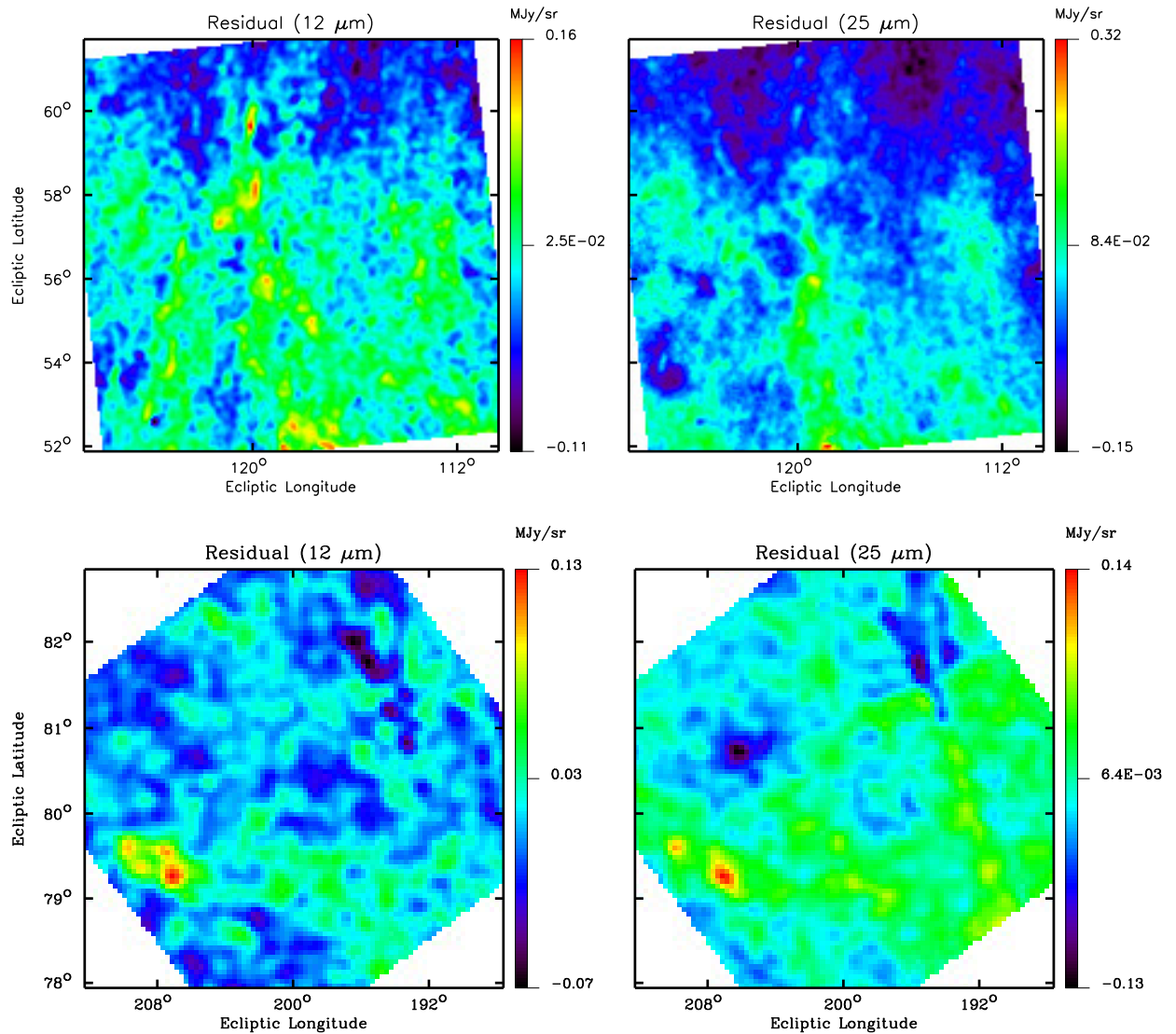
Figure 4.8: Residual maps at 12 and 25 *μm* for fields at intermediate distance and furthest away from the Ecliptic plane: *spider* (*top*) and *draco* (*bottom*). For the *spider* field, the gradient is still visible but becomes less obvious for *draco* at latitudes close to the North Ecliptic Pole. Note that for *spider* and *draco* (fields with a significant amount of masking), the residual also shows dust emission ill-fitted by the model (possibly associated with molecular gas).

4.3.4 Removal of residual zodiacal light

The surface brightness gradient in some of the mid-IR residual maps is most likely the result of an imperfect zodiacal light subtraction. This gradient is well modelled by a tilted plane. Here, we discuss two ways to deal with the residual zodiacal light and thus improve mid-IR dust emissivity estimates. In the first method, the excess contribution from the zodiacal light is removed from the residual maps using an iterative process; in the second, we modify the adopted sky model directly.

Method 1

We start by spatially correlating the masked mid-IR IRIS data with H I velocity-integrated maps. After solving for the dust emissivities, we obtain the residual map (R_λ). We then fit a tilted plane to the masked residuals. Fitting such a geometrical shape is a naïve approach but a physically motivated one given that the IPD signal is expected to smoothly increase towards lower ecliptic latitudes. We do not constrain the angle or direction of the plane's inclination, so as to allow for the possibility of an over subtraction of the IPD signal or an imperfect geometrical model. Our model for fitting the residual is the following

$$R_\lambda(x,y) = a_\lambda\, P_x(x,y) + b_\lambda\, P_y(x,y) + k_\lambda\,, \tag{4.4}$$

where the matrices $P_x(x,y) = x$ and $P_y(x,y) = y$. (This is just the matrix form of the scalar plane equation $z = ax + by + k$.) We note that the constant k_λ is a reflection of the cumulative effect of the zodiacal light background plus the CIB signal. This modelled plane is then subtracted from the original IRIS map and new dust emissivities are obtained. We iterate on this procedure 50 times; at each step, we calculate the standard deviation of the residual maps. Our final dust emissivities are those which yield the residual map with the lowest dispersion. A diagram of this iterative method is shown in Figure 4.9. Note that had we fitted and removed a tilted plane prior to the least-squares fit, i.e., on the original IRIS images, we might risk the removal of real cirrus signal with a morphology that by chance could mimic a smooth gradient.

Method 2

The second method estimates the mid-IR dust emissivities by modifying the multilinear sky model presented in Equation 4.1. We do so by adding a new set of terms which parameterize a tilted plane. Our new sky model is given by the following equation which now also accounts
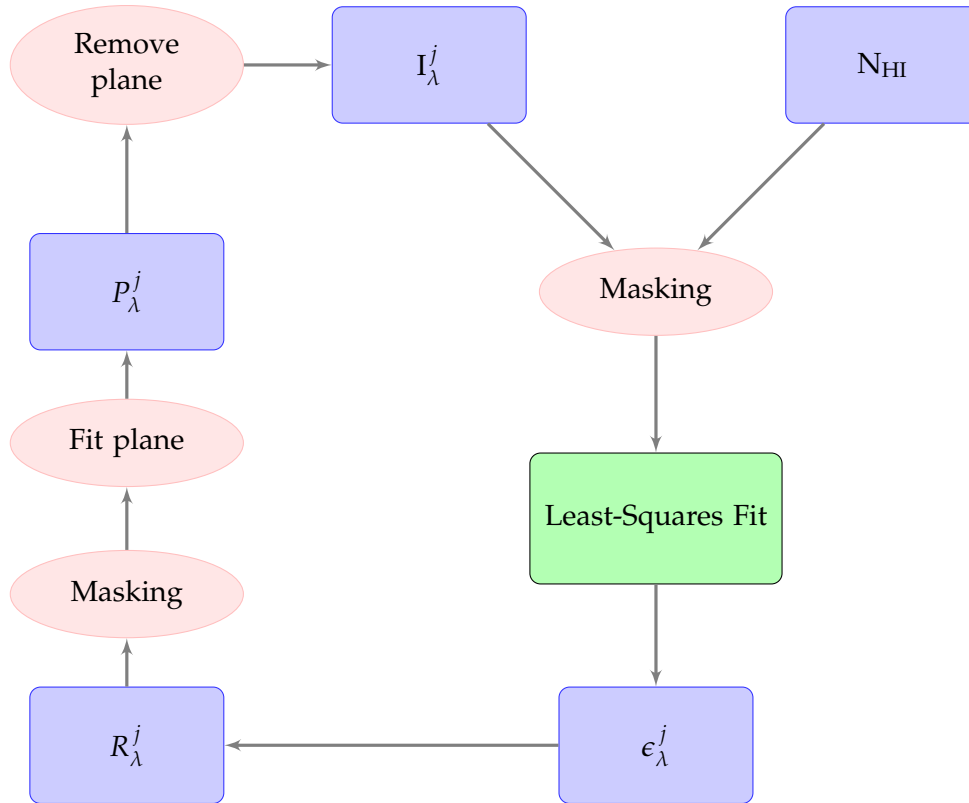
Figure 4.9: Diagram of the iterative procedure used to remove residual zodiacal light from the IRIS data. After 50 iterations, dust emissivities associated with the lowest dispersion residual map are selected.

for the excess radiation in the form of a smooth gradient,

$$I_\lambda(x,y) = \sum_{i=1}^{3} \epsilon_\lambda^i \, N_{HI}^i(x,y) + a_\lambda \, P_x(x,y) + b_\lambda \, P_y(x,y) + d_\lambda \,, \qquad (4.5)$$

where d_λ is the new intercept. Similar to the constant k_λ in Equation 4.4, the value of d_λ is interpreted as the summed contributions of the CIB and the zero-level amplitude of the poorly subtracted zodiacal emission. It is however, impossible to actually separate the contribution of each of these factors to the total intercept.

4.3.5   Results

Planes

Model components and results obtained (using method 1) at the mid-IR wavelengths for the *ag* field, can be seen in Figures 4.10 and 4.11, and in Figures 4.12 and 4.13 for the *spc* field. These images also show the tilted plane removed from the original IRIS map.

Consider whether by fitting a tilted plane to the residual map and later removing it from

the mid-IR images, we would actually be removing real cirrus signal which by nature displayed a diffuse and smooth increase towards a particular direction in the sky. Given that our sky emission model assumes a strong linear spatial correlation between the mid-IR and H I column density, any gradient present in the mid-IR emission maps would show up as well in the velocity integrated H I maps. A visual inspection of the column density maps quickly proves that is not the case. Even in the case of the *spc* field, in which the LVC gas component exhibits a stronger concentration of matter in the lower part of the map that could easily be fitted by a tilted plane, the residual map shows no indication of missing spatial structures which spatially correlate with the H I maps outside of masked regions (see Figures 4.12 and 4.13 as well as 4.16). Even if the H I column density emission was increasing towards a specific direction in the map, when correlating it with a mid-IR map with similar morphology, the residuals resulting from the least-squares fit would no longer have such a spatial signature.

We check the validity of assuming that our modelled tilted planes are in fact poorly subtracted zodiacal emission in the mid-IR data by plotting the removed tilted plane in ecliptic coordinates. Figure 4.14 displays both tilted planes, at 12 and 25 *μm*, for fields *ag* and *g86*. Indeed, we see that the retrieved tilted planes indicate the existence of a smooth residual gradient that can easily be interpreted as leftover zodiacal light given its alignment in the direction of the north Ecliptic pole. Note, however, that for some fields, the tilted plane that best fits the residuals does not necessarily show this alignment. For example, the tilted plane fitted to the mid-IR maps for fields *draco* and *uma* show gradients which do not reflect the expected alignment with the IPD (see Figure 4.15). Given the temporal nature of the initial removal of the zodiacal light in the DIRBE and IRAS maps, we feel that our results could easily be a consequence of an over subtraction of the IPD signal or a variation with the Ecliptic longitude that is not well understood. Whatever the nature of that residual signal, we feel confident that for the purpose of deriving dust emissivities, it should be removed.

Although we cannot determine the zero-level amplitude of the residual zodiacal light with certainty, that constant does not directly affect our estimate of the dust emissivities (see Equation 4.5). Only emission gradients can substantially change the value of the emissivities. Thus by removing such a shape from the mid-IR dust maps, we are more confident in finding physically meaningful estimates of the dust emission.
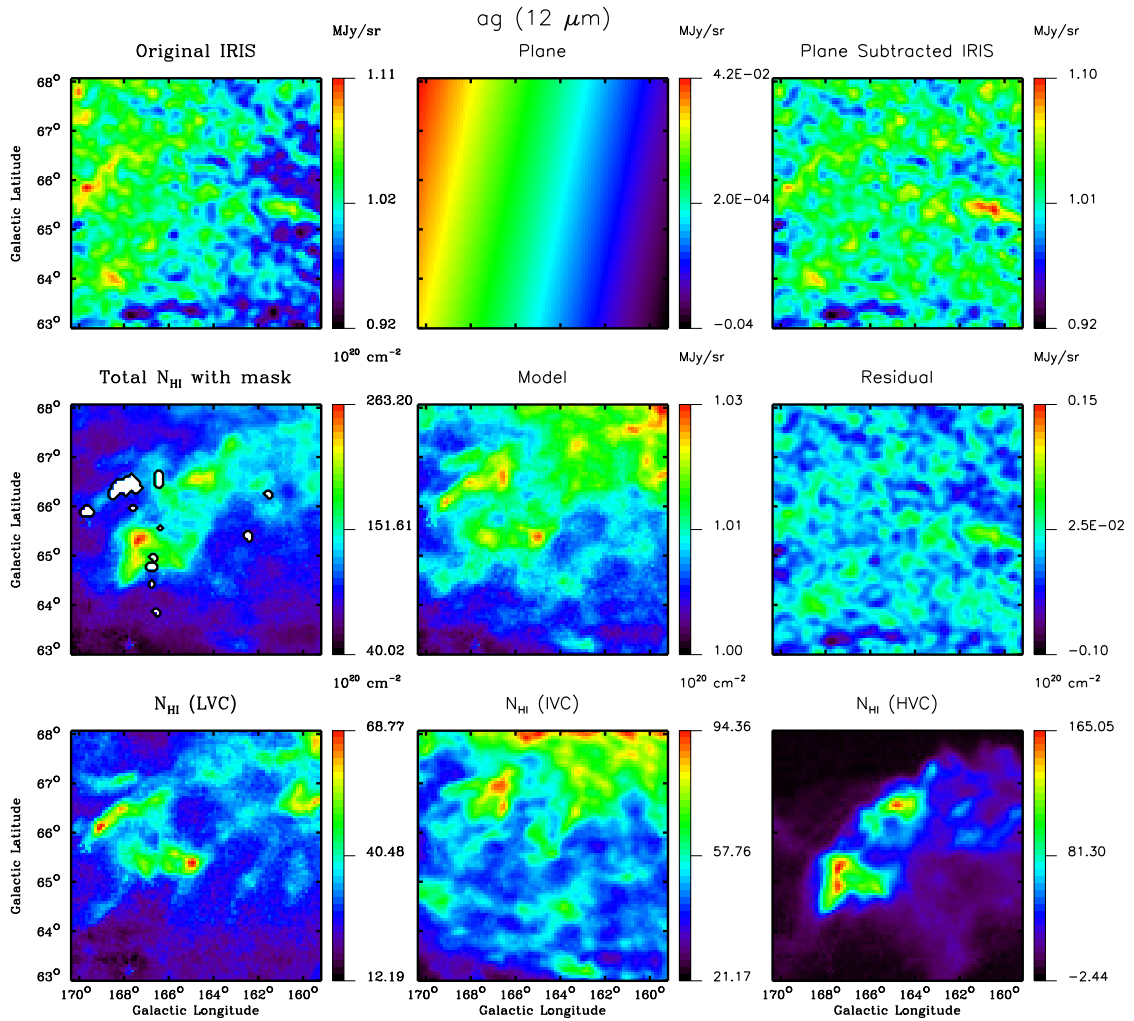
Figure 4.10: Model components and residual for the *ag* field at 12 *μm*. *Top*: original IRIS map, tilted plane that best fits the residual and final plane subtracted map. *Middle*: total H I column density in the line of sight (masked areas in white), model template and residual map obtained using Equation 4.5. *Bottom*: N$_{HI}$ components. Note the scale change for every figure.
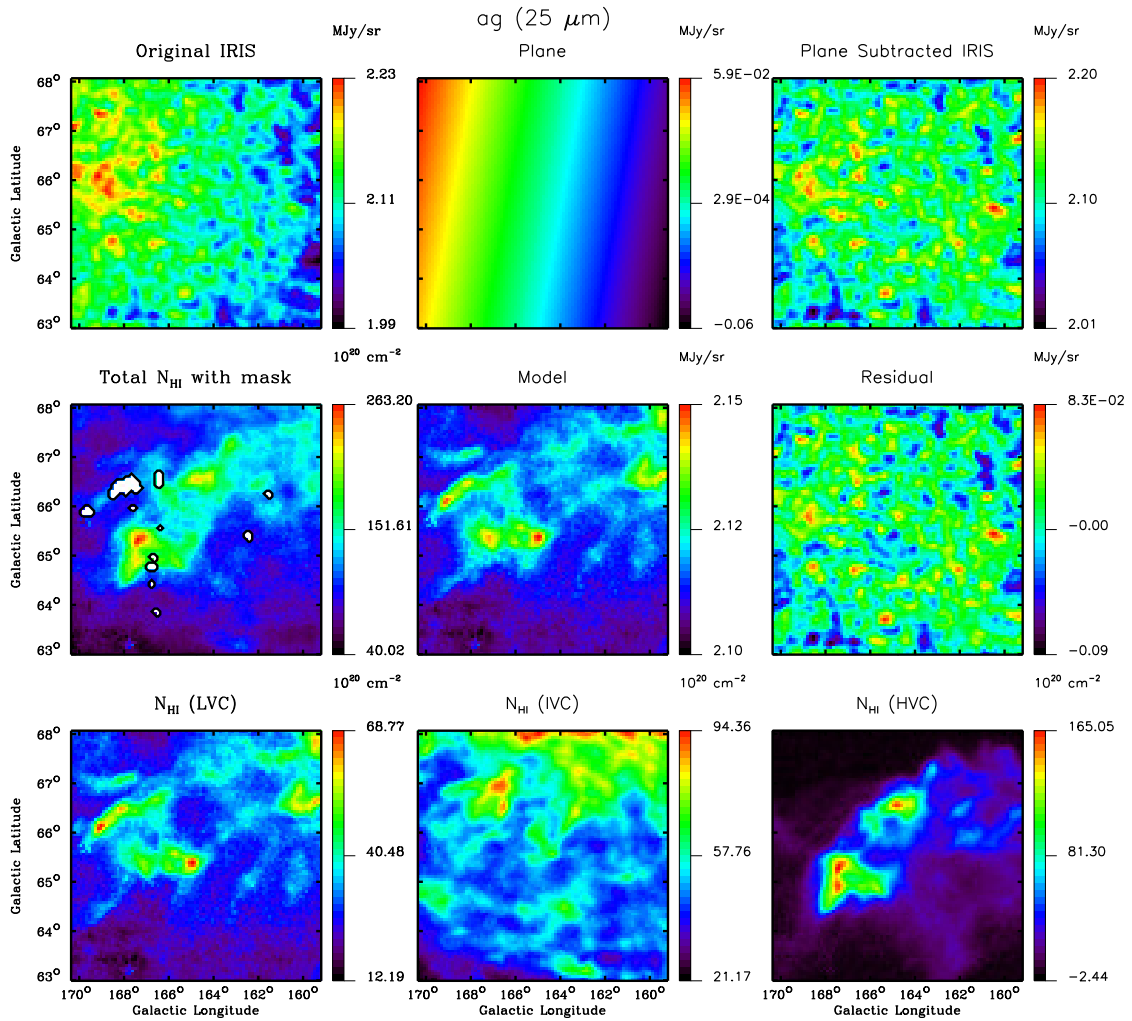
Figure 4.11: Model components and residual for the *ag* field at 25 *µm*. *Top*: original IRIS map, tilted plane that best fits the residual and final plane subtracted IRIS map. *Middle*: total H I column density in the line of sight (masked areas in white), model template and residual map obtained using Equation 4.5. *Bottom*: N_{HI} components. Note the scale change for every figure.
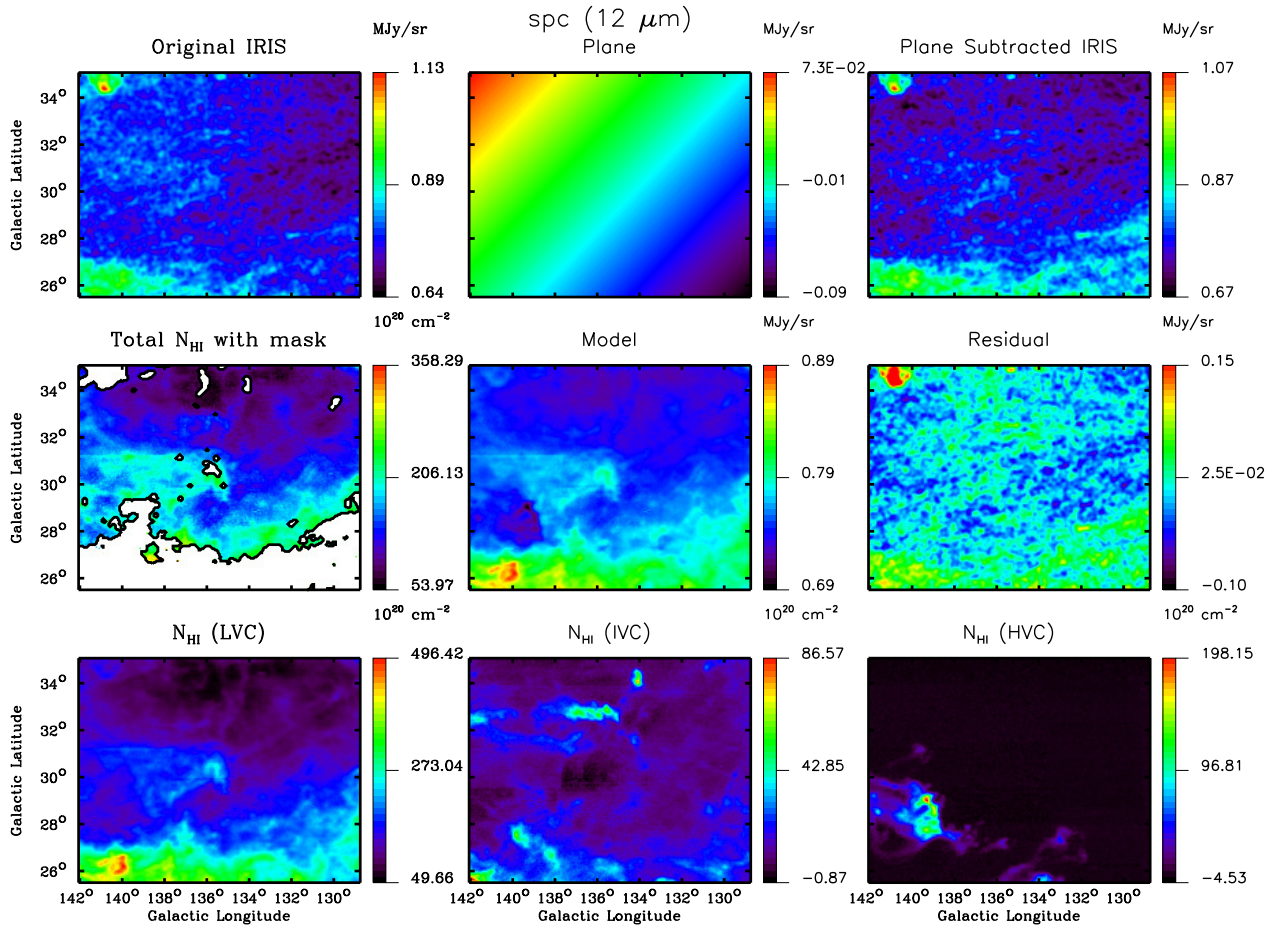
Figure 4.12: Same as Figure 4.10 but for the brighter *spc* field.
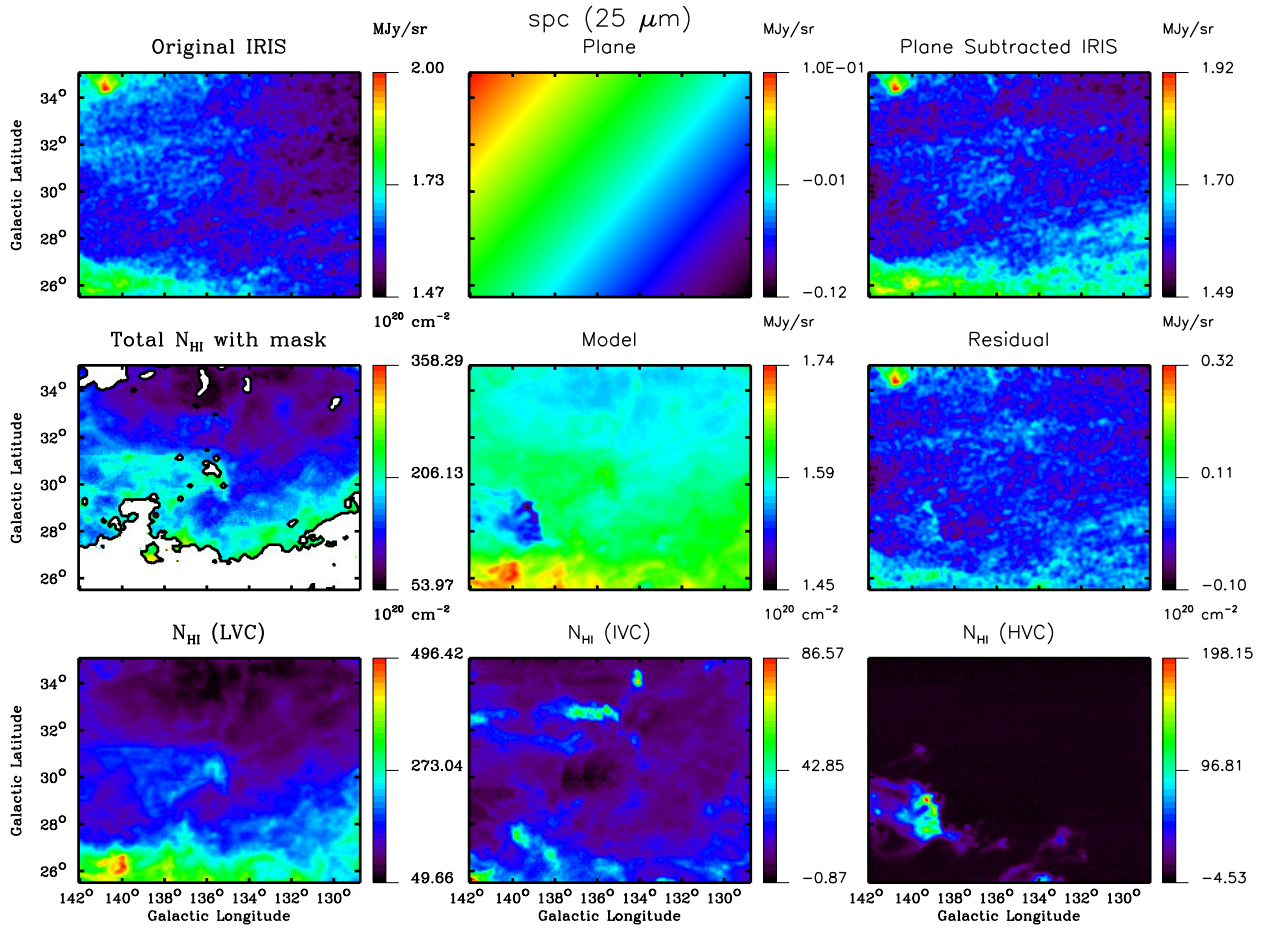
Figure 4.13: Same as Figure 4.11 but for the brighter *spc* field.
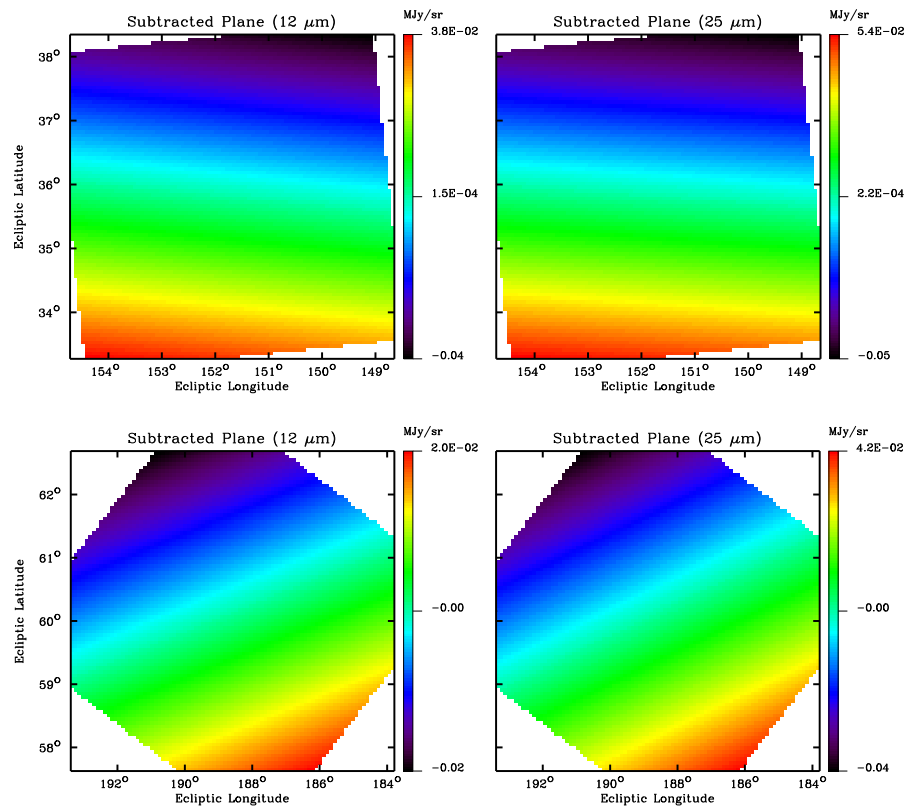
Figure 4.14: Tilted planes found, at 12 and 25 *μm*, to be the best fit for the residual maps. *Top*: *ag* field. *Bottom*: *g86* field. These images show the existence of a surface brightness gradient whose amplitude increases roughly in the direction of the Ecliptic plane.
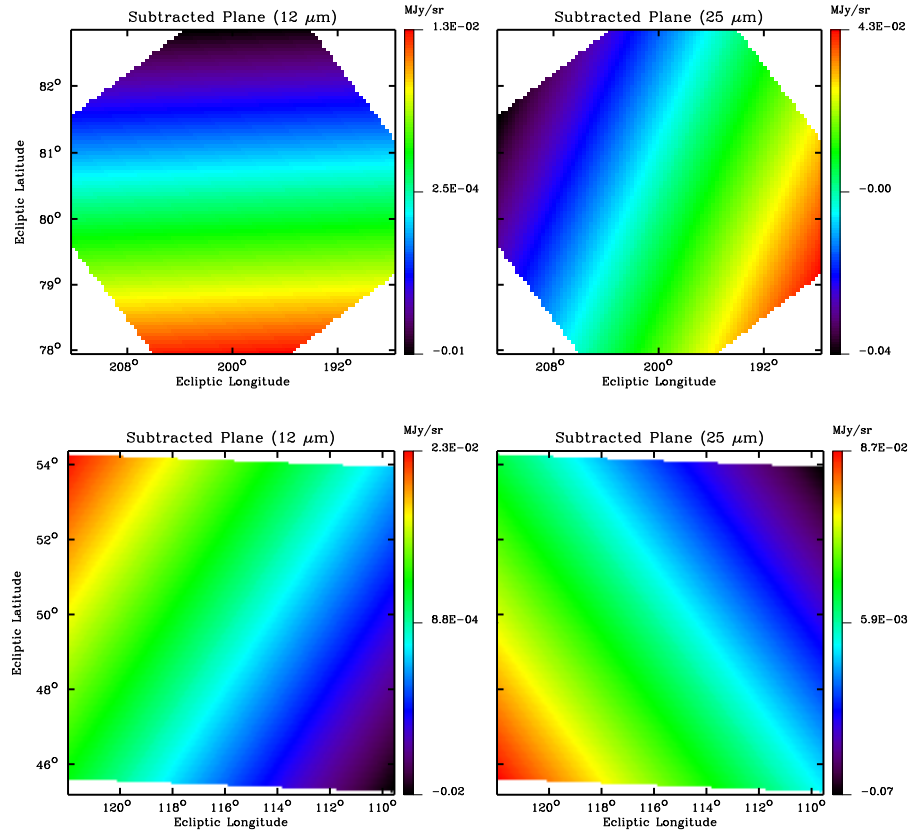
Figure 4.15: Tilted planes found, at 12 and 25 *µm*, to be the best fit for the residual maps. *Top*: *draco* field. *Bottom*: *uma* field. These images show the existence of a surface brightness gradient whose amplitude does not seem to increase towards the direction of the Ecliptic plane. Also, the gradient shape is different in both mid-IR wavelengths.
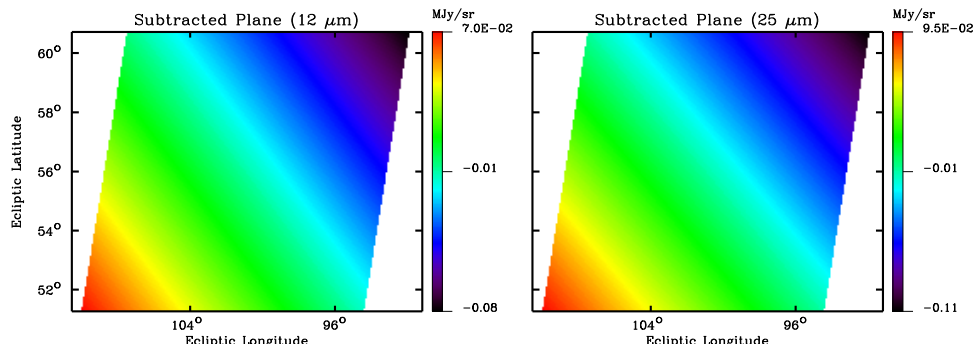
Figure 4.16: Tilted planes found, at 12 and 25 *µm*, to be the best fit for the residual maps for the *spc* field. These images are projected in Ecliptic coordinates.

Emissivities

Tables 4.4 and 4.5 show new dust emissivity estimates, at 12 and 25 μm for Method 2. These are all similar to the values obtained by iteratively fitting a tilted plane to the residual maps as in Method 1. The only exception is the *nep* field, where in both mid-IR wavelengths, we find different emissivity values. This is most likely due to the fact that determining the magnitude of the zodiacal excess at the North Ecliptic Pole remains uncertain and its modelling is ambiguous. Note that for all fields, methods 1 and 2 yield different intercepts. Given the similarity of the results for most fields, the discussion which follows will focus solely on Method 2 (which incidentally is both faster and simpler to code).

Comparing the results of Table 4.2 with 4.4, we see that at 12 μm, fields *bootes* and *nep* now have positive dust emissivities associated with the local gas (ϵ_{LVC}) and *spider* now has a positive ϵ_{IVC}. These values, however, are not significant given the uncertainties. On the other hand, fields *polnor*, *sp* and *mc* now have negative ϵ_{IVC}. With regards to the 25 μm results, Table 4.5 shows an increase in the number of significant ϵ_λ relative to the preliminary results in 4.3. Now, field *sp* is the only one with a negative ϵ_{LVC}, while *ag*, *mc* and *polnor* are the only remaining fields with negative dust emissivities associated with the intermediate velocity gas. Again, we do not attribute physical importance to the negative values of the high velocity dust emissivities. We remove the *nep* field from further analysis, given that the dust emissivities found via Method 1 and 2 were not consistent. These reveal that a tilted plane maybe not the best way to remove the unwanted contribution of poorly subtracted zodiacal emission in the North Ecliptic Pole. In fact, it is even difficult to assess if there is anything to be removed and therefore the preliminary estimates are probably the best we can do.

We would also like to reiterate that these new dust emissivities constitute an improvement over the preliminary values presented earlier. There has been an increase in the number of positive emissivities found. Figure 4.17 shows the change in the mid-IR dust emissivities when a tilted plane is added to the multilinear template model. The procedure worked as expected and the residual maps show almost no trace of leftover gradient. This is evident in the middle right image of Figure 4.10 and 4.11 for 12 and 25 μm. Similar evidence can be found in the residual maps of Figure 4.12 and 4.13 for the *spc* field.

4.3.6 Dispersion of the residual maps

We derive residual maps based on the two different procedures, Method 1 and Method 2. We find that they are similar in both cases, for all fields and mid-IR wavelengths, except for the *nep* field where the dust emissivities found via the 2 methods differ slightly but are within their 3-σ uncertainties. The residual maps no longer show gradients, reducing the typical standard deviation of the residual maps (after masking) to about 0.020 and 0.022 from 0.024 and 0.029 MJy sr^{-1} at 12 and 25 μm, respectively (see Table 4.1). Table 4.6 displays the estimates of σ_R for

Table 4.4. Dust emissivity estimates at IRIS 12 μm

Field Name	ϵ_{LVC}	ϵ_{IVC}	ϵ_{HVC}	a_λ	b_λ	d_λ
ag	0.019 ± 0.032	0.015 ± 0.023	0.003 ± 0.009	-0.791	0.160	1.014
bootes	0.005 ± 0.045	0.014 ± 0.023	0.033 ± 0.067	0.219	-0.450	0.852
draco	0.027 ± 0.038	0.031 ± 0.017	0.003 ± 0.019	0.235	-0.164	0.600
g86	0.030 ± 0.017	0.013 ± 0.007	-0.050 ± 0.094	0.372	-0.196	0.717
mc	0.037 ± 0.043	-0.047 ± 0.037	-0.008 ± 0.009	-0.868	0.646	1.186
n1	0.014 ± 0.028	0.015 ± 0.028	0.000 ± 0.017	0.067	0.241	0.633
pol	0.029 ± 0.006	0.016 ± 0.032	-	-0.378	0.157	0.608
polnor	0.035 ± 0.003	-0.003 ± 0.018	-	-0.620	0.554	0.623
sp	-0.027 ± 0.041	-0.005 ± 0.032	-0.001 ± 0.027	-0.408	-0.106	0.841
spc	0.023 ± 0.005	0.010 ± 0.016	-0.011 ± 0.009	-0.422	0.431	0.697
spider	0.033 ± 0.004	0.009 ± 0.010	-0.053 ± 0.033	-0.417	0.196	0.772
uma	0.035 ± 0.006	0.016 ± 0.014	0.006 ± 0.012	0.112	0.157	0.728
umaeast	0.023 ± 0.008	0.038 ± 0.014	0.000 ± 0.011	-0.109	-0.166	0.791

Note. — These results refer to the case where a tilted plane was added to the template model (4.1) in the least-squares fit. Coefficients that define the tilted plane (a_λ and b_λ) are multiplied by 1000. Dust emissivity estimates at 12 μm for all the fields with a 3σ uncertainty determined by Monte-Carlo simulations. Units in MJy sr^{-1} (10^{20}cm^{-2})$^{-1}$.

Table 4.5. Dust emissivity estimates at IRIS 25 μm

Field Name	ϵ_{LVC}	ϵ_{IVC}	ϵ_{HVC}	a_λ	b_λ	d_λ
ag	0.042 ± 0.032	-0.001 ± 0.024	0.004 ± 0.010	-1.147	0.202	2.132
bootes	0.024 ± 0.045	0.020 ± 0.023	-0.051 ± 0.064	0.286	-0.830	1.805
draco	0.044 ± 0.038	0.029 ± 0.016	0.002 ± 0.018	0.790	0.429	1.311
g86	0.039 ± 0.016	0.021 ± 0.006	-0.049 ± 0.091	0.799	-0.351	1.572
mc	0.041 ± 0.054	-0.049 ± 0.041	-0.009 ± 0.011	-0.577	-0.117	2.132
n1	0.029 ± 0.027	0.027 ± 0.026	-0.002 ± 0.016	-0.030	0.545	1.376
pol	0.028 ± 0.006	0.024 ± 0.029	-	-0.604	0.135	1.432
polnor	0.031 ± 0.003	-0.001 ± 0.017	-	-0.896	0.723	1.441
sp	-0.038 ± 0.040	0.000 ± 0.032	0.024 ± 0.027	-0.833	0.361	1.788
spc	0.024 ± 0.005	0.025 ± 0.016	-0.025 ± 0.009	-0.589	0.562	1.536
spider	0.024 ± 0.003	0.015 ± 0.010	-0.072 ± 0.032	-0.983	0.626	1.680
uma	0.028 ± 0.006	0.025 ± 0.014	-0.001 ± 0.011	-0.470	0.608	1.686
umaeast	0.037 ± 0.008	0.068 ± 0.013	0.018 ± 0.012	-1.028	0.458	1.789

Note. — These results refer to the case where a tilted plane was added to the template model (4.1) in the least-squares fit. Coefficients that define the tilted plane (a_λ and b_λ) are multiplied by 1000. Dust emissivity estimates at 25 μm for all the fields with a 3σ uncertainty determined by Monte-Carlo simulations. Units in MJy sr^{-1} (10^{20}cm^{-2})$^{-1}$.
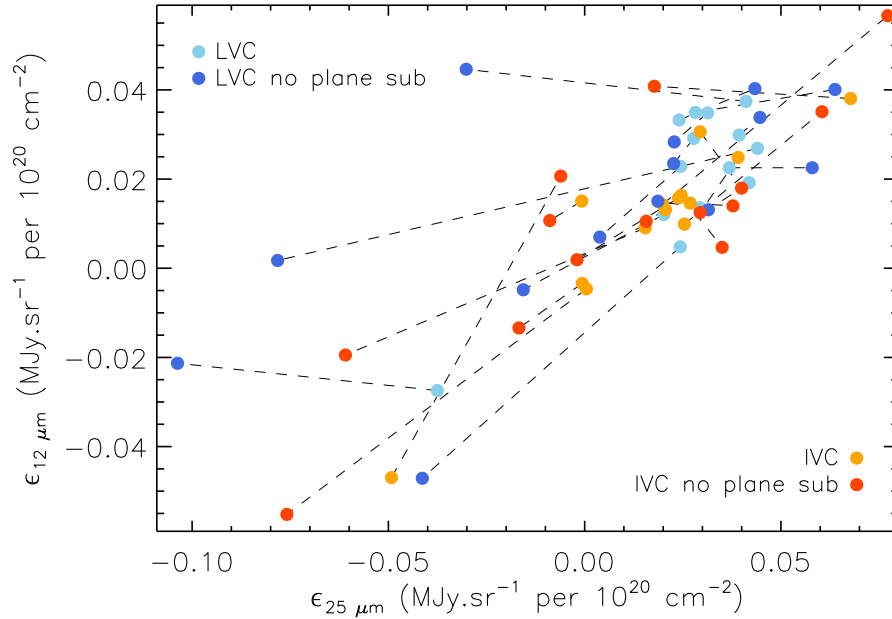
Figure 4.17: Comparison of dust emissivity estimates at mid-IR wavelengths with or without a correction for the excess zodiacal light emission. Dashed lines connect old to new mid-IR dust emissivity estimates for each field. A number of ϵ_λ move from the unphysical negative ϵ quadrants to the top right physically meaningful quadrant.

all fields and IRAS wavelengths.

4.3.7 Revised Uncertainties

In order to estimate the dust emissivity uncertainties, we employed the same method explained in detail in §4.3.1. However, the multilinear model has changed (from Equation 4.1 to Equation 4.5). We argued before that I_λ and R_λ displayed evidence of poorly subtracted unwanted contributions from zodiacal light. This additional uncertainty must now be taken into account. The first step is to determine the dispersion of the residual maps obtained from the least-squares fit. Since we have eliminated a surface brightness gradient which plagued the preliminary residual maps, the value for σ_R is now smaller than the one obtained earlier. From Table 4.6, we find that the mean standard deviations of the faint field 12 and 25 μm residual maps have been reduced to 0.020 and 0.022 MJy sr^{-1} from 0.024 and 0.029 MJy sr^{-1}. It follows that σ_{CIB} is also reduced when compared to the case where there has been no correction for zodiacal light contamination. Table 4.7 shows the average dispersion values, σ_{CIB} for both cases at all IRAS wavelengths, keeping bright and faint fields separate. We also remove a tilted plane from the longer IRAS wavelength maps and calculate new dust emissivities at 60 and 100 μm (see §4.5). The most extreme change is seen in σ_{CIB} at 25 μm, where it is reduced

Table 4.6. Dispersion of the residual masked maps in the IR and derived σ_{CIB}

Field Name	12 μm		25 μm		60 μm		100 μm	
	σ_{R}	σ_{CIB}	σ_{R}	σ_{CIB}	σ_{R}	σ_{CIB}	σ_{R}	σ_{CIB}
ag	0.021	0.012	0.024	0.013	0.030	0.025	0.077	0.071
bootes	0.019	0.011	0.022	0.013	0.037	0.034	0.087	0.084
draco	0.018	0.010	0.019	0.013	0.031	0.028	0.104	0.101
g86	0.016	0.006	0.016	0.008	0.030	0.026	0.096	0.093
mc	0.024	0.018	0.033	0.023	0.035	0.032	0.071	0.067
n1	0.015	-	0.013	0.003	0.022	0.018	0.066	0.062
pol	0.020	0.013	0.020	0.014	0.038	0.035	0.144	0.139
polnor	0.021	0.013	0.021	0.016	0.038	0.035	0.121	0.118
sp	0.019	0.011	0.019	0.012	0.025	0.020	0.061	0.055
spc	0.020	0.012	0.023	0.018	0.038	0.035	0.105	0.101
spider	0.023	0.016	0.024	0.019	0.040	0.037	0.149	0.146
uma	0.023	0.015	0.024	0.017	0.042	0.039	0.167	0.163
umaeast	0.021	0.012	0.027	0.020	0.032	0.027	0.099	0.092

Note. — Standard deviation of the residuals map (σ_{R}) and derived σ_{CIB} at IR wavelengths for all fields. Units in MJy sr^{-1}.

Table 4.7. Average σ_{CIB} estimates in the IR derived from masked fields

	No correction		Tilted plane removed	
Wavelength	Faint	Bright	Faint	Bright
12	0.020 ± 0.009	0.018 ± 0.009	0.012 ± 0.004	0.013 ± 0.002
25	0.023 ± 0.006	0.036 ± 0.014	0.012 ± 0.007	0.017 ± 0.003
60	0.027 ± 0.008	0.036 ± 0.004	0.026 ± 0.007	0.034 ± 0.005
100	0.079 ± 0.020	0.137 ± 0.041	0.072 ± 0.016	0.123 ± 0.029

Note. — These σ_{CIB} estimates represent the mean value for the faint and bright fields. The last two columns refer to the case where a tilted plane has been subtracted from the IRIS data. The difference before and after removing a tilted plane is most striking at 25 μm. The mean for the σ_{CIB} (for both cases) at 60 μm matches the value obtained by Planck Collaboration *et al.* (2011c) while at 100 μm our result is lower but within the margin of error. Wavelengths in μm and σ_{CIB} in MJy sr^{-1} units.

by a factor of 2 in the faint fields (this result will be discussed later in §4.8).

We proceed as in §4.3.1, but now add the contribution of a tilted plane (with associated statistical errors) to each $\mathrm{I}_{\lambda}{}^{j}$. The latter is now defined as

$$
\begin{aligned}
\mathrm{I}_{\lambda}{}^{j}(x,y) &= \mathrm{I}_{\lambda,0}(x,y) + \sum_{i=1}^{3} \mathcal{N}^{i}{}_{\mathrm{HI}}(\sigma_{\mathrm{HI}}) + \mathcal{N}_{\mathrm{IR}}(\sigma_{\mathrm{IR}}) + \mathcal{N}_{\mathrm{CIB}}(\sigma_{\mathrm{CIB}}) \\
&+ a_{\lambda}^{j} P_{\mathrm{x}}(x,y) + b_{\lambda}^{j} P_{\mathrm{y}}(x,y)
\end{aligned}
\tag{4.6}
$$

where $\mathrm{I}_{\lambda}{}^{j}(x,y)$ represents the sky model for each new iteration j. Again, $\mathcal{N}_{\mathrm{HI}}$ and $\mathcal{N}_{\mathrm{IR}}$ are 2D random realizations of white noise with σ_{HI} and σ_{IR} standard deviations. The estimates for $\mathcal{N}_{\mathrm{HI}}$ (uncertainties associated with the H I column density maps) and $\mathcal{N}_{\mathrm{IR}}$ (obtained from the HCONs and shown in Table 3.1) remain the same as in §4.3.1. We update our estimate of σ_{CIB} for the faint fields (based on new estimates for σ_{R}) and produce new CIB maps, $\mathcal{N}_{\mathrm{CIB}}$, with a power spectrum $P(k) \propto k^{-1}$ and standard deviation σ_{CIB}. $P_{\mathrm{x}}(x,y)$ and $P_{\mathrm{y}}(x,y)$ are defined as before. The a_{λ}^{j} and b_{λ}^{j} are new coefficients used to parameterize the tilted planes. Each is picked randomly from a gaussian probability distribution built based on the modelled tilted plane least-squares fit uncertainties of a and b. The model uncertainties of a and b are very small, leading to only very small orientation changes in the tilted plane. Given that we do not constrain the direction of the modelled gradient a priori, we also tested a series of models where the plane was rotated by a random angle between $0°$ and $360°$ to determine
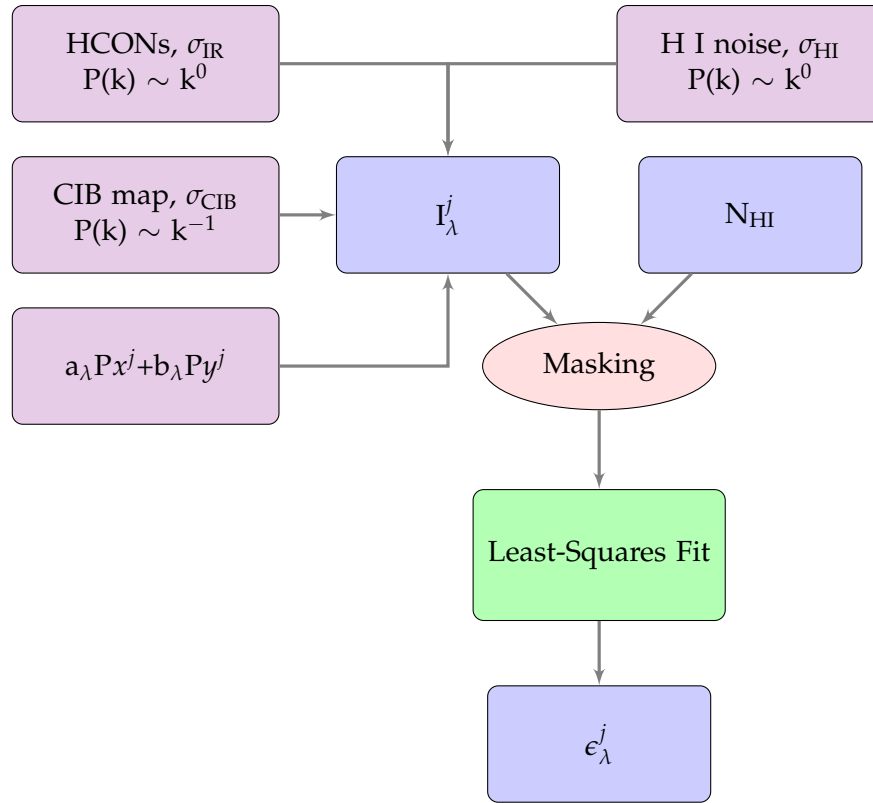
Figure 4.18: Diagram of the procedure followed to determine the dust emissitivies uncertainties. We iterate this procedure 1000 times.

the effect on our new Monte-Carlo dust emissivity estimates. We find that for about half the fields and for both mid-IR wavelengths, this leads to bimodal and sometimes trimodal probability distributions which can no longer be characterized statistically by a mean and standard deviation. For this reason, we opt not to rotate the fitted plane, and simply draw a^j and b^j from a gaussian distribution as described above. An schematic view of the error estimation process can be seen in Figure 4.18.

Probability distributions for ϵ_λ

In Figures 4.19 to 4.22, we present the ϵ_λ probability distributions obtained from the Monte-Carlo simulations. These are obtained after 1000 iterations. At both mid-IR wavelengths, we can see that the probability distribution for the ϵ_{HVC} can be very wide when compared to the local and intermediate ones. This wide range of parameter space is because the column densities for HVC gas here are small and contribute little to the multilinear model, thus allowing a wide range of possible ϵ_{HVC} estimates. We find the probability distribution of the simulated dust emissivities to be well approximated by a gaussian at both mid-IR wavelengths. With this model, we calculate the mean and standard deviations of these distributions, recording them (as mean and 3σ error) in Tables 4.4 and 4.5.
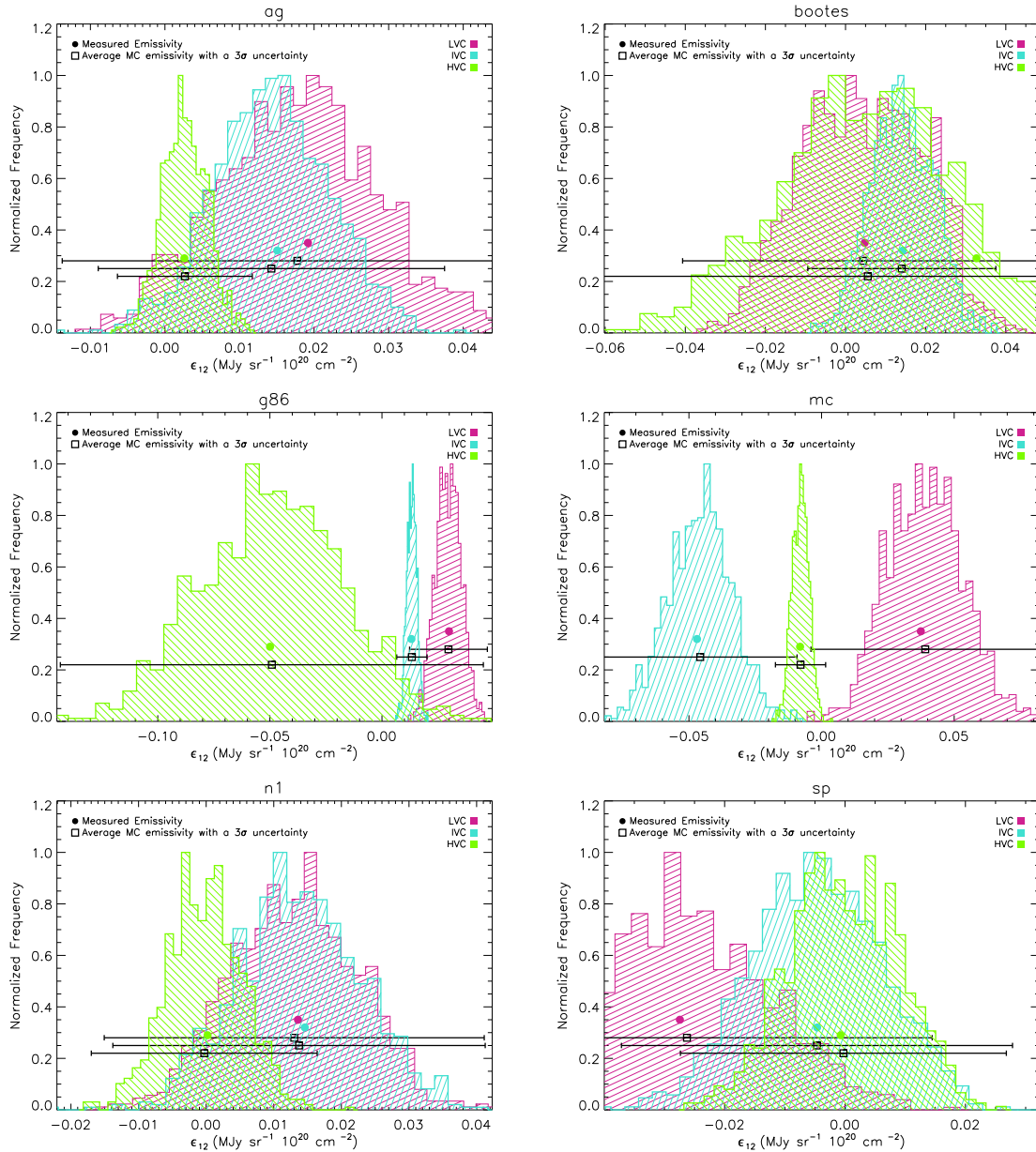
Figure 4.19: Histograms of the dust emissivities obtained in the Monte-Carlo simulation for the fainter fields at 12 μm. Violet, blue and green circles are the estimates for the local, intermediate and high-velocity dust emissivities. Black squares and horizontal lines represent the mean and 3σ level of the simulated distribution. Note that the range of ϵ_{12} changes from plot to plot.
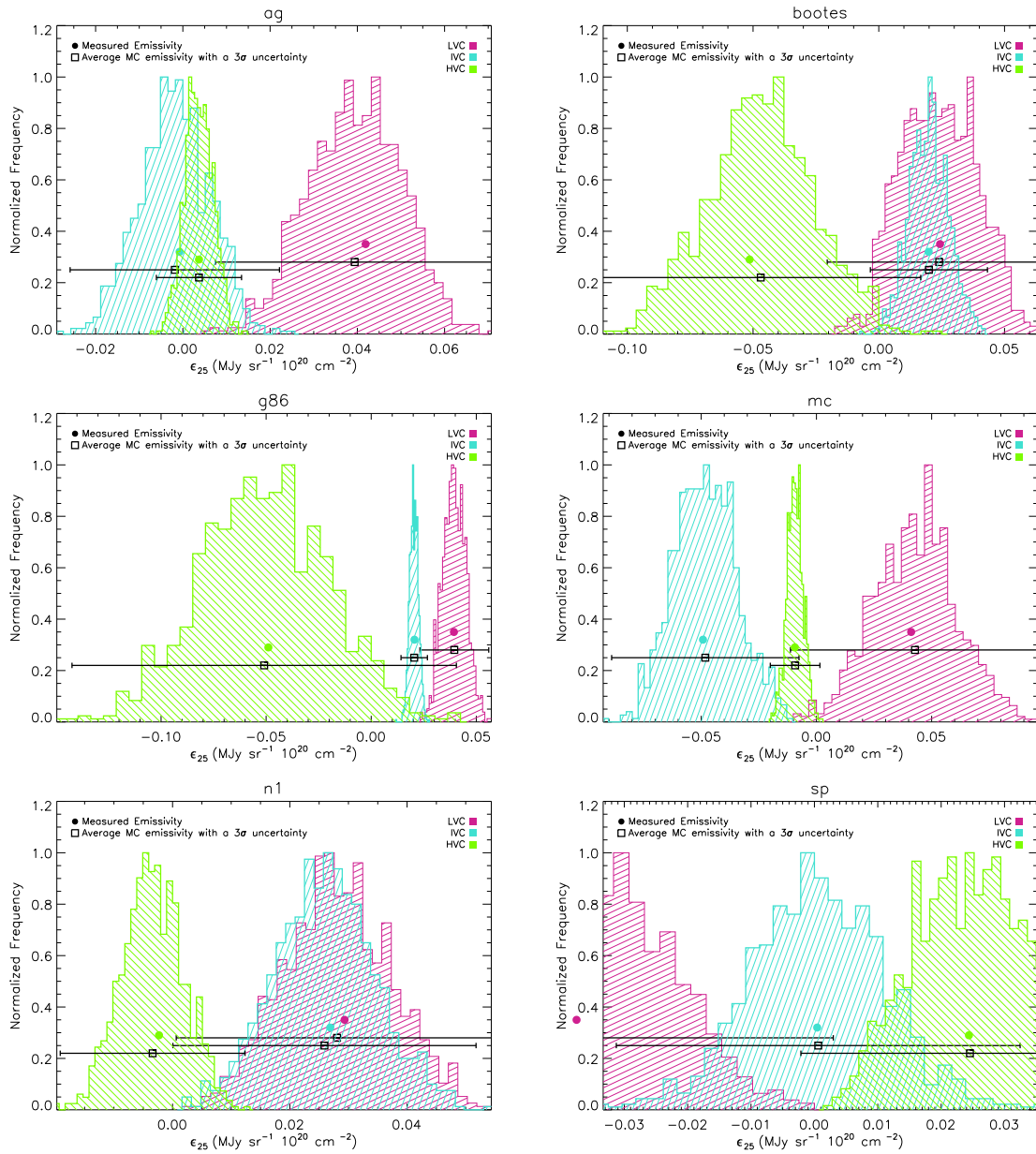
Figure 4.20: Same as Figure 4.19 for the 25 μm faint fields.
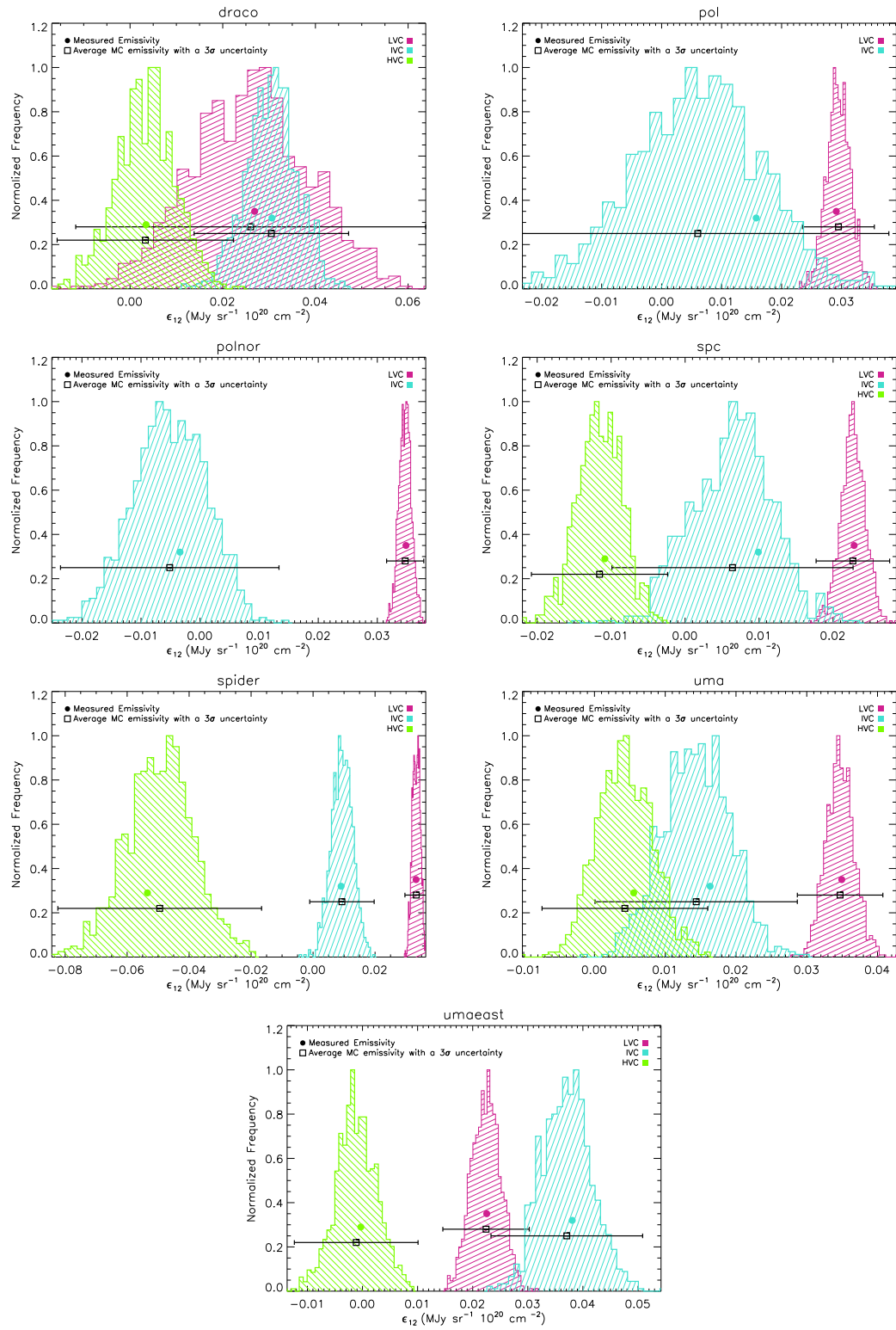
Figure 4.21: Same as Figure 4.19, but for the 12 μm bright fields.
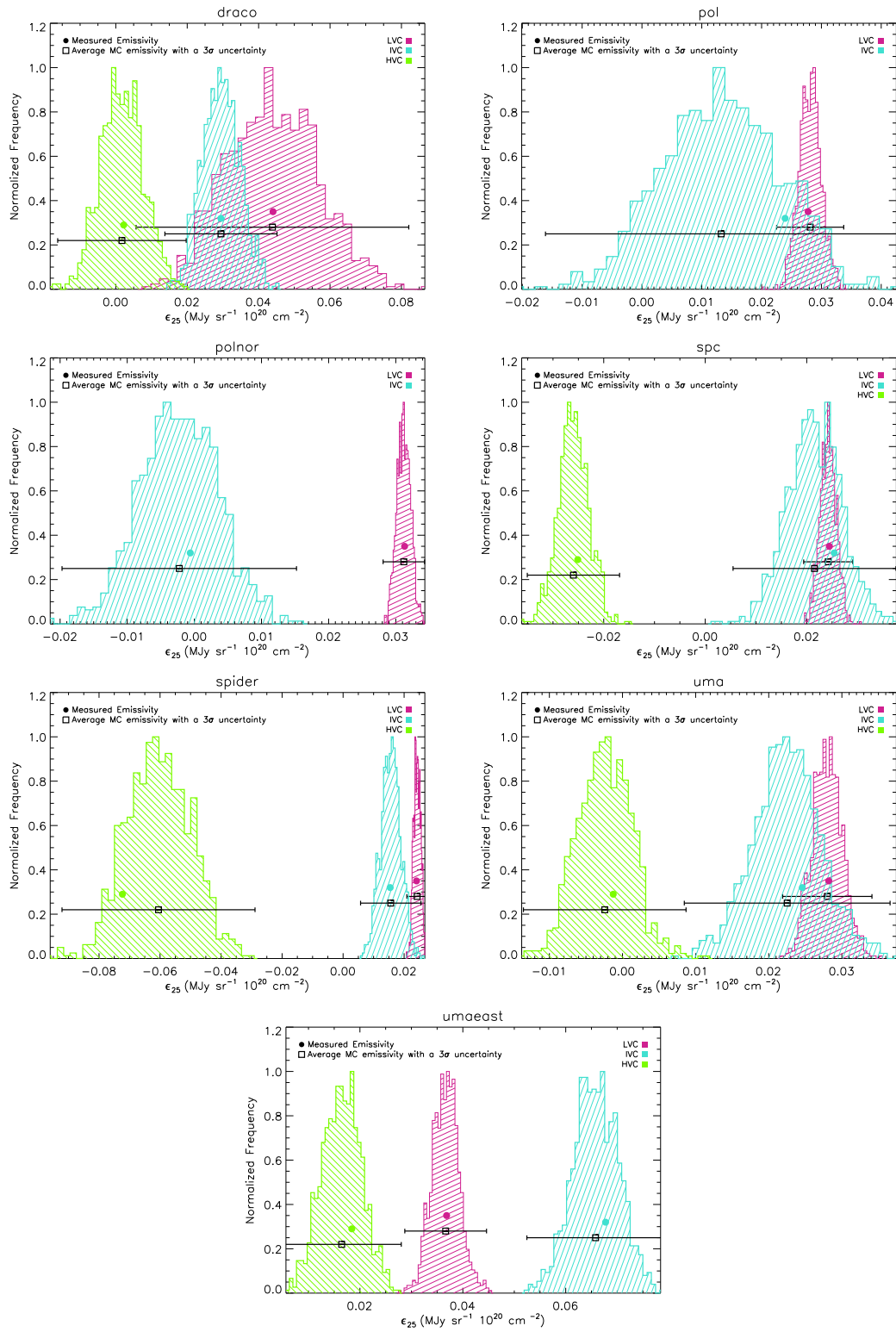
Figure 4.22: Same as Figure 4.19, but for the 25 *μm* bright fields.

4.4   Significance of ϵ_λ at mid-IR wavelengths

For about half of our survey fields, the calculated dust emissivities are not significant given the large dispersion found in the Monte-Carlo simulations. At 12 μm, we report a 3σ-detection of dust emission associated with local gas for 7 of the fields. These are *g86*, *pol*, *polnor*, *spc*, *spider*, *uma* and *umaeast*. Fields *draco*, *g86*, *uma* and *umaeast* show significant detections of $\epsilon_{\rm IVC}$. This represents a detection rate at 12 μm of about 50% and 30% for $\epsilon_{\rm LVC}$ and $\epsilon_{\rm IVC}$, respectively. At 25 μm, all fields show dust emission associated with local gas except for *bootes*, *mc* and *sp*. At intermediate velocities, we find that again only 7 fields show positive detections (*draco*, *g86*, *n1*, *spc*, *spider*, *uma* and *umaeast*). This corresponds to a detection rate at 25 μm of about 75% and 50% for $\epsilon_{\rm LVC}$ and $\epsilon_{\rm IVC}$, respectively. With the exception of the *umaeast* field at 25 μm, there is no evidence of mid-IR dust emission associated with any high velocity gas which is in agreement with most previous studies.

In order to check the bias of our original estimates for $\epsilon_{\rm LVC}$, $\epsilon_{\rm IVC}$ and $\epsilon_{\rm HVC}$, we compare these to the mean of the distribution of the Monte-Carlo simulation results shown earlier. A comparison of the original results (circles) and Monte-Carlo means (open squares) in Figures 4.19 to 4.22 shows that there is no evidence of any significant bias. All estimated dust emissivity estimates are within the derived 3σ uncertainties of the probability distributions. This is also the case in Planck Collaboration *et al.* (2011c), where no significant bias was found for $\epsilon_{\rm LVC}$ and $\epsilon_{\rm IVC}$.

We also compare these new dust emissivity estimates with the preliminary ones obtained in §4.3.2 (shown earlier as Figure 4.17). Most of the new mid-IR dust emissivity estimates tend to cluster towards the same space in the color diagram. This seems to indicate that once a tilted plane is removed from the data, both $\epsilon_{\rm LVC}$ and $\epsilon_{\rm IVC}$ values are more similar among the different fields. At 12 μm, the mean $\epsilon_{\rm LVC}$ and $\epsilon_{\rm IVC}$ are 0.030 ± 0.005 and 0.025 ± 0.012 MJy sr^{-1} 10^{-20} cm^{-2}, while at 25 μm the mean estimates are 0.033 ± 0.007 and 0.030 ± 0.017, respectively. We note, however, the much higher $\epsilon_{\rm IVC}$ found at 25 μm for the *umaeast* field. Without that result, the mean 25 μm $\epsilon_{\rm IVC}$ is 0.024 ± 0.005 MJy sr^{-1} 10^{-20} cm^{-2}. The above means are calculated with the positive 3σ detection fields only and the uncertainties stem from the dispersion found in the different fields, regardless of their emissivity errors.

4.5   Dust emissivities at 60 and 100 μm

Here, we compare our estimates of dust emissivities at 60 and 100 μm with the work of Planck Collaboration *et al.* (2011c) to check that the chosen masks are indeed masking the same morphology, and result in the same emissivities. We also look for the signature of any leftover zodiacal light at far-IR wavelengths. First, and as mentioned in the §4.2.1, we compare our estimates of the dust emissivities for the case where no tilted plane has been removed from the

data to check if our masking procedure matches the one adopted in Planck Collaboration *et al.* (2011c). We find that the emissivities are similar to within the 1σ errors. Figure 4.23 illustrates this.
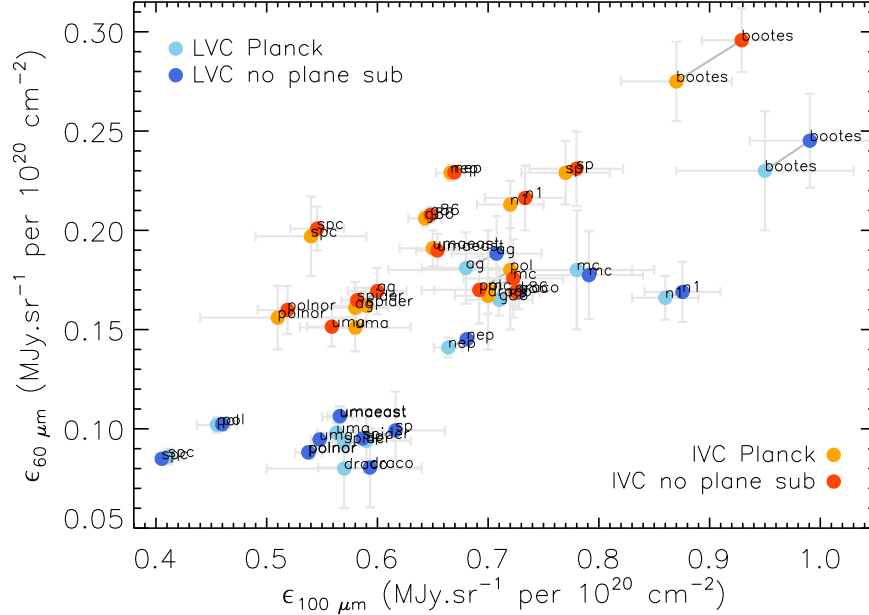
Figure 4.23: Comparison of dust emissivity estimates at far-IR wavelengths without any residual zodiacal light correction. Our measurements are comparable to the ones obtained by Planck Collaboration *et al.* (2011c) to within the 1σ uncertainties.

A visual inspection of the residual maps in Figures 4 to 11 in Planck Collaboration *et al.* (2011c) does not reveal any obvious gradients, as we have seen in the 12 and 25 μm residual maps. Moreover, just like in §4.3.3, we display the far-IR residual maps (R_λ) in ecliptic coordinates and find only a very faint indication of a possible surface brightness gradient in fields closer to the Ecliptic plane. Nevertheless, we calculate dust emissivity estimates in the far-IR using the methodologies described in Method 1 and Method 2. We find no considerable difference between the 2 methods. Just like in the 12 and 25 μm range, these estimates differ only by about 1% and therefore we present here the results from Method 2. Tables 4.8 and 4.9 show the new dust emissivity estimates at 60 and 100 μm for the case where a tilted plane has been removed from the data. At 60 μm, the mean ϵ_{LVC} and ϵ_{IVC} are 0.122 ± 0.054 and 0.213 ± 0.053 MJy sr^{-1} 10^{-20} cm^{-2}, while at 100 μm the mean estimates are 0.613 ± 0.138 and 0.675 ± 0.150, respectively.

There are significant differences (bigger than the 1σ uncertainties) between our Method 2 far-IR dust emissivity estimates and the ones reported in Planck Collaboration *et al.* (2011c) (comparable to our estimates where no correction has been applied). Figure 4.24 shows the 60 and 100 μm dust emissivity estimates using Method 2 and one where no tilted plane has

Table 4.8. Dust emissivity estimates at IRIS 60 μm

Field Name	ϵ_{LVC}	ϵ_{IVC}	ϵ_{HVC}	a_λ	b_λ	d_λ
ag	0.229 ± 0.057	0.213 ± 0.035	0.009 ± 0.017	-0.360	-0.590	0.439
bootes	0.131 ± 0.071	0.372 ± 0.048	-0.262 ± 0.126	-0.443	-0.207	0.400
draco	0.020 ± 0.060	0.197 ± 0.022	0.020 ± 0.034	-0.276	-0.609	0.464
g86	0.182 ± 0.025	0.205 ± 0.012	-0.151 ± 0.172	0.008	0.289	0.270
mc	0.173 ± 0.066	0.214 ± 0.059	0.004 ± 0.018	0.493	-0.304	0.307
n1	0.162 ± 0.045	0.223 ± 0.049	-0.006 ± 0.029	0.072	-0.093	0.331
pol	0.097 ± 0.010	0.220 ± 0.051	-	-0.882	-0.196	0.413
polnor	0.090 ± 0.007	0.168 ± 0.036	-	-0.303	0.120	0.402
sp	0.121 ± 0.058	0.220 ± 0.056	-0.052 ± 0.052	0.034	0.162	0.382
spc	0.087 ± 0.007	0.220 ± 0.033	0.030 ± 0.019	0.329	0.055	0.363
spider	0.096 ± 0.007	0.164 ± 0.019	-0.084 ± 0.077	-0.119	-0.096	0.419
uma	0.096 ± 0.010	0.155 ± 0.030	-0.006 ± 0.022	0.056	-0.002	0.389
umaeast	0.101 ± 0.015	0.203 ± 0.025	0.019 ± 0.022	-0.259	0.117	0.386

Note. — Dust emissivity estimates at 60 μm with a 3σ uncertainty determined by Monte-Carlo simulations. These results refer to the case where a tilted plane was added to the template model (4.1) in the least-squares fit. Coefficients that define the tilted plane (a_λ and b_λ) are multiplied by 1000. Units in MJy sr^{-1} (10^{20}cm^{-2})$^{-1}$.

Table 4.9. Dust emissivity estimates at IRIS 100 μm

Field Name	ϵ_{LVC}	ϵ_{IVC}	ϵ_{HVC}	a_λ	b_λ	d_λ
ag	0.730 ± 0.121	0.624 ± 0.080	0.033 ± 0.038	-0.158	-0.342	0.764
bootes	0.764 ± 0.163	1.070 ± 0.108	-0.723 ± 0.270	-0.854	-1.085	0.755
draco	0.371 ± 0.140	0.836 ± 0.049	0.085 ± 0.072	-0.986	-2.349	0.881
g86	0.773 ± 0.056	0.633 ± 0.027	-0.374 ± 0.393	-1.221	1.328	0.616
mc	0.469 ± 0.146	0.708 ± 0.135	-0.016 ± 0.040	-0.088	2.375	1.058
n1	0.833 ± 0.103	0.771 ± 0.109	-0.016 ± 0.066	0.525	-0.148	0.510
pol	0.545 ± 0.022	0.616 ± 0.122	-	-0.063	2.523	0.132
polnor	0.567 ± 0.015	0.519 ± 0.081	-	-1.547	2.489	0.409
sp	0.692 ± 0.134	0.639 ± 0.126	-0.154 ± 0.116	0.970	0.698	0.525
spc	0.467 ± 0.016	0.587 ± 0.073	0.093 ± 0.044	0.780	1.614	0.453
spider	0.608 ± 0.017	0.506 ± 0.043	-0.345 ± 0.160	0.473	-1.000	0.762
uma	0.593 ± 0.024	0.589 ± 0.066	-0.108 ± 0.046	0.818	-0.679	0.523
umaeast	0.555 ± 0.033	0.679 ± 0.058	0.060 ± 0.050	-0.602	0.162	0.474

Note. — These results refer to the case where a tilted plane was added to the template model (4.1) in the least-squares fit. Coefficients that define the tilted plane (a_λ and b_λ) are multiplied by 1000. Dust emissivity estimates at 100 μm for all the fields with a 3σ uncertainty determined by Monte-Carlo simulations. Units in MJy sr^{-1} (10^{20}cm^{-2})$^{-1}$.

been removed. There is no preferential shift of dust emissivity values in one direction which suggests that we are not removing real signal when subtracting a tilted plane from the data.
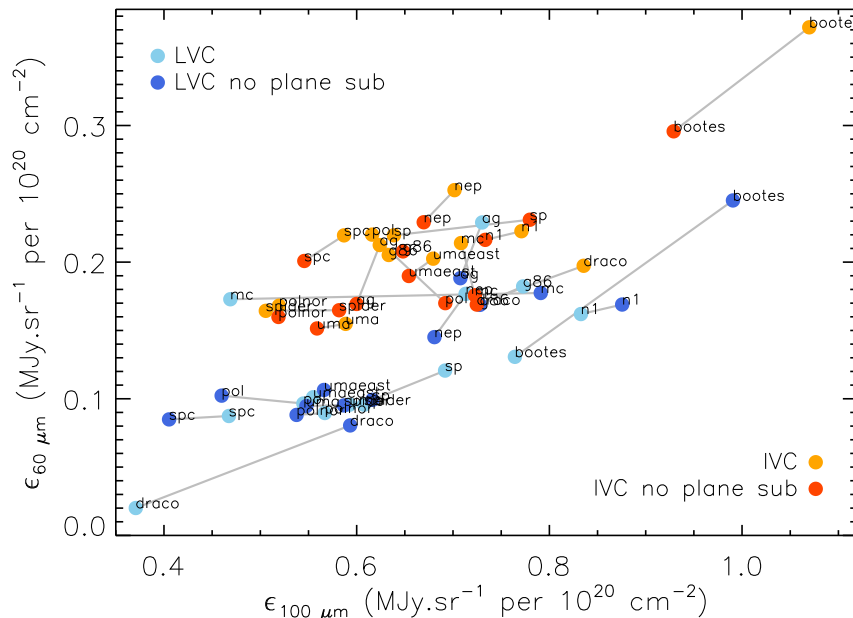
Figure 4.24: Comparison of dust emissivity estimates at far-IR wavelengths with or without any residual zodiacal light correction.

Ratios of Method 2 (tilted plane removal) emissivities to the standard (no tilted plane removal) emissivities are presented in Table 4.10. We note that greater differences are seen for the ϵ_{LVC} and ϵ_{IVC} estimates for the *bootes* and *draco* field. These also happen to be the fields in which we believe there is some dust processing and therefore ϵ_{IVC} is considerably bigger than its local counterpart at 60 μm. The plane removed in these fields shows a gradient which is compatible with an imperfect zodiacal light removal, but in this case with an oversubtraction since its gradient seems to increase towards to the North Ecliptic Pole. The only evidence connecting large changes in emissivities to fields with low ecliptic latitudes lies in *ag* and *spider*. In the other remaining fields, the removed plane shows very little tilt and the dust emissivity estimates are similar to what was previously derived in the Planck Collaboration *et al.* (2011c). The far-IR residual maps obtained via Method 2 show residuals consistent with possible molecular structures and have equal or smaller dispersion than the ones obtained in the case where there is no correction for residual zodiacal emission. We find no convincing evidence which points towards preferring a model for the dust emissivities where a tilted plane is subtracted from the 60 and 100 μm data, but acknowledge the need for further investigation on the matter.

Table 4.10.   Comparison of dust emissivities at 60 and 100 μm

Field Name	60μm			100 μm		
	R_{LVC}	R_{IVC}	R_{HVC}	R_{LVC}	R_{IVC}	R_{HVC}
ag	1.265	1.320	0.976	1.074	1.076	0.893
bootes	0.568	1.352	2.018	0.804	1.230	2.411
draco	0.251	1.182	0.787	0.650	1.194	0.848
g86	1.105	0.996	1.681	1.088	0.985	1.556
mc	0.960	1.259	0.235	0.601	1.012	0.542
n1	0.976	1.045	6.372	0.968	1.071	1.551
pol	0.946	1.223	-	1.197	0.856	-
polnor	1.018	1.077	-	1.054	1.018	-
sp	1.283	0.959	1.231	1.172	0.829	1.282
spc	1.016	1.115	-5.993	1.137	1.087	-1.858
spider	1.028	1.015	0.837	1.066	0.857	0.431
uma	0.976	1.025	0.939	1.052	1.015	0.899
umaeast	0.954	1.060	2.339	0.980	1.045	1.492

Note. — These results refer to the case where a tilted plane was added to the template model (4.1) in the least-squares fit. R is the ratio between our 60 and 100 μm dust emissivities and the ones obtained in Planck Collaboration *et al.* (2011c).

4.6 Mid-IR to submillimeter SEDs

We present spectral energy distributions covering the range from the mid-IR to the submillimeter for all fields. These are built from dust emissivity estimates determined in this work along with those published in the far-IR (60 and 100 μm) and submillimeter (857, 545 and 353 GHz) frequencies (Planck Collaboration *et al.*, 2011c). We also add our own estimates (using Method 2) for dust emissivities at 60 and 100 μm. We present SEDs for all three components of dust emission: dust associated with local, intermediate and high-velocity i.e., H I gas. With the exception of the *umaeast* field at 25 μm, all ϵ_{HVC} estimates plotted represent upper limits. The emissivity estimates are also compared to a theoretical model (DustEM, see Compiègne *et al.*, 2011) which predicts the typical shape of the dust emission in the diffuse ISM. The DustEM model of the diffuse ISM was found by fitting a series of different grain size distributions and compositions to UV and visible extinction data and IR and submillimeter observations from ISO and COBE telescopes. The model grain population was composed of PAHs, small and large amorphous carbon grains, and silicate grains. The different types of grains were 7.7, 1.6, 14.2 and 76.5% of the total mass of dust in the model, respectively. We divide their diffuse dust model spectrum by 0.77 to get the SED on a per H I scale instead of H (see discussion on the fraction of ionized H and H_2 in Compiègne *et al.* 2011).

Figures 4.25 and 4.26 show the SEDs for the fainter and brighter fields, respectively. At mid-IR wavelengths, SED variations are seen from field to field most likely reflecting changes with environment. The emissivities of dust associated with different velocity gas differ for the same field at each wavelength suggesting some sort of dust evolution or processing.

At 12 μm, we find that most faint fields show upper limits of ϵ_{LVC} consistent with the value predicted by the DustEM model with the exception of the *pol*, *spc*, *umaeast* and *sp* field which are lower. In the case of positive detections of ϵ_{LVC}, fields *polnor* and *uma* show emissivities which match the expected value of about 0.04 MJy sr^{-1} (10^{20}cm^{-2})$^{-1}$ while *g86*, *spc*, *spider* and *pol* estimates are below it. These results are also clearly shown in Figures 4.27 and 4.28 where most ϵ_{LVC}'s at 12 μm are consistently lower (albeit with some variations) than the colours for the expected DustEM diffuse dust model. In contrast, when it comes to ϵ_{IVC} emissivities, we find that the predicted value is high compared to what we find in our analysis. This suggests a smaller abundance of PAHs may be enough to explain the 12 μm color in the IVCs dust SED.

The variations seen at 12 μm, however, are not always accompanied by a similar change at 25 μm which suggests different relative contributions from the different dust populations for the emission at these mid-IR wavelengths. At 25 μm, all upper limits on the local emissivities are again consistent with the theoretical model estimate except for *sp*. All of fields with detected emission at the 3 σ level show values similar to or greater than what DustEM predicts. The slightly higher emissivity at 25 μm is also seen in the observational constraint set by the DIRBE data as seen in Figure 1.3. For dust associated with the intermediate velocity gas, some

upper limits are consistent with the standard model but not for *ag*, *mc* and *polnor* which are lower. *umaeast* ϵ_{IVC}'s is above the value set by DustEM. In the case of the *draco* cloud (a field known to have significant IVC gas) that might indicate a greater emission of either PAHs or VSGs (which contribute equally at 25 *μm* in the DustEM model) but the same is not found for our other IVC, field *g86*.

We also include our far-IR estimates (derived using Method 2) and those obtained by Planck Collaboration *et al.* (2011c) in the SEDs as shown by the circle and star symbols, respectively, in Figures 4.25 and 4.26. As discussed in §4.5, our IVC dust emissivity estimates at 60 *μm* are consistently higher than the ones found by the previous authors. For the local dust, we see similar or greater emission with the exception of *bootes* and *draco*. These two fields also display the same trend at 100 *μm*. In general, at these wavelengths, our estimates are consistent with what was previously reported.

Furthermore, we note that the higher 25 *μm* local emissivity exhibited in faint fields *ag*, *g86* is somewhat accompanied by a similar increase at 60 *μm*, which can suggest a greater abundance of PAHs and VSGs relative to bigger grains (comparing to abundances predicted by the theoretical model) in the local, low velocity gas of these regions. However, the high 60 *μm* do not necessarily reflect an increase in the 25 *μm* emission, suggesting larger VSGs grains. Values above the standard DustEM estimate are also seen for ϵ_{IVC} (faint and bright) at 60 *μm* but they are not always accompanied by an increase at 25 *μm*. All of the brighter fields show slightly lower or similar ϵ_{LVC} at 25 *μm* but higher ϵ_{IVC} than the estimates predicted by DustEM. This differs from the consistently higher emissivities seen in the faint fields but is still suggestive of a dust processing favouring smaller size grains in the IVC of these bright fields. Finally, for *g86*, the LVC and IVC SEDs do not agree in the submillimeter but they do in the far-IR which could be interpreted as hotter grains.
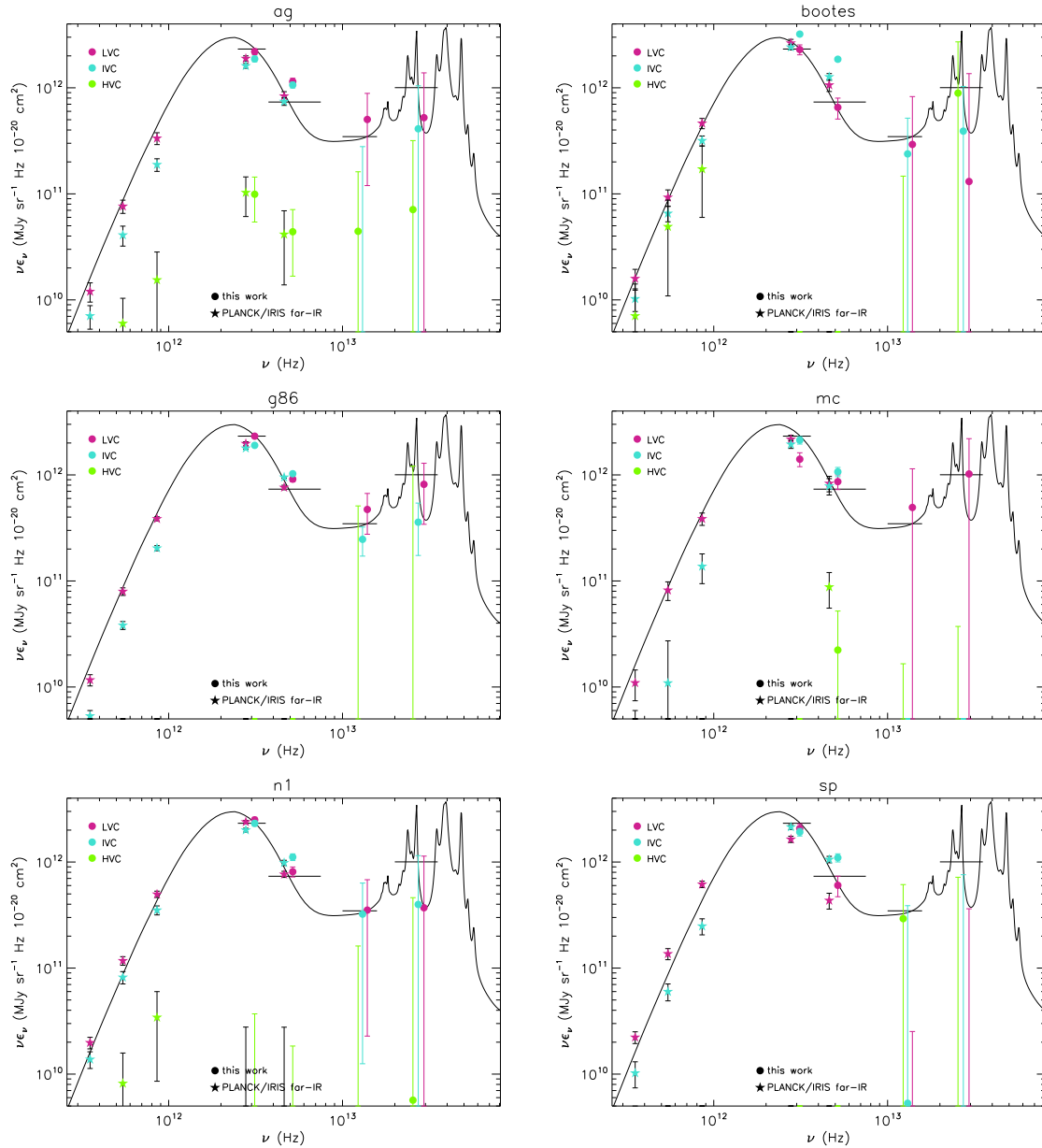
Figure 4.25: SEDs from the mid-IR to the submillimeter for the fainter fields. Violet, blue and green circles are the estimates for the local, intermediate and high-velocity dust emissivities with associated 3σ error bars (at 12 and 25 μm) and 1σ error bars at 60 and 100 μm. For clarity, these have been offset from the filter's effective wavelength. The 3σ error bars have been chosen to more readily show significant detections and upper limits. Star symbols locate the results from the work of Planck Collaboration *et al.* (2011c) and their 1σ uncertainties. Overplotted in black is the standard dust model for the diffuse ISM as predicted by the DustEM code. This is not a fit to any of the data here, and is simply to supply a common reference curve. The black horizontal lines at the IRAS wavelengths show the SED value of the dust model as it would be seen through the IRAS filters.
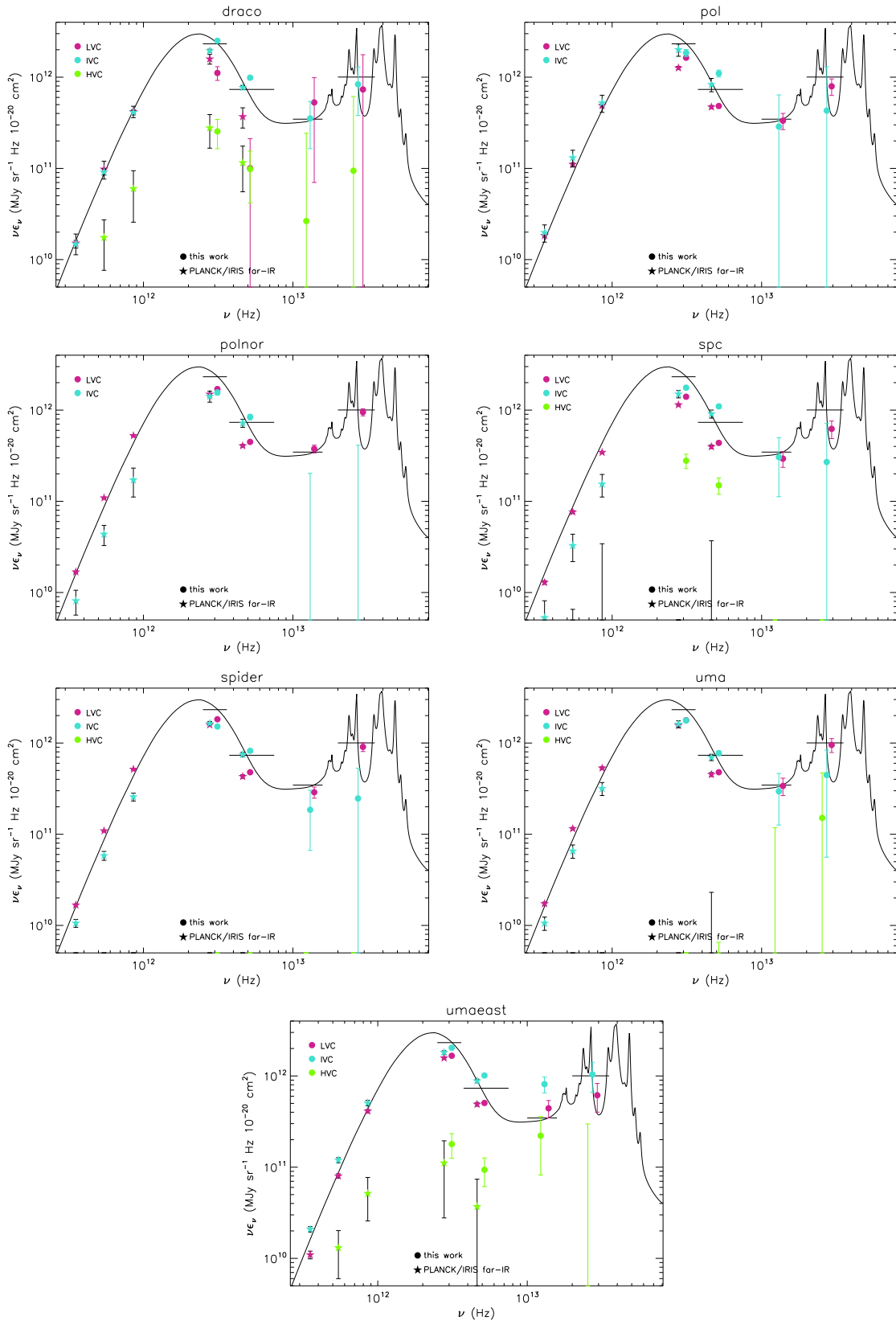
Figure 4.26: Same as Figure 4.25 for the brighter fields.
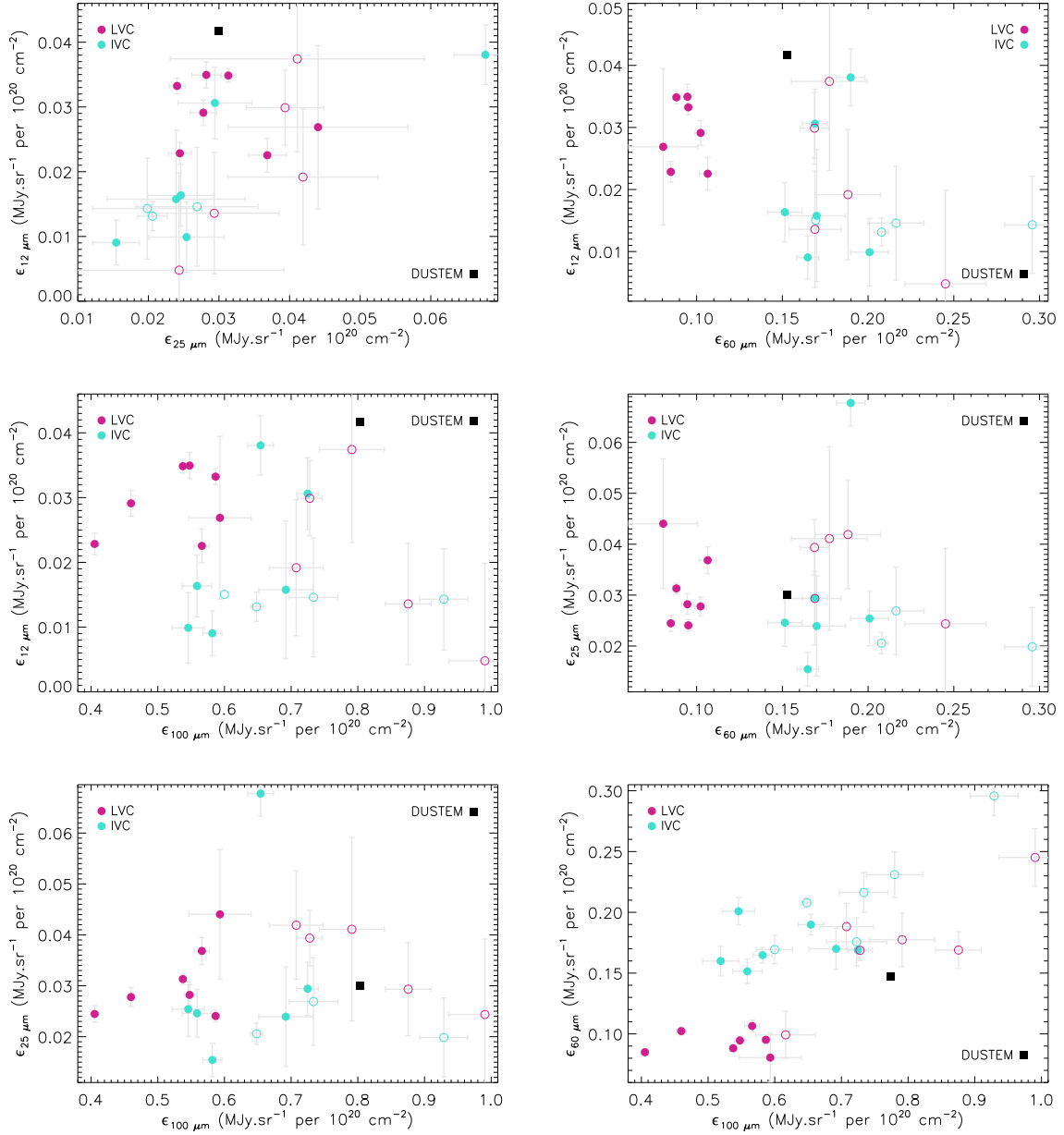
Figure 4.27: Diagrams of the dust emissivities. Filled circles represent bright fields while open circles are for faint fields (the *nep* field is excluded). Local dust emissivities are presented in violet, while IVCs are in blue as indicated in the plots. The black square marks the corresponding IRAS colors of the standard DustEM diffuse ISM dust model (divided by 0.77 as in the SEDs). Shown in grey are the 1σ error bars.

4.7   Color-Color Diagrams

4.7.1   Emissivity correlations

Figure 4.27 shows the possible correlations between dust emissivities using all IRAS wavelengths. For these plots, we have also used our estimates (without any correction for zodiacal emission) of the dust emissivities at 60 and 100 μm. We also plot the corresponding IRAS colors of the standard DustEM diffuse ISM dust model. These data suggest that LVCs in bright fields (represented by violet full circles) have similar or higher 12 μm emissivity than faint fields (represented by violet open circles), while at 25 μm there is no apparent distinction (see top right plot of Figure 4.27). There is also indication that IVCs (blue circles) have lower or comparable 12 and 25 μm emission compared to the local dust (violet circles), but that these emissivities are still similar to the typical DustEM diffuse ISM dust at 25 μm. At 12 μm, the IVCs emissivity is for most fields lower by at least a factor of 2 than what is expected from the model (top plots of Figure 4.27), except for the *draco* and *umaeast*. The IVCs in these fields also display a high ϵ_{25}.

At 60 μm, both bright and faint IVCs show higher emissivity than the bright LVCs (see top and middle right plots in Figure 4.27). The bright LVCs in turn show lower ϵ_{60} than their faint field counterpart. This trend is roughly the same at 100 μm.

The DustEM model at both far-IR wavelengths (60 and 100 μm) is close to the location occupied by the faint LVC fields which points to the dust in these fields being representative of the conditions expected in the average diffuse ISM. We note that the optimal DustEM diffuse ISM dust model SED was determined using the same spatial correlation technique as in this thesis with the difference being that their dust template model is based on one H I column density component integrated between -300 to 300 km s^{-1}. Therefore, their dust emissivity estimate is a weighted average of many different velocity dust components along a certain line of sight. Of more importance, this is averaged over the entire high Galactic latitude sky. We also average over smaller areas in the sky, and calculate emissivities for dust associated with different velocity gas which could partially explain why the DustEM data point seems to fall in between both velocity dust populations.

4.7.2   Color ratios

Figure 4.28 shows trends between dust colors. Here we plot all possible color ratio combinations. The most noticeable result in these plots is the lower 12/25 μm ratio (in relation to the standard DustEM value) found for both faint LVC and IVC dust. This is indicative that either there is more 25 μm emission or less 12 μm emission compared to what is modelled. In the case of the IVCs, the top left plot of Figure 4.27 shows that these have a low ϵ_{12} but a somewhat standard ϵ_{25}, while the LVCs show a slightly lower than typical ϵ_{12} but standard
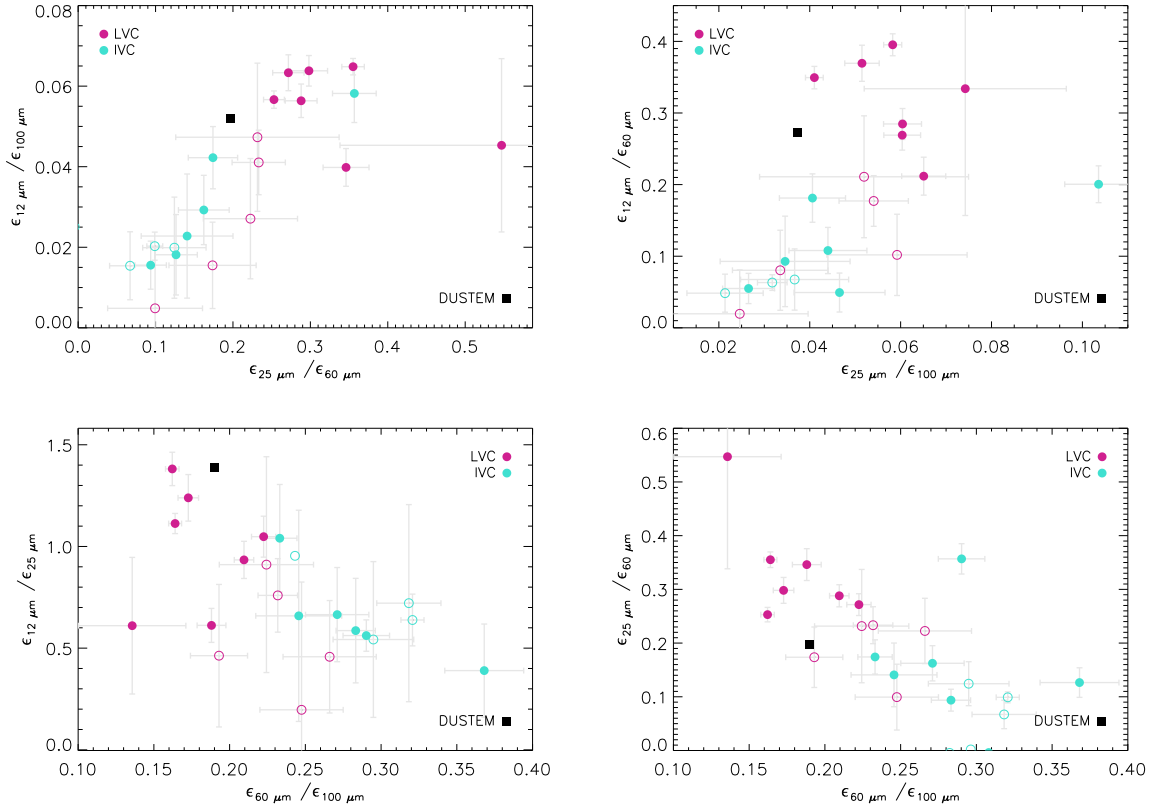
Figure 4.28: Color-color plots of the dust emissivities. Filled circles represent bright fields while open circles are for faint fields (the *nep* field is excluded). Local dust emissivities are presented in violet, while IVCs are in blue as indicated in the plots. The black square marks the corresponding IRAS colors of the standard DustEM diffuse ISM dust model. Shown in grey are the 1σ error bars.

or high ϵ_{25}. This can be suggestive of a scenario where there is lower relative abundance of PAHs in IVCs, and higher abundance of VSGs in LVCs in comparison to the standard diffuse ISM dust model. IVCs show lower 25/60 (bottom right plot in Figure 4.28) and 25/100 (top right plot of Figure 4.28) color ratios than their LVC counterpart (the outlier is the *draco* field.). We have seen than their ϵ_{25} are comparable to the standard value, which leaves us with a high ϵ_{60} and ϵ_{100} (trends already exposed in the bottom right plot of Figure 4.27). IVCs also have a low $\epsilon_{12}/\epsilon_{60}$ and $\epsilon_{12}/\epsilon_{100}$, a trend also shared with the faint LVCs. In fact, IVCs and faint LVCs seem to roughly share the same dust properties.

On the other hand, IVCs clearly display a higher 60/100 ratio than LVCs. Comparison with the SEDs and Figure 1.3 suggest dust in intermediate velocity gas has undergone some processing favouring the production of smaller size particles capable of emitting more at shorter wavelengths (such as large VSGs) rather than an increase in the ISRF that would produce more PAH emission at 12 and 25 μm as well. We calculate color ratios based on the averages found in §4.4 and §4.5, and present them in Table 4.11.

Table 4.11. Mean IRIS color ratios relative to 100 μm

		12 μm	25 μm	60 μm
This work	LVC	0.049 ± 0.014	0.053 ± 0.017	0.199 ± 0.098
This work	IVC	0.036 ± 0.026	0.044 ± 0.033	0.316 ± 0.066
Boulanger & Perault (1988)		0.042	0.054	0.212
Arendt *et al.* (1998)		0.046	0.048	0.171
DustEM (IRAS colors)		0.052	0.037	0.190

Note. — Color ratios in this work are estimated dividing the mean dust emissivity at each λ at each velocity component by the corresponding 100 μm emissivities. These are $\epsilon_{\text{LVC}} = 0.613 \pm 0.138$ and $\epsilon_{\text{IVC}} = 0.675 \pm 0.150$ MJy sr^{-1} 10^{-20} cm^{-2}.

4.7.3 Previous estimates

In their Table 2, Boulanger & Perault (1988) report the dust colors based on cosecant laws at high Galactic latitudes of which translate to $R_{12/100} \sim 0.042$, $R_{25/100} \sim 0.054$ and $R_{60/100} \sim 0.212$. These values are in remarkable agreement to our local estimates. Previous work by Arendt *et al.* (1998) with the DIRBE data revealed the dust color ratios $R_{12/100}$, $R_{25/100}$ and $R_{60/100}$ to be approximately 0.046, 0.048 and 0.171 (see their Table 4). As pointed out in Chapter 1, these authors calculated the slope and intercept of the linear least-squares fit between the 100 μm and H I column density. We note that they have applied an iterative cut-off method to the H I column density which ranged from 1.5×10^{20} to 5×10^{20} cm^{-2} depending on region being fitted. Their H I velocity integrated maps were produced from 3 different data sets with the smallest interval of velocities ranging from -150 to 100 km s^{-1}(which includes most local, IVC and HVC gas). We find color ratios (Table 4.11) for local dust, at all IR wavelengths, higher than what they reported. We also add to this Table the IRAS colors of the diffuse ISM dust from the DustEM model. We recall that Arendt *et al.* (1998) had determined the ratios at 12, 25 and 60 μm based on a $\epsilon_{100\mu m}$ dust template, while we do the least-squares fit analysis for all IRAS wavelengths. For IVCs, the situation slightly changes as the $R_{12/100}$ and $R_{25/100}$ are now smaller but the $R_{60/100}$ is up by a factor of about 1.6. However, we note that the mean R_{12} obtained is the average value of 4 fields only (0.013, 0.016, 0.031 and 0.038 for *g86*, *uma*, *draco* and *umaeast*). If we take the most significant detected values, the mean ϵ_{12} becomes 0.035 which translates into a $R_{12/100}$ of about 0.051 which is similar to the value found for the local dust.

Nevertheless, these results again indicate that IVCs have undergone dust evolution towards smaller size dust distributions. In the context of the Galactic fountain model (Bregman

1980), it is supposed that IVCs form from dust and hot gas that has been ionized and shocked from supernova events in the Galactic plane and has risen to the halo. The shocks can efficiently shatter the big grains into smaller size grains, VSGs (Jones *et al.* 1996). Therefore, the shattering of big grains could provide the abundance of VSGs required for the strong 60 μm emission. Also, the lower 12 μm seems to agree with the study of Micelotta *et al.* (2010) which found that PAHs were effectively destroyed in 100 km s^{-1} shocks. Although such shocks can also give rise to enhanced PAH abundances by shattering of the larger grains, these authors have shown that PAHs cannot survive in the post-shocked gas. The slightly lower IVCs 25 μm emission seen is not easy to interpret because it is the sum of both PAHs and VSGs emission. While there is evidence of reduced abundance of PAHs, there seems to be an increase in the number of VSGs, and therefore, the almost average 25 μm emission might just be the result of those two effects.

4.7.4 Luminosity

In order to explore whether the low 12 and 25 μm emission seen in the IVCs is a consequence of reduced abundances of PAHs and VSGs or perhaps a lower ISRF, we plot the ratio of luminosity or total power (in each different velocity component SED: LVCs and IVCs) for each field and the luminosity from the typical DustEM diffuse dust versus the mid-IR emissivities. The total luminosity (per H) of the big dust grains can be obtained by summing the SED over the frequencies of thermal emission and is given by

$$L = 4\pi \int \sigma_0 \left(\frac{\nu}{\nu_0} \right)^\beta B_\nu(T)\, \mathrm{d}\nu, \tag{4.7}$$

where B_ν, ν, ν_0, σ_0, T and β are variables already previously described in Equation 1.1. For a constant ISRF strength, the energy absorbed by the big grains must equal their luminosity output given that their are in thermal equilibrium. We use the estimates for σ_0 and T (for a $\beta = 1.8$) obtained in Planck Collaboration *et al.* (2011c) (and consequently, L) for dust associated with local gas and IVCs in the same sample of fields presented here. These were found by fitting a modified blackbody to the measured dust emissivities at IRIS 100 μm to PLANCK 857, 545 and 353 GHz.

We then divide each luminosity estimate by 4.16×10^{-31} W/H. This value is a simple estimate of the luminosity of the big grains (called 'SamC' and 'aSil' in the DustEM model) which contribute 64 % of the total power emitted in their diffuse ISM dust model (5×10^{-31} W/H). We again divide by 0.77 to get the power in a per H I scale. Another estimate can be obtained by using the 'DHGL' SED values at the frequencies (3000, 857, 545 and 353 GHz) as the effective dust emissivities. Then, as in Planck Collaboration *et al.* (2011c), by fitting them with a modified blackbody (again with β fixed to 1.8), we obtain T and σ_0. When integrated over ν, this fit SED provides the luminosity of the 'big' grains in DustEM model. This improvement

will be carried out in the near future, but for now we will use $L_{DustEM} = 4.16 \times 10^{-31}$ W/H. Assuming the ISRF strength is constant, the ratio between luminosities (L for each field and velocity component and L_{DustEM}) measures the relative abundance of traditional big grains with respect to what would be expected from the diffuse DustEM model for a ISRF of G=1 (the strength in the local neighborhood). A ratio below unity indicates that there is less relative contribution to the spectrum by the traditional big grains. We compare that ratio to a color ratio. The latter is the ratio between our measured ϵ_λ and the IRAS emissivities of the standard DustEM diffuse ISM dust model. These plots can be seen in Figure 4.29.

These plots be used to better distinguish the effects of grain abundance from the radiation field strength. The PAHs and VSGs emission is directly proportional to the strength of the radiation field because of their stochastic emission. So is the luminosity. LVCs and IVCs which fall on the 1 to 1 line (represented by the black dashed line), show the effect of the typical dust abundances but a varying ISRF strength.

Both 12 and 25 μm plots show (much more convincingly for the 12 μm case) that the decrease in the abundance of big grains, which is generally accompanied by an increase in the 60 μm emissivities (seen in the bottom plot and also in the color diagrams above), is not accompanied by an increase in the relative abundance of PAHs and smaller VSGs. If that were the case, then we would see enhanced ϵ_{12} emission, but that region in the plot (lower right) is empty of data points. In contrast, the bottom plot displays the relative increase in abundance of the VSGs which shine brightly at 60 μm for all IVCs. At 25 μm, only LVCs seem to have slightly higher than average emissivity for a modest big grain depletion. All of these trends point to IVCs having lower relative abundance of PAHs and higher VSGs, than local dust or LVCs. This is indicative of dust evolution in IVCs via shocks.

Given that the typical luminosity of dust with T=17.9 K and $\sigma_e = 1.0 \times 10^{-25}$ cm^2 (σ_e is measured at 1200 GHz or 250 μm) would be 3.8×10^{-31} W/H (Planck Collaboration *et al.* 2011c), the normalizing value used here for L_{DustEM} is perhaps an upper limit.

Furthermore, to quantify the decrease in the 12 μm emission and increase of the 60 μm emission for IVCs in terms of different relative abundances of dust populations, we compare our dust emissivities with those expected by varying model parameters in the DustEM model. Figure 4.30 shows a diagram of the ϵ_{12} and ϵ_{60} found for our GBT fields. We overplot the estimates of the theoretical DustEM model for a varying ISRF strength and modified abundances of PAHs and VSGs.

We find that the faint 12 and strong 60 μm emission from local dust (bright LVCs) seems to be well described by the standard DustEM diffuse ISM dust model abundance of PAHs, VSGs and big grains but with a slightly lower ISRF strength of about 0.8 of the local neighborhood value. This is not the case for the IVCs. The dust emissivities found are not well explained just by varying the strength of the ISRF, and require different relative abundances of PAHs (half of the standard model) and VSGs (about four times more). We have kept the relative abundance
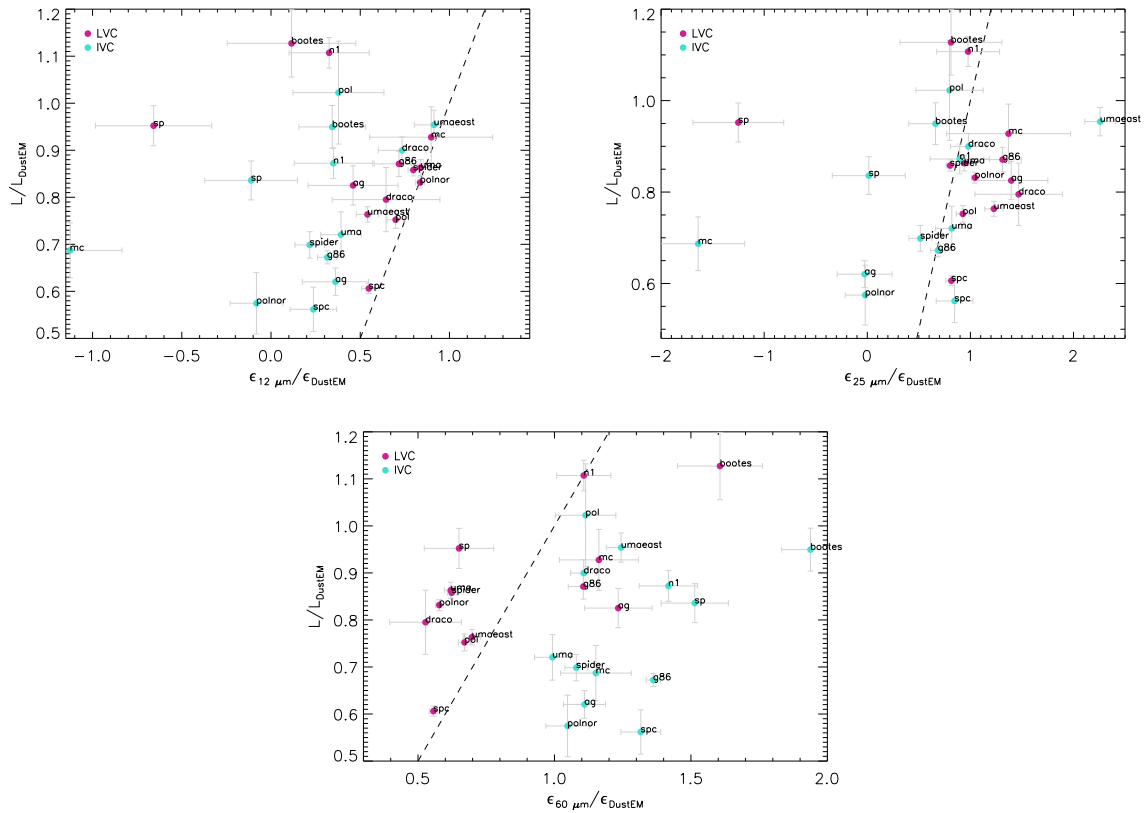
Figure 4.29: Measure of the relative abundance of large grains versus the 12 *µm* (*top left*), 25 *µm* (*top right*) and 60 *µm* (*bottom*) emissivities normalized by ϵ_{DustEM} at the same wavelengths. A ratio L/L_{DustEM} smaller than unity signifies that there is lower abundance of traditional big grains to what would be expected in the DustEM model for the diffuse ISM dust. In the 12 *µm* diagram, the lack of data points at the bottom right part of the plot shows that shattering of large particles (indicated by the bright 60 *µm* emission) is not accompanied by an increase in the abundance of PAHs and smaller VSGs responsible for the mid-IR emission.
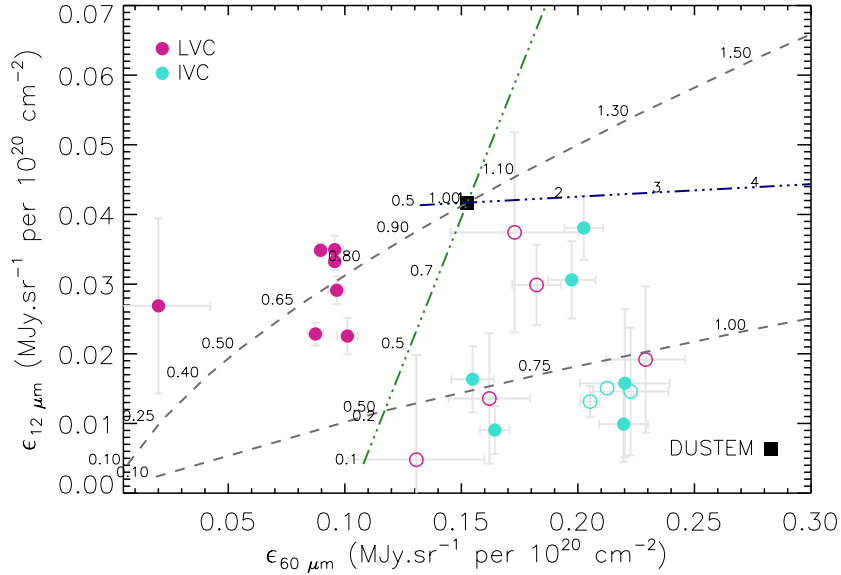
Figure 4.30: Dust emissivities at 12 and 60 μm compared to the estimates by varying model input parameters in the DustEM model. Black dashed lines represent the emissivity values for a varying ISRF strength (upper dashed line) and also half the relative abundance of PAHs and four times more the relative abundance of VSGs (lower dashed line). We also vary the relative abundance of PAHs and VSGs equally (dark green dashed-dotted line) and relative abundance of VSGs only (dark blue dashed-dotted line).

of the big grains the same. This quantifies the amount of dust processing in these intermediate velocity clouds and agrees with our suggestions of dust evolution as demonstrated in the above color-color and luminosity diagrams.

4.8 Cosmic Infrared Background Anisotropies (CIBA) at mid-IR wavelengths

Previously, Kashlinsky & Odenwald (2000) set limits on the CIBA using the DIRBE data. They estimated the CIB fluctuations to be less than 1, 0.5, 0.8 and 1.1 nW m^{-2} sr^{-1} at 12, 25, 60 and 100 μm. Our estimates from the faint fields are about 3 times greater (see Table 4.7 and converted values in second column of Table 4.12). We cannot provide a direct estimate of the CIB average value at mid-IR wavelengths since the intercept values we obtain after the least-squares fit (in §4.3.5) are heavily contaminated by the poorly subtracted Zodiacal emission zero level. Here, we use our CIBA values to estimate a mean value of the CIB at all our mid- and far-IR wavelengths.

From Figure 15 in Planck Collaboration *et al.* (2011d), we expect the ratio between the CIBA and mean CIB to be about 0.15 at far-IR and submillimeter wavelengths. However,

Table 4.12. CIBA and derived mean CIB at Infrared Wavelengths

λ	CIBA	Ratio	$\langle CIB_{pr} \rangle$	$\langle CIB \rangle$
12	< 3.00	0.49	< 6.25	< 11.14
25	< 1.44	0.37	< 3.91	< 7.98
60	< 1.30	0.26	< 4.93	< 5.32
100	< 2.16	0.21	< 10.14	< 11.13

Note. — Units for CIBA and mean CIB are in nW m^{-2} sr^{-1}. The CIBA values are derived from the standard deviations of the masked residual maps of the faint fields. $\langle CIB_{pr} \rangle$ and $\langle CIB \rangle$ are calculated using the ratio and represent the case where a tilted plane has been removed or no correction has been made, respectively. We have put our estimates at 12 and 25 μm as upper limits given the still possible existence of residual zodiacal emission in our residual maps.

there is evidence suggesting that this ratio increases with higher frequencies (Lagache, private communication). In such a model, the far-IR and submillimeter data are well fitted by a linear relation ($y = ax + b$) in log space with $a = 0.38$ and $b = -4.57$. We extrapolate the inferred model to 60, 25 and 12 μm (the shortest wavelength fitted was 100 μm) to obtain the ratio estimates shown in Table 4.12 and from these, estimates of the mean CIB. We plot our results and compare them to other estimates in Figure 4.31. We also compare our estimates to the Béthermin *et al.* (2011) model which theorizes the CIB mean spectrum based on number counts studies. We note that although our CIBA estimate at 25 μm is higher than the one determined by Kashlinsky & Odenwald (2000), we derive a lower mean CIB due to the high ratio value adopted in our analysis. In fact, we use the same ratio (0.1) used by Mazin & Raue (2007) to estimate the CIB mean values based on the Kashlinsky & Odenwald (2000) CIBA estimates.

When compared to the CIB estimates compiled in Table 1 of Bethermin & Dole (2010), our values are all greater than the lower limits therein, as set by resolved sources. Upper limits derived from measurements of γ-ray absorption are also quoted (see references in Bethermin & Dole, 2010). In particular, Mazin & Raue (2007) estimate the mean CIB to be about 5 nW m^{-2} sr^{-1} at 12 and 25 μm from TeV measurements of blazars (with upper limit of about 7 nW m^{-2} sr^{-1}). Those are both in agreement with our results. However, our 12 μm estimate of about 6.25 is slightly bigger than the upper limit of 4.7 nW m^{-2} sr^{-1} calculated by Renault
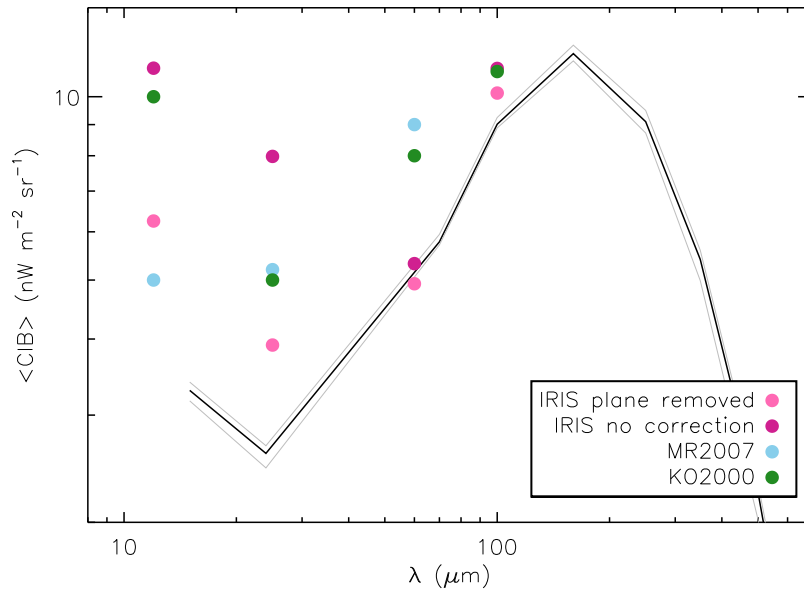
Figure 4.31: Derived estimates for the mean CIB and comparison with previous estimates of Kashlinsky & Odenwald (2000) (dots in green) and Mazin & Raue (2007) (dots in light blue). The black line (with lower and upper limits in grey) is the modelled CIB spectrum from Béthermin *et al.* (2011).

et al. (2001). Had we used a ratio of 0.15 found at sub-millimeter wavelengths, that difference would be even greater. At 24 *μm*, Béthermin *et al.* (2010) estimated a lower limit of 2.29 ± 0.09 nW m^{-2} sr^{-1} for the CIB using *Spitzer* data (via number counts between 35 *μ*Jy and 0.1 Jy). By extrapolation, they also derive a mean CIB value of about 2.86 nW m^{-2} sr^{-1} which corresponds to approximately 0.023 MJy sr^{-1}. Our 25 micron estimate of 3.9 nW m^{-2} sr^{-1} is higher than their estimate. The lower limit, found by the same authors at 70 *μm*, from stacking analysis of 5.4 nW m^{-2} sr^{-1} and its extrapolated CIB mean value of 6.6 nW m^{-2} sr^{-1} is however slightly higher than the 4.9 nW m^{-2} sr^{-1} we find at 60 *μm*. The absolute measurements of the CIB that overlap with the IRAS bands exist only at 65 and 100 *μm* and are greater than the mean CIB values we derive (see Bethermin & Dole (2010) and references therein).

Another big source of uncertainty stems from the ratio between the CIB anisotropies and the mean CIB value. If we assume that the ratio at higher frequencies is constant and 0.25, then the mean CIB values are 12, 5.8 and 5.1 nW m^{-2} sr^{-1} (0.048, 0.048 and 0.102 MJy sr^{-1}) at 12, 25 and 60 *μm*. For the case where no tilted plane has been removed from the infrared data, we obtain a greater value for σ_{CIB} (or CIBA) in all wavelengths (see Table 4.7). Using the same extrapolated ratio values, we get greater correspondingly mean CIBs (see the last column of Table 4.12).

4.9 Power spectra of the residual maps

Here, we explore fluctuations left in the residual maps via its power spectra (refer to §2.6.3 for more details on power spectrum). Figures 4.32 and 4.33 show the power spectra of the infrared, H I model and residual maps obtained in the least-squares fit for the faint *ag* field and the brighter *uma* field. Also shown are the power spectra of the HCON difference maps, an attempt at investigating the noise contribution from the IR maps.
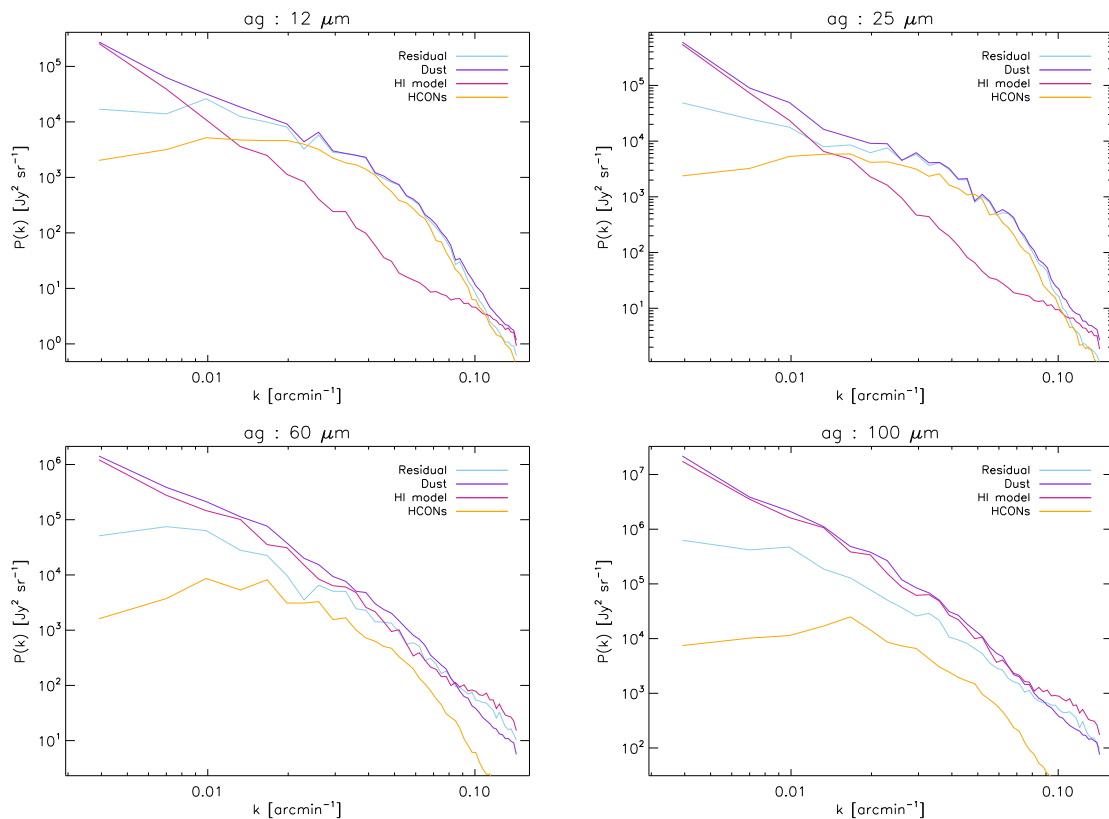
Figure 4.32: Power spectra for the infrared, H I model and residual maps for the *ag* faint field at all IRAS wavelengths. Note the increasing power spectra amplitude as the wavelength increases. The HCONs difference maps average power spectra has been multiplied by 2/3 following the recipe used in §2.6.1.

We can see the effect of the 9′.55 beam in all power spectra, rolling the spectra off steeply at high *k*'s (see the 12 *μm* power spectra in Figure 4.32 for example). The power spectra of the residual maps (in light blue) in the *uma* field reflect the power law behaviour of the dust associated with molecular material which is not well fitted by the multilinear template model and therefore remains in the residual maps. This is the case in all IR wavelengths and its power law slope is similar to the one displayed by cirrus dust (about -3 or a bit shallower). On the other hand, the power spectra behaviour of the *ag* residual maps is flatter suggesting that the residuals are not dominated by residual dust or H I gas structures ill-fitted by the template
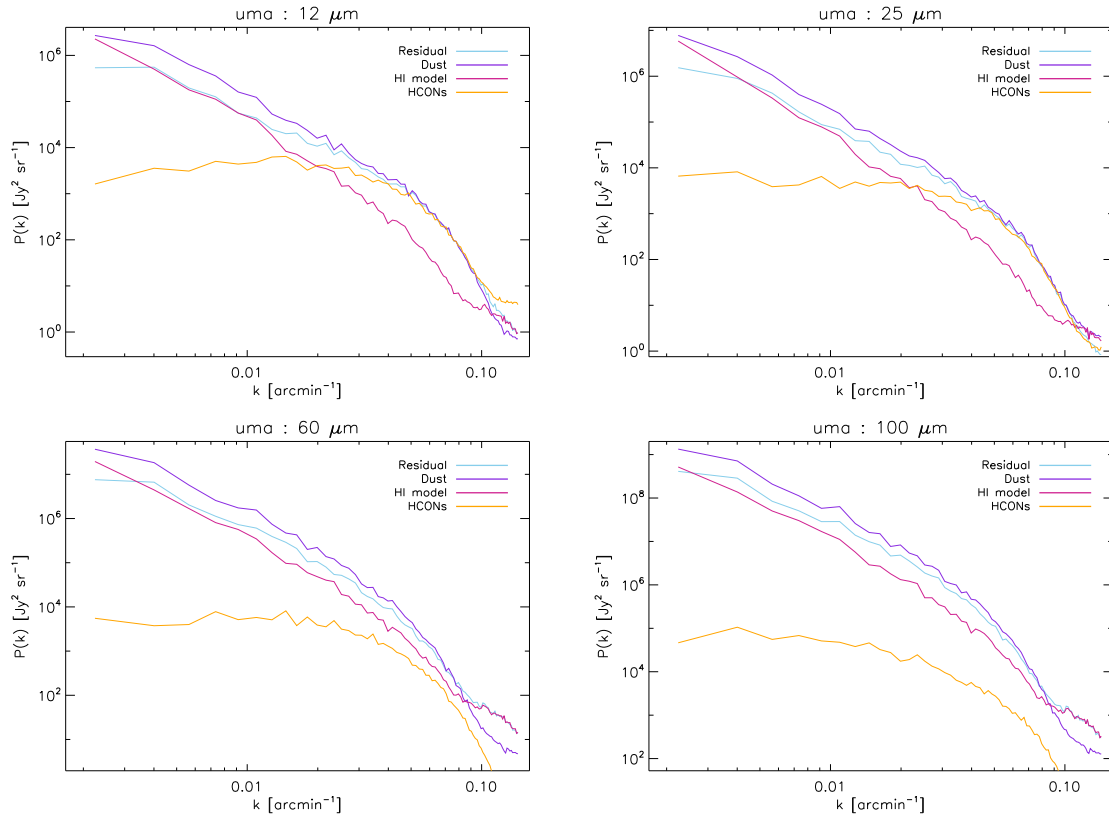
Figure 4.33: Same as Figure 4.32 for the *uma* bright field.

model. The noise amplitude from the HCONs is almost comparable to the cirrus dust signal amplitude at 12 and 25 *μm* for this field at intermediate and large *k*'s. This is due to the increase in zodiacal light and decrease of the cirrus emission at lower wavelengths. This trend is seen in all faint fields. For brighter fields, like *uma*, the cirrus signal power spectrum is higher by almost 2 orders of magnitude at high *k*'s. This difference is even greater at longer wavelengths. The H I model power spectrum seems to be a good model as it matches closely the IR maps power spectrum for most cases. However, at shorter wavelengths this is less accurate as the noise power spectrum takes over at earlier *k*'s. The little hump at the largest *k*'s (beyond the beam) in the H I model power spectrum reflects the modified Bessel smoothing chosen to grid the GBT H I data (visible in Figure 2.12 as well). This shape is present in the power spectrum of the residual maps since they carry the noise signature of the H I column density maps as well.

We have also noted that in a few fields and at the mid-IR wavelengths, the amplitude of noise power spectrum from approximately 0.03 to 0.06 arcmin^{-1} was higher that the residual one. One possible explanation for this could be due to an increase in the dispersion of the HCONs maps when replacing parts of it with no coverage. However, upon further inspection, we note that the bump seems to result from point-source-like regions in the HCONs difference maps (see Figure 4.34 for the *ag* field). These are visible at the shorter IR wavelengths which
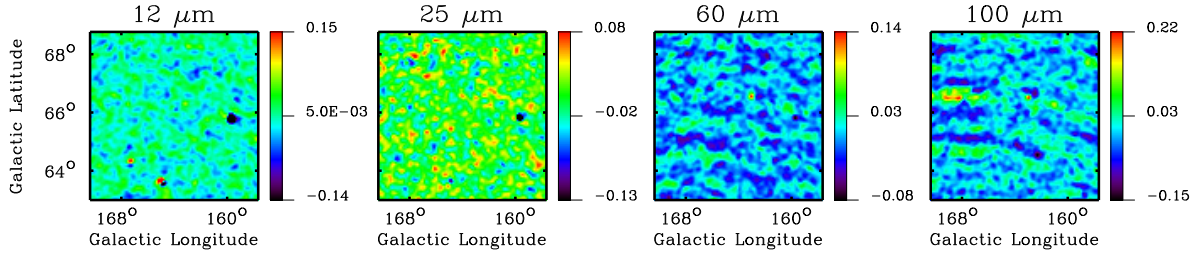
Figure 4.34: HCONs 1 and 3 difference map for the *ag* field for all IR wavelengths. The 'point sources' like regions (holes in black) are well seen at 12 and 25 *μm*. These seem to be causing the HCONs power spectrum to be higher that the actual IR maps power spectrum in the *k* range from 0.03 to about 0.06 arcmin^{-1}.

suggests the possibility that some transients objects (maybe asteroids) left their signature in the IRAS plates and were not removed from the individual HCONs. As a preliminary fix, we replace these point-source-like features with the mean brightness level from the pixels in the HCONs difference map which are not contaminated. Also, note that these features only show up here because the point source removal from the IRIS data occurs in the HCON$_0$ (which is the combination of the 3 HCONs weighted by their coverage map) and therefore such features are not propagated to the final IR maps. A better solution to this problem would be to remove the point sources at an earlier stage on each individual HCON which we will do in the future.

To better quantify the shape of the residual maps power spectra, we fit a model containing a power law modified by the beam plus the noise power spectrum. The beam is assumed to be Gaussian with a FWHM of 9$.'$55 which causes the fast drop in power of the residual at large *k*'s. The noise model adopted here is the average power spectra of the HCONs difference maps. We assume that the behaviour of the residual power spectrum (before being affected by the beam and the noise) is well described by $P(k) \sim A\,k^{-\alpha}$, where A is an amplitude and α is the slope. We fit such a model to the residual maps at 100 *μm* and find that for the fainter fields the average slope is about -1.50 ± 0.25, while for the brighter maps that increases to -2.40 ± 0.25. This estimate is comparable to the -2.53 ± 0.03 slope fit to the cirrus power spectrum for the faint *n1* field at 100 *μm* by Pénin *et al.* (2012). For 60 *μm*, the mean is 1.83 ± 0.65 and 2.43 ± 0.25 for the faint and bright fields, respectively. Figure 4.35 shows the residual map fit for the bright *spc* field at both far-IR wavelengths. In general, the slope of the power spectra of the residual maps for the faint fields is flatter than for the bright ones, indicating the presence of residual emission connected to cirrus or molecular gas in the bright fields. The faint field values are slightly higher than the expected power law behaviour for the CIBA at these wavelengths which is around -1 (Planck Collaboration *et al.*, 2011d). On the other hand, the modelling procedure fails often when fitting the residual maps at 12 and 25 *μm*. This is because the noise power spectrum is very large and approaches the residual power spectrum amplitude at small *k*'s. Therefore, it is increasingly difficult to produce a good fit with such a small number of points with which to fit a slope. This is especially evident for the faint fields. Figure 4.36 compares the residual power spectrum fit at 25 *μm* for a faint and
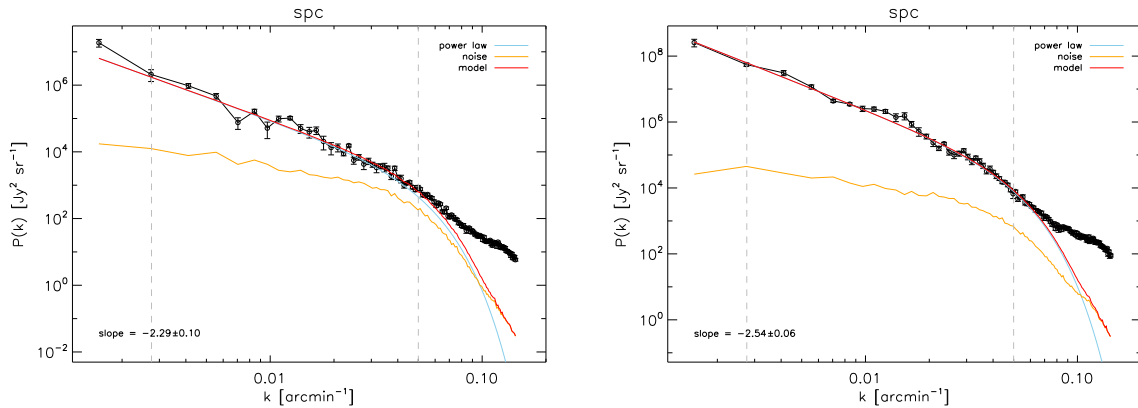
Figure 4.35: Power law fit of the residual power spectrum at 60 (*left*) and 100 (*right*) μm. For high k's, beyond the range used in the fit (marked with grey dashed lines), the data (in black) and the model (in red) diverge because of the contribution of the H I noise (not affected by the beam) has not been included.
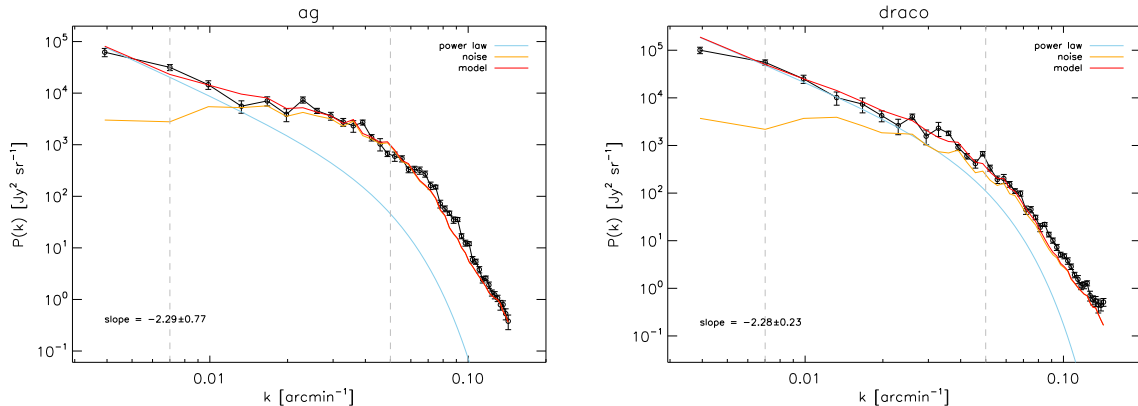
Figure 4.36: Power law fit of the residual power spectrum at 25 μm for the faint *ag* field (*left*) and bright *draco* field (*right*). Grey dashed lines mark the k range used in the fit.

a bright field. Given the high uncertainty and small number of points available to constrain the power law parameters in the faint fields, we are not able to achieve robust fits for most power spectra of faint fields residual maps at 12 and 25 μm. On the other hand, the situation is not so grim for the bright fields, and using most of them, we find a mean slope of about -2.55 ± 0.22 and -2.72 ± 0.13 at 12 and 25 μm, respectively. Assuming that contamination by zodiacal light is not an issue, on top of the N_{HI} and IRIS (HCONs) noise, the residual maps for the faint fields should be left only with the CIB anisotropies, while the brighter maps would also contain the dust emission associated with structures ill-fitted by the multilinear template model such as molecular regions. Assuming that to be the case, our analysis reveals that dusty molecular regions have a power spectrum that behaves as a power law of about -2.4 at far-IR wavelengths.

There seems to be a common shape to the power spectra of the residual maps for the faint

fields. In order to quantify that behaviour more robustly, we calculate the mean of $P(k)$ for each common k for all faint fields. The range of k's is set by the size of the smallest faint field. Figure 4.37 shows the power spectra of the faint fields residual maps and its mean for all IRAS wavelengths. We fit the mean power spectrum using the same model described above. Our k limits for the fit are between about 0.004 and 0.048 arcmin^{-1}. If indeed whatever is left in the IR residual maps of the faint fields is the imprint of the CIB fluctuations, then the power spectrum of the CIBA is well fitted by a power law with an exponent of -1.61 ± 0.14, -1.93 ± 0.28, -1.59 ± 0.27 and -1.63 ± 0.09 at 12, 25, 60 and 100 μm. However, these estimates should be taken as upper limits because of the possible contamination (although small) of regions in the residual maps which are ill-fitted by the multilinear template model (i.e., masked regions). We would like to add that the bump visible at high k's (behind the beam turnover) in the 60 and 100 μm power spectra of the residual maps (either faint or bright fields) is the signature of the H I noise. This becomes increasingly strong for longer wavelengths because the residual maps carry the H I noise (which does not change with wavelength) multiplied by the dust emissivities whose value increase with wavelength. In the future, we plan to take into account the H I noise and thus include all noise sources in the model used to fit the residual maps power spectra. Note that we have chosen our range of k's used in the fit to exclude that part of the residual power spectrum where the H I noise dominates.

In the near future, we will do a consistency test to these results (and the value of CIBA of -1 used in the Monte-Carlo simulations) by building maps with the power spectrum slope estimates obtained above. We expect the dispersion on these maps to be similar to the ones reported in the first column of Table 4.12.
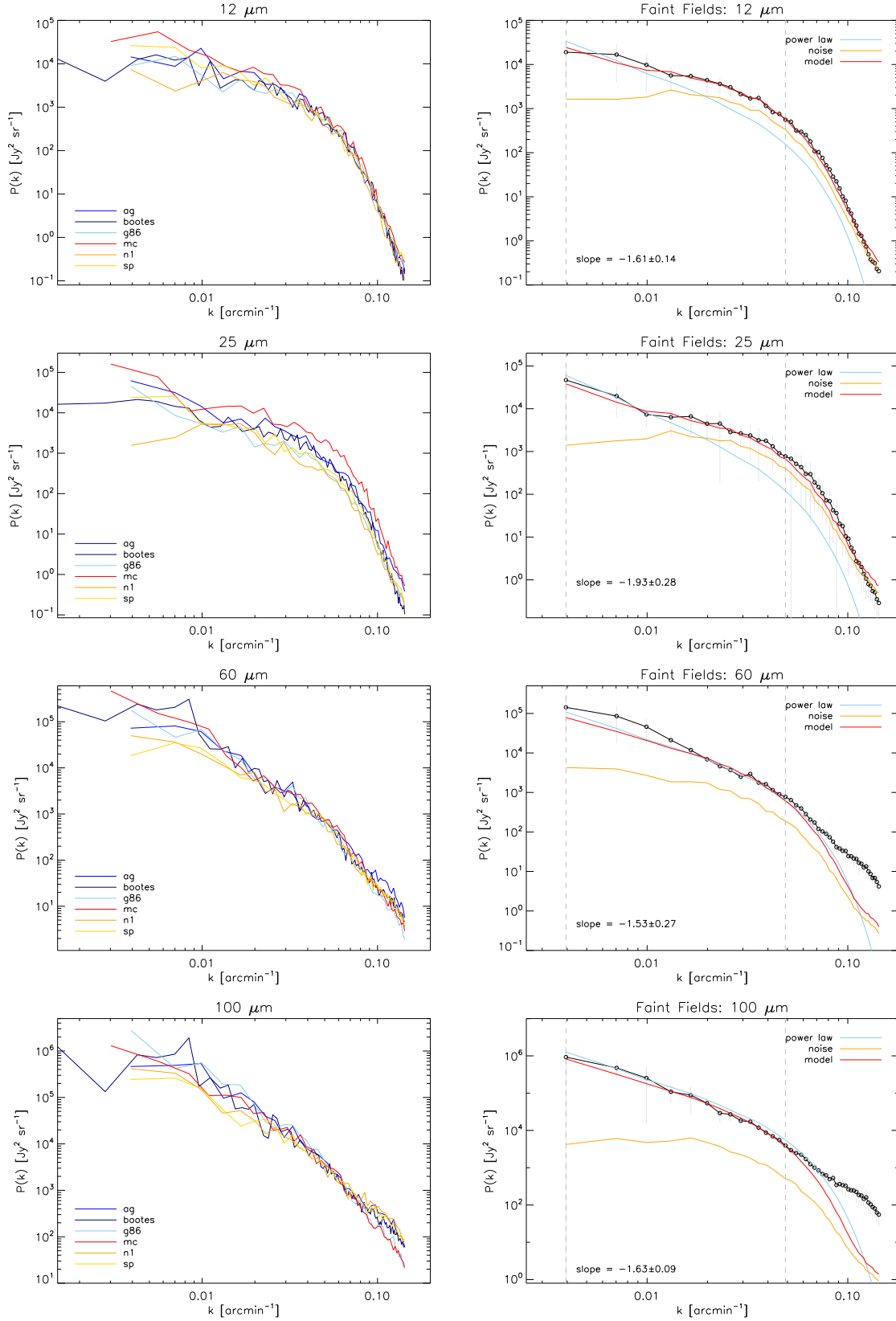
Figure 4.37: Power spectra of the residual maps of the various faint fields (*Left*). Average of the power spectra of the residual maps for the faint fields and corresponding model fit (*Right*). The model fitted is a power law, taking into account the beam and the noise power spectra obtained from the HCONs difference maps, but ignoring the contribution of the H I noise at high k. Grey dashed lines mark the k range used in the fit.

4.10 Conclusions

We have conducted an analysis of the IR emission (with emphasis on the the mid-IR range) for 14 fields located at high Galactic latitudes. Such analysis was accomplished by spatially correlating IRIS/IRAS maps and H I column density maps in order to calculate emissivities, units of MJy sr^{-1} (10^{20}cm^{-2})$^{-1}$, of dust associated with different velocity gas at a resolution of 9$'$ (about 4 times higher than previous large data sets surveys). Our findings are the following:

- Preliminary least-squares fits analysis revealed that the residual maps contain some sort of gradient consistent with an imperfect removal of Zodiacal light emission. This was specially evident at 12 and 25 μm.

- We have developed two methods to remove the contribution of a tilted plane which produced similar results. The first one consisted in iteratively fitting the residual map from the least-squares fit until its dispersion is minimal. The second one included the parameterization of the tilted plane on the multilinear template model which now describes the IR emission as,

$$I_\lambda(x,y) = \sum_{i=1}^{3} \epsilon_\lambda^i \, N_{HI}^i(x,y) + a_\lambda \, P_x(x,y) + b_\lambda \, P_y(x,y) + d_\lambda \,.$$

  The two methods gave equivalent results, as expected.

- We obtain mid-IR (at 12 and 25 μm) dust emissivities (for the first time) for LVCs, IVCs and HVCs at 9$'$ resolution and construct the SED of the emissivity from the mid-IR to the sub-millimeter.

- We find color ratios of the emissivities, $R_{12/100} = 0.049 \pm 0.014$, $R_{25/100} = 0.053 \pm 0.017$, $R_{60/100} = 0.199 \pm 0.098$ for the local dust (LVCs), which is in agreement with values previously found by Boulanger & Perault (1988) and Arendt *et al.* (1998), not distinguishing between LVC and IVC. The uncertainties reflect the dispersion seen between fields.

- For the intermediate velocity clouds (IVCs), we find dust colors of $R_{12/100} = 0.036 \pm 0.026$, $R_{25/100} = 0.044 \pm 0.033$, $R_{60/100} = 0.316 \pm 0.066$. The $R_{60/100}$ is higher compared to LVCs but consistent with the value previously found for IVCs.

- Both IVCs and faint LVCs seem to have similar dust properties in that they share a lower 12/60 and 12/100 ratio and higher 60/100 ratio than the bright LVCs.

- The high 60 μm dust emissivity found for IVCs reinforces the idea that these structures undergo shocks which alter the large grain population to the extent that emission from a population of grains with smaller sizes, typical of VSGs, becomes apparent. The low

$R_{25/60}$ may reflect a lower abundance of PAHs and smaller VSGs compared to the population of larger VSGs that produces the strong 60 μm emission. The 12 μm dust emissivity is consistently low for LVCs and even lower for IVCs, suggesting that a low relative abundance of PAHs in IVCs.

- We find upper limits for the CIBA value of 3.00, 1.44, 1.30 and 2.16 nW m^{-2} sr^{-1} at 12, 25, 60 and 100 μm using the standard deviation of the residual maps of the faint fields.

- We fit a power-law to the power spectra of the residual maps for the faint fields and find that a slope of -1.61 ± 0.14, -1.93 ± 0.28, -1.59 ± 0.27 and -1.63 ± 0.09 at the IRAS wavelengths 12 to 100 μm, respectively. This is an estimate of the power spectrum of the CIBA. For the brighter fields, where the residual maps still shows dust emission probably associated with molecular gas, we obtain mean slopes of -2.55 ± 0.22 and -2.72 ± 0.13 at 12 and 25 μm, closer to typical values for cirrus.

Chapter 5

Mid-IR study of supernova remnants in the Galactic Plane

We use this chapter to describe the detection of supernova remnants (SNRs) in the Galactic plane at mid-IR wavelengths. A version of this work has already been published in The Astronomical Journal as "The MIPSGAL view of Supernova Remnants in the Galactic Plane", Pinheiro Gonçalves, D., Noriega-Crespo, A., Paladini, R., Martin, P. G., and Carey, S. J., 142:47 (33pp), 2011 August. We start with a brief introduction in §5.1. The context for this work has already been set in Chapter 1 which includes a review of previous Galactic SNRs IR studies and expands on the origin of the IR emission from these remnants. In, §5.2, we present the Spitzer *IR data used (8 µm from the GLIMPSE survey and the 24 and 70 µm from the MIPSGAL survey, both in the Galactic plane). We add to these observations, more archival data in the radio and X-ray to complement our view of the SNRs in other energy regimes in §5.2.2. In §5.3, we present our detections at 24 and 70 µm and calculate mid-IR fluxes. Discussion of the detections is explored in §5.4. Here, we access the significance of our results by comparing our detection rates to previous studies, calculate color ratios ([F_8/F_{24}] and [F_{70}/F_{24}]) and implied dust temperatures and masses assuming the mid-IR emission is mainly from dust associated with the remnants. In §5.4.4 and §5.4.5, we explore the connections between the SNRs emission in the IR and in other wavelengths. In particular, the synchrotron emission seen at 1.4 GHz and the high energetic emission seen in the X-ray. Finally, in §5.6 we show the 24 µm and RGB (8,24 and 70 µm with radio or x-ray contours over plotted) for our most spectacular detections and discuss the IR emission shown.*

5.1 Introduction

In this work, we search for counterparts of SNRs in the mid-infrared (at 24 and 70 μm) using the higher resolution *Spitzer* data obtained with the Multiband Imaging Photometer (MIPS), in the coordinate ranges $10° < l < 65°$ and $285° < l < 350°$, $|b| < 1°$, complementing the work of Reach *et al.* (2006). We also briefly explore the relation of SNRs IR fluxes with other

wavelength ranges, such as the radio and the X-ray.

5.2 Data used

5.2.1 IR data

Infrared data used in this paper originates from two Spitzer surveys: GLIMPSE using the Infrared Array Camera (IRAC) and MIPSGAL (survey of the inner Galactic plane using MIPS, Carey *et al.* 2009). Both surveys cover the Galactic coordinates $10° < l < 65°$ and $285° < l < 350°$, $|b| < 1°$.

MISPGAL

The MIPS wavelength coverage is approximately 20 to 30 μm at ch 1 (24 μm) and 50 to 100 μm at ch 2 (70 μm), thus covering a potentially rich set of diagnostic lines and dust emission features (see Figure 5.1). In the 24 μm bandpass, the classic [O IV] 25.9 and [Fe II] 26.0 μm tracers can be quite strong (e.g., Oliva *et al.* 1999a and Noriega-Crespo *et al.* 2009), and likewise [O I] 63 and [O III] 88 μm (e.g., Rho *et al.* 2001) within the 70 μm bandpass. Other standard shock excitation tracers, like [Ne II] 12.81 or [Si II] 34.8 μm, are unfortunately not included within the IRAC or MIPS bandpasses. Nevertheless, when dust is present, it is the dominant component of the IR radiation at 24 and 70 μm (see Fig. 5.1).

Although the 24 μm data delivered by the Spitzer Science Center in their Post-BCD products are of a very high quality, the MIPSGAL pipeline was designed to enhance the data a step further. The details are described in Mizuno *et al.* (2008), but briefly the pipeline: (1) carefully deals with saturated and non-saturated data, a key issue in the Galactic Plane; (2) removes a series of artifacts, the most common being a column-to-column jailbar striping, plus (3) that of short-duration afterimage latencies, (4) long-duration responsivity variations, and (5) background mismatches. The MIPSGAL observations were designed to be a 24 μm survey as the high background levels of the Galactic plane at longer wavelengths saturated the 160 μm detectors and placed the 70 μm at a fluence level not well characterized. Since MIPS takes data simultaneously at 70 and 160 μm, and that at 70 μm at first sight looks reasonable, then a concerted effort has been invested by the MIPSGAL team to improve its quality. The specific steps of the 70 μm pipeline are described in Paladini et al. (*in preparation*), but the main issue is to mitigate the effect of the non-linear response of the Ge:Ga photoconducting detectors. Their standard behavior leads to striping of the images, sudden jumps in brightness and a large uncertainty in the calibration for bright sources and regions. The MIPSGAL 70 μm pipeline reduces these effects and decreases the calibration uncertainties to a level of ~15%. This uncertainty on the absolute calibration of the extended emission is consistent with that
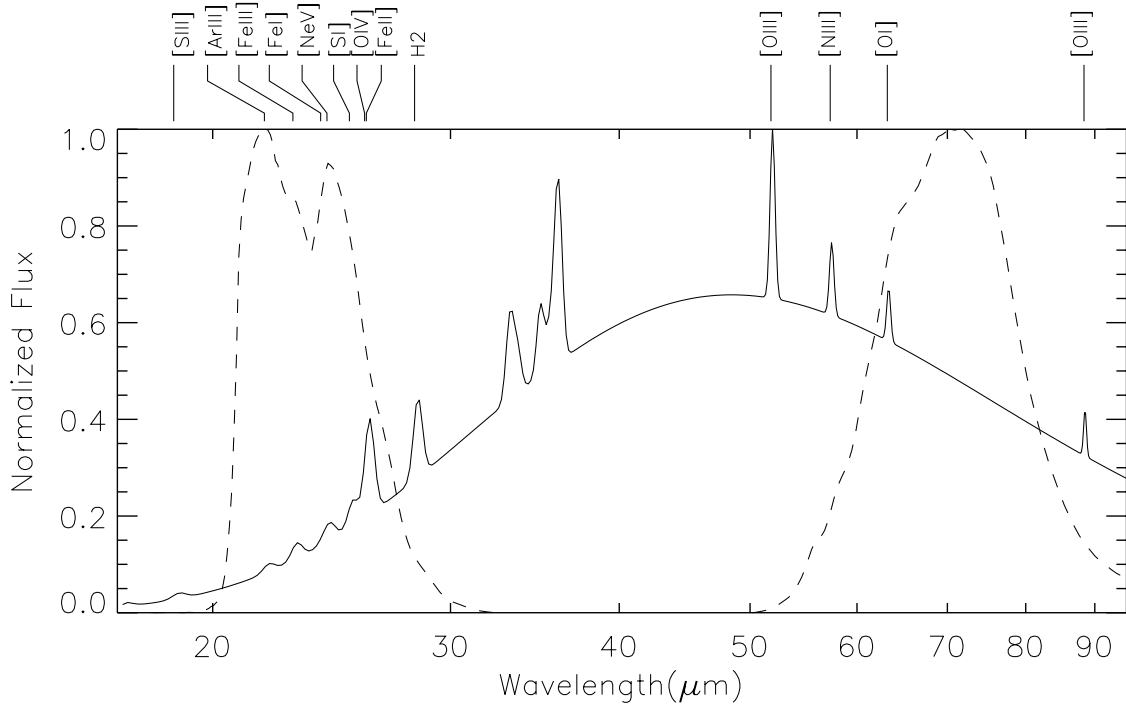
Figure 5.1: A sketch of a dusty SNR spectrum made with a blackbody at 60 K and superimposed the most important fine structure and ionic emission lines (mimicking ISO Short and Long wavelength spectrometer observations of SNR RCW103). Emission lines within the wavelength range of the MIPS filters are annotated. Overplotted (dashed lines) are the normalized response functions of the MIPS filters at 24 and 70 μm. This shows that the contribution of line emission to the MIPS filters is relatively small when a dust continuum is present.

determined by the MIPS team in their calibration at 24 and 70 μm (Engelbracht *et al.* 2007; Gordon *et al.* 2007). The adopted uncertainty in calibration for MIPS 24 μm is 10% . For the 70 μm fluxes, the main errors come from uncertainties in the background estimation and calibration errors (we adopt a conservative value of 20%). Moreover, we have used the 24 μm point source subtracted data. For details in the point source removal procedure see Shenoy et al. (*in preparation)*. Point source sensitivities are 2 and 75 mJy (3σ) at 24 and 70 μm, respectively. The resolution of the 24 μm data is 6″ while for 70 μm it is 18″.

GLIMPSE

At IRAC bands (see Figure 1 in Reach *et al.* 2006) one expects to find a wealth of atomic lines, including Brα (4.05 μm), Pfβ (4.65 μm), [Fe II] (5.34 μm), and [Ar II] (8.99 μm), among others, plus the molecular S(13) through S(4) H_2 rotational lines, and CO transitions at 4-5 μm. This is very much the case in IC 443 (Neufeld & Yuan 2008; Cesarsky *et al.* 1999). We use primarily the 8 μm images from IRAC. Occasionally, other channels can also be used in order to constrain the possible emission mechanisms. The 4.5 μm channel provides a valuable diagnostic of shocked molecular gas (e.g., Reach *et al.* 2006). At 8 μm, our measured flux represents an upper limit since stellar contamination is present. We adopt a conservative value of 10% for the calibration error given the vagaries in color correction plus measurement errors. The IRAC sampling is 1.2″ but the 8 μm resolution is about 2″.

5.2.2   Ancillary data

Most of the supernova remnants in Green's catalog (Green, 2009) were discovered using radio observations. By comparing the emission in at least two different radio wavelengths, one can calculate the spectral index and thus distinguish the kind of emission produced (thermal or non-thermal). In the case of SNRs, we expect to find a spectral index which is characteristic of synchrotron radiation. In contrast, H II regions show a flat spectrum (when optically thin) which is indicative of free-free emission. The SNR radio emission is associated with regions where shock-induced particle acceleration take place within the source.

In addition to data in Green's catalog, the following radio data sets are used for comparison with the infrared images: VLA (Very Large Array) archival data at 20 and 90 cm, available from the Multi-Array Galactic Plane Imaging Survey (MAGPIS; Helfand *et al.* 2006) website[1], VGPS (VLA Galactic Plane Survey; Stil *et al.* 2006)[2] at 21 cm and MOST (Mongolo Observatory Synthesis Telescope; Whiteoak & Green 1996)[3] at about 36 cm.

---

[1]http://third.ucllnl.org/gps/index.html
[2]http://www.ras.ucalgary.ca/VGPS/VGPS-data.html
[3]http://www.physics.usyd.edu.au/sifa/Main/MSC

Wide band (300-10000 eV) X-ray images from the *Chandra* Supernova Remnant Catalog[4] archive are also used for comparison. X-ray emission locates the shock heated plasma, including the important reverse shock in the interior region.

5.3   Detection of SNRs

To describe the amount of (or lack of) infrared emission from SNRs in our sample, we use a similar classification scheme to the one adopted by Reach *et al.* (2006). Detection levels are characterized as follows: (1) detected, (2) possible detection, (3) unlikely detection and (4) not detected (see Table 5.1). Level 1 detections have a good positional match between the infrared contours and those at other energies (radio or X-ray). Level 2 detections display infrared emission within the remnant region but confused with cirrus or nearby H II regions. Level 3 detections show the presence of some infrared emission which does not seem to be correlated with the remnant, although source confusion prevents a clear assessment of the emission origin. Level 4 is characterized by the absence of infrared emission within or nearby the contours of the radio remnant.

Out of a sample of 121 possible radio remnants, 39 are level 1 detections, a detection rate of 32% compared to 18% with GLIMPSE. A few examples of level 1 detections are shown in Figure 5.2. The MIPSGAL sensitivity at 24 μm matches very well that of IRAC at 8 μm (see Carey *et al.* 2009 and Benjamin *et al.* 2003). The fact that we can identify many more SNRs than with IRAC could potentially be due to an extinction effect (lower at 24 μm than at 8 μm by 40%, Draine 2003). However, it is far more plausible that it could simply be the details of how SNRs emit. In the case of SNRs interacting with the ISM where shocks modify the dust grain size distribution (e.g., Guillard *et al.* 2010), 24 μm continuum emission (due to Very Small Grains, VSGs) rises while at 8 μm the emission by stochastically heated PAHs is not as strong.

We calculate flux densities at 8, 24, and 70 μm for SNRs which show obvious infrared counterparts (level 1 detections). The aperture size used for the flux derivations is, in some cases, different from the one listed at radio wavelengths (see Table 5.2). This is done in order to account for the different morphologies a remnant can have in various wavelength ranges. Furthermore, there are cases where the SNR is nearby other unrelated extended Galactic sources whose contamination can lead to an overestimate of the infrared flux (e.g., diffuse Galactic emission and H II regions). To avoid such problems, we examined the MIPS images overlaid with contours from other wavelengths to help constrain the location and shape of the SNR infrared emission; however, such discrimination is not always well achieved. Another issue that arises, especially when dealing with Galactic plane images such as these, is the presence of unrelated infrared emission along the line of sight. This confusion can hinder the detection of SNRs as demonstrated by Arendt (1989) and Saken *et al.* (1992).

---

[4]http://hea-www.harvard.edu/ChandraSNR/index.html

Table 5.1. Infrared detection classification levels of SNRs from Green's catalog

l+b	Name	Size[a]	IA[b]	IS[c]	GR[d]	M[e]	l+b	Name	Size	IA	IS	GR	M
10.5-0.0		6	-	-	-	1	54.4-0.3	HC40	40	3	4	1	1
11.0-0.0		9 × 11	-	-	-	3	55.0+0.3		17	-	-	2	2
11.1-0.7		11 × 7	-	-	-	3	57.2+0.8	4C21.53	12?	4	4	4	3
11.1+0.1		12 × 10	-	-	-	1	59.5+0.1		15	-	-	3	3
11.2-0.3		4	1	2	1	1	296.1-0.5		37 × 25	2	4	3	3
11.4-0.1		8	4	4	3	3	296.8-0.3		20 × 14	4	4	3	1
11.8-0.2		4	-	-	-	2	298.5-0.3		5?	4	4	2	2
12.0-0.1		7	1	1	3	3	298.6-0.0		12 × 9	3	4	2	2
12.2+0.3		5 × 6	-	-	-	3	299.6-0.5		13	-	-	3	4
12.5+0.2		5 × 6	-	-	-	1	302.3+0.7		17	3	4	3	2
12.7-0.0		6	-	-	-	3	304.6+0.1	Kes 17	8	1	1	1	1
12.8-0.0		3	-	-	-	3	308.1-0.7		13	-	-	4	3
13.5+0.2		5	-	-	3	3	308.8-0.1		30 × 20?	-	4	2	2
14.1+0.1		6 × 5	-	-	-	1	309.2-0.6		15 × 12	4	4	3	3
14.3+0.1		5 × 4	-	-	-	1	309.8+0.0		25 × 19	4	4	3	3
15.4+0.1		14 × 15	-	-	-	3	310.6-0.3	Kes 20B	8	-	-	2	3
15.9+0.2		6	4	4	3	1	310.8-0.4	Kes 20A	12	-	-	1	1
16.0-0.5		15 × 10	-	-	-	3	311.5-0.3		5	4	4	1	1
16.4-0.5		13	-	-	-	1	312.4-0.4		38	2	4	3	3
16.7+0.1		4	-	4	3	2	315.4-0.3		24 × 13	2	2	2	2
17.0-0.0		5	-	-	-	2	315.9-0.0		25 × 14	-	-	3	3
17.4-0.1		6	-	-	-	3	316.3-0.0	MSH 14-57	29 × 14	3	4	3	3
18.1-0.1		8	-	-	-	4	317.3-0.2		11	-	-	3	2
18.6-0.2		6	-	-	-	1	318.2+0.1		40 × 35	-	-	3	2
18.8+0.3	Kes 67	14	2	4	3	3	318.9+0.4		30 × 14	-	-	3	2
19.1+0.2		27	-	-	-	3	321.9-0.3		31 × 23	4	3	3	3
20.0-0.2		10	4	4	3	3	322.5-0.1		15	-	-	3	3
20.4+0.1		8	-	-	-	1	323.5+0.1		13	2	1	2	2
21.0-0.4		9 × 7	-	-	-	3	327.2-0.1		5	-	-	-	3
21.5-0.9		4	4	4	3	1	327.4+0.4	Kes 27	21	3	4	2	2
21.5-0.1		5	-	-	-	1	328.4+0.2	MSH15-57	5	4	4	4	3
21.8-0.6	Kes 69	20	3	4	1	1	329.7+0.4		40 × 33	-	-	2	2
22.7-0.2		26	3	4	1	2	332.0+0.2		12	3	4	4	3
23.3-0.3	W41	27	3	4	2	2	332.4-0.4	RCW 103	10	4	4	1	1
23.6+0.3		10	1	2	3	1	332.4+0.1	Kes32	15	2	3	2	2
24.7-0.6		15	4	4	4	4	335.2+0.1		21	4	4	2	2
24.7+0.6		21	4	4	3	2	336.7+0.5		14 × 10	4	4	4	1
27.4+0.0	Kes 73	4	3	1	3	1	337.0-0.1	CTB 33	1.5	4	4	3	3
27.8+0.6		50 × 30	4	4	3	3	337.2-0.7		6	4	4	4	1
28.6-0.1		13 × 9	-	-	3	1	337.2+0.1		3 × 2	-	-	-	3
29.6+0.1		5	-	-	4	3	337.8-0.1	Kes 41	9 × 6	4	4	2	2
29.7-0.3	Kes 75	3	4	4	3	1	338.1+0.4		15?	3	4	4	3
31.5-0.6		18	-	-	3	2	338.3-0.0		8	4	4	3	3
31.9+0.0	3C 391	6	1	1	1	1	338.5+0.1		9	3	4	3	3
32.1-0.9		40	-	-	3	3	340.4+0.4		10 × 7	4	4	4	3
32.4+0.1		6	-	-	-	2	340.6+0.3		6	1	1	2	1
32.8-0.1	Kes 78	17	3	1	3	3	341.2+0.9		16 × 22	-	-	4	3
33.2-0.6		18	2	1	3	2	341.9-0.3		7	3	4	4	3
33.6+0.1	Kes 79	10	2	2	2	1	342.0-0.2		12 × 9	2	4	3	3
34.7-0.4	W44	31	1	4	1	1	342.1+0.9		10 × 9	-	-	4	3
35.6-0.4		15 × 11	-	-	-	1	343.1-0.7		27 × 21	-	-	3	3
36.6-0.7		25?	-	1	2	3	344.7-0.1		10	3	4	1	1
39.2-0.3	3C 396	7	4	4	1	1	345.7-0.2		6	-	-	4	1
40.5-0.5		22	2	4	4	2	346.6-0.2		8	4	4	1	2
41.1-0.3	3C 397	4.5 × 2.5	3	4	1	1	347.3-0.5		65 × 55	-	-	3	3
42.8+0.6		24	-	4	4	4	348.5-0.0		10	-	-	1	1
43.3-0.2	W49B	4 × 3	1	1	1	1	348.5+0.1	CTB 37A	15	2	4	1	1
45.7-0.4		22	-	4	2	2	348.7+0.3	CTB 37B	17?	1	3	3	1
46.8-0.3	HC30	17 × 13	3	1	3	3	349.2-0.1		9 × 6	-	-	3	3
49.2-0.7	W51C	30	4	1	3	3	349.7+0.2		2.5 × 2	1	1	1	1
54.1+0.3		1.5	1	1	3	3							

[a]The radio sizes are given in arcminutes and were taken from Green's catalog. When two dimensions are reported they refer to the major and minor axis of the ellipse.

[b]IRAS survey: Arendt (1989). Similar classification scheme as the one employed for this work

[c]IRAS survey: Saken *et al.* (1992) Detection levels 1 to 4 explained in the text. For the Saken *et al.* (1992) survey, detection classification is as follows: Y (detected), N (not detected), P (possible detections) and ? (not conclusive). We have translated these to the same classification used in this work for ready comparison (Y:1, P:2, ?:3, N:4).

[d]GLIMPSE survey: Reach *et al.* (2006). Similar classification scheme as the one employed for this work

[e]MIPSGAL survey: this paper
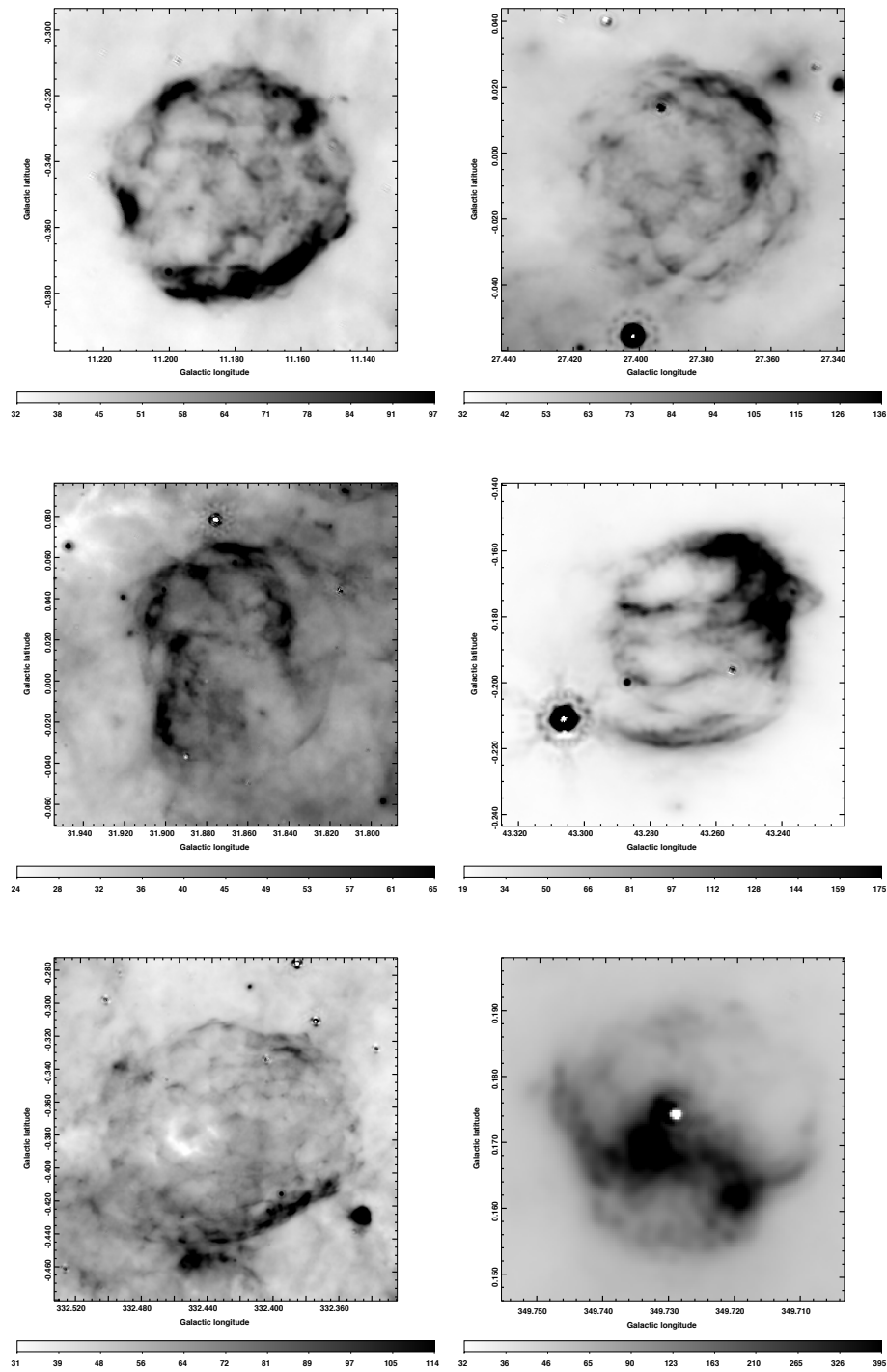
Figure 5.2: Examples of level 1 detections at 24 μm. From left to right, top to bottom: G11.2-0.3, G27.4+0.0 (Kes 73), G31.9+0.0 (3C 391), G43.3-0.2 (W49B), G332.4-0.4 (RCW 103) and G349.7-0.2. The greyscale is linear with the ranges in MJy/sr as displayed in the intensity bars below each image. The angular extents of the images differ.

Table 5.2. Characteristics of detected SNRs in the MIPSGAL survey[a]

l+b	Name[b]	S_{rad}(′)	S_{phot}(′)	F_8(Jy)	F_{24}(Jy)	F_{70}(Jy)	8/24	8/70	24/70	Region[c]
10.5-0.0	10.5	6	4.8	14 ± 2	19 ± 2	227 ± 47	0.75	0.06	0.08	whole
11.1+0.1	11.1	12×10	5.4×3.7	12 ± 2	16 ± 2	297 ± 60	0.71	0.04	0.06	central region
11.2-0.3	11.2	4	4.8	4.6 ± 1.1	40 ± 5	101 ± 23	0.12	0.05	0.40	whole
12.5+0.2	12.5	6×5	1.5	0.9 ± 0.2	1.5 ± 0.2	7.4 ± 1.7	0.64	0.13	0.20	northeastern region
14.1-0.1	14.1	6×5	1	0.9 ± 0.1	10 ± 1	19 ± 4	0.09	0.54	0.05	northwestern region
14.3+0.1	14.3	5×4	4	7.9 ± 1.1	30 ± 4	171 ± 36	0.26	0.05	0.18	whole
15.9+0.2	15.9	7×5	6.5	3.2 ± 2.5	16 ± 2	55 ± 16	0.20	0.06	0.30	whole
16.4-0.5	16.4	13	6.5×4.2	40 ± 5	93 ± 10	950 ± 192	0.43	0.04	0.10	northern arc
18.6-0.2	18.6	6	7	26 ± 4	58 ± 6	554 ± 115	0.44	0.05	0.10	whole
20.4+0.1	20.4	8	8.2	43 ± 5	79 ± 9	1160 ± 230	0.55	0.04	0.07	whole
21.5-0.1	21.5-0.1	5	5.2	12 ± 3	39 ± 4	341 ± 69	0.31	0.04	0.11	whole
21.5-0.9	21.5-0.9	4	1.6	0.4 ± 0.1	0.6 ± 0.1	3.5 ± 0.8	0.63	0.11	0.18	central region
21.8-0.6	Kes69C	20	8.9×6.8	38 ± 6	23 ± 3	458 ± 93	1.6	0.08	0.05	central region
23.6+0.3	23.6	10	15.6×6.2	173 ± 18	355 ± 36	5440 ± 1090	0.49	0.03	0.07	whole
27.4+0.0	Kes 73	4	4.8	3.0 ± 1.2	37 ± 4	87 ± 18	0.08	0.04	0.42	whole
28.6-0.1	28.6A		3.6	7.2 ± 1.0	12 ± 2	294 ± 65	0.62	0.03	0.04	nothwestern arc
	28.6B		2.8	<2.0	3.8 ± 0.5	<35	<0.53	-	$0.11>$	southern filaments
	28.6C		4.1	<1.9	5.7 ± 0.8	<23	<0.32	-	$0.25>$	eastern filament
29.7-0.3	Kes75S	3	2.7×1.4	0.7 ± 0.2	4.8 ± 0.5	<29	0.15	$0.17>$	$0.03>$	southern shell
	Kes75W		0.7×2.2	0.6 ± 0.1	2.9 ± 0.3	5.3 ± 1.1	0.22	0.55	0.12	western shell
	Kes75			1.3 ± 0.3	7.8 ± 0.8	<34	0.17	$0.23>$	$0.04>$	whole (both shells)
31.9+0.0	3C 391	7×5	6.2	10 ± 3	39 ± 4	395 ± 81	0.27	0.03	0.10	whole
	3C391BML		0.8	0.6 ± 0.1	0.9 ± 0.1	13 ± 3	0.74	0.05	0.06	BML
	3C391NWBar		1.4×0.5	0.2 ± 0.1	0.8 ± 0.1	3.9 ± 1.0	0.25	0.05	0.22	northwestern bar
33.6+0.1	Kes 79	10	8.4	18 ± 6	45 ± 5	577 ± 116	0.40	0.03	0.08	whole
	Kes79sf		3.3×0.8	<0.4	1.2 ± 0.2	<10	<0.36	-	$0.11>$	southern filaments
34.7-0.4	W44	35×27	38×28	384 ± 44	348 ± 39	6330 ± 1300	1.10	0.06	0.06	whole
35.6-0.4	35.6	15×11	11	44 ± 8	36 ± 5	487 ± 99	1.21	0.09	0.07	whole
39.2-0.3	3C 396	8×6	7×5	1.7 ± 0.8	8.5 ± 1.0	34 ± 11	0.20	0.05	0.25	whole
	3C396SE		2.7	3.5 ± 2.3	5.3 ± 0.6	158 ± 32	0.66	0.02	0.03	southeastern plume
	3C396NW		2.8×4.9	0.7 ± 0.2	4.9 ± 0.6	<22	0.14	$0.02>$	$0.14>$	northwestern arc
41.1-0.3	3C 397	4.5×2.5	5×3.6	4.3 ± 0.8	17 ± 2	34 ± 14	0.25	0.13	0.50	whole
	3C397SE		0.6	< 0.1	0.6 ± 0.1	0.6 ± 0.1	< 0.18	< 0.17	0.95	ionic shock region
43.3-0.2	W49B	4×3	5	5.7 ± 0.7	77 ± 8	529 ± 107	0.07	0.01	0.15	whole
	W49BMol		1.2×0.5	0.3 ± 0.1	0.6 ± 0.1	6.7 ± 1.4	0.52	0.04	0.08	molecular shock region
	W49BIon		1.3×0.6	0.2 ± 0.1	3.1 ± 0.3	4.3 ± 0.9	0.09	0.03	0.28	ionic shock region
54.4-0.3	HC40NE	40	5.6	5.9 ± 0.7	2.9 ± 0.4	38 ± 8	2.04	0.16	0.08	northeastern region
	HC40TR	40	9.3×4.2	3.8 ± 0.5	8.0 ± 0.9	131 ± 27	0.47	0.03	0.06	north top region
296.8-0.3	296	20×14	3.5×7.9	<0.6	1.5 ± 0.2	<11	<0.39	-	$0.14>$	western arc
304.6+0.1	Kes 17	8	4.7×3.8	17 ± 2	17 ± 2	149 ± 31	1.02	0.12	0.11	whole
310.8-0.4	Kes20Ana	12	1.1	0.3 ± 0.1	1.4 ± 0.2	20 ± 4	0.21	0.02	0.07	northern arc
	Kes20Ase	12	1.2	0.8 ± 0.1	0.8 ± 0.1	<17	1.1	$0.05>$	$0.04>$	southeastern ridge
311.5-0.3	311	5	4	2.1 ± 0.4	3.5 ± 0.5	58 ± 14	0.60	0.04	0.06	whole
332.4-0.4	RCW 103	10	10×8.7	51 ± 6	101 ± 11	648 ± 134	0.50	0.08	0.16	whole
	RCW103M		3.8×0.8	0.9 ± 0.3	5.9 ± 0.6	10 ± 3	0.16	0.09	0.58	molecular region
336.7+0.5	336	14×10	2.3	0.6 ± 0.2	2.4 ± 0.3	6.3 ± 2.5	0.25	0.09	0.38	bow
337.2-0.7	337	6	5	2.4 ± 0.6	6.3 ± 0.8	13 ± 5	0.38	0.18	0.48	whole
340.6+0.3	340	6	5.4	14 ± 2	19 ± 2	193 ± 40	0.75	0.07	0.10	whole
344.7-0.1	344	10	9	4.8 ± 1.9	24 ± 3	117 ± 28	0.20	0.04	0.21	whole
345.7-0.2	345	6	1.8	<0.4	1.7 ± 0.2	4.8 ± 1.0	<0.13	0.05	0.36	southern arc
348.5-0.0	348	10	1.4×3.6	1.3 ± 0.2	2.0 ± 0.3	13 ± 3	0.66	0.10	0.15	central blob
348.5+0.1	CTB37A	15	7.8	27 ± 6	27 ± 4	336 ± 86	0.89	0.08	0.09	eastern shell
348.7+0.3	CTB37B	17	8.2×3.8	18 ± 3	32 ± 4	401 ± 82	0.58	0.05	0.08	interface
349.7+0.2	349	2.5×2	2.1	4.1 ± 0.6	32 ± 4	240 ± 49	0.13	0.02	0.13	whole

[a]The color ratios are obtained using the flux density value for the partial or whole region depending on the infrared morphology. The radio sizes (S_{rad}) are given in arc-minutes and were taken from Green's catalog. The photometry size (S_{phot}) refers to the size used for obtaining the infrared fluxes. The integrated fluxes have not been color corrected since the mechanism for the infrared emission is uncertain. Also, no extinction correction has been applied. Furthermore, the 8 μm fluxes were multiplied by the extended source aperture correction factor as described in. The tabulated errors are the combination of the 1σ errors plus the systematic calibration errors associated to each wavelength. Upper flux limits are given for remnants where point source contamination or apparent lack of emission (3σ detection) is present.

[b]Name or designation used to identify remnants.

[c]Locations and areas used for photometry of subregions of remnants as identified in the figures in the appendix.

Flux densities of the detected remnants were obtained using either a circular or elliptical aperture with a background removed. The background was determined using the median value of the sky brightness around the remnant via two methods. We used an annulus around the source for cases where the external source contamination in the neighborhood is negligible. However, that method was often not feasible due to considerable overlap of sources (extended or point-like) with the periphery of the SNR. For those cases, the sky brightness was estimated with a user-selected region characteristic of the local background emission. In order to quantify the magnitude of background variations, we measured the surface brightness on several regions around one of the faintest $24\mu m$ SNR, G21.8-0.6. We used aperture sizes similar to the one used for the remnant and found that the standard deviation relative to the mean background value across the field, for our three wavelengths are of the order of 12% (8 μm), 10% (24 μm) and 20% (70 μm).

Another consideration for photometry measurements is point source contamination, especially at 8 μm (as discussed in § 5.2.1). Finally, since we are dealing with spatially extended emission, we applied corrections to the 8 μm estimates to account for internal scattering in the detectors as instructed by the IRAC data handbook[5]. The 'infinite' radius aperture is most appropriate for the angular extent of the remnants; we multiplied the surface brightness measurements by 0.74.

5.4   Discussion

5.4.1   Comparison of detections with previous IR surveys

Out of the previous 18 detections (level 1) using GLIMPSE (Reach *et al.* 2006), we confirm 16 at the same level with MIPSGAL (Table 1). The remaining two remnants are confused with the background and are reported as possible detections in our analysis. Of the other 23 (level 1) infrared counterparts found in this work, 10 are not in the initial sample from Green's catalog used by Reach *et al.* (2006) and the remaining 13 are mostly bright X-ray remnants which seem to be brighter at 24 μm. Regarding the SNRs identified by Arendt (1989), all of their level 1 detections are also seen in MIPSGAL with the exception of G12.0-0.1 and G54.1+0.3 which are both level 3 in the MIPS data. Comparing with Saken *et al.* (1992), six SNRs have been detected in common (level 1). They also reported a level 1 detection of 8 others, which we classify as level 2 or 3. Again, we observe that these cases are mostly regions where there is a large contamination by nearby or overlapping H II regions making a clear identification challenging even at the superior Spitzer resolution.

---

[5]http://ssc.spitzer.caltech.edu/irac/iracinstrumenthandbook/IRAC-Instrument-Handbook.pdf

5.4.2 Lack of IR signature

Given the strong ambient emission in the inner Galactic plane, it is not surprising that many SNRs, either too big or too old, and having low infrared surface brightness, do not have an identifiable infrared signature. Also, as noted by Williams *et al.* (2006), the environs in which SNRs are encountered need to be sufficiently dense to promote collisional heating of the dust, thus making it distinguishable. Examples of non-detections in this survey are G18.1-0.1 and G299.6-0.5.
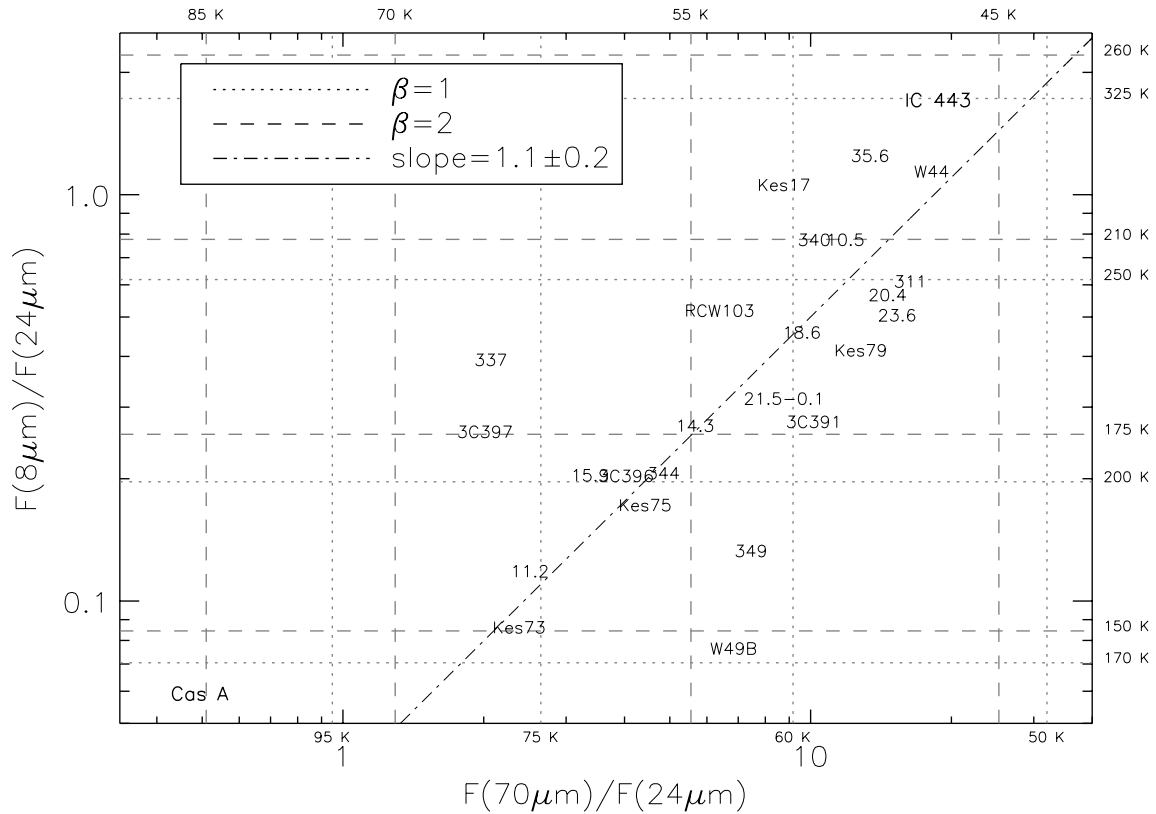
5.4.3 Color-color diagrams

Table 5.2 shows flux densities (at 8, 24 and 70 μm) and color ratios for the detected remnants. Figure 5.3 contains a logarithmic plot of $[F_8/F_{24}]$ *versus* $[F_{70}/F_{24}]$ for which SNRs are detected as a whole (see last column of Table 5.2). Two other SNRs are plotted: for Cas A, values are retrieved from Hines *et al.* (2004) and for IC443 from Noriega-Crespo et al. *(in preparation)*. The data show a linear trend with a slope of 1.1 ± 0.2: remnants with a low $[F_8/F_{24}]$ ratio statistically have a low $[F_{70}/F_{24}]$ ratio. Furthermore, there seems to exist an age effect, with older remnants (such as IC443 and W44) showing higher $[F_{70}/F_{24}]$ and $[F_8/F_{24}]$. The opposite seems to be more characteristic of younger remnants, such as Cas A, Kes 73 and G11.2-0.3.

In some remnants, infrared emission is only detected in certain parts inside the radio/X-ray contours. Figure 5.4 shows surface brightness ratios of these localized regions. To assess the mechanism of the infrared emission, we also calculate surface brightnesses for regions of SNRs known to be either interacting with neighboring molecular regions (such as the BML region in 3C391) and/or that show molecular emission lines (such as W49B) or known to have ionic lines (such as 3C396). For this exercise, we used regions of some remnants for which the main emission mechanism had previously been identified by Reach *et al.* (2006) (see their Figure 22). These are also identified in the SNR figures in the appendix. Remnants with colors characteristic of ionic shocks seem to occupy the lower left part of the $[I_{70}/I_{24}]$ versus $[I_8/I_{24}]$ diagram, while remnants whose colors are consistent with molecular shocks and photodissociation regions are found in the upper right part. However, given the small number of examples and the fact that all three passbands (8, 24 and 70 μm) contain dust emission and lines, we suggest that the $[I_{70}/I_{24}]$ and $[I_8/I_{24}]$ color ratios are not a completely secure method of distinguishing between different emission mechanisms.

We plot some other color ratios for comparison. The locus for pure synchrotron is for spectral index of 0.3 to 1 [1]. For the diffuse ISM, we used the color ratios obtained by Compiègne *et al.* (2010) for two regions (with different abundances of very small grains) in the Galactic plane at a longitude of approximately $59°$. We have also included color ratios for evolved

---

[1] α is the spectral index and the radio flux density is defined as $S_\nu \propto \nu^{-\alpha}$, where ν is the frequency.

Figure 5.3: Color-color plot of the SNRs in our sample detected and measured as a whole. For comparison, we have also plotted the location of Cas A and IC443 in this diagram. We find that this sample is well fitted by a slope of 1.1 ± 0.2 in this logarithmic representation, showing that 8 and 70 μm emission are related roughly by a constant while they change dramatically with respect to 24 μm. Vertical lines show the range of expected temperatures for a modified blackbody using only the flux measured at 24 and 70 μm while for the horizontal lines, the temperatures are calculated using the flux at 8 and 24 μm. Dotted and dashed lines correspond to a β of 1 or 2, respectively. If the IR emission at longer wavelengths is mainly due to dust then the range of temperatures for our sample of SNRs is roughly between 50 and 85 K for β=1 and between 45 and 70 K for β=2.
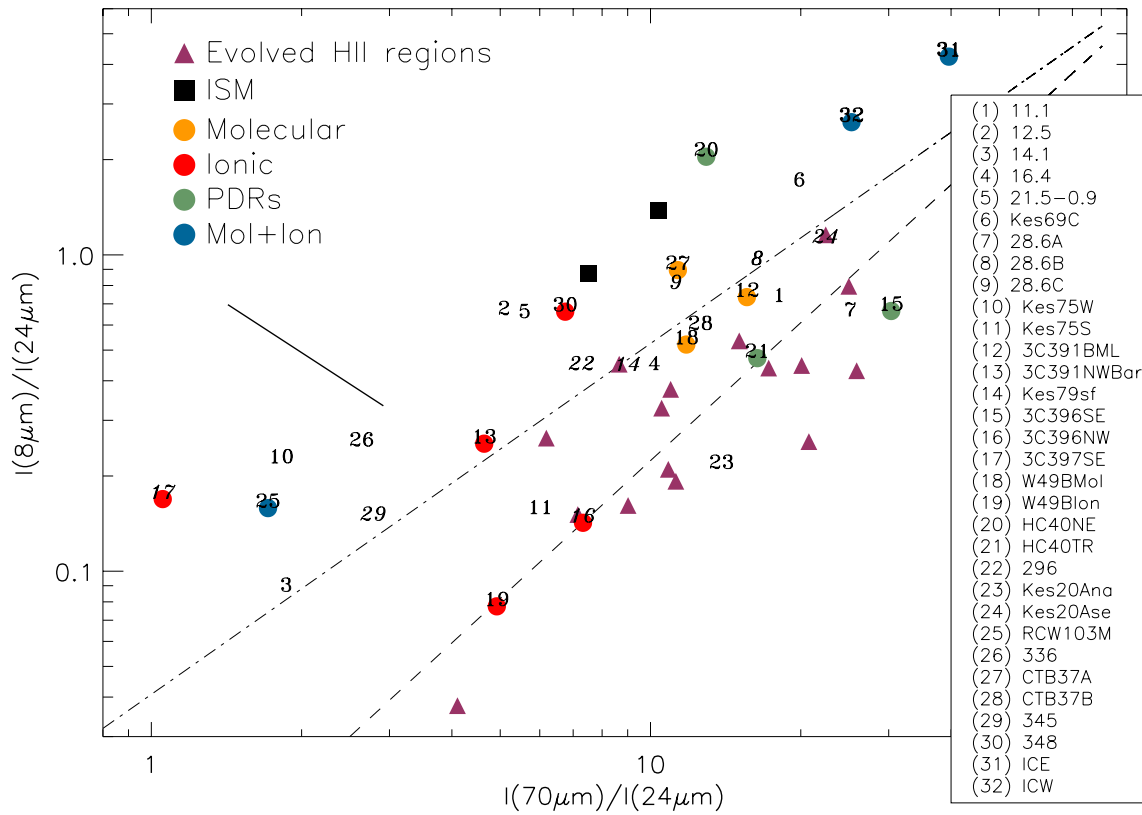
Figure 5.4: Color-color plot based on surface brightnesses of localized regions in SNRs in our sample. Ratios for SNRs known to have molecular interactions, atomic fine-structure line emission or PDRs colors are also shown. ICE and ICW refer to IC443, eastern (strong [O I] emission at 63 μm) and western (interacting with a nearby H II region) regions, respectively. Colors of pure infrared synchrotron emission are plotted as a straight line. Color ratios for the diffuse ISM (Compiègne *et al.*, 2010) and evolved H II regions (Paladini et al. *(in preparation)*) are also included. Remnants with upper flux limits are represented in italic. For comparison, we plot the slope (dotted-dashed line) of 1.1 ± 0.2 found for the sample of detected remnants and measured as a whole (see Figure 5.3). Also depicted is a dashed line showing a different trend for evolved HII regions.

H II regions (found near Galactic longitudes of 35°; Paladini *et al.* 2012). Are the color ratios $[F_{70}/F_{24}]$ and $[F_8/F_{24}]$ good discriminators between such very different regions? Based on Figure 5.4, the plotted colors of individual evolved H II regions often seem indistinguishable from SNRs using Spitzer colors. However, the overall trend for SNRs is displaced from the H II regions and covers a broader range of colors. This is similar to what Arendt (1989) found for older SNRs and compact H II regions using IRAS colors.

Although line contamination is significant for radiative remnants, for younger ones the majority of the IR emission should be due to dust grains. For instance, for RCW 103 (age approximately 2000 yr; Carter *et al.* 1997) we calculate the ratio of line emission (using ISO data) versus dust continuum within MIPS filters. We find that line emission contributes about 6% and 3% of the observed flux at 24 and 70 μm, respectively. If emission from the remnants comes primarily from shocked hot dust, then we can derive the dust temperature just by assuming a simple modified blackbody emission. If dust has a thermal spectral energy distribution

$$S_\nu \propto B_\nu(T)\, \nu^\beta \,, \tag{5.1}$$

where β is the dust emissivity index (which depends on the dust composition, $\beta \sim 1$ to 2), then flux ratios imply certain temperatures. Figure 5.3 shows temperatures based on the $[F_8/F_{24}]$ and $[F_{24}/F_{70}]$ ratios. The latter flux ratio yields dust temperatures for our SNR sample ranging between 45 and 70 K for $\beta = 2$ and from 50 to 85 K for $\beta = 1$. This is a very crude estimate of the dust temperature given that we are just considering one population of dust grains in temperature equilibrium when it is far more likely that there are several populations plus non-equilibrium emission. Applying the same simple dust model to the $[F_8/F_{24}]$ ratio, we obtain temperature values higher than 145 K (for $\beta = 2$) with younger SNRs having color temperatures lower that older remnants. This trend is similar to what was obtained by Arendt (1989) using color temperatures based on the IRAS 12 to 25 μm ratio. The infrared colors are not well explained by a single equilibrium dust temperature and atomic and molecular line emission might significantly contribute to the infrared emission for SNRs.

However, assuming that the infrared emission at 24 and 70 μm is cospatial, entirely due to dust, and well fitted by a single temperature modified blackbody, then SNR dust masses are given by the following equation:

$$M_{\text{dust}} = \frac{d^2 F_\nu}{\kappa_\nu B_\nu(T_{\text{dust}})} \,, \tag{5.2}$$

where d is the distance to each SNRs, F_ν is the flux density and κ_ν is the dust mass absorption coefficient. For the dust mass absorption coefficient, we use the diffuse ISM model by Li & Draine (2001) which consists of a mixture of amorphous silicate and carbonaceous grains. Distances are retrieved from Green's catalog. Results are reported in Table 5.3. Note that these derived dust masses, based on the 24 and 70 μm fluxes from MIPS, are overestimated given the

probable contamination of these fluxes by line emission which can be substantial in radiative remnants. On the other hand, these masses can be underestimated if there is a non-negligible contribution from stochastically-heated dust. Even in the case where all of the flux in these bands is due to dust, mass estimates are based on a single color temperature (24/70) which can be reasonable for younger remnants but not ideal for older remnants given that their IR SED generally requires more that one dust population (Arendt 1989 and Saken *et al.* 1992).

5.4.4   Infrared-to-Radio Ratio

According to Haslam & Osborne (1987), the comparison between mid-infrared (60 *μm* from IRAS) and radio continuum (11 cm) emission is a good diagnostic for distinguishing between thermal from non-thermal radio emitters (see also Fuerst *et al.* 1987 and Broadbent *et al.* 1989). H II regions are shown to have infrared to radio ratios of the order of $\geq$ 500 while ratios for SNRs are thought to be lower than 20. Moreover, Whiteoak & Green (1996) using MOST found that SNRs have a ratio of infrared (60 *μm*) to radio (843 MHz or 36 cm) of $\leq$ 50 while H II regions have again ratios of the order of 500 or more.

We use the 1 GHz flux densities provided in Green's catalog (Green, 2009). Those values were converted to 1.4 GHz (21 cm) flux densities using the spectral indices quoted in the same catalog. We compare those to the 24 and 70 *μm* emission from MIPSGAL. Figure 5.5 shows the spread in the ratio of the infrared to radio for the detected SNRs. Note that these ratios are often defined by $q_{IR^{\sim}} = \log(F_{IR^{\sim}}/F_{21cm})$ where $F_{IR^{\sim}}$ and F_{21cm} are the flux densities (in Jy) at specific mid-infrared wavelengths and in the radio.

There seems to be a group with ratios (or high q_{24} and q_{70}) similar to those of H II regions. In particular, we suggest that the morphology of the remnant G23.6+0.3 (and possibly G14.3+0.1) resembles more closely an H II region and so whether it is a SNR should be reconsidered. See also its infrared to radio ratios compared to H II regions (Figs. 5.3 and 5.4). Image in Figure 5.12 (and Figure 5.9) clearly shows a composite infrared emission, with the 24 *μm* (probing hot and small particles) matching the radio, while the 8 and 70 *μm* emission do not spatially coincide with the 24 *μm*. In particular, the 8 *μm* appears as an outer layer which marks the transition between the ionized region and colder gas. The 70 *μm* emission is also seen along the same location as the 8 *μm*, which is consistent with the premise that we are now probing a colder dust population.

There is a strong empirical correlation between infrared and radio emission (at 1.4 GHz) found in spiral galaxies Helou *et al.* (1985). The radio emission in this range is thought to be mainly due to synchrotron emission with only 10% attributed to thermal bremsstrahlung produced by H II regions (Murphy 2009 and references therein). In our Galaxy and other local star forming galaxies, the bulk of the mid and far-infrared arises from warm dust associated with star forming regions. In older systems, things are more complicated due to cold cirrus

Table 5.3. Color temperatures and dust masses based of the 24 and 70 μm fluxes for selected SNRs [a]

SNRs	$T_{24/70}$ [b]	Distance [c]	M_{dust} [d]
G11.2-0.3	63	4.4	0.034
G15.9+0.2	60	8.5	0.081
Kes 73	63	8.5	0.11
Kes 75	58	<7.5	<0.045
3C 391	51	8.5	1.1
Kes 79	50	7.8	1.5
W44	48	2.8	2.5
3C 396	58	7.7>	0.046>
3C 397	65	7.5>	0.029>
W49B	54	10	1.6
RCW 103	55	3.1	0.18
G337.2-0.7	65	2.0-9.3	<0.018
G349.7+0.2	54	14.8	1.6
CasA [e]	87	3.4	0.008
IC443 [e]	48	0.7-2	<0.27

[a] Color temperatures and dust masses are obtained using a dust emissivity index of $\beta = 2$.

[b] Approximate values for the dust temperature (K).

[c] Distances (kpc) taken from Green's catalog.

[d] Dust mass in solar masses ($M_\odot$).

[e] Cas A and IC443 are included for comparison. Estimates are based on the flux densities obtained by Hines *et al.* (2004) and Noriega-Crespo et al. (*in preparation*), respectively.
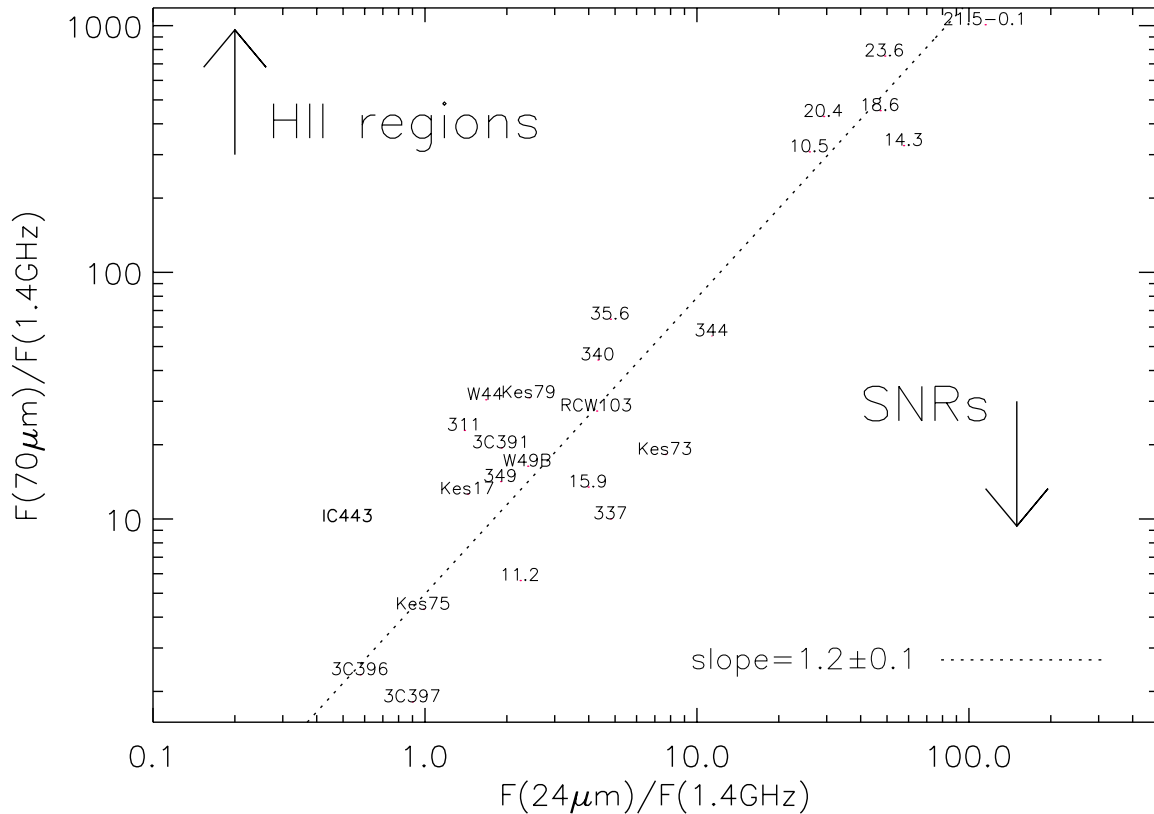
Figure 5.5: Ratio of MIPS 70 μm and radio continuum at 1.4 GHz ($q_{70} = \log(F_{70\text{-m}}/F_{1.4\text{GHz}})$) versus ratio between 24 μm and radio again (q_{24}). There is a considerable range in the positions of the SNRs. The ratios are correlated and are well fitted by a slope of 1.2. There seems to exist a group of catalogued sources which have ratios more characteristic of H II regions (upper population in the plot). The infrared counterparts in the lower part of the plot show ratios of infrared (70 μm) to radio comparable to what was found for SNRs in previous studies (e.g., Broadbent *et al.* 1989) which suggested ratios of infrared (60 μm) to 2.7 GHz lower than 20. The location of IC443 is also shown. Cas A falls off the plot and below the trend with ratios (0.1, 0.05).

and evolved stars (e.g., AGBs). We look for a similar correlation using the infrared and radio emission from our SNR sample. We estimate the mid-infrared emission as the sum of the integrated emission in each MIPS passband (24 and 70 μm) and obtain an integrated mid-infrared flux F_{MIR} in units of W/m^2 (see Helou *et al.* 1985). The F_{MIR} is an approximation (underestimate) of the mid-infrared bolometric flux (given that the bandpasses of 24 and 70 μm filters do not overlap). Figure 5.6 shows the correlation between infrared and 1.4 GHz non-thermal radio flux. The slope of the correlation is 1.10 ± 0.13 when combining all data (plus IC443). Again, two distinct populations seem to exist, an upper main trend and a lower one. Using only the lower one (i.e., objects which have 70 μm to 1.4 GHz ratios closer to H II regions and high values of q_{24} and q_{70} in Figure 5.5), we obtain a slope of 0.93 ± 0.13 while for the upper trend we get 0.96 ± 0.09.

The correlation with the slope fixed to unity leads to the dimensionless parameter q_{MIR} (Helou *et al.*, 1985) which represents the ratio of mid-infrared to radio and is defined as

$$q_{MIR} \equiv \log\left(\frac{F_{MIR}}{3.75 \times 10^{12}\,\mathrm{Wm}^{-2}}\right) - \log\left(\frac{F_{1.4\,\mathrm{GHz}}}{\mathrm{Wm}^{-2}\,\mathrm{Hz}^{-1}}\right). \tag{5.3}$$

Our results show that remnants from the lower trend population in Figure 5.6 have q_{MIR} larger than 2.06 (up to 2.60). The other group has q_{MIR} ranging from 0.06 and 1.41. Specific q values for each remnant are displayed on Table 5.4. For reference, a previous study by Bell (2003) reported a median value of q_{TIR} (i.e., the ratio of the total 8-1000 μm IR luminosity to the radio power) of 2.64 for a sample of 162 galaxies. But note this would be higher because it is based on the total IR emission.

Table 5.5 reports on the average and dispersion of the monochromatic q_8, q_{24} and q_{70} parameters for the two trends. For comparison, a study of extragalactic VLA radio sources by Appleton *et al.* (2004) obtained $q_{24} = 0.84$ and $q_{70} = 2.15$ while Boyle *et al.* (2007) found $q_{24} = 1.39$ for somewhat fainter galaxies. Later on, Seok *et al.* (2008) using AKARI data for some LMC SNRs compared the ratio of 24 μm to radio fluxes; their correlation implies $q_{24} = 0$. If SNRs are the sole contributors of synchrotron emission in a star-forming galaxy, then by comparison with the above q_{24}'s for galaxies they concluded that about 4 to 14% of the 24 μm emission in galaxies is due to SNRs. By doing a similar exercise using the upper trend remnants, for which $q_{24} = 0.39$ (see Table 5.5), we find that 10 to 35% of the 24 μm galactic emission seen would be due to the remnants. Likewise, at 70 μm that contribution would be 11%. The rest would be due to dust heated in H II and photo-dissociation regions, as well as diffuse emission.

5.4.5   High-energy emission from SNRs

In this section, we explore the relationship between the infrared and X-ray energetics of SNRs. Shocks produce hot plasma whose thermal energy is transferred to the dust grains via col-
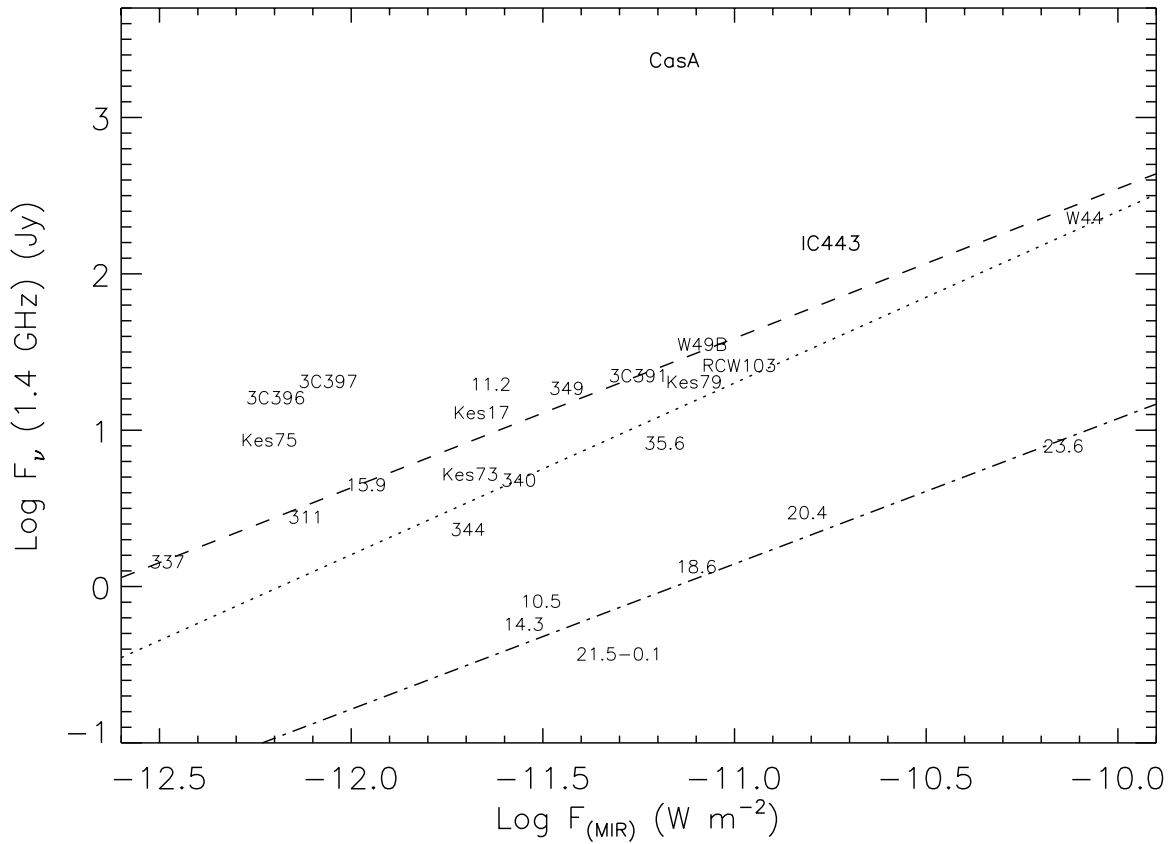
Figure 5.6: Correlation between radio and infrared emission. For the entire population, the slope of the correlation is 1.10 (dotted line). There seem to exist two trends. The upper population is more characteristic of SNRs while the lower population looks more like H II regions. The latter are the same objects with the high values of q_{24} and q_{70} in Figure 5.5. The slopes for the upper and lower populations are 0.96 (dashed line) and 0.93 (dot-dashed line), respectively, not significantly different. Again, IC443 and Cas A are also included for comparison. Cas A stands out due to its strong radio synchrotron emission.

Table 5.4. F_{MIR}-radio ratios for selected SNRs

Name	q_{MIR}	Name	q_{MIR}
G10.5-0.0	2.06	G35.6-0.4	1.37
G11.2-0.3	0.54	3C396	0.06
G14.3+0.1	2.16	3C397	0.10
G15.9+0.2	0.86	W49B	0.83
G18.6-0.2	2.24	Kes 17	0.69
G20.4+0.1	2.18	G311.5-0.3	0.91
G21.5-0.1	2.60	RCW103	1.07
G23.6+0.3	2.43	G337.2-0.7	0.83
Kes 73	1.06	G340.6+0.3	1.22
Kes 75	0.32	G344.7-0.1	1.41
3C391	0.87	G349.7+0.2	0.76
Kes 79	1.05	CasA [a]	-1.05
W44	1.02	IC443 [b]	0.53

[a] Values for infrared and radio emission from Cas A were taken from Hines *et al.* (2004).

[b] Values for infrared emission from IC 443 were taken from Noriega-Crespo et al. (*in preparation*).

Table 5.5. q_{IR} values for different wavelengths [a]

q_{IR}	All sample	Upper trend	Lower trend
q_{24}	0.71 ± 0.42	0.39 ± 0.11	1.68 ± 0.05
q_{70}	1.55 ± 0.60	1.17 ± 0.19	2.70 ± 0.04
q_{MIR}	1.19 ± 0.53	0.83 ± 0.15	2.28 ± 0.04

[a] q_{24} and q_{70} parameters are monochromatic. They are defined as $q_{IR} = \log(F_{IR}/F_{21cm})$ where F_{IR} and F_{21cm} are the flux densities (in Jy) at specific mid-infrared wavelengths and in the radio. q_{MIR} is a dimensionless parameter which represents the ratio of mid-infrared to radio (it is defined in Eq. 5.3). Individual q_{MIR} values for each remnant are presented in the Table 5.4.

lisions and then re-emitted in the infrared (Ostriker & Silk 1973; Draine 1981; Dwek 1987). Heating up the dust grains takes energy from the X-ray gas, thus cooling it and a good tool to measure this transfer of energy is the ratio of infrared to X-ray power, usually referred to as IRX (Dwek *et al.* 1987), which compares dust cooling (gas-grain collisions) with X-ray cooling (continuum and lines). The gas cooling function increases at lower plasma temperatures given that more lines become available due to recombination. On the other hand, at high temperatures of around 10^7 K, most of the energy is released through the bremsstrahlung continuum (Raymond *et al.* 1976). Assuming that line emission in the infrared is not energetically significant compared to the X-ray lines, then most of the line cooling must happen in the X-ray domain. This implies that if the observed powers in the infrared and X-ray are comparable then dust must be the essential contributor to the cooling in the infrared.

Table 5.6 shows the values of IRX for a sample of SNRs. The total X-ray fluxes (with energy range from 0.3 to 10 keV) were retrieved from the *Chandra* Supernova Remnant Catalog[4]. Infrared flux densities (in Jy) were measured for regions approximately matching those in the X-ray. We obtain the IR flux by integrating under the SED using simple linear interpolation in log space plus $\nu F \nu$ constant across the 24 μm passband. Also, note that the flux densities used in this analysis are not corrected for extinction. For our sample, IRXs range from about 1.6 for remnant RCW103 to 240 for W44.

These data are presented as SEDs in Figure 5.7, in the logarithmic form λF_λ vs. λ which is convenient for assessing the energetics. The radio values are obtained from Green's catalog (Green, 2009). We also include Cas A and IC443 for comparison. Their infrared flux densities are taken from Hines *et al.* (2004) and Noriega-Crespo et al. (*in preparation*) while the X-ray fluxes are from the Chandra Supernova Remnant Catalog and Dwek *et al.* (1987), respectively. In Figure 5.7, the remnants are sorted according to increasing approximate age (see Table 5.6). Although the ages for some remnants are uncertain, this Figure shows that hot dust grain cooling (24 μm) tends to be the most important contributor in early phases of the remnant, while in the later stage the warm dust traced by the 70 μm emission is the main contributor to plasma cooling. It also appears that older remnants tend to have greater IRXs. This can potentially be either due to an increase in the dust-to-gas ratio and/or a change in the size distribution favoring smaller sizes.

---

[4]http://hea-www.harvard.edu/ChandraSNR/index.html

Table 5.6. Infrared to X-ray ratios for selected SNRs

Name	Total MIR Flux (10^{-9} erg cm^{-2} s^{-1})	X-ray Flux$_{(0.3-10 \text{ KeV})}$ [a] (10^{-9} erg cm^{-2} s^{-1})	IRX	Age[b]
G11.2-0.3	11	4.0	2.8	1600 (1)
G15.9+0.2	5.3	0.96	5.6	500-2400 (2)
Kes73	9.9	1.8	5.6	500-1000 (3)
Kes75	2.7	0.21	13	884 $</>$ 2400 (4)
3C391	20	0.62	32	4000 (5)
Kes79	16	0.17	93	6000 (6)
W44[c]	2.0	0.093	240	20000 (7)
3C396	3.0	0.19	16	7100 (8)
3C397	8.1	1.3	6.2	5300 (9)
W49B	30	6.0	5.1	1000-4000 (10)
RCW103	27	17	1.6	2000 (11)
G337.2-0.7	1.6	0.93	1.7	750-3500 (12)
G349.7+0.2	14	0.33	42	2800 (13)

[a] X-ray fluxes were retrieved from the *Chandra* Supernova Remnant Catalog.

[b] Age is given in years and the values were taken from the following literature: (1) Clark & Stephenson (1977); (2) Reynolds *et al.* (2006); (3) Tian & Leahy (2008) ; (4) upper limit for the spin-down age of the associated pulsar Livingstone *et al.* (2006)/ based on ionization time-scales Morton *et al.* (2007); (5) Chen *et al.* (2004); (6) Sun *et al.* (2004) ; (7) Wolszczan *et al.* (1991); (8) Harrus & Slane (1999); (9) Safi-Harb *et al.* (2005); (10) e.g., Hwang *et al.* (2000); (11) Carter *et al.* (1997); (12) Rakowski *et al.* (2006) ; (13) Slane *et al.* (2002)

[c] Infrared and X-ray flux values are for a central rectangular region of W44.
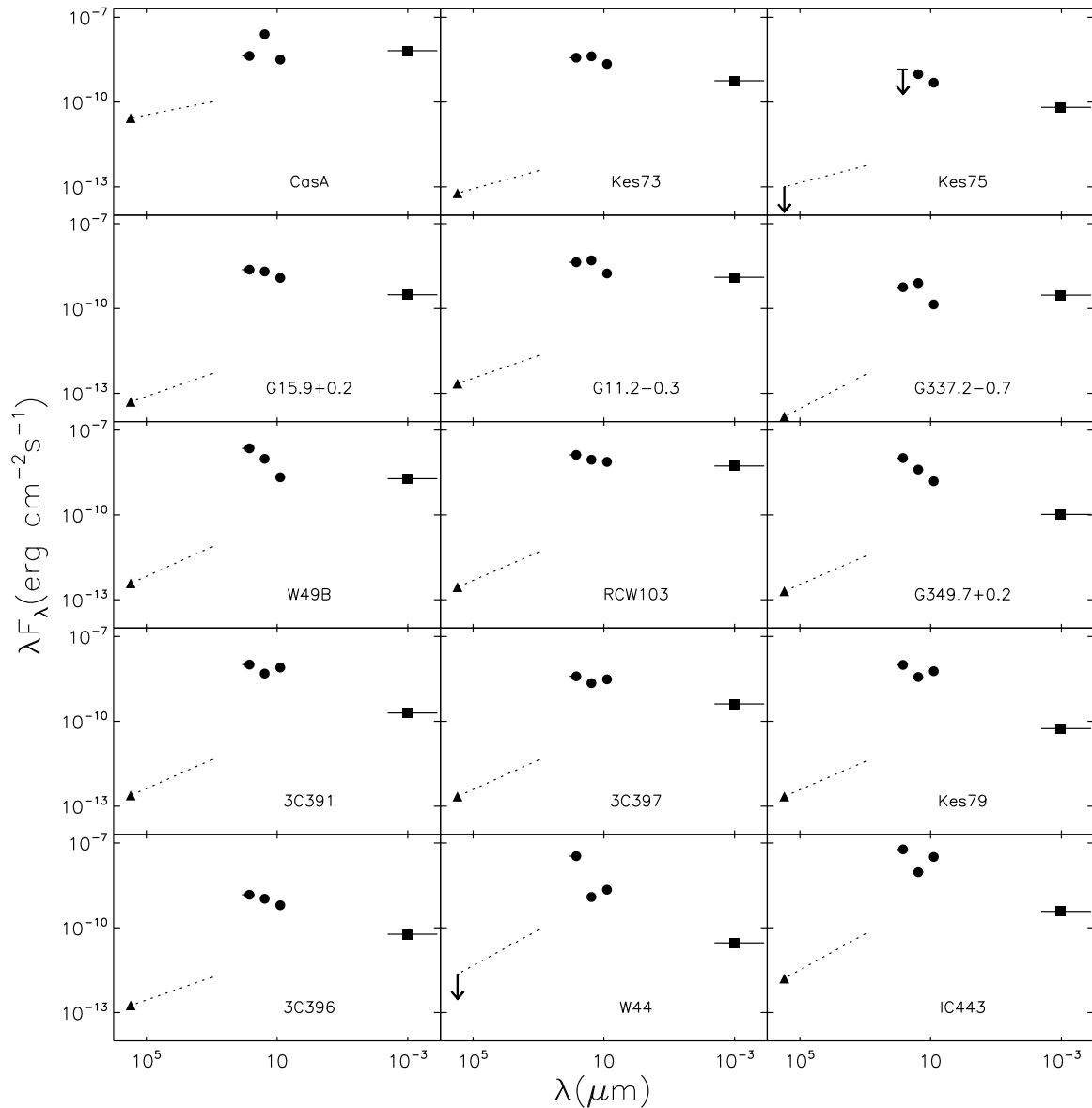
Figure 5.7: SEDs of Chandra SNRs ordered according to approximate remnant's age (increasing left to right, top to bottom). For the radio, the synchrotron spectrum is shown by the dotted line for the appropriate spectral index, anchored in the observed range at 1 GHz (triangles). The circles indicate the power in the infrared at 8, 24 and 70 μm. In the X-ray, the band (0.3-10 keV) of the Chandra images is used (squares). Horizontal lines represent the width of the bandpass. We also include Cas A and IC443 for comparison. Their infrared flux densities are taken from Hines *et al.* (2004) and Noriega-Crespo et al. (*in preparation*) while the X-ray fluxes are from the Chandra Supernova Remnant Catalog and Dwek *et al.* (1987), respectively. Again, note that for W44 the infrared and X-ray values apply only to the central region while the radio estimate is for the whole remnant. The integrals over the infrared and X-ray range reveal their contributions to cooling the shocked plasma.

5.5 Conclusions

We have compiled a catalog of SNRs detected within the MIPSGAL survey at 24 and 70 μm, with complementary measurements at 8 μm from the GLIMPSE survey. In order to better assess the nature of the detected infrared emission, we have compared it with radio and X-ray data. Our main findings are the following:

- The detection rate of SNRs given the MIPSGAL sensitivity is 32%, 39 out of the 121 candidates from Green's SNR catalog.

- We find a linear trend (slope $= 1.1 \pm 0.2$) in the logarithmic relationship between $[F_8/F_{24}]$ versus $[F_{70}/F_{24}]$. If there is indeed an age effect, then the youngest SNRs will have the lowest $[F_8/F_{24}]$ and $[F_{70}/F_{24}]$ ratios.

- The $[I_{70}/I_{24}]$ and $[I_8/I_{24}]$ color ratios provide a method of distinguishing between different emission mechanisms. This is not completely secure and the color ratios of some SNRs overlap with those of H II regions.

- Assuming a simple modified blackbody model (at 24 and 70 μm), we retrieve SNRs dust temperatures which range from 45 to 70 K for a dust emissivity of $\beta = 2$.

- Using the previous color temperature ($T_{24/70}$), we find rough estimates of dust masses ranging from about 0.02 to 2.5 M$_\odot$. Note that the dust masses obtained here may be overestimated given the possible contribution of line emission to the MIPS fluxes.

- We also compare infrared fluxes with their corresponding radio fluxes at 1.4 GHz and find that most of the remnants have ratios of 70 μm to 1.4 GHz characteristic of SNRs, although six (about 18% of the detected sample) have ratios closer to those found for H II regions.

- The slope of the logarithmic correlation between 'total' mid-infrared flux (24 and 70 μm) and the 1.4 GHz non-thermal radio flux is close to unity (1.10) as found for galaxies. q_{MIR} values were calculated for each fully detected remnant and they range between approximately 0.06 and 2.60.

- Whether the strong 24 μm emission is the result of line emission or hot dust, it is clear that there is a good morphological association of the 24 μm and X-ray features in bright X-ray remnants. The mechanism for the 24 μm emission for these remnants is most likely grains heated by collisions in the hot plasma. The morphology of this mid-infrared emission is also generally distinct from the other infrared wavelengths which implies that the emission at 8 and 70 μm has a different origin.

- We present SEDs (radio, infrared, X-ray) for a sample of remnants and show that the energy released in the infrared is comparable to the cooling in the X-ray range. Moreover, IRX seems to increase with age.

5.6 Appendix

Images of the infrared emission for our most spectacular detections at 24 μm follow. The order is the same for all the figures and consists of the black and white 24 μm image (colorbar in units of MJy/sr) on the left and the 3-color image on the right, with 8, 24 and 70 μm being blue, green and red, respectively. Overlaid in each image are contours either from radio or X-ray observations when available (see §5.2.2). Images are all in Galactic coordinates, and our remarks on north (up), east (left), etc., are with respect to this system. Indicated is the angular scale which can be compared with the few arcminute resolution of *IRAS*. A short summary on the observed IR emission and other relevant information is presented as well. For more information on all detected SNRs, we encourage the reader to see the Appendix in Pinheiro Gonçalves *et al.* (2011).

5.6.1 First Galactic Quadrant

G11.2-0.3

This fairly young remnant (1600 yr) contains a millisecond pulsar PSR J1811-1925 at the center (Kaspi *et al.*, 2001). It is clearly seen in the radio as a circular shell of approximately 4′ diameter (spectral index of 0.6) and it is located at a distance of 4.4 kpc (Green 2009, and references therein). Using staring observations with *Spitzer*, Rho *et al.* (2009) found Fe emission with temperature and density representative of ejecta material in regions with high Fe content. Koo *et al.* (2007) detected near-infrared [Fe II] and H_2 filaments within and outside the radio borders of the remnant, respectively. While the H_2 emission is most likely the result of some sort of interaction between the shockwave and the progenitor wind, the [Fe II] emission is thought to be the combination of ejecta and surrounding ISM with a morphology characteristic of an 'asymmetric explosion'. Recently, new near-infrared spectroscopic observations of dense Fe knots Moon *et al.* (2009) strengthened the belief that the SN explosion happened along the north-south direction (in Galactic coordinates). The 24 μm image (Figure 5.8) reveals peaks of mid-infrared emission that coincide morphologically with X-ray emission (Figure 5.8). Previously detected in the IRAC wavelengths, this remnant shows 8 μm emission in the eastern part but since it is diffuse, a clear association is not possible. The same diffuse pattern is seen in the 70 μm image. Both filaments detected in the southern rim at 8 μm have correlated emission in the 24 and 70 μm images, although unresolved. The IRAC colors for these filaments suggest
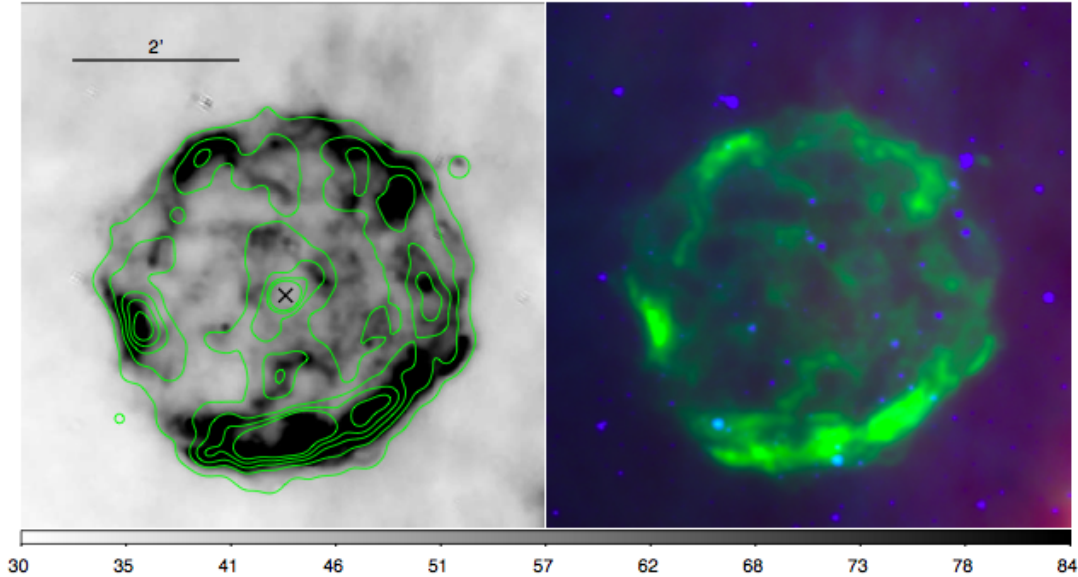
Figure 5.8: SNR G11.2-0.3. Contours from Chandra observations: levels are $2, 6, 9, 13, 16 \times 10^{-7}$ photons/cm^2/sec/pixel. The cross marks the location of the associated pulsar (AX J1811.5-1926).

molecular emission from shocked gas (Reach *et al.* 2006). The blob in the most eastern part of the remnant is detected both at 24 and 70 μm and so it is most likely due to dust.

G14.3+0.1

This is another class II remnant from Brogan *et al.* (2006). While the 8 μm IRAC image shows emission localized in the eastern part, the 70 μm emission fills the radio contours uniformly. The 24 μm emission also fills the contours with two peaks located north and south of the remnant's centre (see Figure 5.9).

G15.9+0.2

Chandra observations showed that this remnant is young ($\leq$ 2400 yr) with an X-ray point source (Reynolds *et al.*, 2006). The obtained X-ray spectrum implied high element abundances characteristic of ejected material. The infrared detections are presented in Figure 5.10. This remnant was not detected in either the GLIMPSE or IRAS surveys. The 24 μm emission is bright in the southern-most part. There are also traces of emission in the north rim. At 8 μm, the emission is very faint and mainly seen around the south-eastern radio contours. The 70 μm image shows diffuse emission extending along the south-eastern part; nevertheless, it is unclear if this is associated with the remnant. Also, in the same area, the remnant seems to be encountering interstellar material, although no maser emission has been reported (Green *et al.*, 1997).
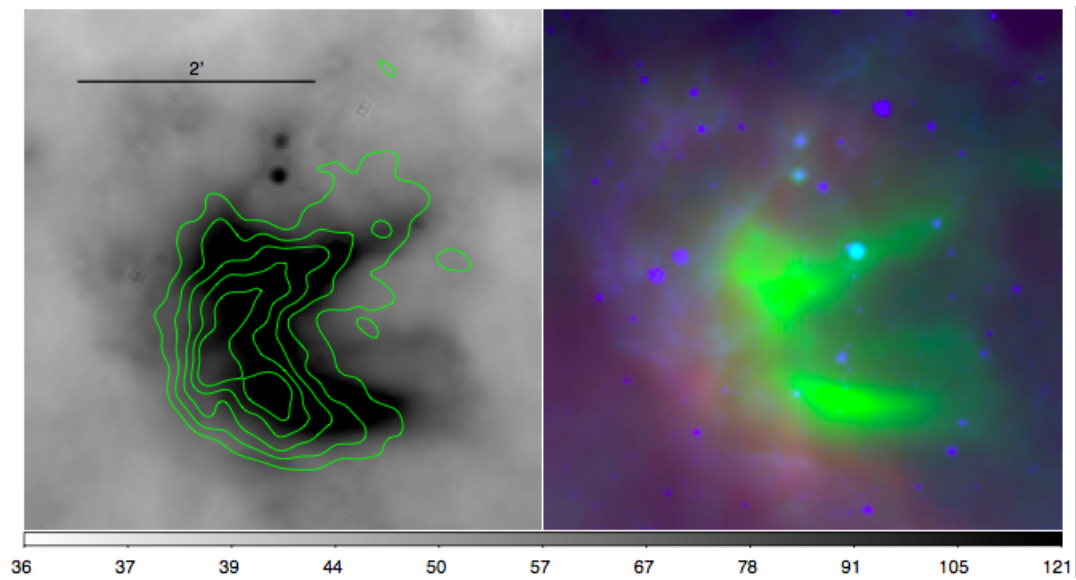
Figure 5.9: SNR G14.3+0.1. Contours from VLA 20 cm observations: levels are 16, 20, 24 and 28 mJy/beam.
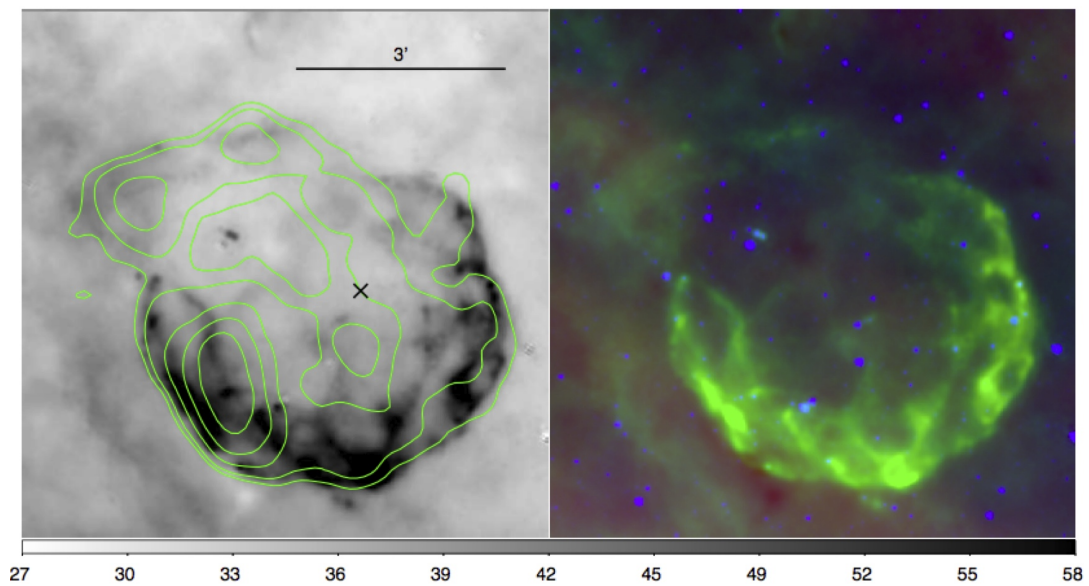
Figure 5.10: SNR G15.9+0.2. Contours from VLA 20 cm observations: levels are 0.05, 0.12, 0.34, 0.7 and 1.2 Jy/beam. The cross marks the location of an X-ray source (CXOU J181852.0-150213)
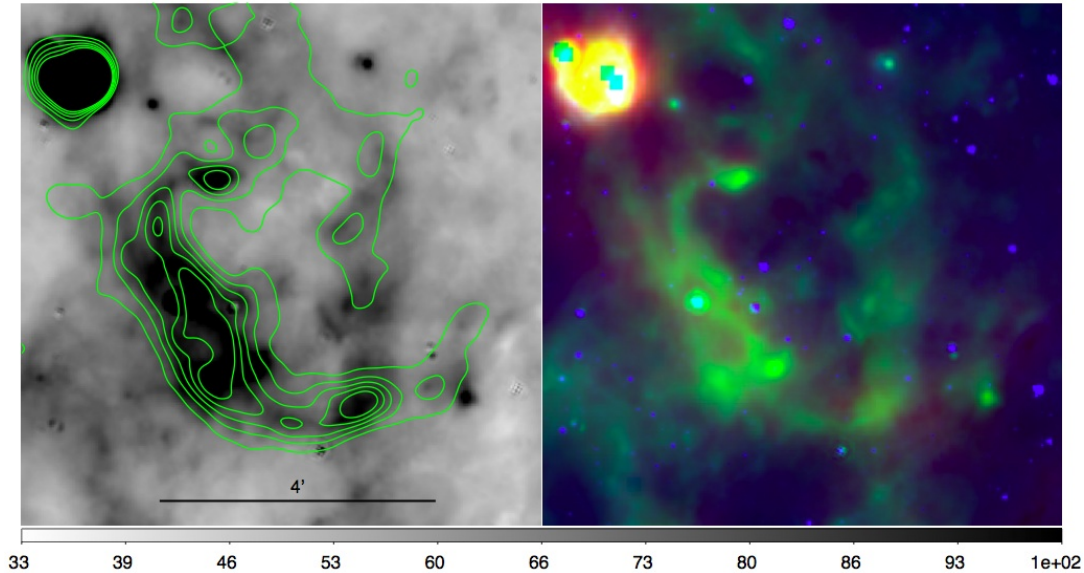
Figure 5.11: SNR G18.6-0.2. Contours from VLA 20 cm observations: levels are from 18 to 30, in steps of 4 mJy/beam.

G18.6-0.2

Another partial shell class II remnant from Brogan *et al.* (2006) is shown in Figure 5.11. There is a good correspondence between the radio contours and the infrared emission, in particular, for 24 μm. At 70 μm the strongest infrared emission matches the brightest radio peaks and, at 8 μm, there is diffuse emission which seems to occupy those regions as well, but no clear association can be established based on this filter alone.

G23.6+0.3

This remnant has a radio spectral index of -0.34 (Shaver & Goss, 1970). Its odd elongated radio shape is seen to spatially coincide with the 24 μm emission (Figure 5.12). The 8 and 70 μm emissions are more prominently displaced towards the south and west of the radio boundaries. No maser association has been reported.

G27.4+0.0 or Kes 73

This remnant has a 4′ diameter shell-like structure in the radio. Tian & Leahy (2008) reported that this SNR can be as far as 9.8 kpc and be 500-1000 yr old. Vasisht & Gotthelf (1997) discovered a low period (12s) X-ray signal from the central compact source (1E 1841-045). The SNR is not detected at the IRAC wavelengths but it is spectacularly seen at 24 μm (Figure 5.13). This mid-infrared emission traces the X-ray contours extremely well, with both peaking in the northwestern ridge.
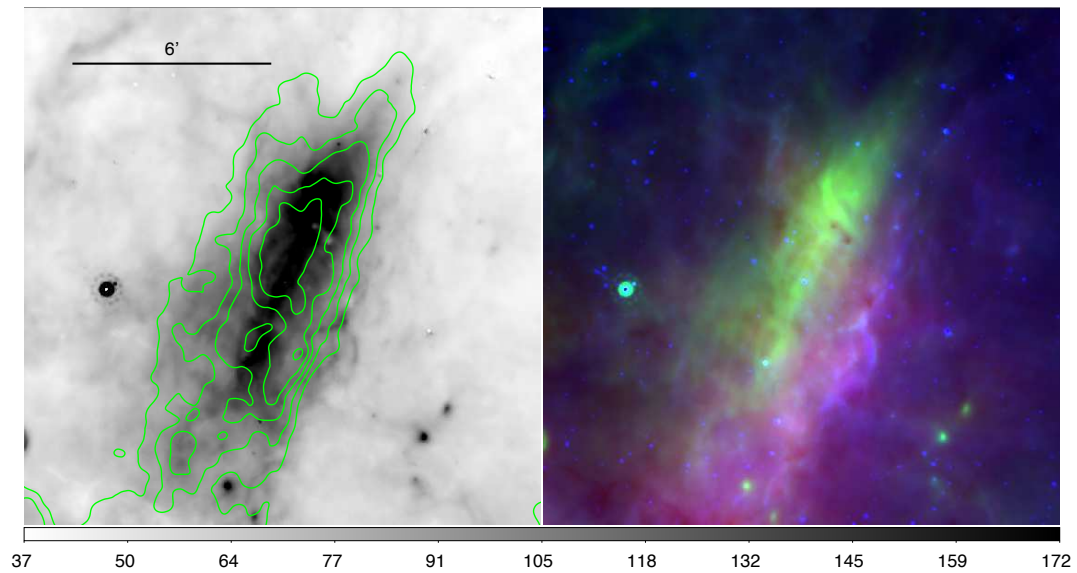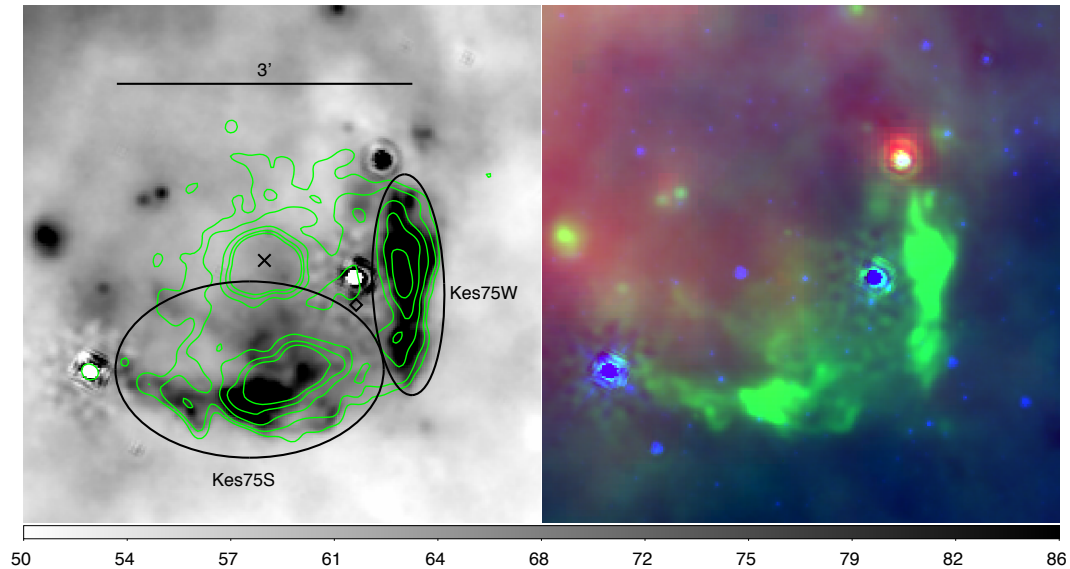
Figure 5.12: SNR G23.6+0.3. Contours from VLA 20 cm observations: levels are from 10 to 22, in steps of 3 mJy/beam.
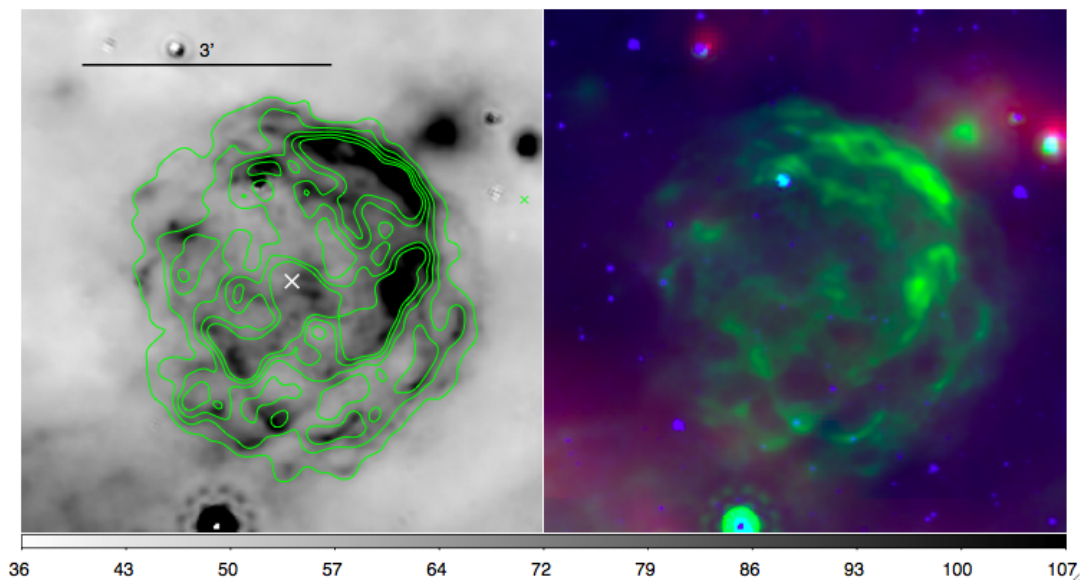
Figure 5.13: SNR G27.4+0.0. Contours from Chandra observations: levels are from 2 to 10×10^{-7}, in steps of 2×10^{-7} photons/cm^2/sec/pixel. The cross represents the location of the central X-ray source AX J1841.3-0455.

Figure 5.14: SNR G29.7-0.3. Contours from Chandra observations: levels are 1.3, 1.8, 3.2, 5.5 and 8.7×10^{-7} photons/cm^2/sec/pixel. The cross marks the location of the pulsar AX J1846.4-0258. Regions used for partial photometry are also indicated in the figure (in black).

G29.7-0.3 or Kes 75

This composite remnant has an associated pulsar (PSR J1846-0258; Gotthelf *et al.*, 2000) and is thought to have an upper distance limit of 7.5 kpc (Leahy & Tian, 2008). This remnant was not detected in GLIMPSE or IRAS surveys but was well identified using targeted MIPS observations by Morton *et al.* (2007) where most of the emission at 24 *µm* originates from two bright shells located south and west of the remnant's centre. Figure 5.14 shows a clear detection at 24 *µm* which traces accurately the brighter X-ray regions with the central X-ray peak being the only exception; there is no 8 *µm* emission there and the 70 *µm* emission appears to be non-existent too. There is also no significant infrared emission at 8 or 70 *µm* associated with the bright 24 *µm* features. Unrelated 70 *µm* emission shows up diffusely in the eastern part of the remnant which overestimates the 70/24 color ratio measured for this region (*Kes75S*).

G31.9+0.0 or 3C 391

Green's SNR catalog describes this object as a shell-type remnant with a spectral index of about 0.49. Previous infrared spectral observations with ISO revealed the existence of ionic lines (Reach & Rho, 2000), in particular [Fe II] at 26 *µm* and [S II] at 35 *µm* towards the direction of the BML (Broad Molecular Line) region at Galactic coordinates 31.84, 0.03 (Figure 5.15). Besides the previous elements, [O IV] at 26 *µm* was also detected but found to be three times brighter in the radio peak (bar at Galactic coordinates 31.87, 0.06) than in the BML region.

Right above this radio peak, the remnant is encountering a nearby molecular cloud (Wilner *et al.*, 1998). All of the above line emitters contaminate the MIPS channels and therefore contribute to fluxes reported in Table 5.2. Furthermore, Reach *et al.* (2002) also found clumps of H_2 emission in the BML which was again confirmed with IRAC color ratios by Reach *et al.* (2006). Two 1720 MHz OH masers were detected within the remnant (Frail *et al.*, 1996). IRAC images show emission associated with the western maser where the previously mentioned BML is located. Mid-infrared 24 and 70 μm emission from MIPSGAL is clearly seen in this region as well (Figure 5.15). Previous IRAC observations by Reach *et al.* (2006) revealed a rim of [Fe II] emission which matches the brightest radio emission in the north part of the remnant. The same feature is seen in the 24 μm image which suggests that the bulk of emission at this location can be due to [Fe II] at 26 μm. Reach *et al.* (2006) also found that the infrared emission in the middle knots (east and west at the 'waist'; the one in the west has the same location as the BML) is produced by shocked molecular gas. These knots are well detected at 24 μm (with some likely contribution from H_2 S(0) at 28 μm) and are especially strong at 70 μm. The southeastern rim structure (at 24 μm) coincides with an enhancement in the radio and the second maser.

Remnant 3C391 is characterized by a faint outer rim that can be seen both in the radio at 20 cm and in the infrared at 24 μm (Figure 5.15; see also Su & Chen 2008). This is the collisionless shock where the blast wave encounters the ISM. Although the radio structure is spatially correlated with the faint mid-infrared, a spectral index analysis shows that this 24 μm emission is too strong to have only a synchrotron origin.

G33.6+0.1 or Kes 79

This remnant has a 'shell-like' radio morphology (e.g., Velusamy *et al.*, 1991) with a centrally compact X-ray source (Seward *et al.*, 2003). The southern filaments seen in the Chandra image are well detected and have a similar morphology in the 24 μm image (Figure 5.16). Those are located in the same region in which Reach *et al.* (2006) noticed the existence of a dark cloud, and where previous CO and HCO^+ observations suggested an interplay with a nearby molecular cloud (Green & Dewdney, 1992). These authors also noted that this must be an evolved remnant given its large linear size. Furthermore, using Chandra observations Sun *et al.* (2004) did not encounter evidence of ejecta material, reinforcing the conclusion that this must be an older remnant (around 6000 yr old). The 24 μm emission fills and traces the brightest X-ray contours (so called inner-shell) in the central part of the remnant while 8 μm diffuse emission is present in the northern part of the remnant, but not likely to be associated. Likewise, at 70 μm it appears that the main contribution to the flux is probably the IRAS source 18501+0038 (represented by a white circle in Figure 5.16).
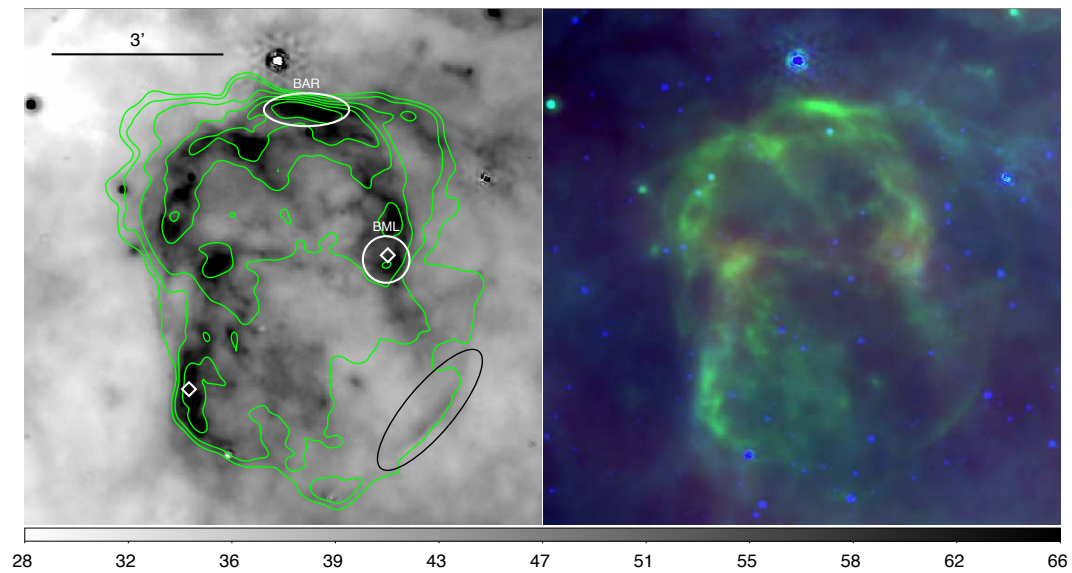
described by Bhattacharya. The ellipse (in white), in the southern extent, just on the remnant locates a portion of the possible collisionless shock. Regions used for partial photometry are also indicated in the figure (in white).
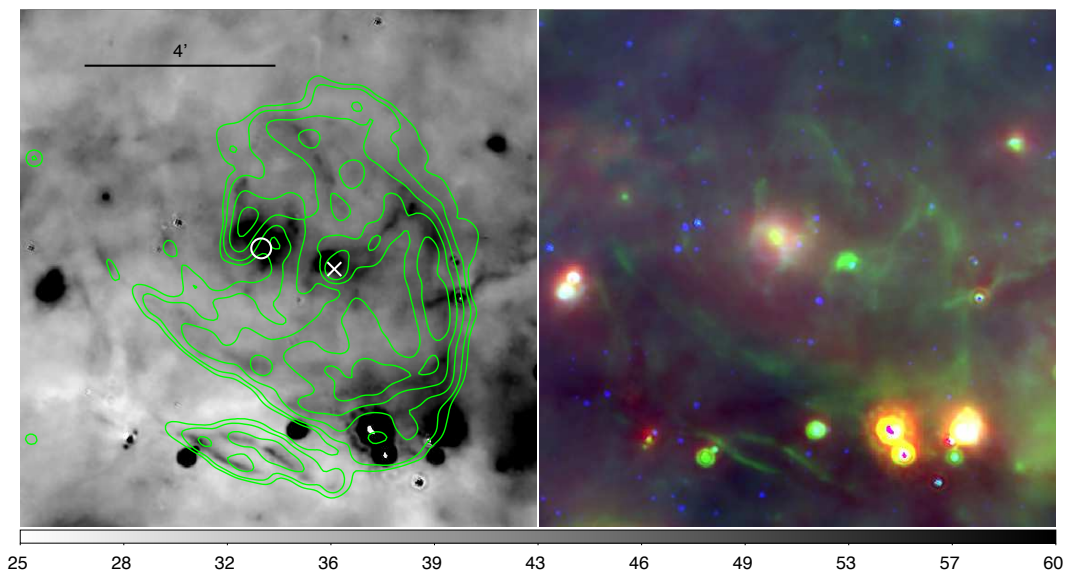
Figure 5.16: SNR G33.6+0.1. Contours from Chandra observations: levels are 1.5, 2, 3.6, 6.3 and 10×10^{-7} photons/cm^2/sec/pixel. The cross marks the location of PSR J1852+0040 and the circle represents an IRAS point source.
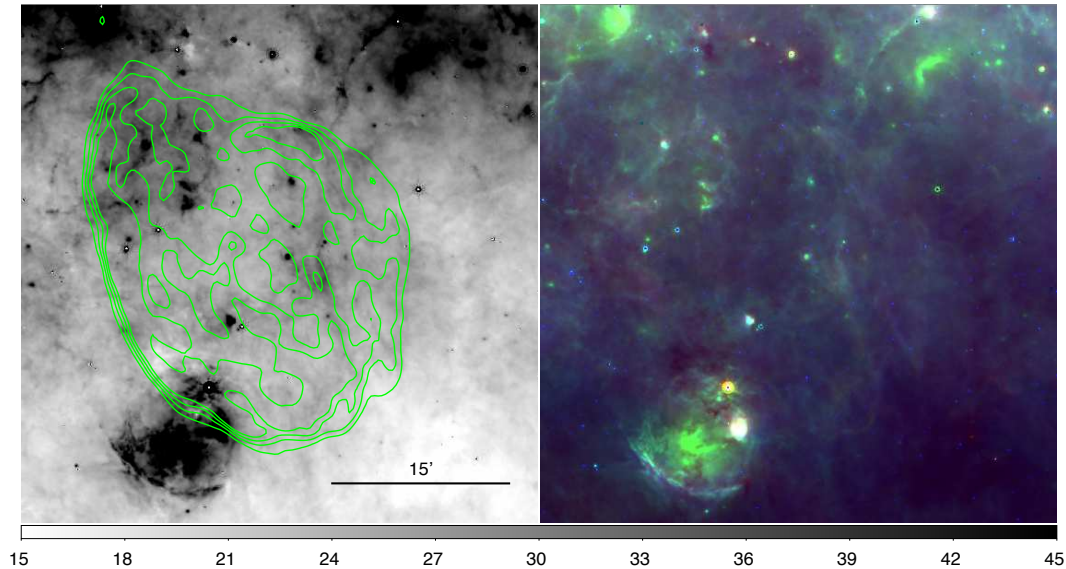
Figure 5.17: SNR G34.7-0.4. Contours from VGPS 21 cm observations: levels are 35, 52, 68 and 85 Jy/beam.

G34.7-0.4 or W44

This evolved object is classified as a 'mixed-morphology' remnant (Rho & Petre, 1998) due to its radio shell with inner X-ray filled emission. It is mainly detected at 70 μm possibly indicating that it has had time to evolve (see Figure 5.17). This is in agreement with the inferred age of about 20000 yr from the characteristic age of the associated pulsar (Wolszczan *et al.*, 1991). In the 70 μm image, the western filaments trace well the radio contours. In all the infrared wavelengths, there is emission associated to the northern region. This is one of the most stunning detections in GLIMPSE data where Reach *et al.* (2006) found that emission at 4.5 μm (which is mostly from shocked molecular gas) matches well the radio contours. Previously, Reach *et al.* (2005) also detected near-infrared shocked H$_2$ and millimeter wave molecular lines, which revealed the interaction of the remnant with a GMC. Moreover, the existence of extended maser emission has also been reported (Hewitt *et al.*, 2008) inside of the remnant. Recent *Spitzer* spectral line analysis (Neufeld *et al.*, 2007) revealed the emission of [Fe II] around 26 μm and some H$_2$ at 28 μm which can be contributors to the faint emission seen in the MIPSGAL 24 μm image. At 8 μm the object is easily confused with the diffuse background.

G39.2-0.3 or 3C396

Several filaments are observed at 24 μm (Figure 5.18). Specifically, the top interior part of the remnant is only observed in this wavelength. Also, recent near-infrared observations (Lee *et al.*, 2009) revealed the presence of [Fe II] and H$_2$ in the northwestern part of the shell matching the radio emission. The 24 μm image shows the exact same features which suggests that
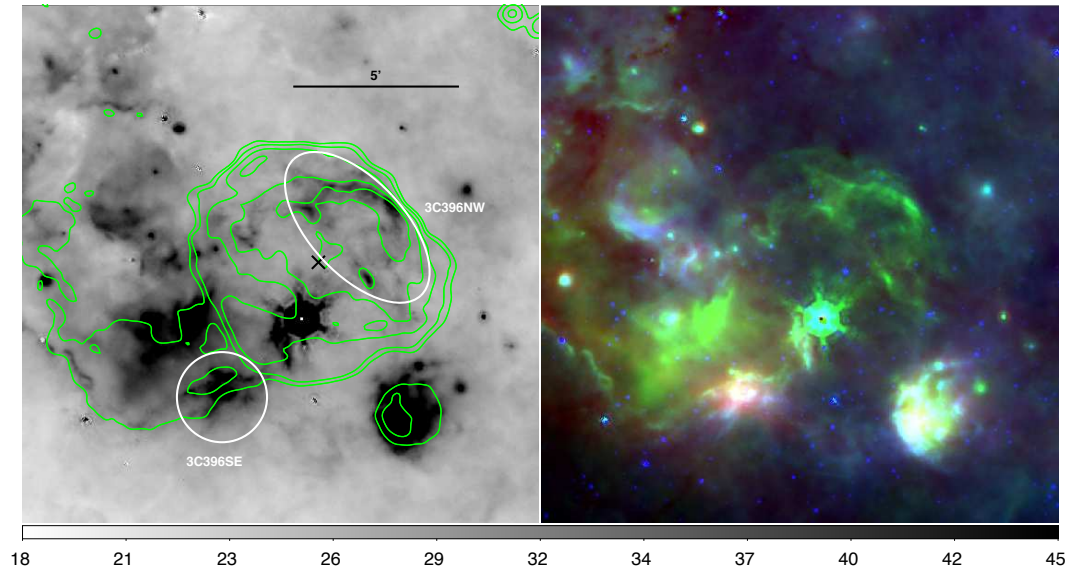
Figure 5.18: SNR G39.2-0.3. Contours from 20cm VLA observations: levels are 1, 4, 12, 26 and 45 mJy/beam. The cross represents the location of the X-ray source J190406.5+052646. Regions used for partial photometry are also indicated in the figure (in white).

some emission is probably due to lines in the MIPSGAL band. Other filaments near the centrally projected hot point source (IRAS 19017+0522) are seen at 8, 24 and 70 μm. Previously, Reach *et al.* (2006) had argued that those filaments had colors consistent with PDRs. In that case, the suite of *Spitzer* passbands is probing the dust emission from PAHs to big grains. The tail of radio emission mentioned in Patnaik *et al.* (1990) is partially traced by 24 and 70 μm with some spatial mismatch. There is a bright filament in the south part of this tail, which is detected in all of the infrared wavelengths. Moreover, in the eastern part of the tail, a filament of infrared emission (8) seems to match exactly the radio contour. The infrared emission that is in between the tail and the remnant is most likely to be caused by thermal dust grains. Recently, with the help of *Chandra* data and updated CO observations, Su *et al.* (2011) infer an approximate distance of 6.2 kpc and an age of about 3000 yr.

G41.1-0.3 or 3C 397

This is another shell-type morphology remnant with spectral index of 0.48 (Green, 2009). Its uncommon rectangular shape on the upper edge suggests interactions with the ISM, specifically a dense molecular cloud inferred through CO observations (Safi-Harb *et al.*, 2005). Based on Chandra data, the same authors propose that the remnant is about 5300 yr old and is now starting the radiative stage. More recent CO observations indicate that the remnant is within a 'molecular cavity' at a distance of about 10.3 kpc (Jiang *et al.*, 2010). The 8 and 70 μm images show some emission in the north part of the remnant (Figure 5.19). The 24 μm image reveals
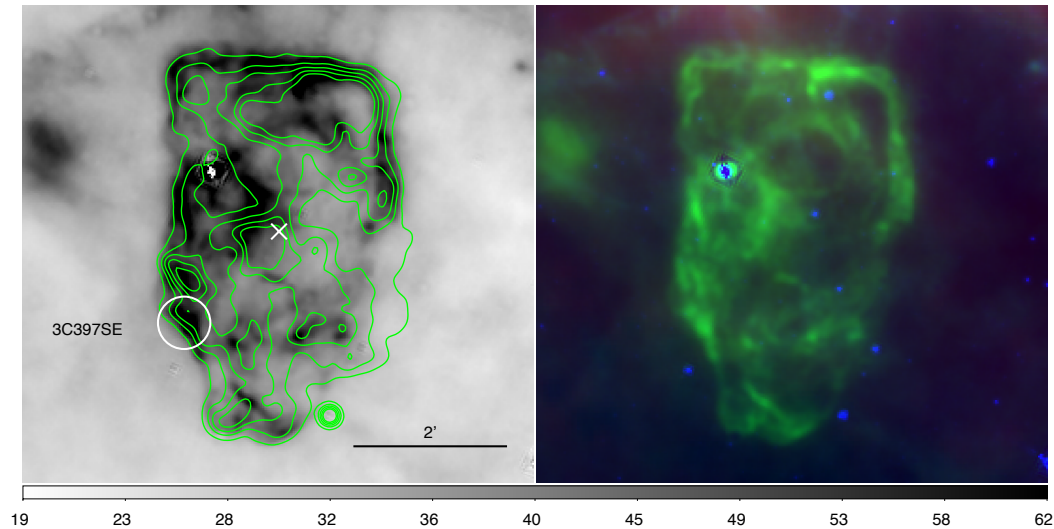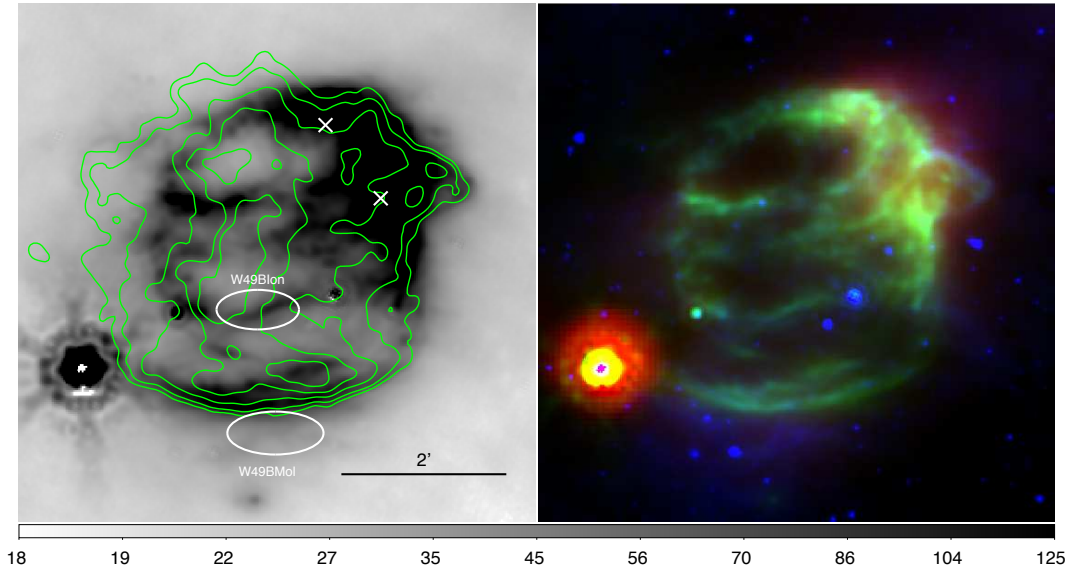
Figure 5.19: SNR G41.1-0.3. Contours from Chandra observations: levels are 2, 4.3, 6.5, 8.8 and 11×10^{-7} photons/cm^2/sec/pixel. The cross represents the location of the X-ray source J1907.5+0708. Region used for partial photometry is also indicated in the figure (in white).

rich filamentary structure that nicely resembles the entire X-ray counterpart. The GLIMPSE survey reported a faint detection in regions where IRAC colors suggested shocked emission from ionic lines (Reach *et al.* 2006).

G43.3-0.2 or W49B

W49B is characterized by an odd 'barrel'-shaped morphology in the radio (Moffett & Reynolds, 1994). Reach *et al.* (2006) reported that most of the emission at the IRAC wavelengths is consistent with shocked ionic and molecular emission lines. Later on, near-infrared observations revealed that the [Fe II] morphology, at 1.64 μm, is similar to the radio structure and the 2.12 μm H$_2$ can be found primarily in the south (right below the [Fe II] ridge) and in the northwestern part of the remnant (Keohane *et al.*, 2007). With the help of Chandra data, these authors also reported an overabundance of heavy elements thus suggesting that the X-ray emission is dominated by the ejected material as found previously by Hwang *et al.* (2000) using ASCA data. Both MIPS channels (see Figure 5.20) show interesting filamentary structure and are brighter in the same locations, thus indicating that there is a strong dust continuum contribution as the primary emission mechanism in the far-infrared. However, note that the 24 μm image seems to trace well the ionic shocked component within the X-ray contours.

Figure 5.20: SNR G43.3-0.2. Contours from Chandra observations: levels are 2, 3.1, 6.5, 12 and 20×10^{-7} photons/cm^2/sec/pixel. The crosses represent the location of the X-ray source J1911.0+0906 and γ-ray source J1911.0+0905. Regions used for partial photometry are also indicated in the figure (in white).

5.6.2 Fourth Galactic Quadrant

G304.6+0.1 or Kes 17

Infrared emission from the northwestern part was detected in the GLIMPSE data and attributed to shocked molecular gas (Reach *et al.*, 2006). Those filaments are also present in the 24 μm image (Figure 5.21). Moreover, at the same wavelength, there is emission along the south which spatially coincides with the radio ridge. At 70 μm, there is just filled emission around the northwestern shell.

G332.4-0.4 or RCW 103

This young remnant (age about 2000 yr) has a shell-like radio morphology and is at a distance of 3.1 kpc (Green, 2009 and references herein). It has a soft X-ray point source near the centre of the remnant (Tuohy & Garmire, 1980). The 24 μm image (Figure 5.22) shows extensive diffuse and filamentary emission related to the remnant, spatially correlated with the radio. Numerous small filaments trace the outer borders of the synchrotron emission. There is a dark arc in the centre left of the remnant where the IR and X-ray shells seem to be incomplete. For the southern bright rim, Reach *et al.* (2006) found colors indicating shocked molecular gas along with some ionic emission, which corroborated the reported detection of ionized species by Oliva *et al.* (1999b). Around 24 μm, the ISO spectrum showed strong emission mainly
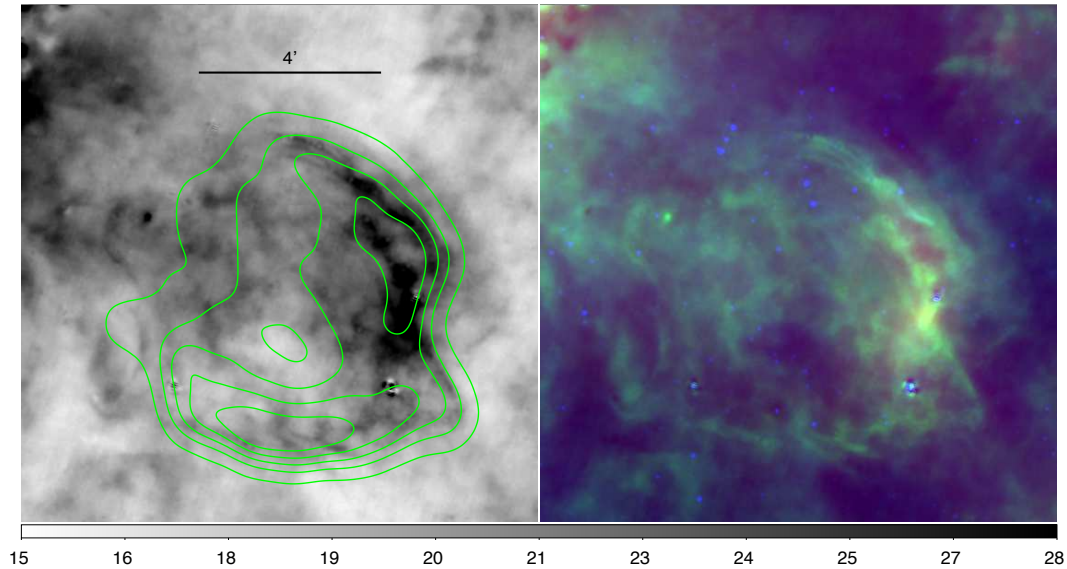
Figure 5.21: SNR G304.6+0.1. Contours from MOST observations: levels are 0.06 to 0.5, in steps of 0.11 Jy/beam.

from [Fe II] as well as [O IV]. These authors also reported that heavy elements are in the gas phase given their solar-like abundances and therefore most of the infrared emission in that rim must be the result of fine-structure lines. The 24 μm morphology is very similar to the X-ray emission, as seen in other young remnants.

G337.2-0.7

The radio contours from MOST observations indicate that this is a compact circular shell remnant (Whiteoak & Green, 1996). It has not been detected in the IRAC bands or IRAS surveys. The remnant is more complex in the X-ray and mid-infrared (Figure 5.23), with the 24 μm emission composed of several filaments forming two distorted apparent shells. The interior one is almost complete and is located in the western part. The other is visible as two long filaments mainly in the north-south direction in the eastern part of the remnant. Both relate closely to the contours of the Chandra X-ray emission. There is some 70 μm diffuse emission in the north-eastern part but unlikely to be related with the remnant.

G344.7-0.1

Dubner *et al.* (1993) reported an angular size of 33 pc in the radio which agrees with the estimate of a middle-aged remant as based on the X-ray plasma temperature found using ASCA data (Yamauchi *et al.* 2005). Figure 5.24 shows that the emission at all three infrared wavelengths is brightest at the central radio peak. Previous GLIMPSE analysis (Reach *et al.* 2006)
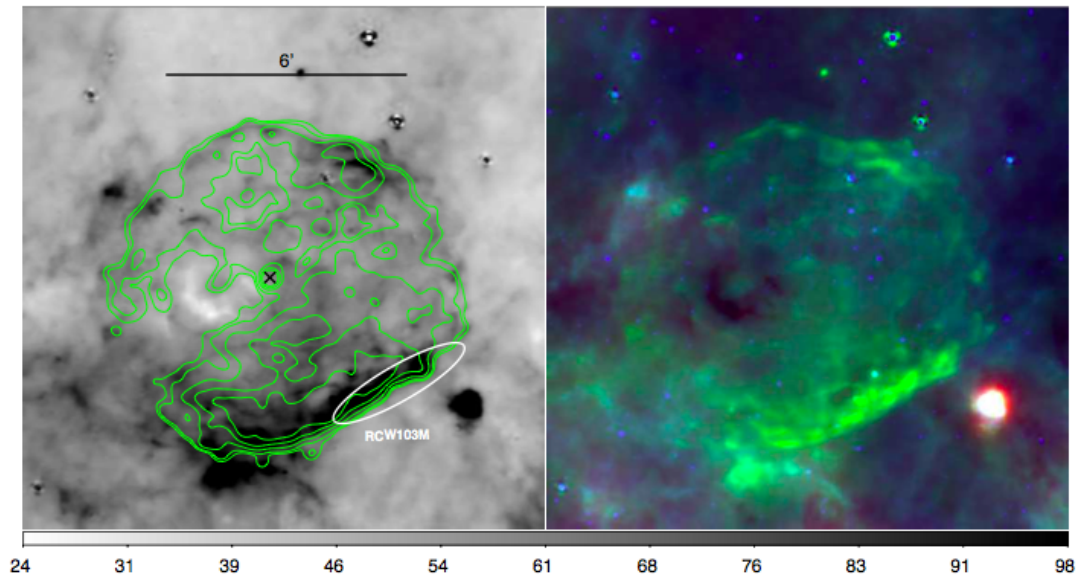
Figure 5.22: SNR G332.4-0.4. Contours from Chandra observations: levels are 0.8, 1.1, 2, 3.4 and 5.5×10^{-6} photons/cm^2/sec/pixel. The cross shows the location of the X-ray source 2E 1613.5-5053. Region used for partial photometry is also indicated in the figure (in white).
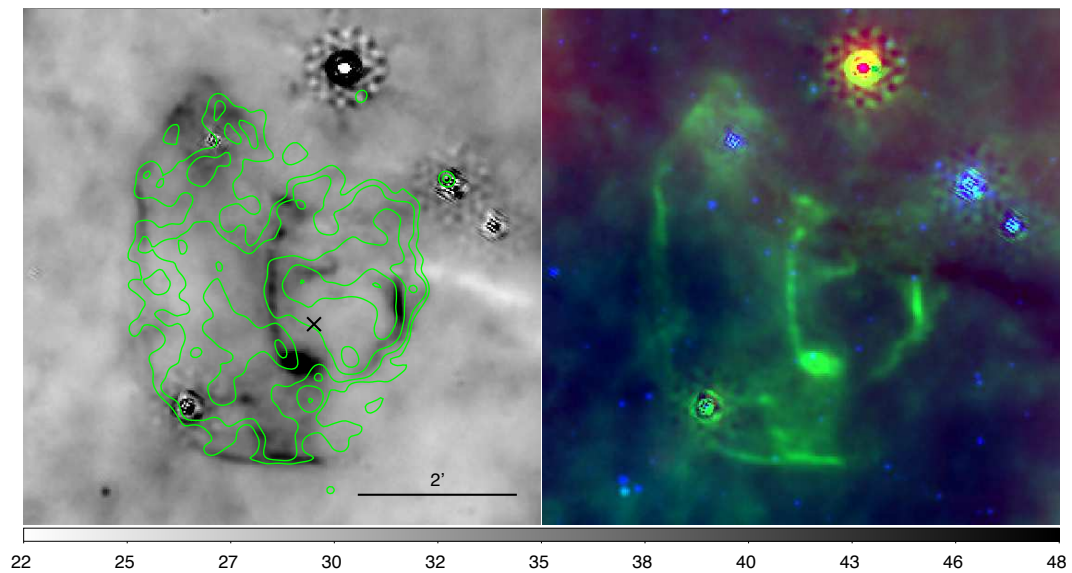
Figure 5.23: SNR G337.2-0.7. Contours from Chandra observations: levels are 0.8, 1, 1.6, 2.6 and 4×10^{-7} photons/cm^2/sec/pixel. The cross shows the location of the X-ray source J163931.4-475019.

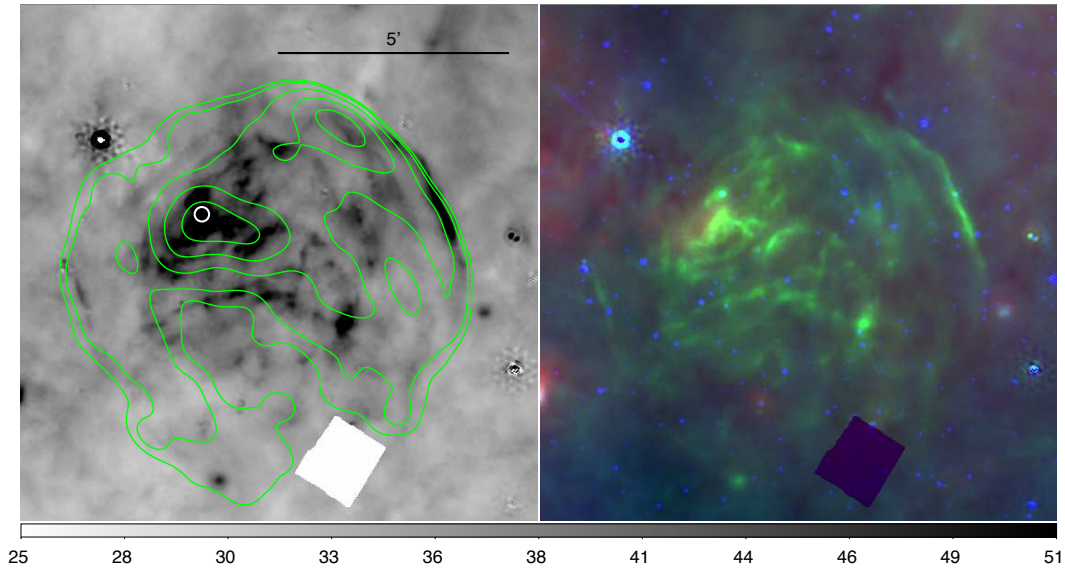**Figure 5.24:** SNR G344.7-0.1. Contours from MOST observations: levels are 16, 21, 35, 58 and 90 mJy/beam. Circle represents the location of a catalogued IRAS point source corresponding to the diffuse emission peak.

showed that this structure had colors consistent with shocked ionized gas (R06). Although now clearly diffuse emission, this peak was catalogued as IRAS 17003-4136. The 24 μm image also shows a few striking filaments associated with the outer radio boundaries, especially where compressed at the northwest.

G349.7+0.2

OH maser emission was found in the remnant's interior by Frail *et al.* (1996) and evidence of interaction with a molecular cloud was later strengthened by Reynoso & Mangum (2001) with CO observations. With extremely similar X-ray and radio morphology, its corresponding brightness in both regimes is also high (Lazendic *et al.*, 2005). The infrared emission is present with a similar morphology at all three wavelengths (Figure 5.25). The infrared is strongly peaked within the X-ray contours, but not closely related, except for the 24 μm emission. Previous GLIMPSE analysis showed infrared emission in all of the IRAC bands (Reach *et al.*, 2006).
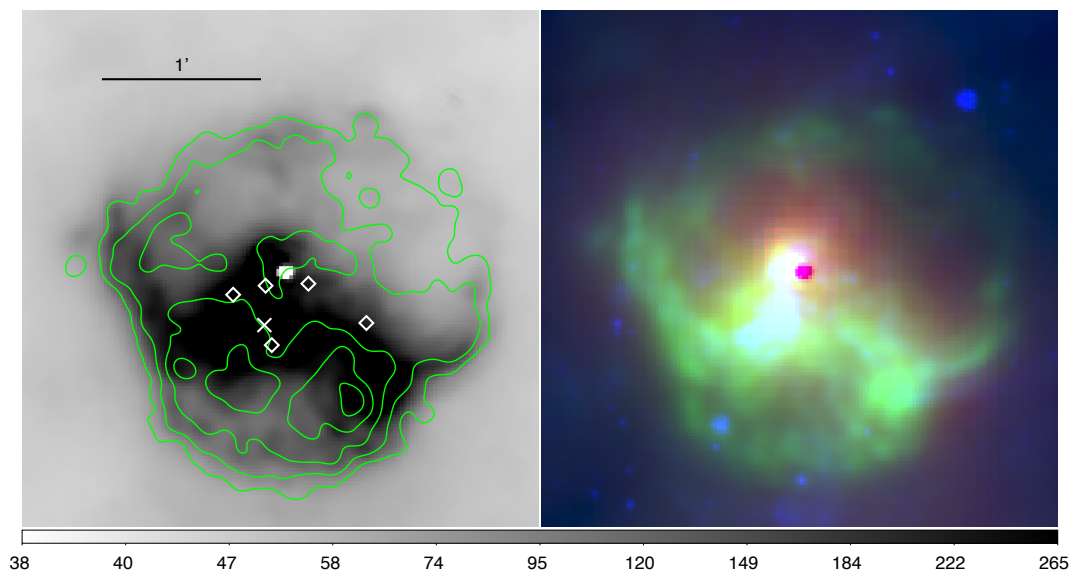
Figure 5.25: SNR G349.7-0.2. Contours from Chandra observations: levels are 0.3, 0.7, 1.9, 3.8, 6.5 and 10×10^{-7} photons/cm^2/sec/pixel. Masers are represented by diamonds and the cross marks the location of X-ray source J171801.0-372617.

Chapter 6

Summary and future work

Here we summarize this work and give a general overview of the main results (§6.1). For more detailed conclusions, we refer the reader to the end of Chapters 4 and 5. Preliminary efforts for future work are discussed in §6.2.

6.1   Summary

6.1.1   H I observations

We have proposed and carried out H I 21-cm emission line observations with the GBT ($9'$ resolution). The complete survey spans about 800 square degrees in the sky, the vast majority of observed fields being in the North Galactic Hemisphere. We took advantage of the high velocity resolution of the GBT (0.16 km s^{-1}) to build H I column density maps for each field for different velocities gas components. These integrated maps are used primarily to do spatial correlation analysis with IR maps in order to obtain dust emissivities. We calculated errors as described in Boothroyd *et al.* (2011) and derived uncertainties associated with the H I velocity integrated maps (see Chapter 2).

6.1.2   Mid-IR dust emissivities in the diffuse ISM

We used the H I 21-cm and IR (IRIS/IRAS) data (described in Chapters 2 & 3) to calculate and look for changes in the dust emissivities associated with different velocity gas (LVCs, IVCs and HVCs) via spatial correlation analysis (Chapter 4). Such analysis is an essential step to better understand the processing/evolution of dust associated with gas in different Galactic environments (local *versus* halo dust). A least-squares fitting method was used to determine the mid-IR IRIS dust emissivities at 12 and 25 μm (and 60 and 100 μm too), the coefficients in the multilinear template we used to characterize dust emission. We found residual maps that

showed an infrared brightness gradient compatible with an imperfect removal of zodiacal emission. In order to remove such foreground, we have implemented two methods which produced similar results. We chose the method that fits the mid-IR sky brightness with a multilinear template model that includes a parameterized tilted plane.

The mid-IR dust emissivities (and far-IR) obtained were combined with submillimeter emissivities previously calculated (with PLANCK data) in Planck Collaboration *et al.* (2011c) to build SEDs for each of the survey fields. We compared the SEDs to the standard diffuse ISM dust model (DustEM). We investigated correlations between the different dust emissivities and color ratios. We found LVCs color ratios in agreement with values previously derived for gas integrated over a wide range of velocity. The high $R_{60/100}$ of the IVCs suggests dust evolution through shocks that efficiently shatter large grains to produce a high relative abundance of smaller grains, VSGs. Moreover, our analysis at 12 μm seems to indicate a depletion of PAHs, which agrees with significant destruction of these molecules via shocks. The 25 μm emission is also consistent with a lower abundance of PAHs and more small VSGs contributing at this wavelength. A study of the effects of varying the ISRF strength, PAHs and VSGs relative abundances using DustEM will be carried out in the future to more accurately assess the origin of the relatively low 12 μm and high 60 μm emissivities found in IVCs.

Once the foreground Galactic contributions from the cirrus and zodiacal emission have been removed from the residual maps of the faint fields, only the extragalactic CIB emission remains. The fluctuations in the residual maps were assessed. We found new upper limits for the CIBA at IRAS wavelengths. Using the faint fields (which have little contamination of molecular gas in the residual maps), we also provided an estimate of the power spectrum of the CIBA. For the brighter fields, we found steeper slopes consistent with the power spectrum behaviour of cirrus clouds.

6.1.3   Infrared emission of SNRs in the Galactic Plane

The *Spitzer* MIPSGAL legacy survey was used to detect infrared counterparts to supernova remnant candidates in the Green's catalog. This survey scanned most of the Galactic Plane at 24 and 70 μm (from $10° < l < 65°$ and $285° < l < 350°$, $|b| < 1°$). We complement our comprehensive mid-IR study with the 8 μm IRAC data from the GLIMPSE survey, which has approximately the same Galactic coverage. The study of SNRs in the IR is important as it probes their dust content and the emission lines enhanced by density gradients produced by strong collisions. Our search achieved a mid-IR detection rate of 32% (39 out of 121 remnant candidates). We found evidence of younger SNRs showing low F_8/F_{24} and F_{70}/F_{24} color ratios. Although these color ratios can be used to differentiate between the various IR emission mechanisms, we find that this marker is not always robust. We also found color ratios in some candidates similar to those of H II regions. We reported SNRs dust temperatures be-

tween 45 to 70 K (for $\beta = 2$) using a simple modified blackbody at 24 and 70 μm. From the color temperature ($T_{24/70}$) found, we made upper estimates for the SNRs dust mass (0.02 to 2.5 $M_\odot$). Using archival radio data at 1.4 GHz (from the MAGPIS and VGPS surveys and from the MOST telescope), we found that most candidates have IR-to-radio ratios characteristic of SNRs. However, six (about 18% of the detected sample) have ratios closer to those found for H II regions. The slope of the logarithmic correlation between 'total' mid-infrared flux (24 and 70 μm) and the 1.4 GHz non-thermal radio flux is close to the value seen in galaxies.

We also found that there is a strong morphological association between the mid-IR 24 μm emission and the X-ray emission (traced by *Chandra* data) in bright X-ray remnants. We suggested that the bright 24 μm emission in these remnants is most likely due to collisionally heated dust grains in the hot plasma. The morphology of the 24 μm emission generally differs from what is seen at 8 and 70 μm, indicating a different emission mechanism. We built SEDs for a sample of selected remnants from the radio, IR to X-ray wavelengths. We found evidence that the ratio of IR to X-ray power seems to increase with the remnant's age and their cooling at high energies is comparable to the energy released in the IR.

A detailed overview of the IR morphology and other relevant features of each detected remnant can be found in the appendix of Pinheiro Gonçalves *et al.* (2011).

6.2   Future work

6.2.1   Gaussian Decomposition of the H I profiles

Based on the numerous clouds of atomic gas in any line of sight, gaussian decomposition methods can be a useful tool in separating different velocity structures. Indeed, the main motivation behind such methods is to attain a good statistical description of the physical properties of the H I gas. It has been known for quite some time that the ISM is a three phase medium, with the most abundant component (H) found either in a neutral or ionized form depending on the medium conditions (e.g., McKee & Ostriker 1977). When in the neutral state, the gas can be in two stable configurations, either in a cold ($\sim$ 80 K) or warm phase ($\sim$ 8000 K). Although we cannot infer the kinetic temperature directly from the 21-cm emission line, it is expected that the warmer gas will display a broader profile, a natural consequence of its thermal energy distribution, while the colder gas typically has a narrower (though turbulently broadened) profile. Given the two stable phases in which the neutral H I can be found, is it reasonable to assume that the dust associated with each will behave similarly?

Based on the large amounts of H I data available (from our GBT survey) with high spatial and frequency resolution, we end with some preliminary statistical profile studies of H I emission spectra. A simple assumption is that the whole H I spectrum can be decomposed into gaussian profiles. Assuming that the 21-cm emission line is well approximated by a gaussian,
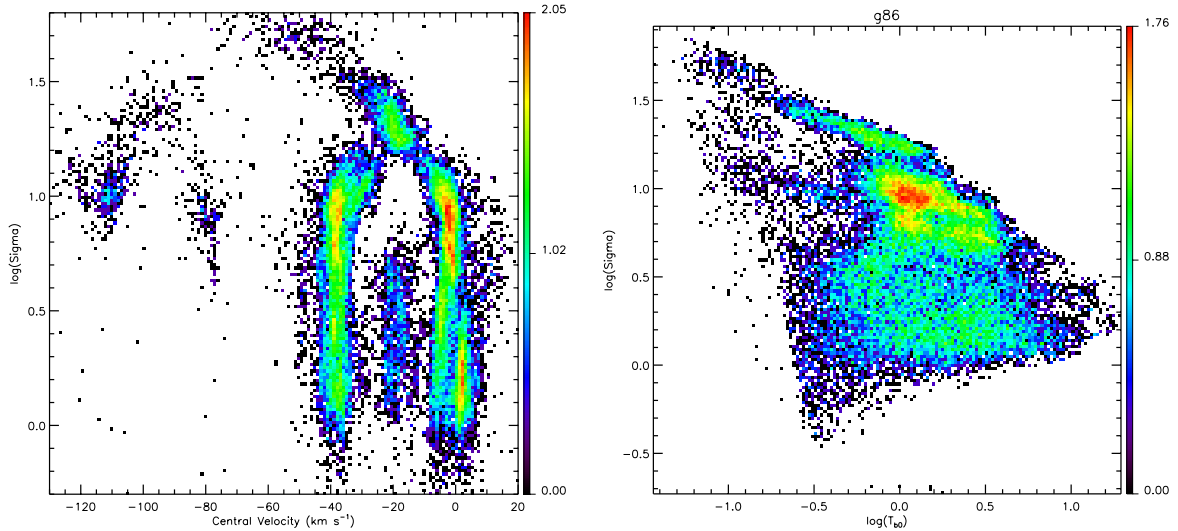
Figure 6.1: 2D histograms for IVC G86 line profile parameters from GBT 21-cm single-dish observations. *Left*: Centroid velocity *vs σ*. *Right*: Peak brightness temperature *vs σ*. The colorbar represents the log of the number of gaussians in each bin of the histogram (150 bins for each axis).

more complex H I profiles can be seen as the sum of multiple gaussian distributions. Our group has developed an iterative gaussian decomposition code to study the statistical properties of the H I gas in our survey fields. This code follows the decomposition methodology adopted by Haud (2000) to analyze the Leiden-Dwingeloo survey at a resolution of 36′. We have already used this code for some fields to explore the statistical characteristics and distribution of the profiles found.

Some statistics for the decomposed profiles obtained from the intermediate velocity cloud field *g86* are shown in Figure 6.1. In addition to this in-house code, we have developed a complementary tool which can project the zero-th moment map of specific regions (user-selectable) in 2-D histograms like Figure 6.1. The plot on the right in Figure 6.2 was obtained using this tool by selecting the over dense region at -40 km s^{-1} in the left histogram in Figure 6.1.

Results from this work will also be checked against the theoretical predictions from Saury *et al.* (2013) that studied the effects of thermal instability in a turbulent medium.

6.2.2 More on dust emissivities studies in the diffuse ISM

We can use the aforementioned gaussian decomposition method to complement or refine our method in selecting velocity components for 21-cm H I column density maps obtained with the GBT. For example, separate maps from narrow and broader line components can be used to further study color variations associated with cold and warm H I in the same way as described in Chapter 4.
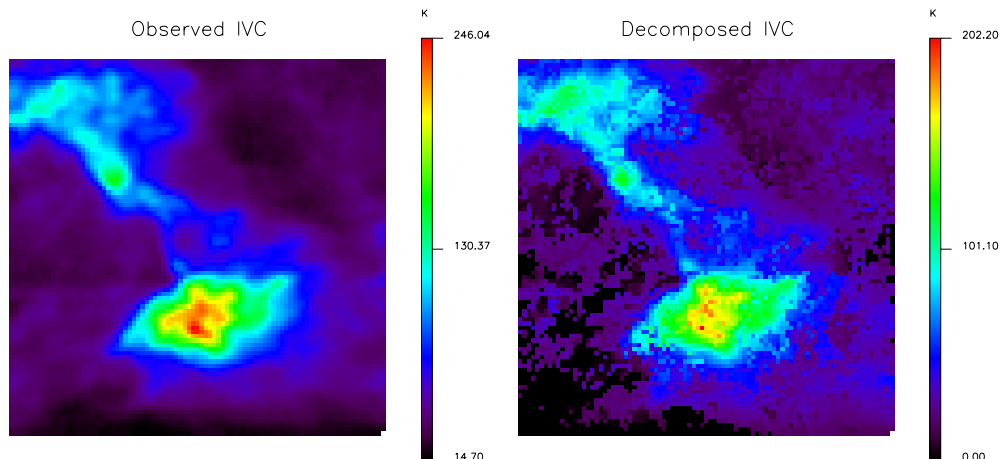
Figure 6.2: 0-*th* moment maps for G86. *Left*: observations. *Right*: result after decomposition and selecting the region in Figure 6.1 (*left*) at $-40 \, \text{km s}^{-1}$.

The 857 GHz masks developed in Chapter 4 were a good proxy for determining sites of possible molecular content within the survey fields. As explained in Planck Collaboration *et al.* (2011c), this wavelength was picked because we assume a constant temperature for all dust along the line of sight within each velocity component and only small color variations are expected. However, we know that for certain fields such as *bootes*, the dust spatially associated with the intermediate velocity gas has a different emissivity from the local dust and such a feature is more easily seen at 100 *μm*. We plan to do the spatial correlation analysis on the same fields but using 100 *μm* IRIS/IRAS masks.

We propose to do a similar type of spatial correlation analysis (with the same sample of fields) but now omitting the term ϵ_{HVC} in our multilinear model. This will also allow us to see if there is any significant change in the local and IVCs dust emissivity estimates; are they robust? Additionally, to study the nature of any residual IR emission (once the multilinear template best fit model is removed from the IRIS maps), we also propose to do an SED of the correlation between residual maps, now extending to mid-IR wavelengths.

6.3   Final Remarks

This thesis encompasses the study of dust and gas in different ISM environments. We have explored the relation between H I column density and infrared dust emission in the diffuse ISM as well as the infrared emission of SNRs in the dense medium of the Galactic Plane. These reflect multiple stages and processes the Galactic ISM goes through including dust evolution. Further interesting science on the properties of dust will no doubt be revealed through IR-focused missions such as AKARI and WISE.

Bibliography

Appleton, P. N., Fadda, D. T., Marleau, F. R., Frayer, D. T., Helou, G., Condon, J. J., Choi, P. I., Yan, L., Lacy, M., Wilson, G., Armus, L., Chapman, S. C., Fang, F., Heinrichson, I., Im, M., Jannuzi, B. T., Storrie-Lombardi, L. J., Shupe, D., Soifer, B. T., Squires, G., & Teplitz, H. I. (2004). *Astrophysical Journal, Supplement,* **154**, 147–150.

Arendt, R. G. (1989). *Astrophysical Journal, Supplement,* **70**, 181–212.

Arendt, R. G., Dwek, E., & Moseley, S. H. (1999). *Astrophysical Journal,* **521**, 234–245.

Arendt, R. G., Odegard, N., Weiland, J. L., Sodroski, T. J., Hauser, M. G., Dwek, E., Kelsall, T., Moseley, S. H., Silverberg, R. F., Leisawitz, D., Mitchell, K., Reach, W. T., & Wright, E. L. (1998). *Astrophysical Journal,* **508**, 74–105.

Arnal, E. M., Bajaja, E., Larrarte, J. J., Morras, R., & Pöppel, W. G. L. (2000). *Astronomy and Astrophysics, Supplement,* **142**, 35–40.

Bajaja, E., Arnal, E. M., Larrarte, J. J., Morras, R., Pöppel, W. G. L., & Kalberla, P. M. W. (2005). *Astronomy and Astrophysics,* **440**, 767–773.

Barlow, M. J., Krause, O., Swinyard, B. M., Sibthorpe, B., Besel, M., Wesson, R., Ivison, R. J., Dunne, L., Gear, W. K., Gomez, H. L., Hargrave, P. C., Henning, T., Leeks, S. J., Lim, T. L., Olofsson, G., & Polehampton, E. T. (2010). *Astronomy and Astrophysics,* **518**, L138+.

Bell, E. F. (2003). *Astrophysical Journal,* **586**, 794–813.

Benjamin, R. A., Churchwell, E., Babler, B. L., Bania, T. M., Clemens, D. P., Cohen, M., Dickey, J. M., Indebetouw, R., Jackson, J. M., Kobulnicky, H. A., Lazarian, A., Marston, A. P., Mathis, J. S., Meade, M. R., Seager, S., Stolovy, S. R., Watson, C., Whitney, B. A., Wolff, M. J., & Wolfire, M. G. (2003). *Publications of the ASP,* **115**, 953–964.

Bernard, J.-P., Reach, W. T., Paradis, D., Meixner, M., Paladini, R., Kawamura, A., Onishi, T., Vijh, U., Gordon, K., Indebetouw, R., Hora, J. L., Whitney, B., Blum, R., Meade, M., Babler, B., Churchwell, E. B., Engelbracht, C. W., For, B.-Q., Misselt, K., Leitherer, C., Cohen, M., Boulanger, F., Frogel, J. A., Fukui, Y., Gallagher, J., Gorjian, V., Harris, J., Kelly, D., Latter, W. B., Madden, S., Markwick-Kemper, C., Mizuno, A., Mizuno, N., Mould, J., Nota, A., Oey,

M. S., Olsen, K., Panagia, N., Perez-Gonzalez, P., Shibai, H., Sato, S., Smith, L., Staveley-Smith, L., Tielens, A. G. G. M., Ueta, T., Van Dyk, S., Volk, K., Werner, M., & Zaritsky, D. (2008). *Astronomical Journal,* **136**, 919–945.

Bethermin, M. & Dole, H. (2010). In: *Cosmic Radiation Fields: Sources in the early Universe (CRF 2010),* (Raue, M., Kneiske, T., Horns, D., Elsaesser, D., & Hauschildt, P., eds) p. 2,.

Béthermin, M., Dole, H., Beelen, A., & Aussel, H. (2010). *Astronomy and Astrophysics,* **512**, A78.

Béthermin, M., Dole, H., Lagache, G., Le Borgne, D., & Penin, A. (2011). *Astronomy and Astrophysics,* **529**, A4.

Blagrave, K., Lockman, F. J., & Martin, P. G. (2010). In: *Astronomical Society of the Pacific Conference Series,* (Kothes, R., Landecker, T. L., & Willis, A. G., eds) volume 438 of *Astronomical Society of the Pacific Conference Series* p. 156,.

Blair, W. P., Ghavamian, P., Long, K. S., Williams, B. J., Borkowski, K. J., Reynolds, S. P., & Sankrit, R. (2007). *Astrophysical Journal,* **662**, 998–1013.

Bohlin, R. C., Savage, B. D., & Drake, J. F. (1978). *Astrophysical Journal,* **224**, 132–142.

Boothroyd, A. I., Blagrave, K., Lockman, F. J., Martin, P. G., Pinheiro Gonçalves, D., & Srikanth, S. (2011). *Astronomy and Astrophysics,* **536**, A81.

Borkowski, K. J., Williams, B. J., Reynolds, S. P., Blair, W. P., Ghavamian, P., Sankrit, R., Hendrick, S. P., Long, K. S., Raymond, J. C., Smith, R. C., Points, S., & Winkler, P. F. (2006). *Astrophysical Journal, Letters,* **642**, L141–L144.

Boulanger, F., Abergel, A., Bernard, J.-P., Burton, W. B., Desert, F.-X., Hartmann, D., Lagache, G., & Puget, J.-L. (1996). *Astronomy and Astrophysics,* **312**, 256–262.

Boulanger, F. & Perault, M. (1988). *Astrophysical Journal,* **330**, 964–985.

Boyle, B. J., Cornwell, T. J., Middelberg, E., Norris, R. P., Appleton, P. N., & Smail, I. (2007). *Monthly Notices of the Royal Astronomical Society,* **376**, 1182–1188.

Bregman, J. N. (1980). *Astrophysical Journal,* **236**, 577–591.

Broadbent, A., Osborne, J. L., & Haslam, C. G. T. (1989). *Monthly Notices of the Royal Astronomical Society,* **237**, 381–410.

Brogan, C. L., Gelfand, J. D., Gaensler, B. M., Kassim, N. E., & Lazio, T. J. W. (2006). *Astrophysical Journal, Letters,* **639**, L25–L29.

Burstein, D. & Heiles, C. (1982). *Astronomical Journal,* **87**, 1165–1189.

Calabretta, M. R. & Greisen, E. W. (2002). *Astronomy and Astrophysics,* **395**, 1077–1122.

Carey, S. J., Noriega-Crespo, A., Mizuno, D. R., Shenoy, S., Paladini, R., Kraemer, K. E., Price, S. D., Flagey, N., Ryan, E., Ingalls, J. G., Kuchar, T. A., Pinheiro Gonçalves, D., Indebetouw, R., Billot, N., Marleau, F. R., Padgett, D. L., Rebull, L. M., Bressert, E., Ali, B., Molinari, S., Martin, P. G., Berriman, G. B., Boulanger, F., Latter, W. B., Miville-Deschenes, M. A., Shipman, R., & Testi, L. (2009). *Publications of the ASP,* **121**, 76–97.

Carter, L. M., Dickel, J. R., & Bomans, D. J. (1997). *Publications of the ASP,* **109**, 990–997.

Cesarsky, D., Cox, P., Pineau des Forêts, G., van Dishoeck, E. F., Boulanger, F., & Wright, C. M. (1999). *Astronomy and Astrophysics,* **348**, 945–949.

Chen, Y., Su, Y., Slane, P. O., & Wang, Q. D. (2004). *Astrophysical Journal,* **616**, 885–894.

Churchwell, E., Babler, B. L., Meade, M. R., Whitney, B. A., Benjamin, R., Indebetouw, R., Cyganowski, C., Robitaille, T. P., Povich, M., Watson, C., & Bracker, S. (2009). *Publications of the ASP,* **121**, 213–230.

Clark, D. H. & Stephenson, F. R. (1977). *The historical supernovae*.

Compiègne, M., Flagey, N., Noriega-Crespo, A., Martin, P. G., Bernard, J., Paladini, R., & Molinari, S. (2010). *Astrophysical Journal, Letters,* **724**, L44–L47.

Compiègne, M., Verstraete, L., Jones, A., Bernard, J.-P., Boulanger, F., Flagey, N., Le Bourlot, J., Paradis, D., & Ysard, N. (2011). *Astronomy and Astrophysics,* **525**, A103.

de Vries, H. W., Heithausen, A., & Thaddeus, P. (1987). *Astrophysical Journal,* **319**, 723–729.

Desert, F.-X., Boulanger, F., & Puget, J. L. (1990). *Astronomy and Astrophysics,* **237**, 215–236.

Douvion, T., Lagage, P. O., Cesarsky, C. J., & Dwek, E. (2001). *Astronomy and Astrophysics,* **373**, 281–291.

Draine, B. T. (1981). *Astrophysical Journal,* **245**, 880–890.

Draine, B. T. (2003). *Annual Review of Astron and Astrophys,* **41**, 241–289.

Draine, B. T. (2011). *Physics of the Interstellar and Intergalactic Medium*.

Draine, B. T. & Anderson, N. (1985). *Astrophysical Journal,* **292**, 494–499.

Draine, B. T. & Lee, H. M. (1984). *Astrophysical Journal,* **285**, 89–108.

Dubner, G. M., Moffett, D. A., Goss, W. M., & Winkler, P. F. (1993). *Astronomical Journal,* **105**, 2251–2259.

Dwek, E. (1987). *Astrophysical Journal,* **322**, 812–821.

Dwek, E. & Arendt, R. G. (1992). *Annual Review of Astron and Astrophys,* **30**, 11–50.

Dwek, E., Petre, R., Szymkowiak, A., & Rice, W. L. (1987). *Astrophysical Journal, Letters,* **320**, L27–L33.

Dwek, E. & Werner, M. W. (1981). *Astrophysical Journal,* **248**, 138–151.

Engelbracht, C. W., Blaylock, M., Su, K. Y. L., Rho, J., Rieke, G. H., Muzerolle, J., Padgett, D. L., Hines, D. C., Gordon, K. D., Fadda, D., Noriega-Crespo, A., Kelly, D. M., Latter, W. B., Hinz, J. L., Misselt, K. A., Morrison, J. E., Stansberry, J. A., Shupe, D. L., Stolovy, S., Wheaton, W. A., Young, E. T., Neugebauer, G., Wachter, S., Pérez-González, P. G., Frayer, D. T., & Marleau, F. R. (2007). *Publications of the ASP,* **119**, 994–1018.

Ewen, H. I. & Purcell, E. M. (1951). *Nature,* **168**, 356.

Fesen, R. A. & Kirshner, R. P. (1980). *Astrophysical Journal,* **242**, 1023–1040.

Frail, D. A., Goss, W. M., Reynoso, E. M., Giacani, E. B., Green, A. J., & Otrupcek, R. (1996). *Astronomical Journal,* **111**, 1651–+.

Fuerst, E., Reich, W., & Sofue, Y. (1987). *Astronomy and Astrophysics, Supplement,* **71**, 63–67.

Gautier, III, T. N., Boulanger, F., Perault, M., & Puget, J. L. (1992). *Astronomical Journal,* **103**, 1313–1324.

Gordon, K. D., Engelbracht, C. W., Fadda, D., Stansberry, J., Wachter, S., Frayer, D. T., Rieke, G., Noriega-Crespo, A., Latter, W. B., Young, E., Neugebauer, G., Balog, Z., Beeman, J. W., Dole, H., Egami, E., Haller, E. E., Hines, D., Kelly, D., Marleau, F., Misselt, K., Morrison, J., Pérez-González, P., Rho, J., & Wheaton, W. A. (2007). *Publications of the ASP,* **119**, 1019–1037.

Gorjian, V., Wright, E. L., & Chary, R. R. (2000). *Astrophysical Journal,* **536**, 550–560.

Gotthelf, E. V., Vasisht, G., Boylan-Kolchin, M., & Torii, K. (2000). *Astrophysical Journal, Letters,* **542**, L37–L40.

Green, A. J., Frail, D. A., Goss, W. M., & Otrupcek, R. (1997). *Astronomical Journal,* **114**, 2058–+.

Green, D. A. (2009). *Bulletin of the Astronomical Society of India,* **37**, 45–+.

Green, D. A. & Dewdney, P. E. (1992). *Monthly Notices of the Royal Astronomical Society,* **254**, 686–692.

Guillard, P., Boulanger, F., Cluver, M. E., Appleton, P. N., Pineau des Forets, G., & Ogle, P. (2010). *ArXiv e-prints,* .

Harrus, I. M. & Slane, P. O. (1999). *Astrophysical Journal,* **516**, 811–816.

Hartmann, D. & Burton, W. B. (1997). *Atlas of Galactic Neutral Hydrogen*.

Haslam, C. G. T. & Osborne, J. L. (1987). *Nature,* **327**, 211–214.

Haud, U. (2000). *Astronomy and Astrophysics,* **364**, 83–101.

Hauser, M. G., Arendt, R. G., Kelsall, T., Dwek, E., Odegard, N., Weiland, J. L., Freudenreich, H. T., Reach, W. T., Silverberg, R. F., Moseley, S. H., Pei, Y. C., Lubin, P., Mather, J. C., Shafer, R. A., Smoot, G. F., Weiss, R., Wilkinson, D. T., & Wright, E. L. (1998). *Astrophysical Journal,* **508**, 25–43.

Hauser, M. G. & Dwek, E. (2001). *Annual Review of Astron and Astrophys,* **39**, 249–307.

Hauser, M. G., Gillett, F. C., Low, F. J., Gautier, T. N., Beichman, C. A., Aumann, H. H., Neugebauer, G., Baud, B., Boggess, N., & Emerson, J. P. (1984). *Astrophysical Journal, Letters,* **278**, L15–L18.

Heiles, C., Reach, W. T., & Koo, B.-C. (1988). *Astrophysical Journal,* **332**, 313–327.

Helfand, D. J., Becker, R. H., White, R. L., Fallon, A., & Tuttle, S. (2006). *Astronomical Journal,* **131**, 2525–2537.

Helou, G., Soifer, B. T., & Rowan-Robinson, M. (1985). *Astrophysical Journal, Letters,* **298**, L7–L11.

Hewitt, J. W., Yusef-Zadeh, F., & Wardle, M. (2008). *Astrophysical Journal,* **683**, 189–206.

Hildebrand, R. H. (1983). *Quarterly Journal of the Royal Astronomical Society,* **24**, 267.

Hines, D. C., Rieke, G. H., Gordon, K. D., Rho, J., Misselt, K. A., Woodward, C. E., Werner, M. W., Krause, O., Latter, W. B., Engelbracht, C. W., Egami, E., Kelly, D. M., Muzerolle, J., Stansberry, J. A., Su, K. Y. L., Morrison, J. E., Young, E. T., Noriega-Crespo, A., Padgett, D. L., Gehrz, R. D., Polomski, E., Beeman, J. W., & Haller, E. E. (2004). *Astrophysical Journal, Supplement,* **154**, 290–295.

Hwang, U., Petre, R., & Hughes, J. P. (2000). *Astrophysical Journal,* **532**, 970–979.

Jiang, B., Chen, Y., Wang, J., Su, Y., Zhou, X., Safi-Harb, S., & DeLaney, T. (2010). *Astrophysical Journal,* **712**, 1147–1156.

Jones, A. P. (2004). In: *Astrophysics of Dust,* (Witt, A. N., Clayton, G. C., & Draine, B. T., eds) volume 309 of *Astronomical Society of the Pacific Conference Series* p. 347,.

Jones, A. P., Tielens, A. G. G. M., & Hollenbach, D. J. (1996). *Astrophysical Journal,* **469**, 740.

Jones, A. P., Tielens, A. G. G. M., Hollenbach, D. J., & McKee, C. F. (1994). *Astrophysical Journal,* **433**, 797–810.

Kalberla, P. M. W., Burton, W. B., Hartmann, D., Arnal, E. M., Bajaja, E., Morras, R., & Pöppel, W. G. L. (2005). *Astronomy and Astrophysics,* **440**, 775–782.

Kalberla, P. M. W., Mebold, U., & Reif, K. (1982). *Astronomy and Astrophysics,* **106**, 190–196.

Kashlinsky, A. & Odenwald, S. (2000). *Astrophysical Journal,* **528**, 74–95.

Kaspi, V. M., Roberts, M. E., Vasisht, G., Gotthelf, E. V., Pivovaroff, M., & Kawai, N. (2001). *Astrophysical Journal,* **560**, 371–377.

Kelsall, T., Weiland, J. L., Franz, B. A., Reach, W. T., Arendt, R. G., Dwek, E., Freudenreich, H. T., Hauser, M. G., Moseley, S. H., Odegard, N. P., Silverberg, R. F., & Wright, E. L. (1998). *Astrophysical Journal,* **508**, 44–73.

Keohane, J. W., Reach, W. T., Rho, J., & Jarrett, T. H. (2007). *Astrophysical Journal,* **654**, 938–944.

Kerp, J., Winkel, B., Ben Bekhti, N., Flöer, L., & Kalberla, P. M. W. (2011). *Astronomische Nachrichten,* **332**, 637.

Kim, S.-H., Martin, P. G., & Hendry, P. D. (1994). *Astrophysical Journal,* **422**, 164–175.

Köhler, M., Stepnik, B., Jones, A. P., Guillet, V., Abergel, A., Ristorcelli, I., & Bernard, J.-P. (2012). *Astronomy and Astrophysics,* **548**, A61.

Koo, B., Moon, D., Lee, H., Lee, J., & Matthews, K. (2007). *Astrophysical Journal,* **657**, 308–317.

Kulkarni, S. R. & Heiles, C. (1988). *Neutral hydrogen and the diffuse interstellar medium* pp. 95–153.

Lagache, G., Haffner, L. M., Reynolds, R. J., & Tufte, S. L. (2000). *Astronomy and Astrophysics, ,* **354**, 247–252.

Lazendic, J. S., Slane, P. O., Hughes, J. P., Chen, Y., & Dame, T. M. (2005). *Astrophysical Journal, ,* **618**, 733–743.

Leahy, D. A. & Tian, W. W. (2008). *Astronomy and Astrophysics, ,* **480**, L25–L28.

Lee, H., Moon, D., Koo, B., Lee, J., & Matthews, K. (2009). *Astrophysical Journal, ,* **691**, 1042–1049.

Leger, A. & Puget, J. L. (1984). *Astronomy and Astrophysics, ,* **137**, L5–L8.

Li, A. & Draine, B. T. (2001). *Astrophysical Journal, ,* **554**, 778–802.

Livingstone, M. A., Kaspi, V. M., Gotthelf, E. V., & Kuiper, L. (2006). *Astrophysical Journal, ,* **647**, 1286–1292.

Low, F. J., Young, E., Beintema, D. A., Gautier, T. N., Beichman, C. A., Aumann, H. H., Gillett, F. C., Neugebauer, G., Boggess, N., & Emerson, J. P. (1984). *Astrophysical Journal, Letters, ,* **278**, L19–L22.

Markwardt, C. B. (2009). In: *Astronomical Data Analysis Software and Systems XVIII*, (Bohlender, D. A., Durand, D., & Dowler, P., eds), volume 411 of *Astronomical Society of the Pacific Conference Series*, p. 251,.

Mathis, J. S., Mezger, P. G., & Panagia, N. (1983). *Astronomy and Astrophysics,* **128**, 212–229.

Mathis, J. S., Rumpl, W., & Nordsieck, K. H. (1977). *Astrophysical Journal,* **217**, 425–433.

Mazin, D. & Raue, M. (2007). *Astronomy and Astrophysics,* **471**, 439–452.

McClure-Griffiths, N. M., Pisano, D. J., Calabretta, M. R., Ford, H. A., Lockman, F. J., Staveley-Smith, L., Kalberla, P. M. W., Bailin, J., Dedes, L., Janowiecki, S., Gibson, B. K., Murphy, T., Nakanishi, H., & Newton-McGee, K. (2009). *Astrophysical Journal, Supplement,* **181**, 398–412.

McKee, C. F. & Ostriker, J. P. (1977). *Astrophysical Journal,* **218**, 148–169.

Meyerdierks, H., Heithausen, A., & Reif, K. (1991). *Astronomy and Astrophysics,* **245**, 247–256.

Micelotta, E. R., Jones, A. P., & Tielens, A. G. G. M. (2010). *Astronomy and Astrophysics,* **510**, A36.

Miville-Deschênes, M.-A., Boulanger, F., Reach, W. T., & Noriega-Crespo, A. (2005). *Astrophysical Journal, Letters,* **631**, L57–L60.

Miville-Deschênes, M.-A., Joncas, G., Falgarone, E., & Boulanger, F. (2003). *Astronomy and Astrophysics,* **411**, 109–121.

Miville-Deschênes, M.-A. & Lagache, G. (2005). *Astrophysical Journal, Supplement,* **157**, 302–323.

Miville-Deschênes, M.-A., Lagache, G., & Puget, J.-L. (2002). *Astronomy and Astrophysics,* **393**, 749–756.

Mizuno, D. R., Carey, S. J., Noriega-Crespo, A., Paladini, R., Padgett, D., Shenoy, S., Kuchar, T. A., Kraemer, K. E., & Price, S. D. (2008). *Publications of the ASP,* **120**, 1028–1042.

Moffett, D. A. & Reynolds, S. P. (1994). *Astrophysical Journal,* **437**, 705–726.

Moon, D., Koo, B., Lee, H., Matthews, K., Lee, J., Pyo, T., Seok, J. Y., & Hayashi, M. (2009). *Astrophysical Journal, Letters,* **703**, L81–L85.

Morton, T. D., Slane, P., Borkowski, K. J., Reynolds, S. P., Helfand, D. J., Gaensler, B. M., & Hughes, J. P. (2007). *Astrophysical Journal,* **667**, 219–225.

Murphy, E. J. (2009). *Astrophysical Journal,* **706**, 482–496.

Neufeld, D. A., Hollenbach, D. J., Kaufman, M. J., Snell, R. L., Melnick, G. J., Bergin, E. A., & Sonnentrucker, P. (2007). *Astrophysical Journal,* **664**, 890–908.

Neufeld, D. A. & Yuan, Y. (2008). *Astrophysical Journal,* **678**, 974–984.

Neugebauer, G., Habing, H. J., van Duinen, R., Aumann, H. H., Baud, B., Beichman, C. A., Beintema, D. A., Boggess, N., Clegg, P. E., de Jong, T., Emerson, J. P., Gautier, T. N., Gillett, F. C., Harris, S., Hauser, M. G., Houck, J. R., Jennings, R. E., Low, F. J., Marsden, P. L., Miley, G., Olnon, F. M., Pottasch, S. R., Raimond, E., Rowan-Robinson, M., Soifer, B. T., Walker, R. G., Wesselius, P. R., & Young, E. (1984). *Astrophysical Journal, Letters,* **278**, L1–L6.

Noriega-Crespo, A., Hines, D. C., Gordon, K., Marleau, F. R., Rieke, G. H., Rho, J., & Latter, W. B. (2009). In: *The Evolving ISM in the Milky Way and Nearby Galaxies* ,.

Oliva, E., Lutz, D., Drapatz, S., & Moorwood, A. F. M. (1999a). *Astronomy and Astrophysics,* **341**, L75–L78.

Oliva, E., Moorwood, A. F. M., Drapatz, S., Lutz, D., & Sturm, E. (1999b). *Astronomy and Astrophysics,* **343**, 943–952.

Ostriker, J. & Silk, J. (1973). *Astrophysical Journal, Letters,* **184**, L113+.

Paladini, R., Umana, G., Veneziani, M., Noriega-Crespo, A., Anderson, L. D., Piacentini, F., Pinheiro Gonçalves, D., Paradis, D., Tibbs, C. T., Bernard, J.-P., & Natoli, P. (2012). *Astrophysical Journal,* **760**, 149.

Palme, H. & Jones, A. (2005). *Solar System Abundances of the Elements* p. 41. Elsevier B.

Paradis, D., Bernard, J.-P., & Mény, C. (2009). *Astronomy and Astrophysics, ,* **506**, 745–756.

Paradis, D., Paladini, R., Noriega-Crespo, A., Lagache, G., Kawamura, A., Onishi, T., & Fukui, Y. (2011). *Astrophysical Journal, ,* **735**, 6.

Patnaik, A. R., Hunt, G. C., Salter, C. J., Shaver, P. A., & Velusamy, T. (1990). *Astronomy and Astrophysics, ,* **232**, 467–476.

Peek, J. E. G., Heiles, C., Putman, M. E., & Douglas, K. (2009). *Astrophysical Journal, ,* **692**, 827–838.

Pénin, A., Lagache, G., Noriega-Crespo, A., Grain, J., Miville-Deschênes, M.-A., Ponthieu, N., Martin, P., Blagrave, K., & Lockman, F. J. (2012). *Astronomy and Astrophysics, ,* **543**, A123.

Pinheiro Gonçalves, D., Noriega-Crespo, A., Paladini, R., Martin, P. G., & Carey, S. J. (2011). *Astronomical Journal, ,* **142**, 47.

Planck Collaboration, Abergel, A., Ade, P. A. R., Aghanim, N., Arnaud, M., Ashdown, M., Aumont, J., Baccigalupi, C., Balbi, A., Banday, A. J., & et al. (2011a). *Astronomy and Astrophysics, ,* **536**, A25.

Planck Collaboration, Abergel, A., Ade, P. A. R., Aghanim, N., Arnaud, M., Ashdown, M., Aumont, J., Baccigalupi, C., Balbi, A., Banday, A. J., & et al. (2011b). *Astronomy and Astrophysics,* , **536**, A21.

Planck Collaboration, Abergel, A., Ade, P. A. R., Aghanim, N., Arnaud, M., Ashdown, M., Aumont, J., Baccigalupi, C., Balbi, A., Banday, A. J., & et al. (2011c). *Astronomy and Astrophysics,* , **536**, A24.

Planck Collaboration, Ade, P. A. R., Aghanim, N., Arnaud, M., Ashdown, M., Aumont, J., Baccigalupi, C., Balbi, A., Banday, A. J., Barreiro, R. B., & et al. (2011d). *Astronomy and Astrophysics,* , **536**, A18.

Rakowski, C. E., Badenes, C., Gaensler, B. M., Gelfand, J. D., Hughes, J. P., & Slane, P. O. (2006). *Astrophysical Journal,* , **646**, 982–1000.

Raymond, J. C., Cox, D. P., & Smith, B. W. (1976). *Astrophysical Journal,* , **204**, 290–292.

Reach, W. T., Abergel, A., Boulanger, F., Desert, F.-X., Perault, M., Bernard, J.-P., Blommaert, J., Cesarsky, C., Cesarsky, D., Metcalfe, L., Puget, J.-L., Sibille, F., & Vigroux, L. (1996). *Astronomy and Astrophysics,* , **315**, L381–L384.

Reach, W. T., Koo, B.-C., & Heiles, C. (1994). *Astrophysical Journal,* , **429**, 672–693.

Reach, W. T. & Rho, J. (2000). *Astrophysical Journal,* , **544**, 843–858.

Reach, W. T., Rho, J., & Jarrett, T. H. (2005). *Astrophysical Journal,* , **618**, 297–320.

Reach, W. T., Rho, J., Jarrett, T. H., & Lagage, P. (2002). *Astrophysical Journal,* , **564**, 302–316.

Reach, W. T., Rho, J., Tappe, A., Pannuti, T. G., Brogan, C. L., Churchwell, E. B., Meade, M. R., Babler, B., Indebetouw, R., & Whitney, B. A. (2006). *Astronomical Journal,* , **131**, 1479–1500.

Reach, W. T., Wall, W. F., & Odegard, N. (1998). *Astrophysical Journal,* , **507**, 507–525.

Renault, C., Barrau, A., Lagache, G., & Puget, J.-L. (2001). *Astronomy and Astrophysics,* , **371**, 771–778.

Reynolds, S. P., Borkowski, K. J., Hwang, U., Harrus, I., Petre, R., & Dubner, G. (2006). *Astrophysical Journal, Letters,* , **652**, L45–L48.

Reynoso, E. M. & Mangum, J. G. (2001). *Astronomical Journal,* , **121**, 347–353.

Rho, J., Jarrett, T. H., Cutri, R. M., & Reach, W. T. (2001). *Astrophysical Journal,* , **547**, 885–898.

Rho, J., Kozasa, T., Reach, W. T., Smith, J. D., Rudnick, L., DeLaney, T., Ennis, J. A., Gomez, H., & Tappe, A. (2008). *Astrophysical Journal,* , **673**, 271–282.

Rho, J. & Petre, R. (1998). *Astrophysical Journal, Letters,* , **503**, L167+.

Rho, J., Reach, W. T., Tappe, A., Rudnick, L., Kozasa, T., Hwang, U., Andersen, M., Gomez, H., Delaney, T., Dunne, L., & Slavin, J. (2009). In: *Cosmic Dust - Near and Far*, (Henning, T., Grün, E., & Steinacker, J., eds), volume 414 of *Astronomical Society of the Pacific Conference Series*, p. 22,.

Safi-Harb, S., Dubner, G., Petre, R., Holt, S. S., & Durouchoux, P. (2005). *Astrophysical Journal, 618*, 321–338.

Saken, J. M., Fesen, R. A., & Shull, J. M. (1992). *Astrophysical Journal, Supplement, 81*, 715–745.

Saury, E., Miville-Deschênes, M.-A., Hennebelle, P., Audit, E., & Schmidt, W. (2013). *ArXiv e-prints,* .

Savage, B. D. & Mathis, J. S. (1979). *Annual Review of Astron and Astrophys, 17*, 73–111.

Schlegel, D. J., Finkbeiner, D. P., & Davis, M. (1998). *Astrophysical Journal, 500*, 525.

Seok, J. Y., Koo, B.-C., Onaka, T., Ita, Y., Lee, H.-G., Lee, J.-J., Moon, D.-S., Sakon, I., Kaneda, H., Lee, H. M., Lee, M. G., & Kim, S. E. (2008). *Publications of the Astronomical Society of Japan, 60*, 453–+.

Seward, F. D., Slane, P. O., Smith, R. K., & Sun, M. (2003). *Astrophysical Journal, 584*, 414–417.

Shapiro, P. R. & Field, G. B. (1976). *Astrophysical Journal, 205*, 762–765.

Shaver, P. A. & Goss, W. M. (1970). *Australian Journal of Physics Astrophysical Supplement, 14*, 133–+.

Sibthorpe, B., Ade, P. A. R., Bock, J. J., Chapin, E. L., Devlin, M. J., Dicker, S., Griffin, M., Gundersen, J. O., Halpern, M., Hargrave, P. C., Hughes, D. H., Jeong, W., Kaneda, H., Klein, J., Koo, B., Lee, H., Marsden, G., Martin, P. G., Mauskopf, P., Moon, D., Netterfield, C. B., Olmi, L., Pascale, E., Patanchon, G., Rex, M., Roy, A., Scott, D., Semisch, C., Truch, M. D. P., Tucker, C., Tucker, G. S., Viero, M. P., & Wiebe, D. V. (2010). *Astrophysical Journal, 719*, 1553–1564.

Slane, P., Chen, Y., Lazendic, J. S., & Hughes, J. P. (2002). *Astrophysical Journal, 580*, 904–908.

Spitzer, L. (1978). *Physical processes in the interstellar medium*.

Stepnik, B., Abergel, A., Bernard, J.-P., Boulanger, F., Cambrésy, L., Giard, M., Jones, A. P., Lagache, G., Lamarre, J.-M., Meny, C., Pajot, F., Le Peintre, F., Ristorcelli, I., Serra, G., & Torre, J.-P. (2003). *Astronomy and Astrophysics, 398*, 551–563.

Stil, J. M., Taylor, A. R., Dickey, J. M., Kavars, D. W., Martin, P. G., Rothwell, T. A., Boothroyd, A. I., Lockman, F. J., & McClure-Griffiths, N. M. (2006). *Astronomical Journal, 132*, 1158–1176.

Strom, R. G. & Greidanus, H. (1992). *Nature, 358*, 654–+.

Su, Y. & Chen, Y. (2008). *Advances in Space Research,* **41**, 401–406.

Su, Y., Chen, Y., Yang, J., Koo, B.-C., Zhou, X., Lu, D.-R., Jeong, I.-G., & DeLaney, T. (2011). *Astrophysical Journal,* **727**, 43–+.

Sun, M., Seward, F. D., Smith, R. K., & Slane, P. O. (2004). *Astrophysical Journal,* **605**, 742–750.

Tappe, A., Rho, J., & Reach, W. T. (2006). *Astrophysical Journal,* **653**, 267–279.

Taylor, A. R., Gibson, S. J., Peracaula, M., Martin, P. G., Landecker, T. L., Brunt, C. M., Dewdney, P. E., Dougherty, S. M., Gray, A. D., Higgs, L. A., Kerton, C. R., Knee, L. B. G., Kothes, R., Purton, C. R., Uyaniker, B., Wallace, B. J., Willis, A. G., & Durand, D. (2003). *Astronomical Journal,* **125**, 3145–3164.

Tian, W. W. & Leahy, D. A. (2008). *Astrophysical Journal,* **677**, 292–296.

Troja, E., Bocchino, F., & Reale, F. (2006). *Astrophysical Journal,* **649**, 258–267.

Tuohy, I. & Garmire, G. (1980). *Astrophysical Journal, Letters,* **239**, L107–L110.

Vasisht, G. & Gotthelf, E. V. (1997). *Astrophysical Journal, Letters,* **486**, L129+.

Velusamy, T., Becker, R. H., & Seward, F. D. (1991). *Astronomical Journal,* **102**, 676–682.

Vink, J. (2004). *Nuclear Physics B Proceedings Supplements,* **132**, 21–30.

Wakker, B. P. & van Woerden, H. (1997). *Annual Review of Astron and Astrophys,* **35**, 217–266.

Walterbos, R. A. M. & Greenawalt, B. (1996). *Astrophysical Journal,* **460**, 696.

Wardle, M. & Yusef-Zadeh, F. (2002). *Science,* **296**, 2350–2354.

Whiteoak, J. B. Z. & Green, A. J. (1996). *Astronomy and Astrophysics, Supplement,* **118**, 329–380.

Whittet, D. C. B., Bode, M. F., Longmore, A. J., Adamson, A. J., McFadzean, A. D., Aitken, D. K., & Roche, P. F. (1988). *Monthly Notices of the Royal Astronomical Society,* **233**, 321–336.

Williams, B. J., Borkowski, K. J., Reynolds, S. P., Blair, W. P., Ghavamian, P., Hendrick, S. P., Long, K. S., Points, S., Raymond, J. C., Sankrit, R., Smith, R. C., & Winkler, P. F. (2006). *Astrophysical Journal, Letters,* **652**, L33–L36.

Williams, D. R. W. (1973). *Astronomy and Astrophysics, Supplement,* **8**, 505.

Williams, R. M., Chu, Y., & Gruendl, R. (2006). *Astronomical Journal,* **132**, 1877–1889.

Wilner, D. J., Reynolds, S. P., & Moffett, D. A. (1998). *Astronomical Journal,* **115**, 247–+.

Wolszczan, A., Cordes, J. M., & Dewey, R. J. (1991). *Astrophysical Journal, Letters,* **372**, L99–L102.

Wright, E. L. (1998). *Astrophysical Journal*, **496**, 1.

Yamauchi, S., Ueno, M., Koyama, K., & Bamba, A. (2005). *Publications of the Astronomical Society of Japan*, **57**, 459–463.